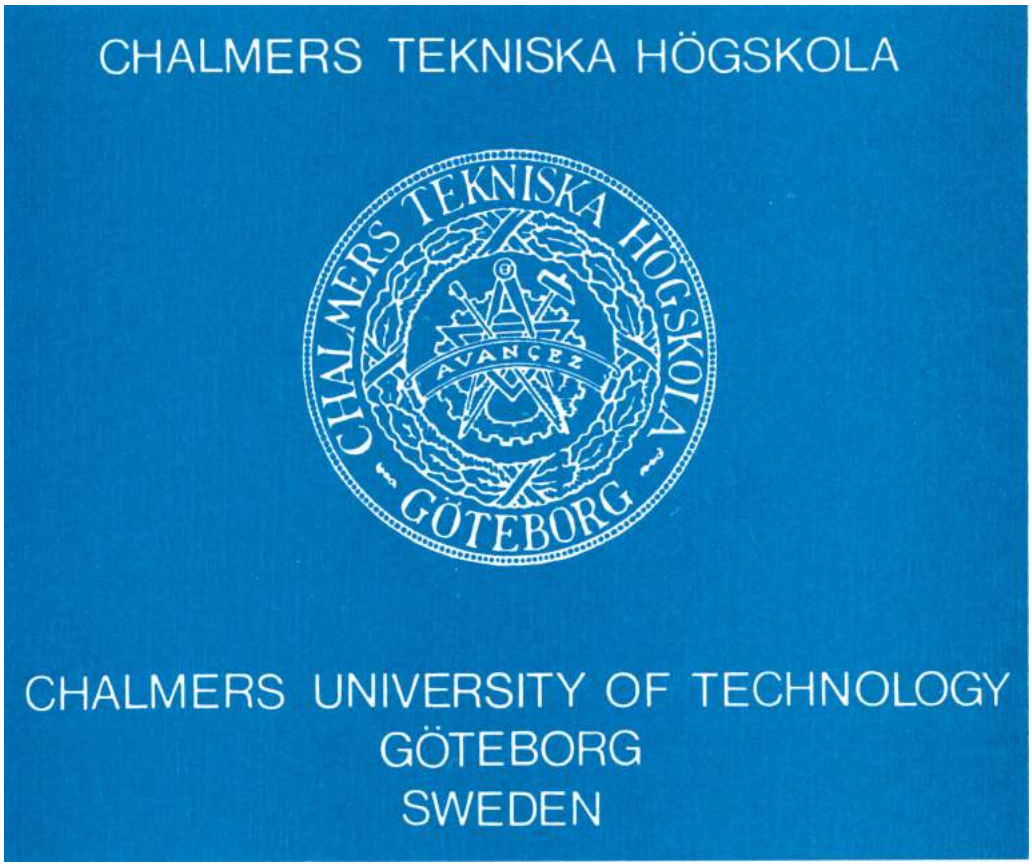

Division of Machine Elements

On the Design and Life Prediction of Transmission Belts made of Elastomer Composites

Dag Fritzson

1988

On the Design and Life Prediction of Transmission Belts made of Elastomer Composites

by

Dag Fritzson

Chalmers University of Technology
Division of Machine Elements
Göteborg, Sweden, 1988

Published and Distributed 1988 by:
Division of Machine Elements
Chalmers University of Technology
S-41296 Göteborg, Sweden

ISBN 91-7032-366-6

PDF version created 2018, i.e., included errata and reformatted.

Abstract

Next to gear transmissions, belt transmissions are the most important mechanical transmissions. Today, belt design and development is based on extensive application tests of belts in the product development process. There is a need for theory development and design support systems. This would enable simulation for prediction and optimization of fatigue life.

The aim of this work is to study certain parts of the belt in detail when the belt is running under loaded conditions. The areas of special interest are those which can be related to failure mechanisms. Thus the model can be used for calculations to predict service life. Here, the attention is focused on V-belts.

A fully three-dimensional finite strain constitutive model has been developed for the anisotropic elastomer composites used in V-belts and the constitutive model has been implemented into FEM-software. This makes it possible to do general stress and strain analysis of machine elements designed of elastomer composites.

Several different failure modes can be identified in V-belt fatigue. Here it is shown that the failure modes thus defined occur for such test conditions that long life can be associated with radial cracks, medium life with separation, and cord break with short life.

In order to monitor the stress-strain state at any location in the belt, while simulating a running belt, "the parametric belt segment model" has been developed. Correlation with V-belt fatigue data for 11 different load cases has been made. Our conclusion is that both failure mode and fatigue life can be predicted using computer simulations.

Friction and wear of materials in a V-belt drive have also been studied.

Keywords: belt transmission, V-belt, fatigue, life prediction, material properties, rubber, elastomer, composite, friction, constitutive theory, viscoelastic, anisotropic, damage, wear

The following reports are included in this dissertation:

I D. Fritzson. Simulation of a V-belt drive with special reference to fatigue mechanisms. Report No. 1988-08-05, Division of Machine Elements, Department of Mechanical Engineering, Chalmers University of Technology, Göteborg, Sweden, 1988.

II D. Fritzson. A three-dimensional finite strain constitutive theory for elastomer composites. Report No. 1988-05-30, Division of Machine Elements, Department of Mechanical Engineering, Chalmers University of Technology, Göteborg, Sweden, 1988.

III D. Fritzson. Fatigue mechanisms of V-belts. Report No. 1988-05-27, Division of Machine Elements, Department of Mechanical Engineering, Chalmers University of Technology, Göteborg, Sweden, (1987).

IV D. Fritzson. Friction of elastomer composites - influence of surface temperature, sliding speed and pressure. Report No. 1988-05-26, Division of Machine Elements, Department of Mechanical Engineering, Chalmers University of Technology, Göteborg, Sweden, (1987).

V D. Fritzson. Material properties of elastomer composites in mechanical transmissions with special reference to V-belts. Report No. 1988-05-25, Division of Machine Elements, Department of Mechanical Engineering, Chalmers University of Technology, Göteborg, Sweden, (1985).

VI D. Fritzson. Change of V-belt geometry in a running transmission. Report No. 1988-05-24, Division of Machine Elements, Department of Mechanical Engineering, Chalmers University of Technology, Göteborg, Sweden, (1984).

Contents

1
Introduction and scope

Mechanical power transmission is important in all technologies. There are various means available for mechanical power transmission: second to gear transmissions, belt transmissions are the most important.

Today, a belt manufacturer's primary feedback on belt designs comes from extensive application or fatigue tests of belts in the product development process. For each design modification, an extensive test program has to be carried out. There is a need for theory development and design support systems. This would allow for simulations for prediction and optimization of fatigue life.

The aim of this work is to study certain parts of the belt in detail when the belt is running under loaded conditions [6]. The areas of special interest are those which can be related to failure mechanisms [3]. Thus the model can be used for calculations to predict service life. Here, the attention is focused on V-belts because they represent one of the most important types, and a type for which there also are fatigue data available.

In order to analyze the function of a transmission based on friction and perform simulations, it is necessary to have knowledge about the friction coefficient [4]. The interaction between belt and pulley in a V-belt drive also has to be understood [7, 2].

The mechanical material properties [5] and a constitutive model [1] must be known for any analysis or simulation of a mechanical system in which sections of elastomer composites are important parts, essential to the functioning of the system.

2
A short review of the reports

2.1 Simulation of a V-belt drive with special reference to fatigue mechanisms

The aim of this report is to study certain parts of the belt in detail when the belt is running under loaded conditions. The areas of special interest are those which can be related to failure mechanisms. Thus the model can be used for calculations to predict service life.

V-belt life prediction methods and failure mechanisms are discussed in detail in reference [3]. Our conclusion was that the methods used today correlate all kinds of failures to cord stress, and do not allow for prediction of the behavior of a new design as experimentally determined constants for each belt type are included in the theory.

"The parametric belt segment model" is developed here. This approach consists of two major parts:

- A global analysis of the belt forces, displacements, slip, sliding direction, etc., in a V-belt drive is performed using the theory for the mechanics of a V-belt drive [7]. Thus, we have at any instant in time, data of all the global variables for a certain belt section.

- A local analysis of the stress - strain state of a small part of the belt is performed using a FEM-model. The model is not larger than necessary to avoid boundary effects. Input data to this model are the global forces, displacements etc., calculated above. Thus, we have, at any instant in time, the stress-strain state at any location in the belt.

This makes it possible to monitor a certain position in the belt and study variables of interest, while simulating a running belt. There is no limitation to a certain V-belt drive configuration. Both two- or three-dimensional FEM-models can also be used.

From observations regarding the fatigue mechanisms the areas of interest are [3]:

- Radial crack growth towards the cord layer. These are normally initiated between the cogs. Variables of interest are those which govern crack growth in the

radial direction. This is referred to as failure mode 1.

- Separation or cracking in the longitudinal direction close to the cord layer, in the cushion layer, or between the cushion and pressure section. Variables of interest are those which govern crack propagation in the longitudinal direction. This failure mechanism is referred to as failure mode 2.

The facts that there are different failure modes [3] and that it is crack propagation mechanisms that are active are recognized, and criteria for crack propagation with combined modes I and II is used.

Simulations for 11 different load cases of a 0.500 inch belt running on two equal size pulleys have been performed. Data are available for different loads, torques, speeds, and diameters of the pulleys. The materials used in the design of the belts are discussed in reference [5] and the constitutive equations are presented in reference [1]. A plane strain model is used in which the longitudinal force and geometric deformation due to bending can essentially be properly represented. Influence from the contact pressure and frictional forces can only be studied by modelling them as body forces. The axial component can not be applied.

For these 11 load cases, experimental fatigue data are available, making it possible to determine the fatigue material constants. There is good correlation between experimental data and the simulations, both fatigue life and failure mode can be predicted.

Our conclusion is that if material constitutive data, material fatigue data, and the belt temperature are known, the belt segment model can be used to evaluate new designs of V-belts in computer simulations.

2.2 A three-dimensional finite strain constitutive theory for elastomer composites

A large class of machine elements is designed of elastomer composites. These materials are anisotropic, owing to the reinforcement of fibers, and they yield hysteresis work when loaded dynamically. They are also subject to damage mechanisms which depend on the strain history, and are very sensitive to changes in temperature. In many applications, such as belt transmission, these mechanisms are highly significant and cannot be neglected.

A fully three-dimensional finite strain constitutive model has been developed, characterized by:

- Anisotropic elasticity, anisotropic rate independent dynamic elasticity, and anisotropic viscoelastic response.
- Uncoupled bulk and deviatoric response.
- Decomposition of the deviatoric response into isotropic and anisotropic parts.
- Separable anisotropic damage mechanisms for mechanical degradation and temperature degradation. The mechanical damage is irreversible, while the temperature damage is reversible.
- Separable damage mechanisms for the elastic response and the viscous (hysteresis) response.

The constitutive model can be used in both rate formulations and total formulations, providing a co-rotational coordinate system is defined in the anisotropic material directions.

The constitutive theory is evaluated against experimental material data for two elastomer composites used in V-belt applications [5]. These materials can be described as transversal isotropic, and the values of the constitutive material constants are determined.

The constitutive model has been implemented into the ABAQUS FEM-software. This makes it possible to do general stress and strain analysis of machine elements designed of elastomer composites. Examples are different types of belts.

2.3 Fatigue mechanisms of V-belts

Knowledge of the failure characteristics of V-belts is important for several reasons, including development of theoretical methods for predicting the life of V-belt transmissions and in product development.

Today, a belt manufacturer's primary feedback on V-belt designs comes from extensive application or fatigue tests of V-belts in the product development process. For each design modification, an extensive test program has to be carried out. Fatigue tests are expensive. This is because a large number of tests have to be performed to achieve statistically significant results. Also, there are many parameters which influence V-belt fatigue, and each test takes a long time (10 - 2000 hours).

There is a need for theory development and design support systems. This would allow for simulations for prediction and optimization of fatigue life. Material fatigue life, given a certain stress, strain and environment history, should be an intrinsic material property, and should not depend on the design in which it is used.

In this report the fatigue characteristics of V-belts are investigated from the experimental point of view, i.e. from fatigue life experiments. However, first we survey published results and theories.

This experimental investigation, like previous work, shows that several different failure modes can be identified in V-belt fatigue. Here it is shown that the failure modes thus defined occur for such test conditions that long life can be associated with radial cracks, medium life with separation, and cord break with short life. Also, any damage severity level can be chosen as the design level.

These different failure modes are not recognized in the fatigue life prediction theory used to date, which is instead based on cord stress. However, if the belt type itself is not to be included in the theory as an experimentally determined constant, the theory has to be developed further in order to account for multiple failure mechanisms, etc.

Our aim is to have a theory in which the only experimental constants are material constants. Such a theory would make it theoretically possible to design a new belt type with a predicted life for a certain application. From the results presented in reference [5] we suggest that as a first step, much greater efforts should be put into modelling and understanding each failure mode and its governing parameter. From the results obtained, a simplified theory can be suggested.

2.4 Friction of elastomer composites - influence of surface temperature, sliding speed and pressure

It is necessary to have knowledge about the friction coefficient in order to analyze the function of a transmission based on friction. In this report, the friction coefficient between materials normally used in V-belt transmissions is experimentally investigated as a function of pressure, sliding speed, surface temperature and environment temperature.

The most important finding of this experimental investigation is that the friction coefficient is highly dependent on the surface structure. However, this structure changes continuously during the tests. Surface sections with a large amount of reinforcement fiber show greater resistance to wear, and display different friction characteristics. As the sample area is quite small, 10 mm times 10 mm, local variations in the surface will affect the total friction force. This phenomenon causes the greatest variation in friction coefficient, thus dominating other effects. It is difficult to conclude that there is a consistent dependency on pressure, slip velocity or surface temperature.

Two methods developed to measure temperatures of the contact surface of rubber samples give satisfactory results and verify one another. In the parameter interval which has been investigated in this test program, normally not more than a 3-4 °Ctemperature increase over the environment is obtained for the highest speed and pressure. The loss heat generated in the friction contact is mostly conducted off through the cast iron disk and not through the rubber composite. However, if stick slip occurs, heat is created inside the rubber material due to hysteresis. This gives rise to higher temperatures in the rubber.

Two reports of tests of whole V-belts are discussed in chapter 4. These reports do not investigate the variation of the friction coefficient with time in any given parameter combinations since these tests were performed over a very short time. However, both reports present test results from belts that were conditioned by being run in a normal V-belt drive. These are compared with results from new V-belts. Conditioning seems to be the most important variable, which confirms the fact that the surface structure changes with time.

From our experience and the results obtained to date, I would suggest that further studies should be done on the surface structure of V-belts in real drive configurations.

2.5 Material properties of elastomer composites in mechanical transmissions with special reference to V-belts

Rubber, or elastomers, is not a well-defined material group in terms of mechanical material properties. For any given material, the mechanical properties are very much dependent on what environment the material is used in, and what kind of loads, deformations, temperatures, etc, it is subject to. It is very seldom possible to find the data needed for a particular analysis in handbooks or even in information from the manufacturer of the material.

Mechanical material properties are needed for analysis or simulation of a mechanical system in which sections of rubber are important parts, essential to the functioning of the system.

This report presents a study of the application of mechanical transmissions with special reference to V-belts. A V-belt is built up of several different reinforced rubber materials and cord, each optimized in terms of its function. Some are heavily reinforced to be able to take the load. Thus the expression "an anisotropic elastomer composite" is more descriptive than the conventional word "rubber".

The material characteristics of elastomer composites used in V-belt applications are highly dependent on strain, temperature and, to a lesser extent, frequency. The fiber reinforced materials are anisotropic, with one material direction differing from the others. The label "transversal isotropic" can be used. For one of the materials the reinforced direction is up to 4 times stiffer than the other directions. Using the concept of complex modulus, some aspects of the material properties can be described. We assume that these variables vary only within certain intervals characteristic of V-belt applications.

Strain amplitudes of 0.005 to 0.045 cover the interval in which elastomer composites are sensitive to strain softening or structural breakdown. The reinforced material direction is the most sensitive one. For all the materials and material directions a reduction in elastic modulus of a factor of 2 - 3 is found to be normal.

A temperature increase from room temperature to 100 - 120 degrees Celsius causes the same reduction as for the variation in strain amplitude above.

The frequency of the sinusoidal deformation is the least important parameter. An increase of 10 - 20 percent of the elastic modulus over a frequency interval of 3 - 60 Hz is normal. The loss modulus is slightly more dependent on frequency.

The bulk modulus is about three orders of magnitude greater than the shear modulus. This means that in many designs these materials may be regarded as incompressible.

The results for the cord were deviant. In this case, the temperature was found to be the only important parameter, especially for the loss modulus. The changes are small compared with changes in the rubber materials mentioned above.

Our conclusion is that in any material description made for elastomer composites for this application, several variables should be studied. The order of importance among these should be anisotropy, strain effects, temperature effects, and finally, frequency

effects.

For polyester cord the temperature is the most important variable.

2.6 Change of V-belt geometry in a running transmission

The interaction between belt and pulley in a V-belt drive has been investigated. Parameters studied were running time, surface roughness and pressure angle of the pulley.

This investigation shows that belt geometry quickly conforms to pulley geometry. The time for this process is very short compared to a normal belt service life. The greatest changes both in width and pressure angle occur during the first hour of running time. This is also true for pressure angle deviations of plus or minus 3 to 4 degrees and light load. In accordance with this result, it becomes possible to assume that the belt fits the pulley almost perfectly when calculating the pressure distribution. If the rate of the "wear" process is proportional to pressure, a logical assumption is constant pressure over the belt height.

What mechanisms cause this behavior? The presence of dust from the rubber, and the fact that surface roughness has some influence, are proof that abrasive wear is one of the mechanisms. V-belts are made of rubber composites subject to viscoelastic behavior. Therefore it may be suspected that some of the permanent changes are caused by viscoelastic creep. The question of the most important mechanism has not been investigated in this report. One way to distinguish them might be to run tests at different temperatures. Viscoelastic behavior for this kind of rubber is usually highly temperature dependent. Neither has the case of different pulley diameters in the drive been studied. It seems reasonable that the belt adapts most to the pulley where the pressure and slip are most severe.

3
Conclusions

The material characteristics of elastomer composites used in V-belt applications are highly dependent on strain, temperature and, to a lesser extent, frequency [5]. The fiber reinforced materials are highly anisotropic. The order of importance among these effects should be anisotropy, strain effects, temperature effects and, finally, frequency effects. For polyester cord the temperature is the most important variable.

A fully three-dimensional finite strain constitutive model has been developed for these materials and the values of the constitutive material constants are determined [1]. The constitutive model has been implemented into the ABAQUS FEM-software. Thus, it is now possible to do general stress and strain analysis of machine elements designed of elastomer composites.

The friction coefficient between materials normally used in V-belt transmissions is highly dependent on the surface structure [4]. However, this structure changes continuously because surface sections with a large amount of reinforcement fiber show greater resistance to wear, and display different friction characteristics. In a V-belt drive, the V-belt geometry very quickly conforms to pulley geometry [2].

Several different failure modes can be identified in V-belt fatigue. It is shown here that the failure modes thus defined occur for such test conditions that long life can be associated with radial cracks, medium life with separation, and cord break with short life [3].

In order to monitor the stress-strain state at any location in the belt, while simulating a running belt, “the parametric belt segment model” is developed [6]. Correlation to V-belt fatigue data for 11 different load cases have been accomplished. Our conclusion is that both failure mode and fatigue life can be predicted using computer simulations.

4

Discussion and future work

This work "On the Design and Life Prediction of Transmission Belts made of Elastomer Composites" represents a beginning in this research field. Many years of research effort are needed before theory and design methods are as well developed as they are for many machine elements made out of steel, such as ball bearings. A natural continuation of this work will be, listed in an approximative priority order, the following projects:

1. Improvement of the FEM-method so it is the constitutive theory which determines the maximum increment in strain allowed. This to reduce computation time. It can be accomplished by implementing a total formulation for strain or by means of reducing the accumulated residual error in strain for a rate formulation [1, 6].

2. Launching an experimental program to determine the fatigue or crack propagation data for the materials and joining methods used in belt design. It is important that the materials and the loads be really representative for the application. For example, it would be best if samples was cut out of real belts.

3. Performing a comparative study of the two-dimensional and the three-dimensional belt segment model, to determine the applicability of the models. This is discussed in reference [6].

4. Performing an extensive analysis program where simulations are done for all belts for which there are accumulated fatigue data, to obtain a large material when correlating to fatigue mechanisms.

5. Incorporating heat transfer in the belt segment model.

6. A further study of V-belt mechanics in exit and entrance zones.

5
Acknowledgements

This work has been carried out at the Division of Machine Elements, Chalmers University of Technology, Göteborg. The head of the Division, Professor Göran Gerbert has supervised this study.

I wish to express my gratitude to Professor Gerbert for his inspiring and constructive guidance.

I also wish to express my gratitude to the former head of the Division, Professor Bengt Jakobsson, who appointed me as a candidate for the doctorate at the Division.

I thank my other colleagues at the Division of Machine Elements, for providing discussions and valuable suggestions.

Valuable discussions with Dr Lennart Josefsson, Prof Jan Hult, and their colleagues at the Div. of Solid Mech. are gratefully acknowledged.

Many thanks to the management at The Gates Corporation and The Dayco Corporation who made the experimental part of this investigation possible. Special thanks to Mr and Mrs Clyde O. Johnson who made my stay in Springfield most enjoyable.

Long and valuable discussions with Dr Jan Hernelind at Fem-Tech AB are gratefully acknowledged.

Financial support from the Swedish Board for Technical Development (STU) for the final computations in [6] is gratefully acknowledged.

I also thank Lars Sjöström at SAAB-SCANIA, Saab Aircraft Division, for giving me access to the software needed for these calculations and to Gunnar Holmberg for his valuable advice.

I thank Linda Schenck for reading the manuscript and correcting the language.

Finally, I want to express my gratitude to my brother Peter and his family, and my parents. Their help and support made this work possible.

Bibliography

[1] D. Fritzson. *A three-dimensional finite strain constitutive theory for elastomer composites*. No. 1988-05-30. Department of Mechanical Engineering, Chalmers University of Technology, Göteborg, Sweden: Division of Machine Elements.

[2] D. Fritzson. *Change of V-belt geometry in a running transmission*. No. 1988-05-24. Department of Mechanical Engineering, Chalmers University of Technology, Göteborg, Sweden: Division of Machine Elements.

[3] D. Fritzson. *Fatigue mechanisms of V-belts*. No. 1988-05-27. Department of Mechanical Engineering, Chalmers University of Technology, Göteborg, Sweden: Division of Machine Elements.

[4] D. Fritzson. *Friction of elastomer composites - influence of surface temperature, sliding speed, and pressure*. No. 1988-05-26. Department of Mechanical Engineering, Chalmers University of Technology, Göteborg, Sweden: Divison of Machine Elements.

[5] D. Fritzson. *Material properties of elastomer composites in mechanical transmissions with special reference to V-belts*. No. 1988-05-25. Department of Mechanical Engineering, Chalmers University of Technology, Göteborg, Sweden: Division of Machine Elements.

[6] D. Fritzson. *Simulation of a V-belt drive with special reference to fatigue mechanisms*. No. 1988-08-05. Department of Mechanical Engineering, Chalmers University of Technology, Göteborg, Sweden: Division of Machine Elements.

[7] G. Gerbert. *Force and slip behaviour in V-belt drives*. Acta Polytechnica Scandinavica, Mech. Eng. Series No. 67. The Finnish Academy of Technical Sciences, Helsinki, Finland, 1972.

Part I

Simulation of a V-belt drive with special reference to fatigue mechanisms

Report I

Simulation of a V-belt drive with special reference to fatigue mechanisms

Dag Fritzson

Report No. 1988-08-05
Division of Machine Elements
Department of Mechanical Engineering
Chalmers University of Technology
Göteborg, S-412 96 Sweden

Abstract

The aim of this report is to study certain parts of the belt in detail when the belt is running under loaded conditions. The areas of special interest are those which can be related to failure mechanisms. Thus the model can be used for calculations to predict service life.

"The parametric belt segment model" is developed. This approach consists of two major parts:

- A global analysis of the belt forces, displacements, slip, sliding direction, etc., in a V-belt drive is performed using the most current theories for the mechanics of a V-belt drive.
- A local analysis of the stress - strain state of a small part of the belt is performed using an FEM-model. Input data for this model are the global forces, displacements, etc. calculated above. Thus, we have, at each instant in time, the stress-strain state at any location in the belt.

There is no limitation to a certain V-belt drive configuration, both a two- or three-dimensional FEM-model can also be used.

It is possible to monitor a certain position in the belt and study variables of interest, while simulating a running belt. The facts that there are different failure modes [6] and that crack propagation mechanisms are active are recognized and criteria for crack propagation with combined mode I and mode II are used.

Simulations for 11 different load case of a 0.500 inch belt running on two equal size pulleys have been performed. For these load cases experimental fatigue data are available, and thus the fatigue material constants are determined. There is good correlation between experimental data and the simulations, both fatigue life and failure mode can be predicted with good accuracy.

The conclusion is that if material constitutive data, material fatigue data, and belt temperature are known, the belt segment model can be used to evaluate new designs of V-belts in computer simulations.

Contents

1
Introduction

The aim of this report is to study certain parts of the belt in detail when the belt is running under loaded conditions. The areas of special interest are those which can be related to failure mechanisms. Thus the model can be used for calculations to predict service life.

V-belt life prediction methods and failure mechanisms were discussed in detail in reference [6]. The conclusion was that the methods used today correlate all kinds of failures to cord stress and do not allow prediction of the behavior of a new design as experimentally determined constants for each belt type are included in the theory.

2

Notation

A	Effective area of the belt cross-section
B	Mean width of the belt
EI	Bending stiffness of the belt
F,$(F_0 = \frac{F}{R^2 k_1})$	Effective belt force (non-dimensional)
$F' = dF/d\varphi$	Derivative with respect to the angular coordinate φ
F_1	Effective belt force in the slack side
F_2	Effective belt force in the tight side
F_c	Belt force due to centrifugal forces
H	Mean belt height
K_I, K_{II}	Stress intensity factors in mode I and II respectively
$\Delta K = K_{max} - K_{min}$	Double amplitude of the stress intensity factor
$K_m = (K_{max} - K_{min})/2$	Mean stress amplitude factor
K_e	"Effective" stress amplitude factor
L	Belt length
M	Bending moment
N	Number of load cycles
R	Reference radius, i.e. pitch radius of the pulley
T	"Tearing" energy
U	Elastically stored energy
W	Strain energy per unit volume
V	Velocity of unloaded belt
a	Center distance, Crack length
c,$(c_0 = \frac{c}{R^2 k_1})$	Longitudinal strain stiffness (non-dimensional)
h	Belt height coordinate
k_1	Radial spring stiffness
p, $(p_0 = \frac{p}{k_1})$	Pressure, i.e. force per unit area (non-dimensional)
r	Radius coordinate
$r' = dr/d\varphi$	Derivative with respect to the angular coordinate φ
s	Length coordinate of belt path
u, w	Belt coordinates
v_b	Belt velocity
v_s	Sliding velocity in the plane of rotation

x, $(x_0 = \frac{x}{R})$	Cartesian coordinate, Radial displacement (non-dimensional)
$x' = dx/d\varphi$	Derivative with respect to the angular coordinate φ
y	Cartesian coordinate
$K = \frac{1}{\rho}$, $K_0 = \frac{R}{\rho}$	Curvature (non-dimensional)
α	Contact angle
β	Wedge angle of the pulley
β_s	Wedge angle in a plane inclined the sliding angle to the radius
γ	Sliding angle in the plane of rotation
ϵ	Longitudinal strain
θ	Inclination angle
$\kappa = \frac{F}{F_P}$	Relative force
$\kappa' = d\kappa/d\varphi$	Derivative with respect to the angular coordinate φ
μ	Coefficient of friction
ρ	Radius of curvature, Density
σ, τ	Stress
σ_e	"Effective" stress
φ	Angular coordinate
ω	Angular velocity

3
A model for V-belt simulation

3.1 Introduction and previous work

A V-belt consists of cord, different elastomer composites or "rubber", and cover. Almost the whole belt force is carried by the cords since they are considerably stiffer in the longitudinal direction than the other parts. The major rubber section take up the pressure between pulley and belt and transmits the friction forces from the sides of the belt to the cord.

When a V-belt is placed in a pulley and loaded by a force, the pressure between belt and pulley compresses the belt because of wedge action. The belt grows narrower and moves in the radial direction. Furthermore, the force variations cause longitudinal motions. The frictional force is counter-directed to the resultant sliding velocity. This means that the direction of the frictional forces must vary along the belt. The basic forces and velocities of a small belt element are shown in Figure 3.1. The belt enters a pulley or leaves a pulley with large but continuous change in belt curvature, owing to the bending stiffness of the belt.

Here, the purpose of modeling the belt is to study certain parts of the belt in detail when the belt is running under loaded conditions. The areas of special interest are those which can be related to failure mechanisms. Thus, the model can be used for calculations to predict service life. A theoretical model that can fulfill these demands should have the following properties.

- It should be able to study arbitrary load/deformation cases, i.e. different pulleys, forces, speeds, temperatures, etc.
- It should be possible to study the stresses, strains, and other relevant variables at every instant in time and at every location of interest in the belt.
- The model should not be limited to certain geometries or designs of the belt. It should be able to describe widely different designs. This would make it possible to evaluate new belts in simulations before any belts are built.
- The model should make it possible to study the effects of different kinds of materials as well as the strength of the bonding of two materials (i.e. the

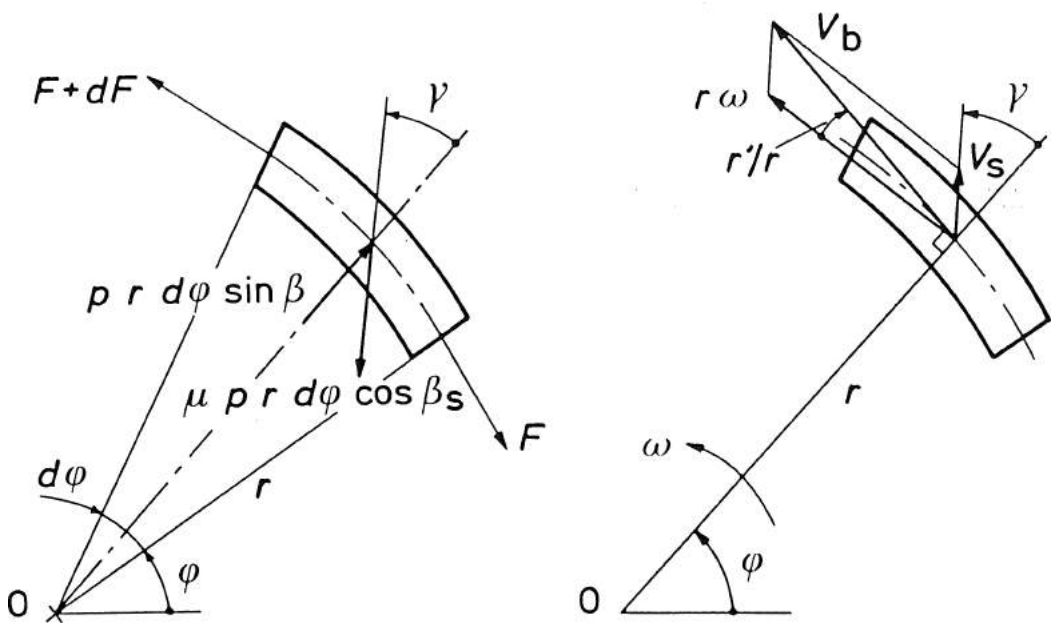

Figure 3.1 *Forces and velocities acting on a belt element in contact with a pulley. F = belt force. p = side pressure. γ = sliding angle in the plane of rotation. v_b = belt velocity. v_s = sliding velocity in the plane of rotation. [16]*

influence of production methods). In fact, it should be possible to calculate the material properties needed to obtain a certain behavior of the belt drive given the design and load case. Material properties, including fatigue data, should be material data and not belt data.

No tool like the one described above exists today, and the question is how closely we can follow these specifications.

V-belt life prediction methods and failure mechanisms were discussed in detail in reference [6]. The conclusion was that the methods used today correlate all kinds of failures to cord stress and do not allow for prediction of the behavior of a new design since experimentally determined constants for each belt type are included in the theory. The only theory that separates different kinds of damage and material data from belt data is presented by Gerbert [11]. "Stresses" that should correlate to fatigue life for each major failure mode are calculated. The main advantage of this method is from the computational standpoint, as it is based on relatively simple analytical formulas. The major drawback of this formulation is the fact that it is an approximate calculation of certain stresses and for such formulations there are always situations where they do not apply. The model has to be evaluated against a large class of different designs and materials for which there are fatigue data and constitutive data, before it can be determined if all important mechanisms are correctly modeled, i.e. the "stress" or variable calculated can successfully be correlated to the evolution of damage, and within what limits the theory applies.

It would be very convenient if any analytical method, such as the one above, could be evaluated against a general stress - strain analyzing method instead of requiring that a large number of experiments be performed. The most developed method is the FEM-

method. It can be used for arbitrary geometry and loading. As a constitutive model for this kind of material has been developed [4], it is theoretically possible to model a whole belt three dimensionally and perform a dynamic analysis simulating a running belt involving friction contact, large displacement, large rotation, etc. However, there are practical limits. It can be estimated from smaller problems studied that even unlimited access to a supercomputer will not be sufficient. Also, it may be suspected that several numerical problems will show up for such large problems involving friction contact, etc.

Therefore we propose the "parametric belt segment model" as a solution to this dilemma. It is discussed in detail in next sections.

3.2 The parametric belt segment model

This approach consists of two major parts:

- A global analysis of the belt forces, displacements, slip, sliding direction, etc., in a V-belt drive is performed using the theory for the mechanics of a V-belt drive. This theory has long been well developed, and confirmed experimentally [12]. Thus, we have at each instant in time, data of all the global variables for a certain belt section.

- A local analysis of the stress - strain state of a small part of the belt is performed using an FEM-model. The model is no larger than is necessary to avoid boundary effects. Input data for this model are the global forces, displacements, etc., calculated above. Thus, we have, at each instant in time, the stress-strain state at any location in the belt.

It is possible to monitor a certain position in the belt and study variables of interest, while simulating a running belt (i.e. tight/slack side tension, seating on the pulley, sliding with friction forces, unseating from the pulley, slack/tight side tension, etc.). Compared with a general FEM-analysis of the whole belt this approach still allows for a detailed study of the conditions inside the belt but with an enormous saving in computation time.

If the contact and friction forces and some other effects such as "dishing" [10] were to be properly included, the model would have to be three dimensional. However, as a first case a plane strain model can be studied. It can simulate effects due to belt forces and bending. Plane strain is not a poor approximation, owing to the fiber reinforcement of the belt material. It is possible to get a rough estimation of the influence of friction forces by modeling them as body forces in the desired direction.

4

The load/deformation cycle of a V-belt

4.1 Introduction

To be able to describe the loading of the belt at any instant in time during a complete load/deformation cycle, we need to calculate the following variables as functions of time and position along the belt: belt curvature K, belt force F, the normal pressure between the belt and pulley p, and the sliding angle γ. The belt force F determines the longitudinal strain of the belt. At the contact with a pulley we have a normal pressure and a frictional force per current area. Projected in three orthogonal directions, the components are (see Appendix A):

$$\text{longitudinal:} \quad -\mu p dA \cos(\beta_s) \sin(\gamma) \tag{4.1}$$

$$\text{axial:} \quad pdA(\cos(\beta) + \mu \sin(\beta_s)) \tag{4.2}$$

$$\text{radial:} \quad pdA(\sin(\beta) - \mu \cos(\beta_s) \cos(\gamma)) \tag{4.3}$$

where

$$\beta_s = \arctan(\tan(\beta) \cos(\gamma)) \tag{4.4}$$

In the calculation we also need data such as geometry of the belt, material data, density of the belt, description of the complete V-belt drive, i.e. number and size of pulleys, which ones are driven or driving, etc.

A point in a belt, which completes a load cycle, experiences different types of load at different time intervals. We can refer a certain part of the load cycle to one pulley and divide that part into the different zones below regardless of whether it is a driven or a driving pulley. This is shown in Figure 4.1. It is analogous to refer either to the length coordinate s of the belt path or to time.

1. Free span zone - entrance side. $s \in [0, s_{Cin}]$
2. Entrance zone. $s \in [s_{Cin}, s_{Ein}]$
3. Non-sliding contact zone. $s \in [s_{Ein}, s_{NS}]$
4. Sliding contact zone. $s \in [s_{NS}, s_{Eout}]$

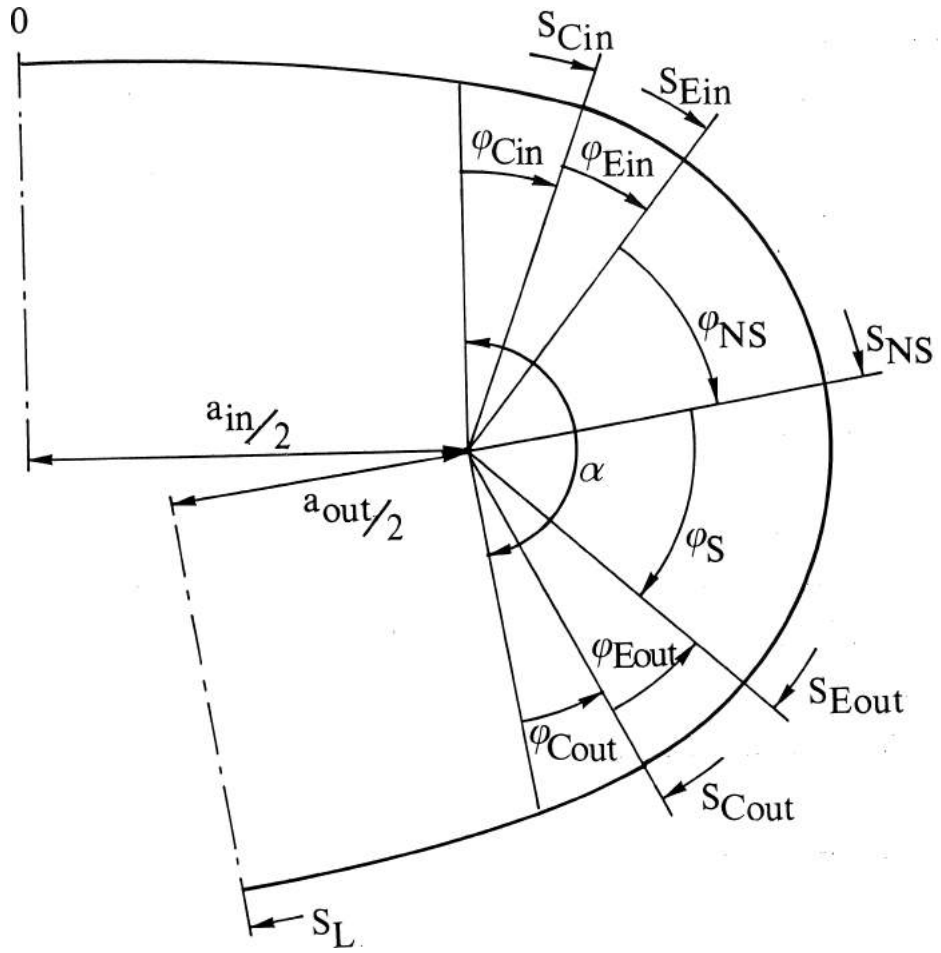

Figure 4.1 *The zones in the part of a load/deformation cycle that are referred to one pulley. s = the length coordinate of the belt path. The figure shows an arbitrary case. For the special case of two equal pulleys we have $s_L = L/2$ and $\alpha = 180°$, where L is the total length of the belt path in the transmission under load.*

5. Exit zone. $s \in [s_{Eout}, s_{Cout}]$

6. Free span zone - exit side. $s \in [s_{Cout}, s_L]$

We have now divided the total load cycle into a part for each pulley regardless of the number of pulleys used.

We now need equations that govern the V-belt variables discussed above (the curvature K, the belt force F, the pressure p, and the sliding angle γ) for the different zones for the cases of either a driven or driving pulley. The equations developed should be in simple closed form expressions so that they can be implemented in procedures used by the FEM-program. This is discussed in the sections below.

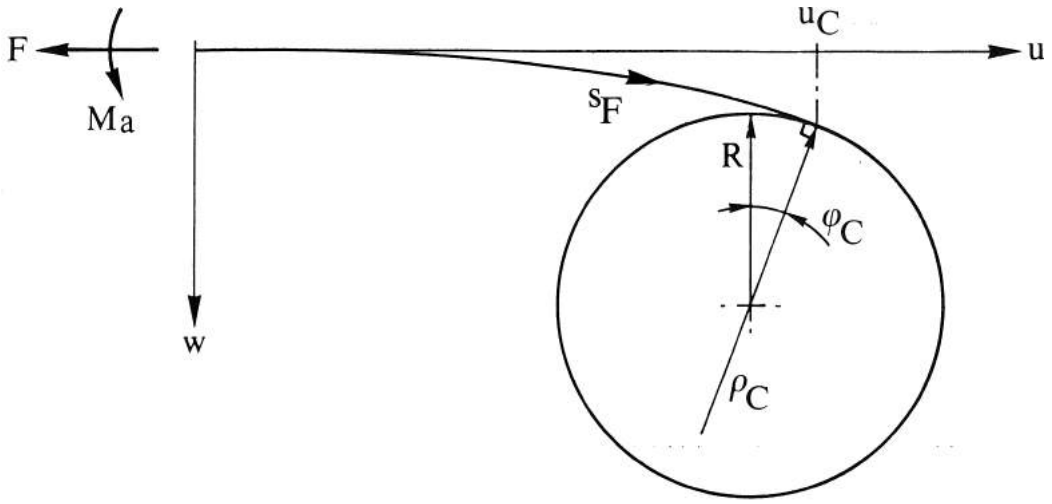

Figure 4.2 *Coordinate system for free span zones. w = the vertical deflection, u = horizontal coordinate, s_F = free span belt path length coordinate, F = belt force, M_a = bending moment, subscript $_C$ denotes the point where the belt contacts the pulley.*

4.2 Free span zones

In these zones the belt is not in contact with the pulleys. The belt force and the bending stiffness are parameters that govern the behavior in these regions. As the deflection from a straight line is small, elementary beam theory can be used, which presumes pure elastic behavior [12].

Small deflections give:

$$\frac{d^2w}{du^2} = \frac{1}{\rho} = \frac{M_a}{EI} + \frac{Fw}{EI} \tag{4.5}$$

Using the boundary conditions

$$\begin{array}{lll} w = 0 & \text{for} & u = 0 \\ \frac{dw}{du} = 0 & \text{for} & u = 0 \\ \rho = \rho_C & \text{for} & u = u_C \end{array} \tag{4.6}$$

the solution becomes

$$w = \frac{EI}{F\rho_C} \cdot \frac{\cosh\left(\sqrt{\frac{F}{EI}}u\right) - 1}{\cosh\left(\sqrt{\frac{F}{EI}}u_C\right)} \tag{4.7}$$

$$\frac{dw}{du} = \sqrt{\frac{EI}{F}}\frac{1}{\rho} \cdot \tanh\left(\sqrt{\frac{F}{EI}}u\right) \tag{4.8}$$

$$\frac{1}{\rho} = \frac{1}{\rho_C} \cdot \frac{\cosh\left(\sqrt{\frac{F}{EI}}u\right)}{\cosh\left(\sqrt{\frac{F}{EI}}u_C\right)} \tag{4.9}$$

$$\varphi_C = \arctan\left(\left(\frac{dw}{du}\right)_{u=u_C}\right) \tag{4.10}$$

$$s_F(u) = \int_0^u \sqrt{1 + \left(\frac{dw}{d\tilde{u}}\right)^2}\, d\tilde{u} \tag{4.11}$$

In normal V-belt applications $\frac{dw}{du} \ll 1$, $w \ll u$ and we can assume $s_F \approx u$. Also, we normally have $\sqrt{\frac{F}{EI}}u_C > 3 \Leftrightarrow \tanh\left(\sqrt{\frac{F}{EI}}u_C\right) \approx 1$. Thus, we obtain the following approximations:

$$\frac{1}{\rho} = \frac{1}{\rho_C} \cdot \frac{\cosh\left(\sqrt{\frac{F}{EI}}s_F\right)}{\cosh\left(\sqrt{\frac{F}{EI}}s_{FC}\right)} \tag{4.12}$$

$$\varphi_C = \arctan\left(\sqrt{\frac{EI}{F}}\frac{1}{\rho_C}\right) \tag{4.13}$$

The length coordinate s is mapped to the free span length coordinate s_F by the relations:

$$\begin{array}{lll} s_F = s & & \text{Entrance side} \\ s_F = s_L - s & & \text{Exit side} \end{array} \tag{4.14}$$

In a general case with an arbitrary number of pulleys which can be of different sizes, a simple method for determining the free span lengths as a function of center distances and wrap angles is needed. The center distances are a_{in} and a_{out} from the pulley in Figure 4.1 to the neighboring pulleys. The following approximations can be employed:

$$s_{Cin} = \frac{1}{2}a_{in} + \varphi_{Cin}R \tag{4.15}$$

$$s_{Cout} = s_L - \frac{1}{2}a_{out} - \varphi_{Cout}R \tag{4.16}$$

$$s_L = \frac{1}{2}(a_{in} + a_{out}) + \alpha R \tag{4.17}$$

4.3 Non-sliding and sliding contact zones

In these regions the belt is in contact with the pulley and the curvature of the belt is close to the pitch radius of the pulley. This means that the entrance and exit zones are excluded, as they have a significant variation in radius of curvature.

In reference [5] results from a study of changes in V-belt geometry of running transmission are presented. It suggests that constant contact pressure over the belt height can be assumed.

In these zones the V-belt theory given in Appendix A applies. Closed form approximations are available. For a certain force variation the extent of the sliding zone φ_S can be determined and also the functions $F = F(\varphi)$, $\gamma = \gamma(\varphi)$, and $p = p(\varphi)$. The driven and driving cases are different. In the non-sliding region $F = F(0)$, $\gamma = 180°$, and $p = p(0)$, i.e. they are all constant. The angular coordinate is mapped to the length coordinate by:

$$\varphi = \frac{s - s_{NS}}{R} \tag{4.18}$$

4.4 Entrance and exit zones

In the exit and entrance regions there are large changes in all variables except the belt force. The bending stiffness of the belt is important and the theory for a thick V-belt has to be used. Such a theory has been developed and one solution for a driven pulley is given in [14]. In this case constant pressure is also assumed. The problem is numerically difficult and involves large scale computations [15], and it is not possible to include the theory in the load function which is used as indata in the FEM-calculations. Closed form approximations that reflect important behavior in those zones have to be developed using data from the only existing solution for the driven case in [14].

In Figure 4.3 the non-dimensional curvature $K_0 = R/\rho$ is presented for the case studied in [14], but with the free span zones and the contact zones in addition to the entrance and exit zone. In the free span zones Equation 4.12 is used and in the contact zone we have $K_0 \approx 1$. The dashed line represents a solution when Equation 4.12 is continued until $K_0 = 1$. We can observe that this equation represents the curvature characteristics quite well inside the entrance and exit zones. This indicates that the belt force and the bending stiffness are important variables and have a major impact on the solution.

We assume that Equation 4.12 represents the most important part of the behavior in the exit and entrance zones. Therefore, it is used as the equation that governs the behavior in these zones. This is the crucial assumption that makes it possible to generalize to different belts and loads other than the single case above.

The entrance and exit zones for the case studied in [14] are shown in Figure 4.4. The non-dimensional curvature K_0, the inclination angle θ, and the non-dimensional radial dispacement x_0 are interrelated by [14]:

$$x_0'' = -\theta' = -(1 - K_0) \tag{4.19}$$

$$x_0' = -\theta \tag{4.20}$$

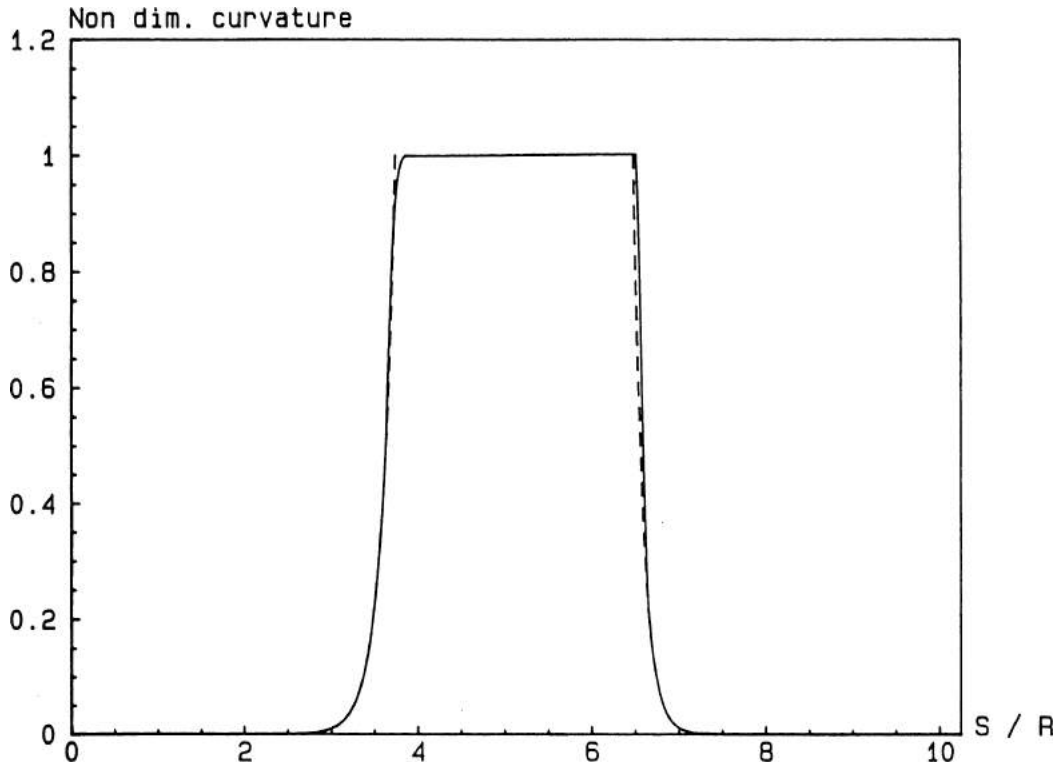

Figure 4.3 *The non-dimensional curvature $K_0 = R/\rho$ as a function of s/R. Data for driven pulley and belt in [14]. The dashed line represents the solution when Equation 4.12 is continued until $K_0 = 1$.*

In the entrance zone the non-dimensional curvature K_0 is represented as:

$$\begin{aligned} K_{0in} &= K_{0Cin} + (1 - K_{0Cin}) \cdot \\ &\quad \left(A_{1in}\psi + A_{2in}\psi^2 + (1 - A_{1in} - A_{2in})\,\psi^3\right) && (4.21) \\ \psi &\in [0,1] && (4.22) \\ \psi &= \frac{s - s_{Cin}}{s_{Ein} - s_{Cin}} = \frac{s_0 - s_{0Cin}}{\varphi_{Ein}} && (4.23) \end{aligned}$$

and in the exit zone we have, analogously:

$$\begin{aligned} K_{0out} &= K_{0Cout} + (1 - K_{0Cout}) \cdot \\ &\quad \left(A_{1out}\psi + A_{2out}\psi^2 + (1 - A_{1out} - A_{2out})\,\psi^3\right) && (4.24) \\ \psi &\in [0,1] && (4.25) \\ \psi &= \frac{s_{Cout} - s}{s_{Cout} - s_{Eout}} = \frac{s_{0Cout} - s_0}{\varphi_{Eout}} && (4.26) \end{aligned}$$

The constants $A_{1in} = 2.6613038$, $A_{2in} = -2.3055004$, $A_{1out} = 0.1666103$, and $A_{2out} = 1.8107287$ are calculated from the numerical solution using linear regression. In Figure 4.5 both curves are plotted for the exit zone.

As we have a polynomial function it can easily be integrated to obtain functions θ and x_0. The boundary conditions θ_{Ein}, θ_{Eout}, x_{0Cin}, and x_{0Cout} are used to determine

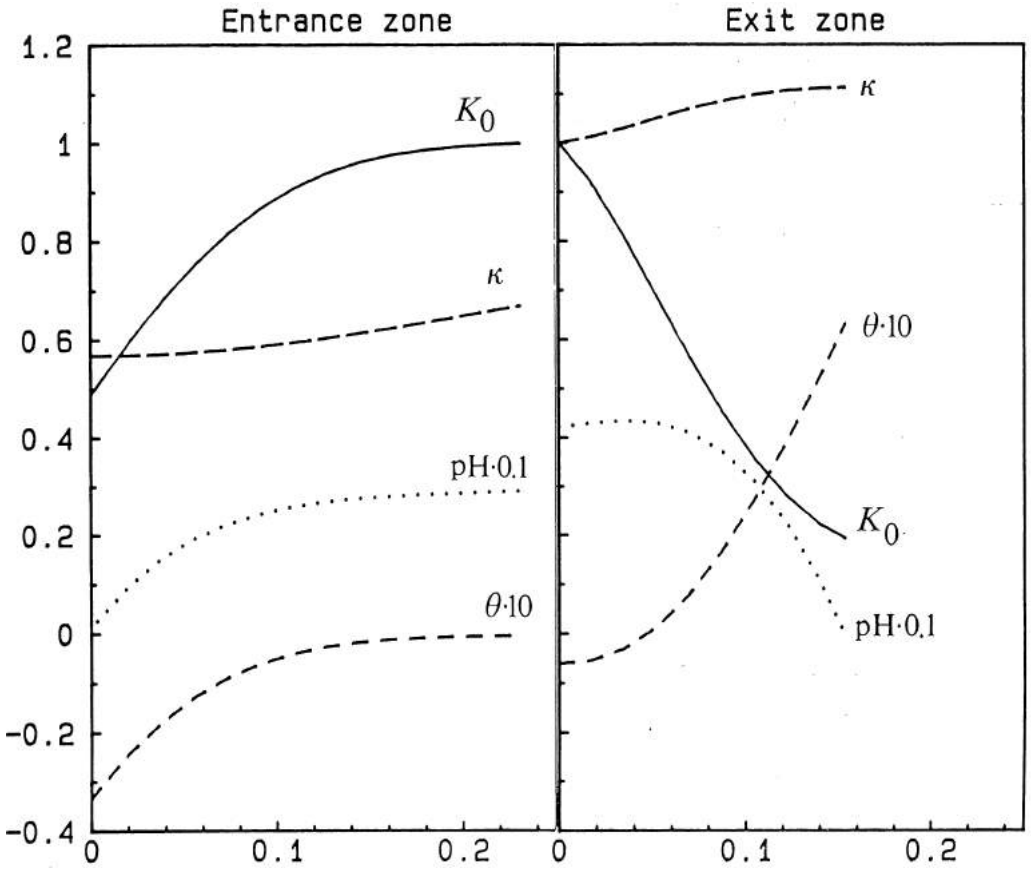

Figure 4.4 *The non-dimensional curvature K_0, the pressure $pH/10$, the relative belt force κ, and the inclination angle $\theta \cdot 10$ in the exit and entrance zones. The abscissa is $\varphi \in [0, \varphi_E]$. Data are valid for a driven pulley according to [14].*

the two integration constants for each zone. Thus, we obtain the equations below in addition to the curvature equations 4.21, and 4.24 above. In the entrance zone we have:

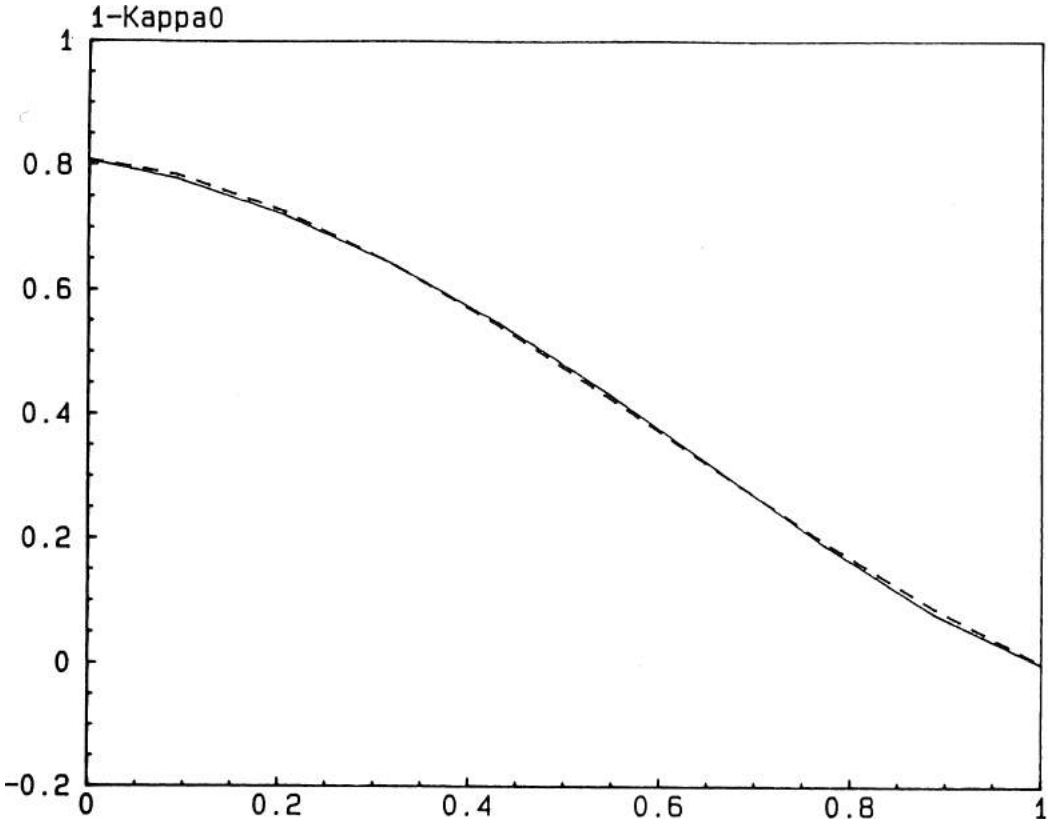

Figure 4.5 *The variable $1 - K_0$ versus ψ in the exit zone for a driven pulley. Fitted curve and original numerical solution from [14].*

$$\theta_{in} = -\varphi_{Ein}\left(1 - K_{0Cin}\right) \cdot \left(-\psi + A_{1in}\frac{\psi^2}{2} + A_{2in}\frac{\psi^3}{3} + \left(1 - A_{1in} - A_{2in}\right)\frac{\psi^4}{4} + A_{4in}\right) \tag{4.27}$$

$$x_{0in} = \varphi_{Ein}^2\left(1 - K_{0Cin}\right) \cdot \left(-\frac{\psi^2}{2} + A_{1in}\frac{\psi^3}{6} + A_{2in}\frac{\psi^4}{12} + \left(1 - A_{1in} - A_{2in}\right)\frac{\psi^5}{20} + A_{4in}\psi + A_{5in}\right) \tag{4.28}$$

$$A_{4in} = -\frac{\theta_{Ein}}{\varphi_{Ein}\left(1 - K_{0Cin}\right)} - \left(-1 + A_{1in}\frac{1}{2} + A_{2in}\frac{1}{3} + \left(1 - A_{1in} - A_{2in}\right)\frac{1}{4}\right) \tag{4.29}$$

$$A_{5in} = \frac{x_{0Cin}}{\varphi_{Ein}^2\left(1 - K_{0Cin}\right)} \tag{4.30}$$

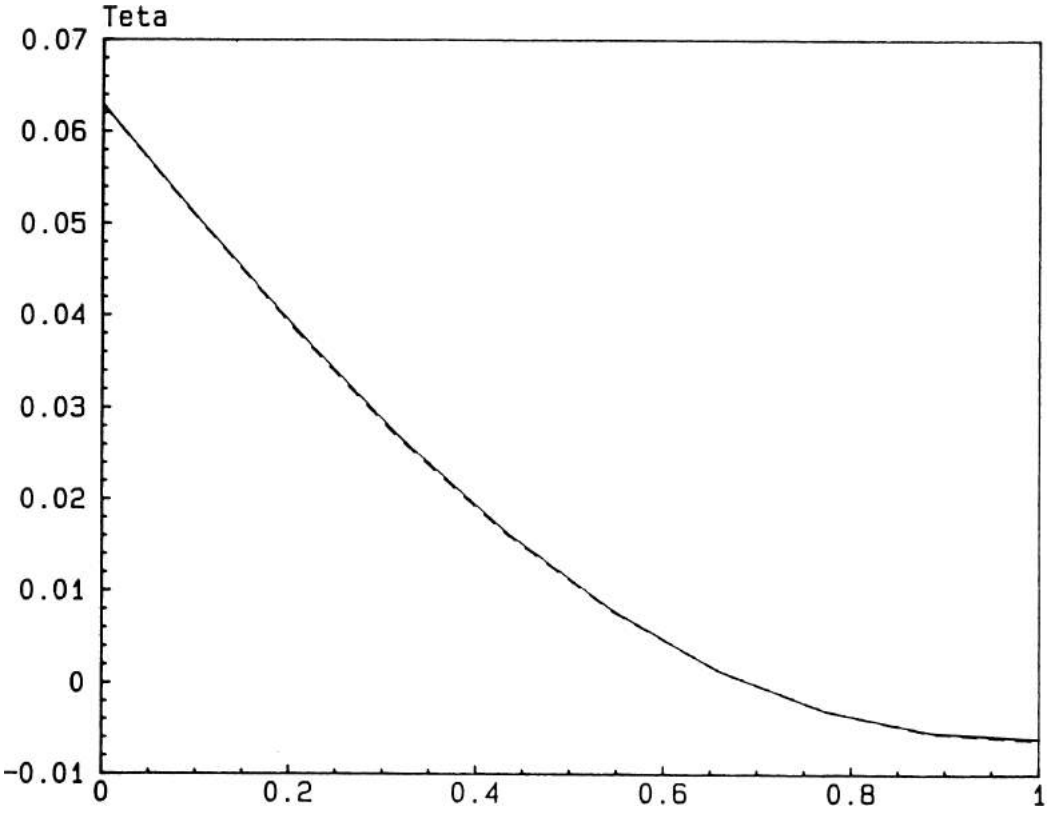

Figure 4.6 *The variable θ versus ψ in the exit zone for a driven pulley. Curve from Equation 4.31 and original numerical solution from [14].*

and in the exit zone:

$$\theta_{out} = \varphi_{Eout}\left(1 - K_{0Cout}\right) \cdot \left(-\psi + A_{1out}\frac{\psi^2}{2} + A_{2out}\frac{\psi^3}{3} + \left(1 - A_{1out} - A_{2out}\right)\frac{\psi^4}{4} + A_{4out}\right) \tag{4.31}$$

$$x_{0out} = \varphi_{Eout}^2\left(1 - K_{0Cout}\right)\left(-\frac{\psi^2}{2} + A_{1out}\frac{\psi^3}{6} + A_{2out}\frac{\psi^4}{12} + \left(1 - A_{1out} - A_{2out}\right)\frac{\psi^5}{20} + A_{4out}\psi + A_{5out}\right) \tag{4.32}$$

$$A_{4out} = \frac{\theta_{Eout}}{\varphi_{Eout}\left(1 - K_{0Cout}\right)} - \left(-1 + A_{1out}\frac{1}{2} + A_{2out}\frac{1}{3} + \left(1 - A_{1out} - A_{2out}\right)\frac{1}{4}\right) \tag{4.33}$$

$$A_{5out} = \frac{x_{0Cout}}{\varphi_{Eout}^2\left(1 - K_{0Cout}\right)} \tag{4.34}$$

In Figures 4.6 and 4.7 these functions and the numerical solution are plotted.

As discussed above we use Equation 4.12 to generalize the solution in the entrance and exit zones to arbitrary cases. The size of the contact zone φ_E is then:

$$\varphi_E = \varphi_{Eref} \cdot \frac{s_{0FB} - s_{0FC}}{s_{0FBref} - s_{0FCref}} \tag{4.35}$$

$$s_{0FB} = \sqrt{\frac{EI_0}{F_0}} \cdot \operatorname{acosh}\left(\frac{1}{K_{0C}} \cdot \cosh\left(\sqrt{\frac{F_0}{EI_0}} s_{0FC}\right)\right) \tag{4.36}$$

where s_{0FB} is the non-dimensional length coordinate when the non-dimensional curvature $K_0 = 1$. The subscript $_{ref}$ indicates data for the reference case in [14]. For $\sqrt{\frac{F_0}{EI_0}} s_{0FC} > 3$ the equations 4.35, 4.36 can be simplified to:

$$\varphi_E = \varphi_{Eref} \frac{\sqrt{\frac{F_{0ref}}{EI_{0ref}}} \ln\left(\frac{1}{K_{0C}}\right)}{\sqrt{\frac{F_0}{EI_0}} \ln\left(\frac{1}{K_{0Cref}}\right)} \tag{4.37}$$

As we have both entrance and exit sides in combination with driven or driving pulley, this gives four different cases where equations 4.35, 4.36 or 4.37 should be applied. However, we have a reference solution only for one driven case. In order to develop closed form approximations we make the assumption that the shape of the non-dimensional curvature function is representative even for a driver case. Thus, $K_{0C} = K_{0Cref}$ both for a driven and driving case ($K_{0Cin} = 1/2.048770$, $K_{0Cout} = 1/5.203121$). Using Equation 4.37 we obtain:

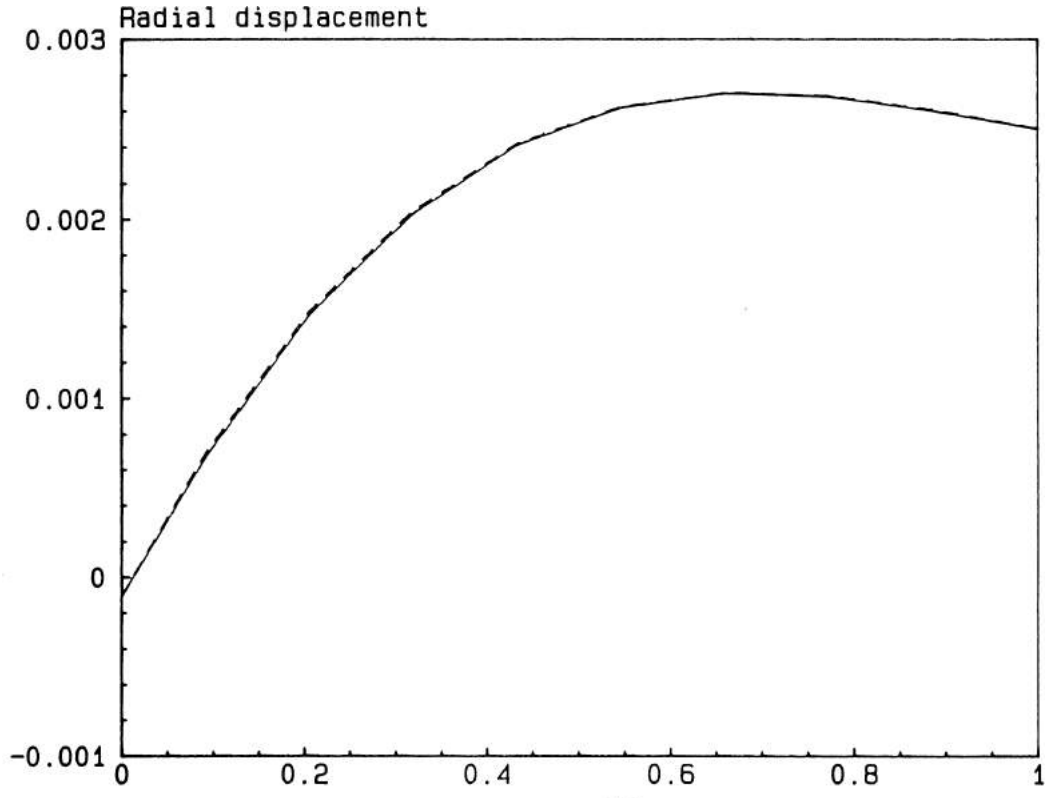

Figure 4.7 *The variable x_0 versus ψ in the exit zone for a driven pulley. Curve from Equation 4.32 and original numerical solution from [14].*

$$\varphi_{Ein} = \varphi_{Einref} \frac{\sqrt{\frac{F_{0inref}}{EI_{0ref}}}}{\sqrt{\frac{F_{0in}}{EI_0}}} \quad \text{Entrance} \tag{4.38}$$

$$\varphi_{Eout} = \varphi_{Eoutref} \frac{\sqrt{\frac{F_{0outref}}{EI_{0ref}}}}{\sqrt{\frac{F_{0out}}{EI_0}}} \quad \text{Exit} \tag{4.39}$$

where $EI_{0ref} = 0.000015$, $F_{0inref} = 0.000574488$, and $F_{0outref} = 0.001123726$. Thus, the curvature function is defined completely for an arbitrary case.

We also need closed form approximations for the pressure p and the sliding angle γ. We have with $k_{02} = 0$ (see [14]):

$$p_0 \sim x_0 \Longrightarrow A_{5i} = 0 \tag{4.40}$$

The sliding angle is determined by [14],(Appendix A):

$$\gamma_N = \arctan\left(\left(x_0 - x_{0E} + (F_0 - F_{0E})\frac{1}{c_0} + \theta_E \tan(\gamma_{NE})\right)\frac{1}{\theta}\right) \tag{4.41}$$

$$\gamma = \arctan\left(\tan(\gamma_N) + (1 - K_0)\frac{h}{R\theta}\right) \tag{4.42}$$

where the subscript $_N$ denotes the neutral layer and the variable h is the height coordinate from the neutral layer towards the bottom of the belt.

In the exit and entrance zone all variables have large changes except the belt force. Therefore it has negligible influence on γ_N . Here we set it to be constant $F_0 = F_{0E} = F_{0C}$. Thus, we have:

$$\gamma_N = \arctan\left((x_0 - x_{0E} + \theta_E \tan(\gamma_{NE}))\frac{1}{\theta}\right) \tag{4.43}$$

Only two boundary conditions θ_E, γ_{NE} need to be determined when using the equations developed above.

The sliding condition gives [12]:

$$\sin\theta \tan\gamma = \frac{\cos\theta v_b - r\omega}{v_b} \tag{4.44}$$

$$v_b = v(1 + F/c) \tag{4.45}$$

Here, the purpose is to detect significant variables for the evolution of γ. As discussed above, the force variation in the exit or entrance region is negligible, and we also have $F/c \ll 1$. This means $v_b =$ constant. Also, the inclination angle θ is so small that we may write:

$$\theta \tan\gamma = \frac{v_b - r\omega}{v_b} \tag{4.46}$$

If we approximate the relative circumferential sliding velocity to be constant in these regions we have $\theta \tan\gamma =$ constant. This means that Equation 4.43 reduces to:

$$\gamma_N = \arctan\left(\theta_E \tan(\gamma_{NE})\frac{1}{\theta}\right) \tag{4.47}$$

Studying the reference case, we have an exit sliding angle $\gamma_{NC} = 1.02°$. Using the approximate Equation 4.47 we obtain $\gamma_{NC} = 3.2°$, a negligible difference which also occurs in a region where the pressure is nearly zero.

γ in the exit zone

The exit zone connects to the sliding contact zone. Thus we know θ_{Eout}. We can also obtain $\theta_{Eout} = -x'_{0Eout}$. However, at the contact point the case should be $\gamma_{NCout} \approx 0°$. It is possible that discrepancies will occur because a somewhat different theory and also different approximative equations are used in the sliding contact zone and the exit zone. Therefore, only values of θ_{Eout} are used that give realistic values of γ_{NCout}. Equation 4.47 is used.

There are two cases:

- Driven pulley: Then $\gamma_{Nout} \in [0°, 180°]$. We set the exit sliding angle at $\gamma_{NCout} = 1°$.
- Driver pulley: Then $\gamma_{Nout} \in [270°, 360°]$. We set the exit sliding angle at $\gamma_{NCout} = 359°$.

Using Equation 4.47 the corresponding values of θ_{Eout} can be calculated. Thus we always get realistic exit sliding angles.

γ in the entrance zone

The entrance zone connects to the non-sliding contact zone in which the theory postulates that $\gamma = 180°$ and $\theta = 0$. At the contact point we have $\gamma_{NCin} \approx 180°$. For this reason we simply set $\gamma_{Nin} = 180°$ in the whole entrance zone. Setting $\theta_{Ein} = 0$ yields numerical problems, therefore we choose the low value of the reference solution $\theta_{Ein} = -0.000418$.

Pressure

For the entrance zone we obtain a boundary value p_{Ein} from the non-sliding contact zone and for the exit zone we have p_{Eout} from the sliding contact zone. Equation 4.40 then gives:

$$p_{in} = \frac{x_{0in}}{x_{0Ein}} p_{Ein} \tag{4.48}$$

$$p_{out} = \frac{x_{0out}}{x_{0Eout}} p_{Eout} \tag{4.49}$$

Discussion of friction force variation

The theory for a thick V-belt [14], which is used in the exit and entrance zones, does not take into account the fact that the belt is elastic, i.e. that a material particle inside the belt can move relative to the neutral layer.

In most cases this relative motion is small compared to the sliding motion, because the friction force and the contact force change relatively slowly. However, in the exit zone on the driver pulley, there is a drastic change in sliding direction for a point on the side of the belt which enters that zone. Theory [14] postulates a nearly momentarily change in friction force, as it assumes full utilization of the friction coefficient.

However in a real belt, which is highly elastic, this will not happen. The structure has to be unloaded before it can take a load in the opposite direction. This behavior can be modeled by using "efficient" coefficient of friction that vary continuously from full friction to zero and full friction again.

Here we have implemented continuous variation of the utilization of the friction in a short interval in the beginning of the exit zone of the driver pulley. This is done by using the cosine function.

The modified theory thus gives more realistic behavior in the exit zone of the driver pulley than the original theory, but more research is needed for the exit and entrance zones.

4.5 Discussion of equilibrium conditions and inertia forces

Equilibrium conditions

The equilibrium conditions must be fulfilled. This is also the case for the different theories, with their basic assumptions, used in the different parts of the load/deformation cycle. However, variables F, p, γ, K obtained are now applied to a two or three dimensional model that differs in some respects from the model for which the theories give an exact solution. Also, the approximate closed form expressions give a small deviation from the exact solution. A third kind of error arises from the fact that only a small belt section is modeled. There may be some influence from the boundary conditions at the ends of the belt segment.

The displacement of the neutral layer is governed in the belt segment model. The curvature K gives the shape and the force F the longitudinal strain. The forces from the contact with the pulley are defined by p, γ, and μ. In order to fulfill the equilibrium conditions there will have to be additional reaction forces at the neutral layer. However, at any position along the belt those reaction forces are small compared with the total belt force. Also, the stiffness of the cord is about three orders of magnitude greater than that of the rubber. Thus, there will be no significant influence from the additional reaction forces on the stress and strain state in the belt.

The influence from the boundary conditions has to be dealt with by modeling a sufficiently long belt segment and only studying the central part.

Inertia forces

The V-belt theories discussed above are based on the assumption that inertia forces are neglected, i.e. the belt moves slowly enough so the inertia forces can be approximated

to zero besides other quantities. However, in real cases an inertia force of about 10 percent of the total force is not uncommon. So even an approximate method for taking account of this force is better than none at all.

At a point in the belt the body force (force per volume) in radial and tangential direction are:

$$B_R = \rho K V^2 (1+\epsilon)^2 \tag{4.50}$$

$$B_T = \rho V \ddot{\epsilon} \tag{4.51}$$

where ρ = the density and V = the velocity of the unloaded belt. The influence of the inertia forces has been discussed in reference [12]. It is shown that the tangential component is not significant in normal V-belt applications. If $\epsilon \ll 1$, it is possible to regard the inertia force in the cord layer F_c as a superimposed quantity to the effective belt force F. Thus, the V-belt theory is valid using the effective belt force. We now have:

$$B_R = \rho K V^2 \tag{4.52}$$

which gives

$$F_c = \rho A V^2 \tag{4.53}$$

where A = effective area of the belt cross-section and ρ = the density.

5

A parametric function of a belt segment

When the load (i.e. the curvature function, the force function, the normal pressure and friction force function), which is a function of time, is applied to the belt, a small section of the belt is studied. This is necessary in order to avoid boundary effects. The belt section which is represented by a FEM-model, should be as stationary as possible to avoid the need for excessive computation. Also, it should be possible to apply the different types of load independently. It should be possible to change the curvature independently of the longitudinal force/strain, etc.

These objectives can be accomplished by representing the path of a curve within the neutral layer of the belt. This should be done with a parametric function, the parameter being the belt path length. To minimize the rotations, the middle point of the belt segment is located at the origin, with the tangent vector equal to zero. Thus, the coordinates of the curve in the neutral layer of the belt can be calculated at any instant in time at any position along the belt path. For a three dimensional model the curve should represent the cord which has the average longitudinal strain. For a two dimensional case there is only one possible curve.

The parametric function is defined below for one side of the vertical axis through the origin (see Figure 5.1). It is analogous for the other section.

The curve length parameter s is divided into n equal intervals Δs. Each interval has a constant curvature K. In interval i we have then:

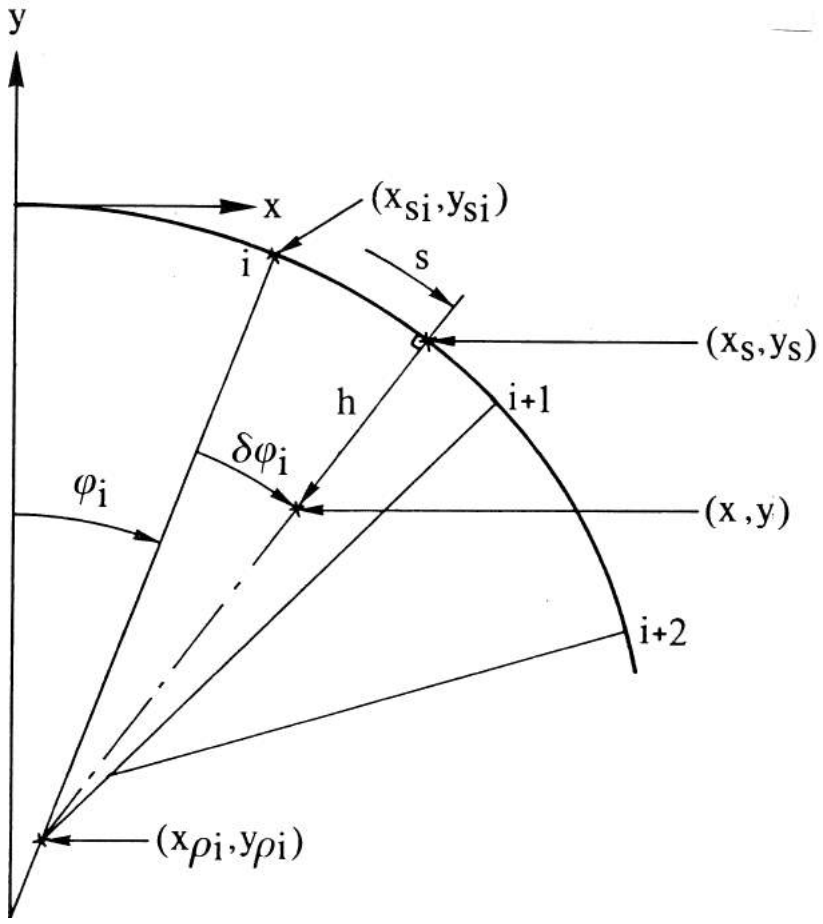

Figure 5.1 *Definition of the parametric belt segment function*

$$s = i \cdot \Delta s + \delta s_i \quad \delta s \in [0, \Delta s] \tag{5.1}$$

$$\varphi = \varphi_i + \delta\varphi_i \quad \delta\varphi \in [0, \Delta\varphi] \tag{5.2}$$

$$\varphi_i = \sum_{k=1}^{i} \Delta s K_i \tag{5.3}$$

$$\delta\varphi_i = \delta s_i K_i \tag{5.4}$$

$$K_i = \frac{1}{2}\left(\frac{1}{\rho_i} + \frac{1}{\rho_{i+1}}\right) \tag{5.5}$$

$$x_s = x_{si} + \frac{2}{K_i}\cos\left(\varphi_i + \frac{\delta\varphi_i}{2}\right)\sin\left(\frac{\delta\varphi_i}{2}\right) \tag{5.6}$$

$$y_s = y_{si} - \frac{2}{K_i}\sin\left(\varphi_i + \frac{\delta\varphi_i}{2}\right)\sin\left(\frac{\delta\varphi_i}{2}\right) \tag{5.7}$$

If $K_i = 0$ then $\delta\varphi_i = 0$ and equations 5.6 and 5.7 are reduced to:

$$x_s = x_{si} + \cos(\varphi_i)\delta s_i \tag{5.8}$$

$$y_s = y_{si} - \sin(\varphi_i)\delta s_i \tag{5.9}$$

For an arbitrary point (x, y) on the belt we need to determine φ, s, and h. Assuming that the point is within interval i, we obtain for the case $K_i \neq 0$:

$$\begin{aligned} \delta\varphi_i &= \arctan\left(\frac{x - x_{\rho i}}{y - y_{\rho i}}\right) - \varphi_i && (5.10)\\ x_{\rho i} &= x_{si} - \frac{1}{K_i}\sin(\varphi_i) && (5.11)\\ y_{\rho i} &= y_{si} - \frac{1}{K_i}\cos(\varphi_i) && (5.12)\\ h &= \sqrt{(x - x_s)^2 + (y - y_s)^2} && (5.13) \end{aligned}$$

and for the case $K_i = 0$:

$$\begin{aligned} \delta\varphi_i &= 0 && (5.14)\\ \delta s_i &= \frac{(y_{si} - y)\tan(\varphi_i) - (x_{si} - x)}{\tan(\varphi_i)\sin(\varphi_i) + \cos(\varphi_i)} && (5.15)\\ h &= \sqrt{(x - x_s)^2 + (y - y_s)^2} && (5.16) \end{aligned}$$

The curve parameter of the neutral layer for the unstrained belt has to be determined as a function of the curve parameter of the strained belt, i.e. the belt path curve s. We then have:

$$s_{org} = \int_0^s \frac{d\tilde{s}}{1 + \epsilon(\tilde{s})} \qquad (5.17)$$

where ϵ is the longitudinal strain which depends on the belt force.

In order to avoid dependency on the special form of the integrand we assume linear variation within each of the intervals discussed above. Thus, we obtain for interval i:

$$\begin{aligned} \delta s_{orgi} &= \frac{\delta s_i}{1 + \epsilon(s_i)}\left(1 - \frac{\epsilon(s_{i+1}) - \epsilon(s_i)}{1 + \epsilon(s_{i+1})} \cdot \frac{\delta s_i}{2\Delta s}\right) && (5.18)\\ \delta s_i &= (1 + \epsilon(s_i))\,\delta s_{orgi} \cdot \\ &\qquad \frac{2}{1 + \sqrt{1 - \frac{(\epsilon(s_{i+1}) - \epsilon(s_i))\cdot 2\cdot(1+\epsilon(s_i))\delta s_{orgi}}{\Delta s(1+\epsilon(s_{i+1}))}}} && (5.19)\\ s_{org}(s_i) &= \frac{\Delta s}{2}\sum_{k=1}^{i}\left(\frac{1}{1 + \epsilon(s_k)} + \frac{1}{1 + \epsilon(s_{k-1})}\right) && (5.20) \end{aligned}$$

6
Simulation of test cases

6.1 Test cases

Output data

From observations regarding the fatigue mechanisms the areas of interest are [6]:

- Radial crack growth towards the cord layer. These are normally initiated between the cogs. Variables of interest are stresses that govern crack propagation in the radial direction.
- Separation or cracking in the longitudinal direction close to the cord layer, in the cushion layer, or between the cushion and pressure section. Variables of interest are stresses that govern crack propagation in the longitudinal direction.

The variables above will be studied during the analysis. A complete analysis has to be performed for each case for which there are test data until enough, information is obtained to accomplish a correlation of studied variables to fatigue data.

Input data

As a first case we study the belt for which there are most experimental data available. It is a 0.500 inch belt running on two equal size pulleys. Data are available for different loads, torques, speeds, and diameter of the pulleys. The belt has a cog shape to decrease the bending stiffness and losses. The materials used in the design of the belts are discussed in reference [7] and the constitutive equations have been presented in reference [4].

The belt properties for this belt, as defined in the theory for V-belt mechanics, are represented by three stiffness coefficients. Below, these constants are determined by approximate calculations or by experiments. However, simulations using the FEM-models discussed in the next sections can be used to determine these coefficients very accurately for any load case.

The longitudinal stiffness c is the stiffness of the cord in the belt and is therefore represented by the material data investigated in [7]. Data for the dynamic stiffness

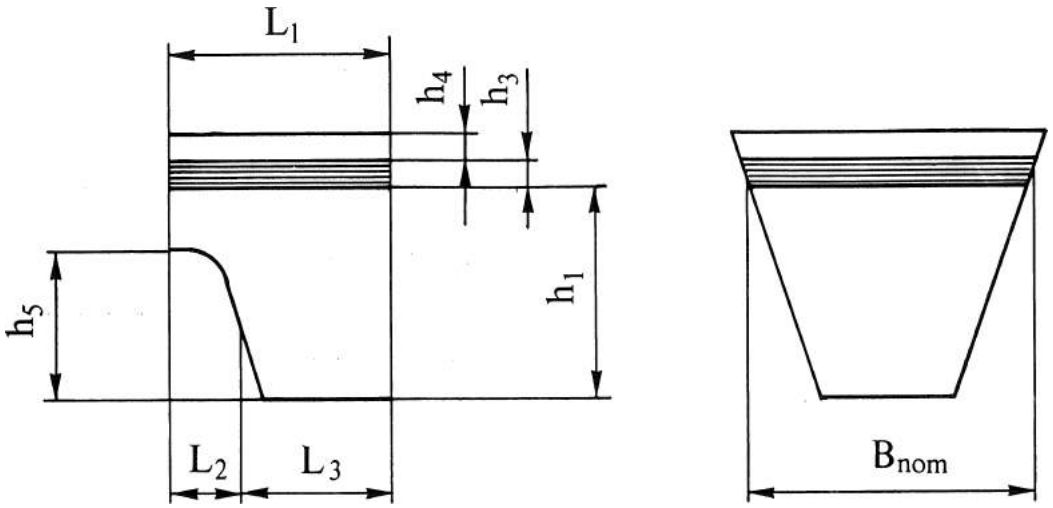

Figure 6.1 *Approximate calculation of mean height and belt width*

at $\epsilon_a = 0.0025$ and $f = 5$Hz are used. The temperature influence on the longitudinal belt stiffness can approximately be modeled as:

$$c = A_c \cdot E1 \cdot (76.6 + (102 - T)\, 0.52877) \tag{6.1}$$

where A_c is the total area of the cords in the belt, $E1$ the constant used in [7], and T temperature in degrees Celsius.

The radial stiffness k_1 is approximately calculated from the axial stiffness of a belt material section (see Appendix A). This axial stiffness can easily be calculated from material data and geometry. Neglecting the top fabric layer which has no significant influence on V-belt mechanics, the height and width of the belt are calculated as given in figure 6.1. The nominal belt width is located in the middle of the cord layer.

$$H = (h_1 + h_3)\frac{l_3}{l_1} + (h_1 + h_3 - h_5)\frac{l_2}{l_1} \tag{6.2}$$

$$B = B_{nom} - 2\tan(\beta)\left(\frac{H}{2} - \frac{h_3}{2}\right) \tag{6.3}$$

For the 0.500 inch belt we have $H = 6.5862$ mm and $B = 11.1542$ mm. The most representative material stiffness is that of material 1 in the fiber reinforced direction [7]. At a strain amplitude of 0.005 and a frequency of 34Hz we can approximately model the temperature influence on the Young's modulus as:

$$E_{33} = E0 \cdot (12.75 + (95.5 - T)\, 0.62903) \tag{6.4}$$

where $E0$ is the constant used in [7].

The bending stiffness EI of the belt is here experimentally determined at room temperature. The Young's modulus E_{22} of material 1 at $\epsilon_a = 0.045$ and $f = 34$Hz is used to model the temperature influence. Thus we obtain:

$$EI = E0 \cdot 834.0\,(1 + (20 - T)\, 0.001786) \tag{6.5}$$

where $E0$ is the constant used in [7].

6.2 A two dimensional model

A plane strain model is the best two-dimensional approximation available because of the heavy fiber reinforcement in the axial direction and also because of the influence from the pulley which prevents motion in the axial direction when the belt is bent around the pulley. In this plane strain model the longitudinal force and geometric deformation due to bending can essentially be properly represented. Influence from the contact pressure and frictional forces can only be studied by modeling them as body forces. The axial component can not be applied. A certain belt width is needed to refer the contact forces to. It should be less than or equal to half the belt width, as the forces act on both sides. A conservative choice is $B/2$. From Equation 4.1 we obtain the longitudinal component of the body force and from equations 4.3 4.52 the radial component.

$$B_l = -\mu p \frac{2}{B} \cos(\beta_s) \sin(\gamma) \frac{1}{\cos(\beta)} \tag{6.6}$$

$$B_r = p \frac{2}{B} \left(\sin(\beta) - \mu \cos(\beta_s) \cos(\gamma) \right) \frac{1}{\cos(\beta)} + \rho K V^2 \tag{6.7}$$

In the Cartesian coordinate system (see Figure 5.1) we have:

$$B_x = \cos(\varphi) B_l + \sin(\varphi) B_r \tag{6.8}$$

$$B_y = -\sin(\varphi) B_l + \cos(\varphi) B_r \tag{6.9}$$

The belt properties are represented by three stiffness coefficients discussed above. The bending stiffness EI is then experimentally determined, but it can also be calculated using the plane strain FEM-model.

The load/deformation is applied in two steps:

1. An initial step which is not repeated. The belt is bent from its original curvature until it is straight, and the load of the low tension side F_1 and centrifugal forces F_c is applied.

2. The load/deformation cycle: Begins at the middle of a low tension side. This step will be repeated until the desired number of cycles is completed. The constitutive material response predicts that 4 - 10 cycles are needed to obtain stabile conditions [7, 4].

The load/deformation cycle is defined as a certain material point in the belt having moved one revolution and arrived back to the original position.

The plane strain FEM model is shown in Figure 6.2. It incorporates two different materials. The *pressure* section of heavily fiber reinforced filled elastomer and a very thin *cushion* close to the cord. In this model the neutral layer is represented by the upper boundary in which the displacement of every node is governed.

The model has two different types of sections.

- A central section where the variables of interest are studied. Examples are stresses and strains. This section has the fine resolution of the mesh needed to calculated the stresses and strains accurately.

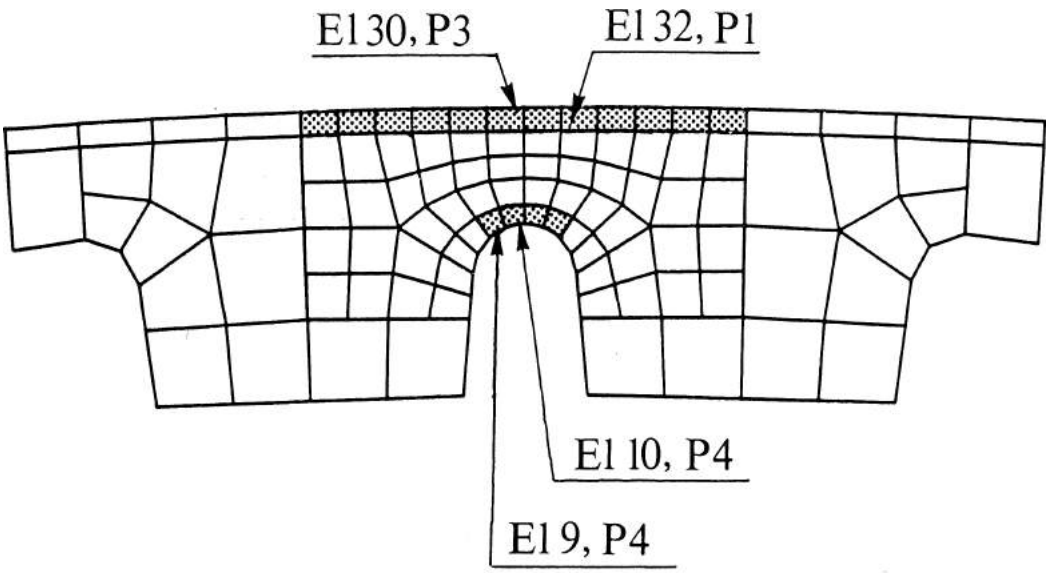

Figure 6.2 *A plane strain FEM model of a V-belt section*

- A trailing section and a leading section, the only purpose of which is to provide realistic boundary conditions for the central section. Therefore they are very coarsely modeled.

6.3 A three-dimensional model

A three-dimensional model is not principally different from the two-dimensional model with regard to the analysis scheme, but offers more information and is also much more demanding computationally. The main differences are:

- A cord layer has to be introduced. It can be modeled with individual cords or an anisotropic material layer can be used. ABAQUS also offers a "rebar" option which can be used to model cords. The necessary material properties for the cord layer have been experimentally determined [7]. Boundary conditions that allow effects such as "dishing" to develop are used. This means that the cord layer can move radially.

- The contact and friction forces can be applied on the side of the belt when the belt is in contact with the pulley. Equations 4.1, 4.3, and 4.2 can be used directly.

As seen, there is no difference in principle from the analysis scheme used for the two-dimensional case. The greatest difference, and also the limiting factor, is the computation aspect. It can be expected that a three-dimensional model will need about 10 to 30 times longer computation time. The results of the two-dimensional analysis will determine whether a three-dimensional analysis is feasible with available software and hardware.

As, in this case, we have a three-dimensional model available, a highly detailed analysis can be performed to obtain values for the radial and bending stiffness coefficients used in the V-belt theory.

6.4 Correlation to fatigue mechanisms

The following is a discussion of empirical relations for crack propagation with respect to fatigue mechanisms. The main work available in this field and for this class of materials is empirical. So, when developing a formula for fatigue life prediction of components in those materials, the only criteria we have is the correlation to available fatigue data.

In order to obtain a first expression that can be evaluated, we first discuss the qualitative concept of linear elastic fracture mechanics.

The cyclic rate growth, or how much the crack length increases for one load cycle, is dependent on many parameters, such as:

- The maxima and minima of the stress intensity factor.
- Temperature, which depends on the ambient temperature, the hysteresis work, the friction energy loss, and the heat conduction. The temperature is very important for fatigue of elastomers.
- Effects from the environment other than the temperature. Among these are oxidation, ozone cracking, etc. This is very significant for different types of elastomers.

Here we consider the first two items.

If the mechanical crack growth rate $\frac{da}{dN}$ and the "double stress intensity factor amplitude" ΔK_I (compressive load does not give any contribution to crack propagation, the crack closes) are plotted for pure mode I loading which is the technically most important, then it is normally possible to distinguish three different intervals [1] as follows (see Figure 6.3).

- There is an asymptote ΔK_{th}. Below it no growth occurs and just above it the following equation may be used:

$$\begin{aligned} \frac{da}{dN} &= C\left((\Delta K_I)^n - (\Delta K_{th})^n\right) \\ C,\, n,\, \Delta K_{th} &= \text{material constants} \end{aligned} \tag{6.10}$$

- There is a region where $\ln\left(\frac{da}{dN}\right)$ is linear in $\ln(\Delta K_I)$. It is usually referred to as Paris law.

$$\begin{aligned} \frac{da}{dN} &= C_1(\Delta K_I)^n \\ C_1,\, n &= \text{material constants} \end{aligned} \tag{6.11}$$

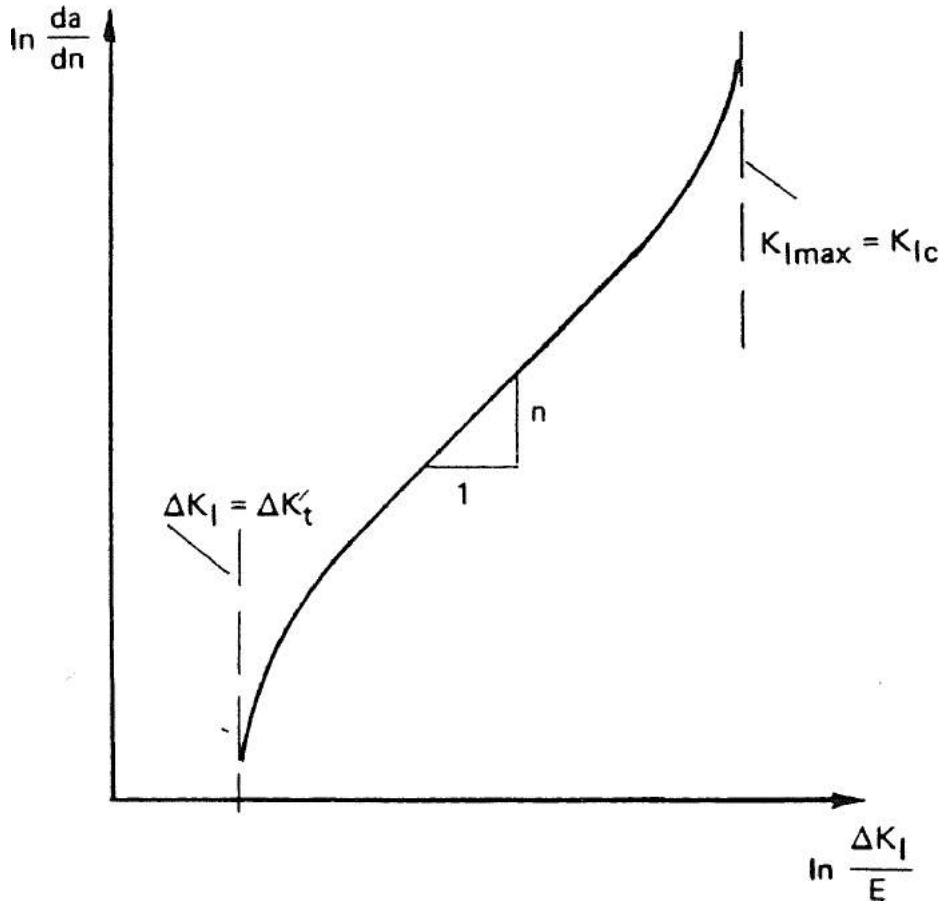

Figure 6.3 *The rate of crack growth for cyclic loading [1].*

- Finally, we have the instability region where the crack growth rate asymptotically reaches infinity for the limit (K_{Ic}).

$$\begin{aligned} \frac{da}{dN} &= C_2 \frac{\lambda^m \Delta K_I^n}{K_{Ic} - \lambda \Delta K_I} \\ \lambda &= \frac{K_{Imax}}{\Delta K_I} \\ C_2,\, n,\, m,\, K_{Ic} &= \text{material constants} \end{aligned} \tag{6.12}$$

If designing for a relatively small final crack a_c the macroscopic stress state around the crack is not much affected and we assume the "double stress amplitude" $\Delta\sigma$ to be constant during the crack growth. Also, we approximate the function f in $\Delta K_I = \Delta\sigma\sqrt{\pi a} \cdot f$ to be independent of the crack length for this short crack. Under these conditions an equation like Equation 6.11 can be integrated analytically. However, if we also assume that the material has small initial cracks $a_i \ll a_c$ and that $n > 2$ we obtain:

$$\begin{aligned} N_c &= C_3(\Delta\sigma)^{-n} \\ C_3,\, n &= \text{material constants} \end{aligned} \tag{6.13}$$

which is a part of the "SN-curve".

In a V-belt both mode I (K_I) and mode II (K_{II}) are active. For a radial crack mode I will dominate and for a longitudinal crack mode II, however mixed modes may occur to some extent.

Consider a crack where both modes are active simultaneously. Use $K_I = \sigma\sqrt{\pi a}$ and $K_{II} = \tau\sqrt{\pi a}$ (assume $f \approx 1$) where the stresses are representative of the stress state around the crack but not disturbed by it. There are two cases: If the stress normal to the crack is positive, then the crack is open. If the stress normal to the crack is negative then the crack is closed.

$$K_I = \begin{cases} \sigma\sqrt{\pi a} & \sigma \geq 0 \\ 0 & \sigma < 0 \end{cases} \tag{6.14}$$

$$K_{II} = \tau\sqrt{\pi a} \tag{6.15}$$

In order to obtain an "effective" stress intensity factor, the equation below can be used [1, 2, 19]. Here no mode III is active.

$$K_e = \sqrt{K_I^2 + K_{II}^2} \tag{6.16}$$

$$J \sim (K_e)^2 \quad \text{The J-integral} \tag{6.17}$$

Now the load spectrum should be studied. For metals the double amplitude of the stress intensity factor ($\Delta K = K_{max} - K_{min}$) is found to be the important parameter, and it is also used in equations 6.10, 6.11, and 6.12. For mixed modes the double amplitude of an "effective" stress intensity factor ΔK_e is needed. However, the equation 6.16 above gives totally unrealistic results and cannot be used if σ and τ are not in phase or if $|\tau_m| < \tau_a$.

It has not been shown that the double amplitude ΔK is the governing parameter for elastomer composites as it is for metals.

For many polymeric materials the mean stress intensity factor ($K_m = (K_{max} + K_{min})/2$) is just as important as ΔK [18, 23, 24].

For rubber vulcanizates, the rate of mechanical crack growth is frequently expressed as:

$$\frac{da}{dN} = CT^n \quad \text{where} \tag{6.18}$$

$$T = -\left(\frac{\partial U}{\partial A}\right)_L \tag{6.19}$$

$$C,\, n = \text{material constants}$$

Here U is the energy stored elastically by the imposed deformation, A represents the new area created when the crack grows, L indicates that the sample is held at constant length when the crack propagates, and T is referred to as the "tearing energy" [21, 22, 20, 8, 25, 24]. For a tensile strip test piece we have:

$$\begin{aligned} T &= kWa && (6.20)\\ W &= \int \sigma d\epsilon \quad \text{Strain energy per unit volume} && (6.21)\\ k &= \text{constant} && (6.22) \end{aligned}$$

By integrating Equation 6.18 for this case we obtain:

$$N_c \sim W^{-n} \tag{6.23}$$

V-belt materials are elastomer composites. None of the cases discussed above is directly relevant. The only fatigue data that exist are in the form of data for V-belt fatigue. There is a need for a test program to determine what governs crack propagation in these materials. It is important that the load history used is representative for the application.

In this study, we can only make a preliminary investigation as we only have a few V-belt simulation cases. This means that only very simple expressions can be tried.

In [11] expressions of type

$$\begin{aligned} N_c &= 10^{(d-e\sigma)} \cdot 2^{(-0.1\Delta T)} && (6.24)\\ d,\, e &= \text{material constants}\\ \Delta T &= \text{temperature change} \end{aligned}$$

are suggested. The temperature influency factor comes from an empirical observation that an increase in temperature of about 10 °C gives a reduction in life by a factor of 2 [11].

Here we suggest an approach that includes knowledge of how the cracks propagate in the belt.

Equations 6.14, 6.15, into 6.16 yields:

$$K_e = \sqrt{\pi a} \begin{cases} \sqrt{\sigma^2 + \tau^2} & \sigma \geq 0 \\ |\tau| & \sigma < 0 \end{cases} \tag{6.25}$$

so that we can define an effective stress:

$$\sigma_e = \begin{cases} \sqrt{\sigma^2 + \tau^2} & \sigma \geq 0 \\ |\tau| & \sigma < 0 \end{cases} \tag{6.26}$$

This effective stress will be monitored for significant peak values (no minor intermediate values will be included), while simulating a running belt. These values are used in an equation of the type 6.13. As we assume here that the *maxima* in K_e is the governing variable, the use of Equation 6.16 is allowed.

To model the temperature influence we use a formula of the type suggested by 6.24. If there is one significant maximum in effective stress at the studied material point, then we have:

$$\begin{aligned} N_c &= C(\sigma_{emax})^{-n} \cdot 2^{(-b\Delta T)} \\ C,\, n,\, b &= \text{material constants} \end{aligned} \tag{6.27}$$

where N_c is the number of cycles until the crack, at that point, has reached the length a_c. This holds for an arbitrary combination of mode I and mode II.

In a V-belt drive there are probably one or more peak values in σ_e for each pulley that contribute to the crack propagation. Driver or driven case will probably be different and we can also expect a variation between different parts of the belt.

For one cycle the crack growth in a certain material point is:

$$\Delta a = C_4 K_e^n = C_4 \sqrt{\pi a} \cdot \sigma_e^n \tag{6.28}$$

During this cycle a can be regarded as a constant as we assume $\Delta a \ll a$. For each stress peak $\sigma_{e,i}$ during this cycle there is a corresponding Δa_i. Thus the total crack growth for one cycle with m contributing peaks is:

$$\Delta a = C_4 \sqrt{\pi a} \cdot \sum_{i=1}^{m} \sigma_{emax,i}^n \tag{6.29}$$

We can now replace Equation 6.27 with:

$$\begin{aligned} N_c &= C\left(\sum_{i=1}^{m} (\sigma_{emax,i})^n\right)^{-1} \cdot 2^{(-b\Delta T)} \\ C,\, n,\, b &= \text{material constants} \end{aligned} \tag{6.30}$$

Using $\sigma_0 = \sqrt[n]{C}$ it can be rewritten to:

$$\begin{aligned} N_c &= \left(\sum_{i=1}^{m} \left(\frac{\sigma_{emax,i}}{\sigma_0}\right)^n\right)^{-1} \cdot 2^{(-b\Delta T)} \\ \sigma_0,\, n,\, b &= \text{material constants} \end{aligned} \tag{6.31}$$

As expected the fatigue life is reduced by a factor m if we have m equally severe peaks per cycle instead of one per cycle.

In a real case, knowledge of the problem studied and the order of the exponent n will determine which peaks and the smallest possible peaks to be included in the calculation.

When studying the V-belt in simulations we have two areas of interest [6].

- Radial crack in the pressure section towards the cord layer. We monitor the material calculation points in the finite-elements. The four elements between the "cogs" marked in Figure 6.2 are studied. We do not know the exact crack propagation direction; it is dependent on load, etc. In order to obtain a worst

case in each studied material point when calculating the parameters studied, the crack propagation direction is continuously varied from $-25°$ to $+25°$ relative to the radial direction. This variation covers the variation observed in experiments. Other intervals have been investigated, see Figures 6.16,6.17, and 6.18, but only a small difference was obtained for variations larger than $\pm 25°$.

- Longitudinal crack in the cushion section below the cords. All elements of this material in Figure 6.2 are monitored. In accordance with experimental observation, only longitudinal crack propagation direction is studied.

Some figures with the stress history of certain studied material points are given in next section. As can be seen in Figures 6.17 and 6.19 there are certain distinguishable maxima and minima in σ_e which are of interest. These can be found using a simple algorithm, such as:

1. Record all maxima and minima for the last load cycle.
2. Disregard all maxima that are less than 25% of the largest maxima, and also all minima that are larger than 25% of the largest maxima. This chosen limit of 25% results in a variation of $\sum \sigma_e^n$ less that 1% if $n > 3$.
3. Eliminate the smaller of two successive maxima without a minimum in between.
4. Eliminate the larger of two successive minima without a maximum in between.

From each simulation we get a point at each crack which has the highest value of the studied parameter, and therefore is the design point. Data from all simulation cases will be correlated to fatigue data.

6.5 Results and discussion

6.5.1 General observations

First we discuss some general observations from the simulations using "the belt segment model". Simulations have been done for 11 load cases. The model was developed on a VAX 11/785 but computations for the 11 load cases were done using a CRAY 1/A.

All the curves in figures in this section refer to what we call "case no. 1". Data are normally given for two material points, one is located between the cogs in the material 1 and the second point is close to the cord layer in material 2. This is shown in Figure 6.2. The first point is in a region where it is likely that the radial crack will start, and the second point where separation or longitudinal crack will develop.

First we study the influence of curvature changes and the friction and contact forces. The radial direction is denoted 1, the longitudinal 2, and the axial 3. The cases with only curvature changes are presented in Figures 6.4, 6.5, and the cases with contact and friction forces as well in Figures 6.6, 6.7. Isotropic elastic material is used with the material constant chosen in such way it will closely resembles the real material

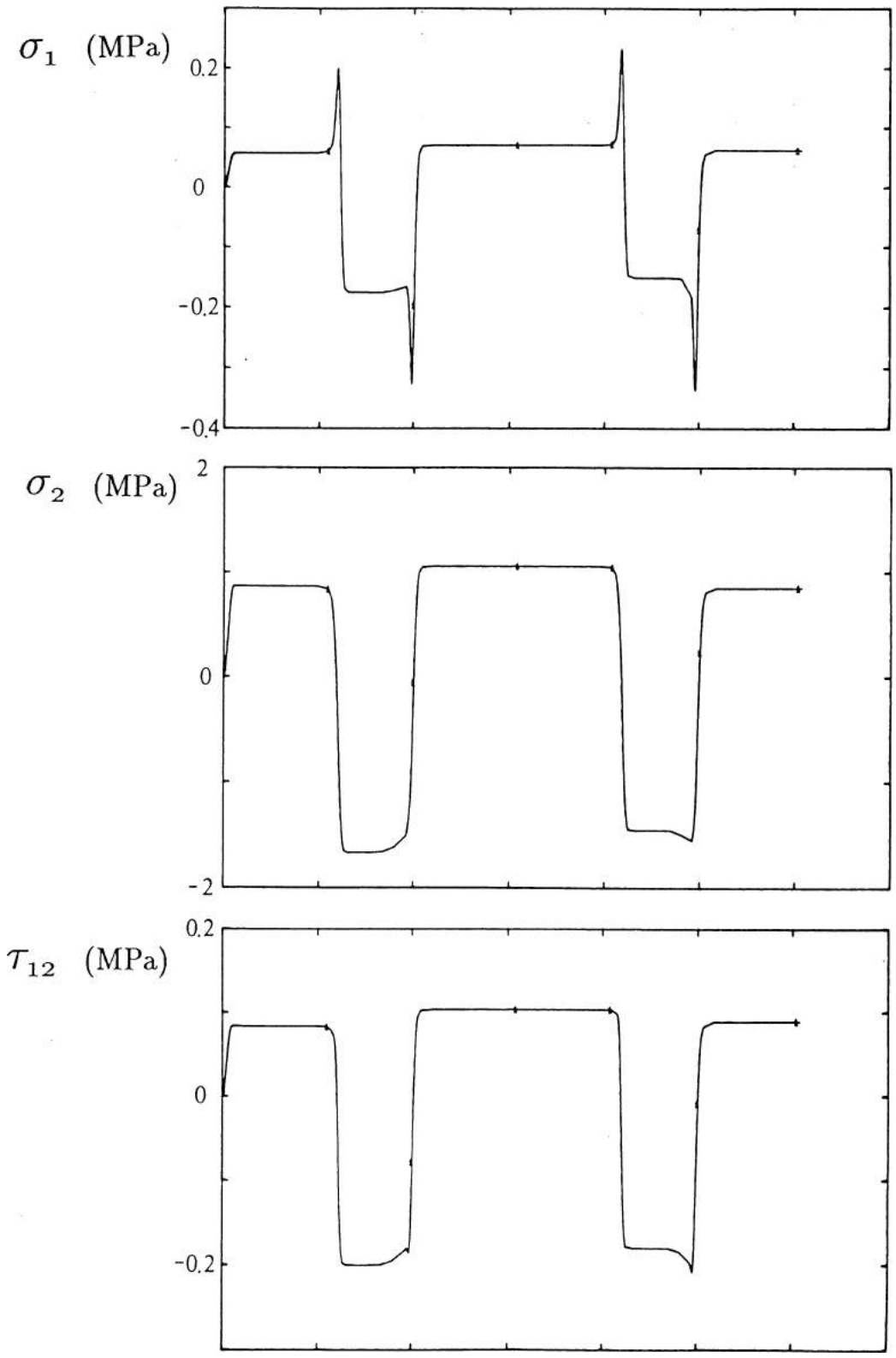

Figure 6.4 *Stresses at integration point 4 in element 10 (between the cogs) for load case 1. Isotropic elastic material 1. No contact or friction forces.*

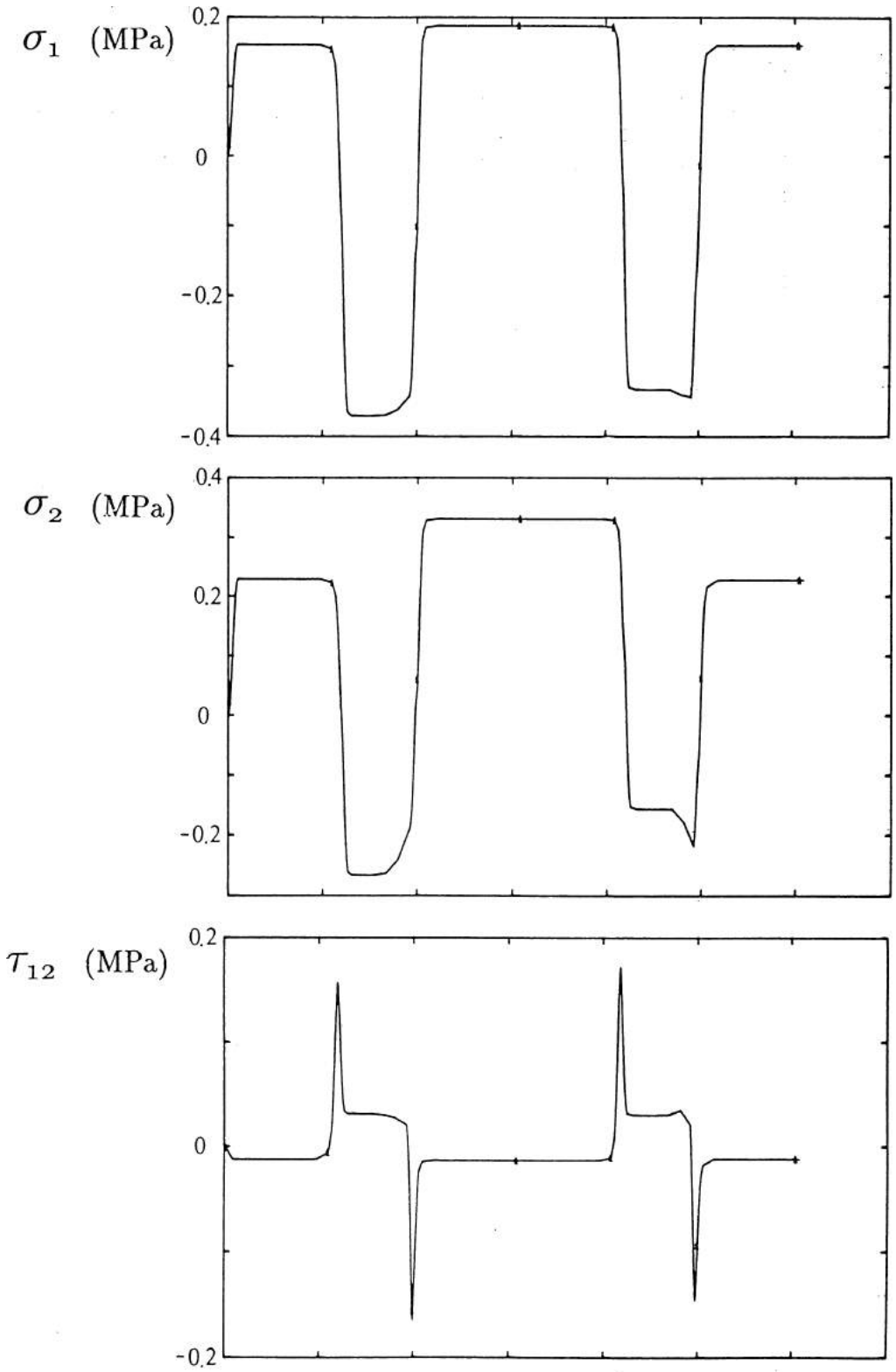

Figure 6.5 *Stresses at integration point 3 in element 30 (below the cord layer) for load case 1. Isotropic elastic material 2. No contact or friction forces.*

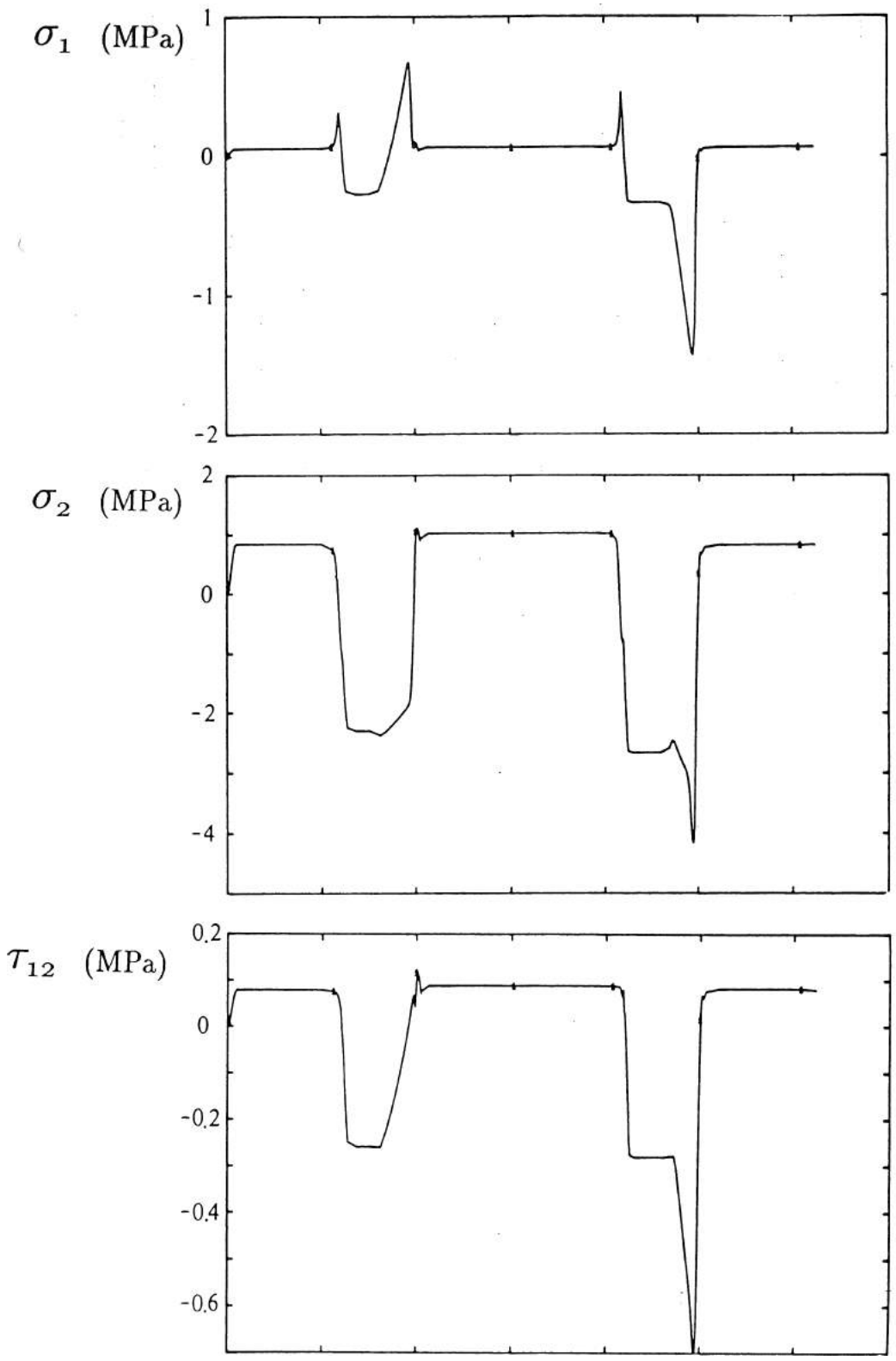

Figure 6.6 *Stresses at integration point 4 in element 10 (between the cogs) for load case 1. Isotropic elastic material 1. With contact and friction forces.*

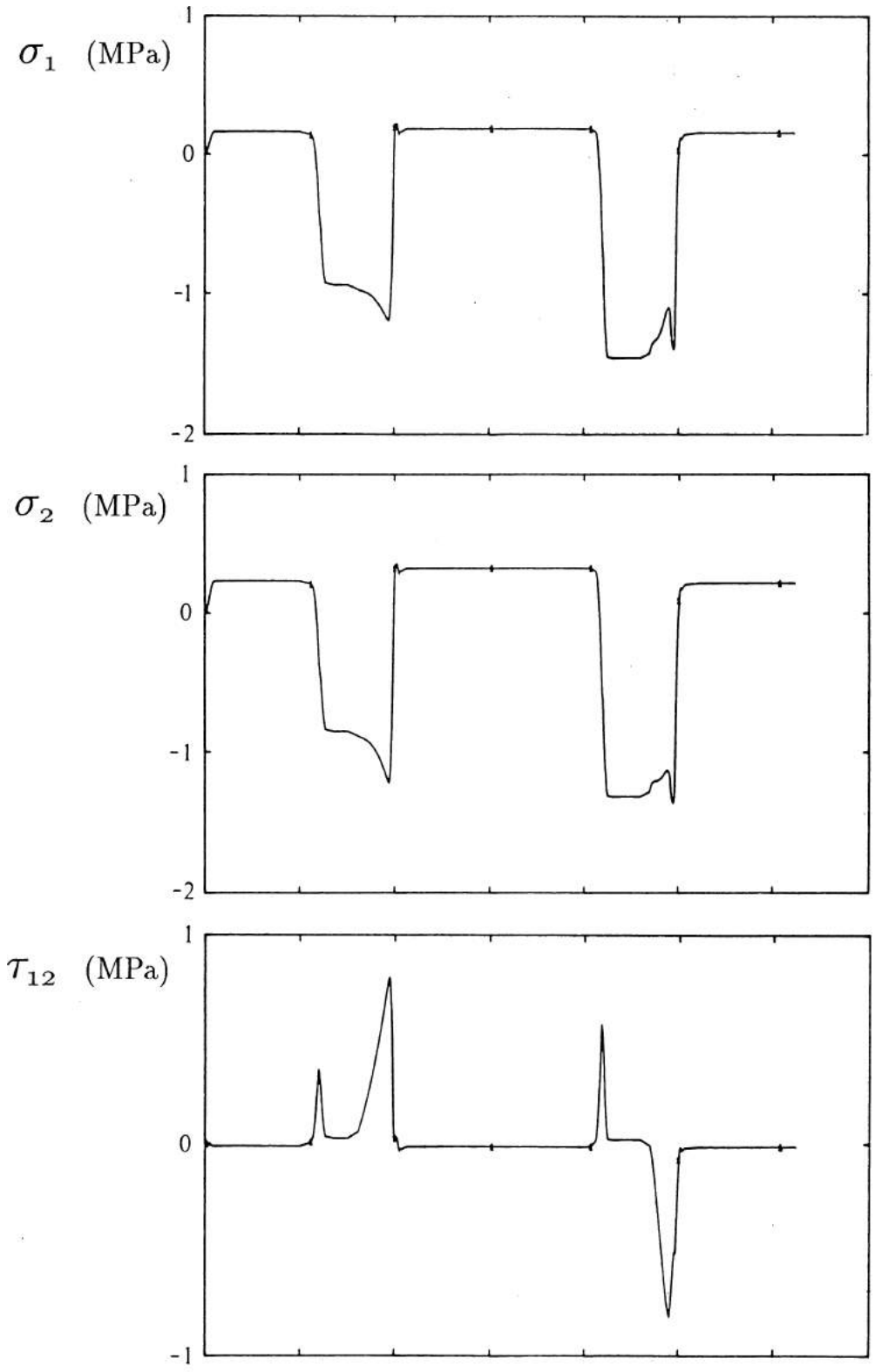

Figure 6.7 *Stresses at integration point 3 in element 30 (below the cord layer) for load case 1. Isotropic elastic material 2. With contact and friction forces.*

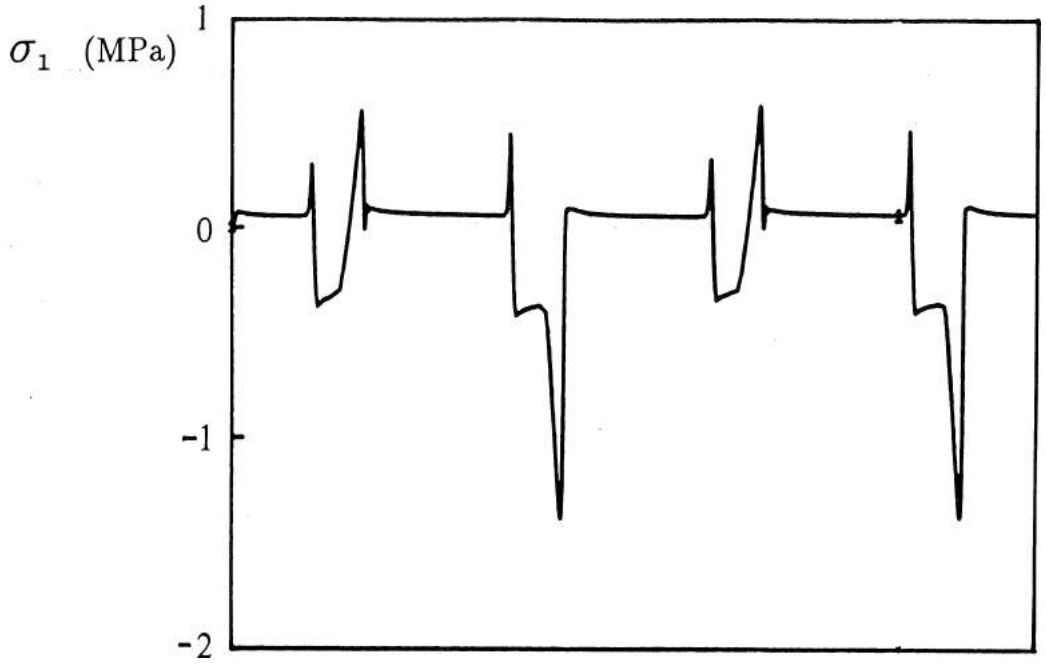

Figure 6.8 *Stress σ_1 at integration point 4 in element 10 (between the cogs) for load case 1. With contact and friction forces. Complete constitutive model.*

in these points for the actual temperature and stress/strain history. Stresses at these points is plotted for the short initial step plus one load cycle.

From the figures where the case with no contact or friction forces are shown it can be concluded that sharp peaks in stress are obtained for the continuous change in curvature at the exit and entrance zones. Also, significant tensile stresses occur between the pulleys. This is not surprising because the stress concentration due to the cog shape of the belt will be effective both for tensile stress or compressive stress. Even for the small change in curvature from that of the manufactured belt to a straight belt causes significant stresses. A longer belt will be less affected from this last effect discussed.

We now study the case when also contact, friction and radial inertia forces are applied. This is done using the conservative assumption that contact and friction forces from one side of the belt is modeled as body forces over half the belt width. As can be seen in the figures, the stresses are strongly affected by power transmission, especially in those regions where sliding occur.

Now we show in Figures 6.8, 6.9, 6.10, 6.11, 6.12, and 6.13 the case when the complete constitutive model for these materials are employed. In order to allow for the effects from damage and viscous mechanisms to develop the simulation is done for two load cycles. It can clearly be seen that these mechanisms are active. The situation will also change with temperature or belt velocity.

If two load cycles, which correspond to four bending cycles, is enough to obtain stabile conditions have not been determined as it was not practical to continue the simulations longer. This is because the computation time is quadratic in the number of load cycles for the FEM-software used. Reference [4] suggests that 4 bending cycles

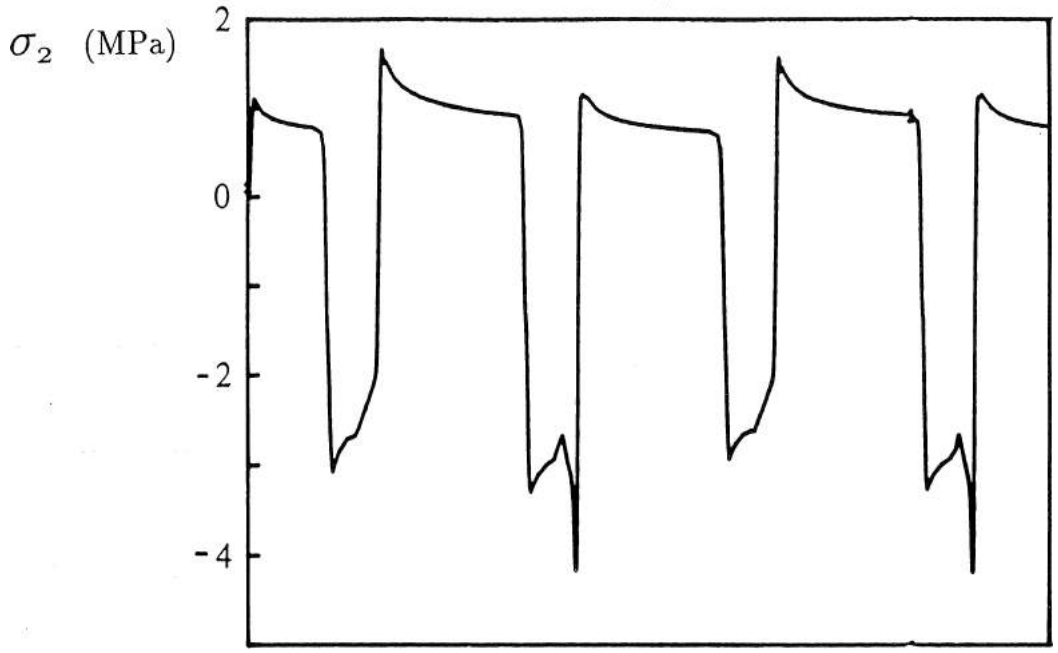

Figure 6.9 *Stress σ_2 at integration point 4 in element 10 (between the cogs) for load case 1. With contact and friction forces. Complete constitutive model.*

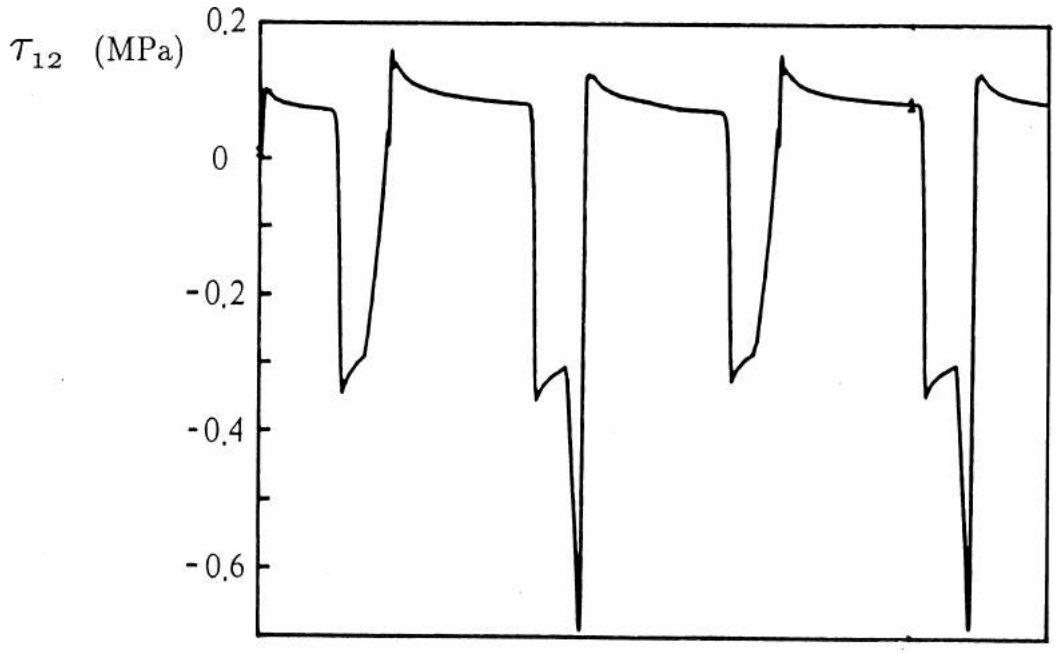

Figure 6.10 *Stress σ_{12} at integration point 4 in element 10 (between the cogs) for load case 1. With contact and friction forces. Complete constitutive model.*

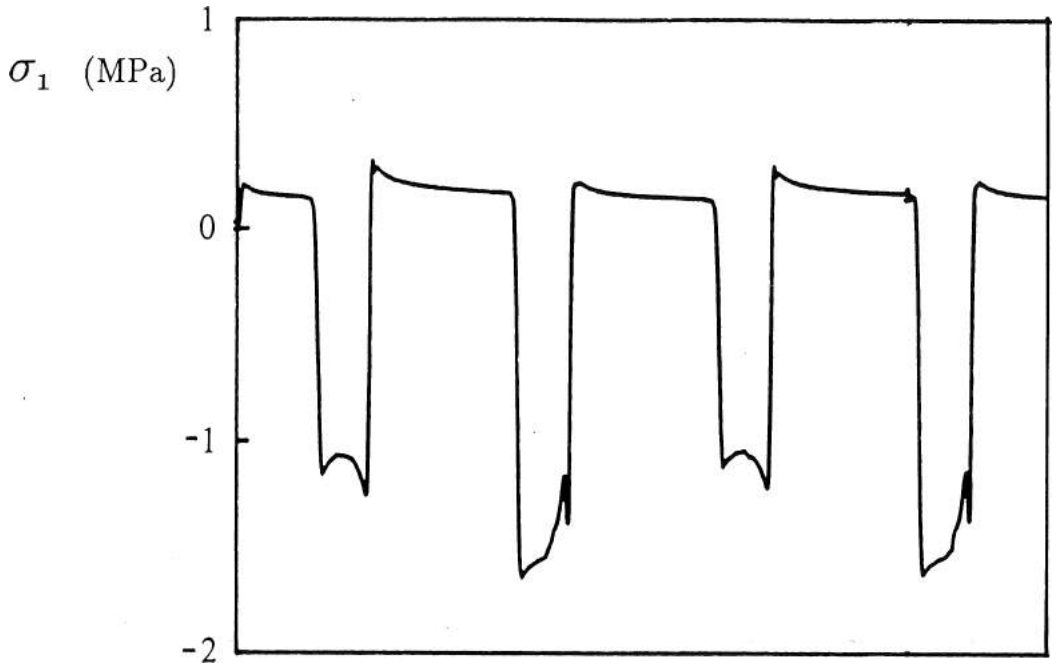

Figure 6.11 *Stress σ_1 at integration point 3 in element 30 (at the cord layer) for load case 1. With contact and friction forces. Complete constitutive model.*

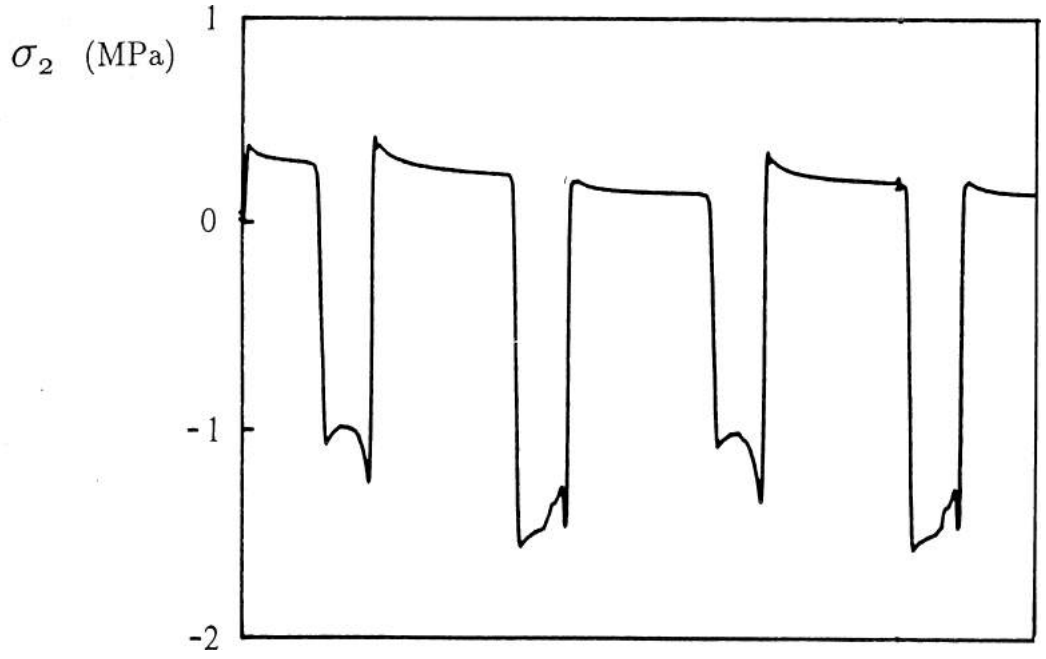

Figure 6.12 *Stress σ_2 at integration point 3 in element 30 (at the cord layer) for load case 1. With contact and friction forces. Complete constitutive model.*

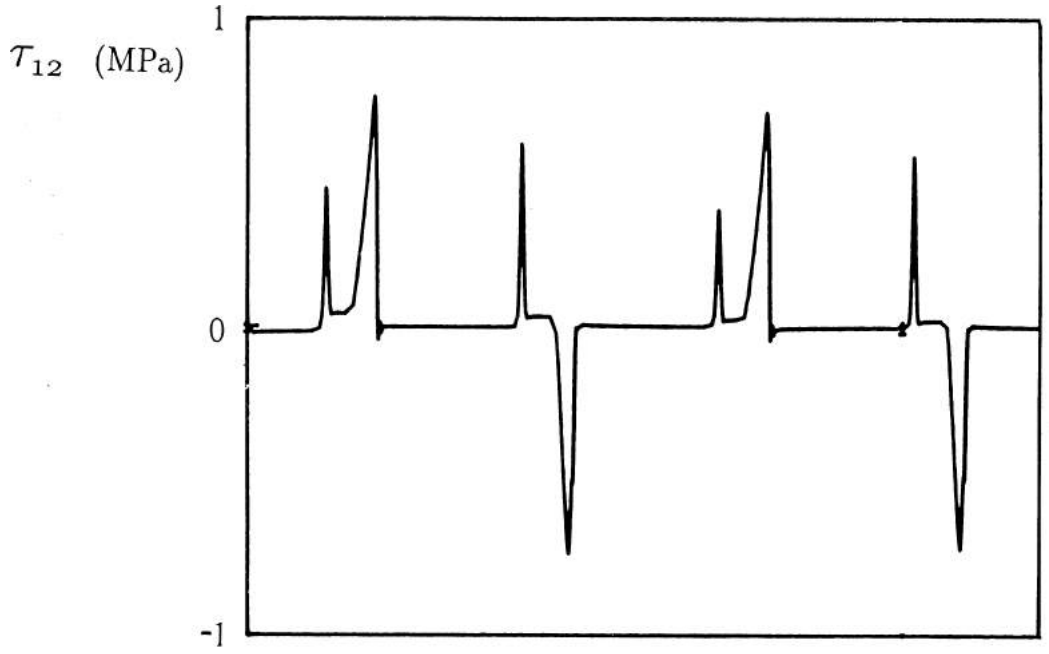

Figure 6.13 *Stress σ_{12} at integration point 3 in element 30 (at the cord layer) for load case 1. With contact and friction forces. Complete constitutive model.*

is a minimum.

Finally, in Figures 6.14 and 6.15 we show the running belt in various positions during the load cycle. This is for the complete case discussed last.

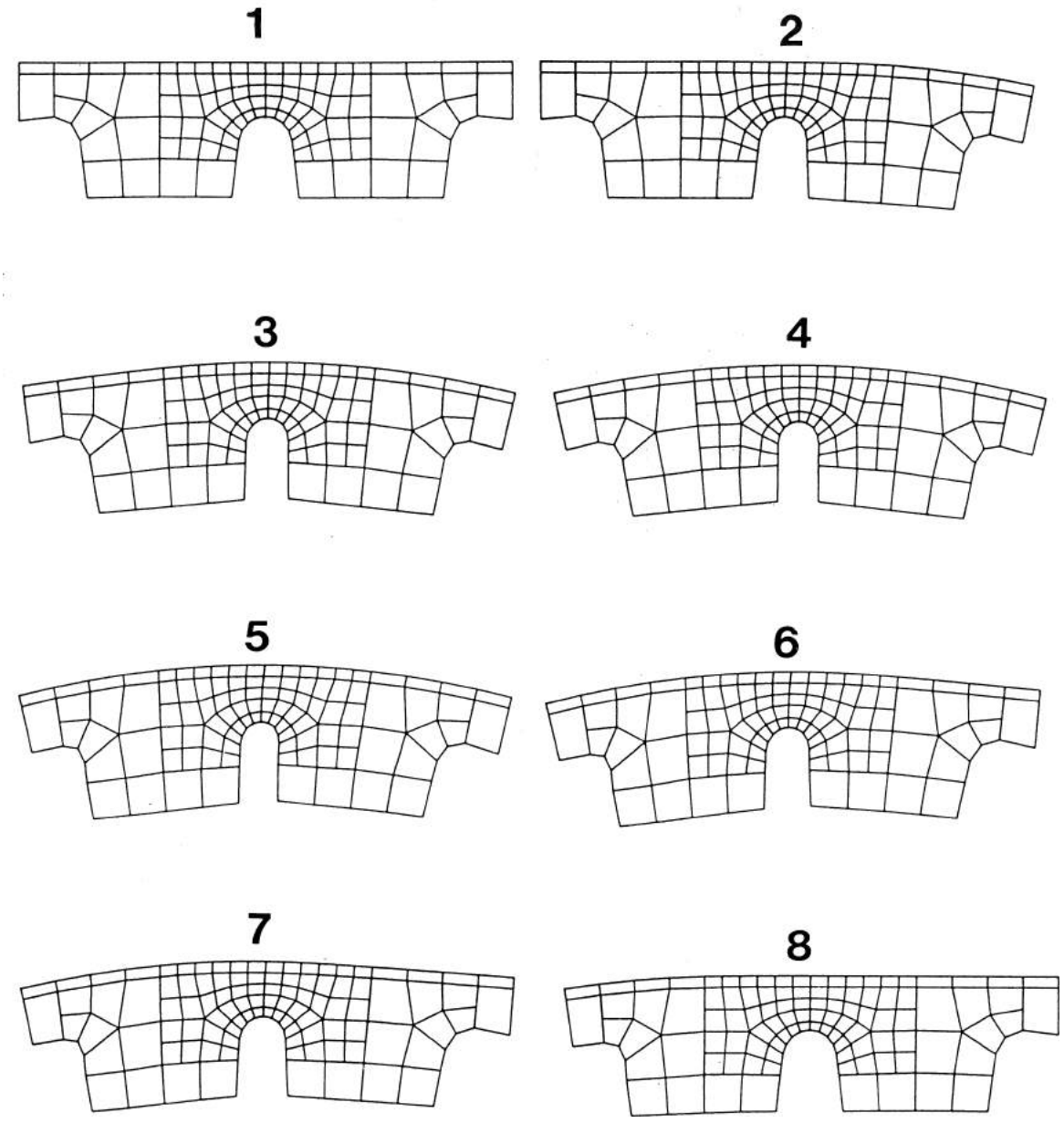

Figure 6.14 *Different belt positions during a load cycle. For driven pulley. 1 - low tension side, 2 - beginning of entrance zone, 3 - end entrance zone, 4 - non-sliding zone, 5 - sliding zone, 6 - beginning exit zone, 7 - middle of exit zone, 8 - end exit zone.*

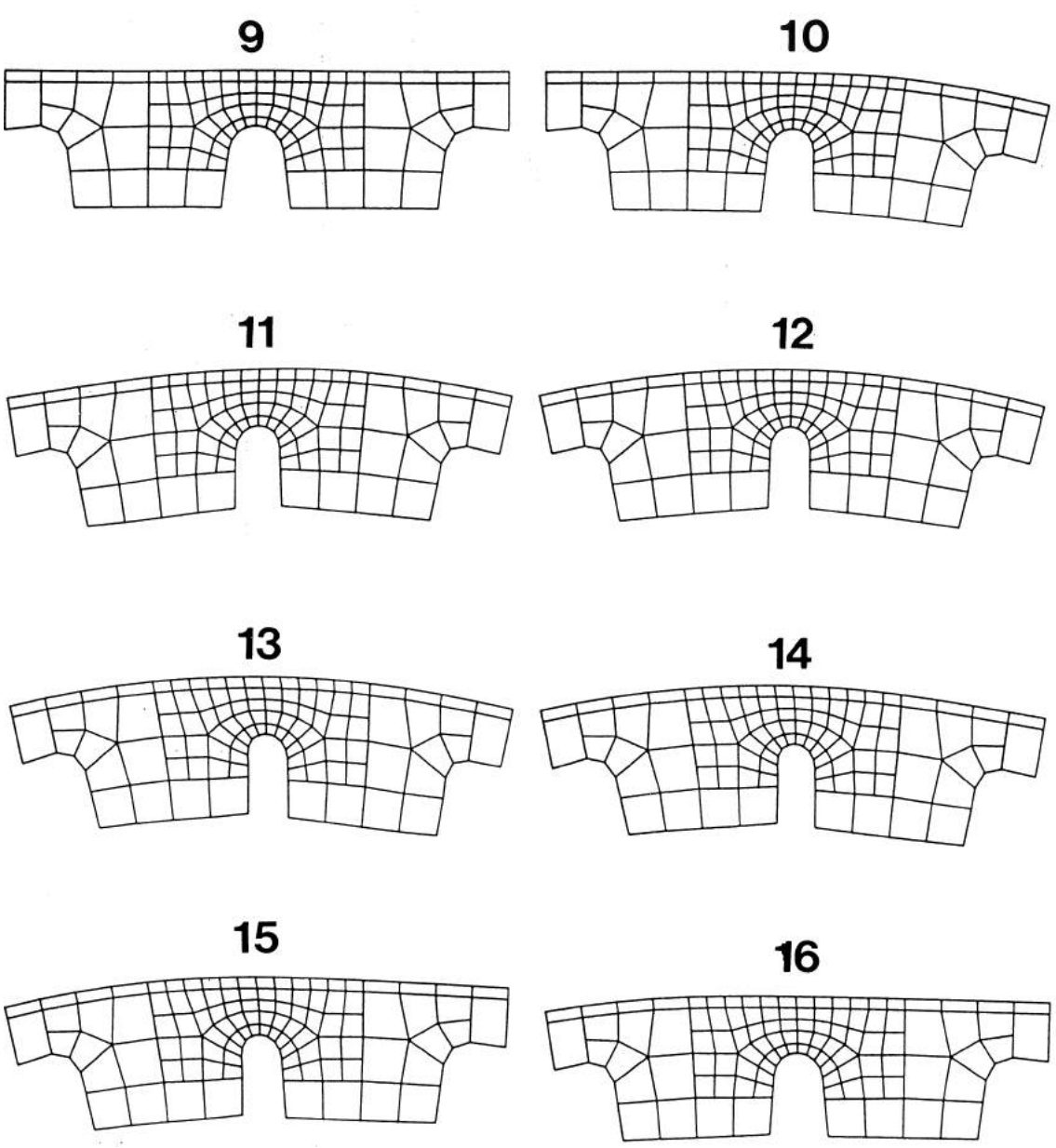

Figure 6.15 *Different belt positions during a load cycle. For driving pulley. 9 - high tension side, 10 - beginning of entrance zone, 11 - end entrance zone, 12 - non-sliding zone, 13 - sliding zone, 14 - beginning exit zone, 15 - middle of exit zone, 16 - end exit zone.*

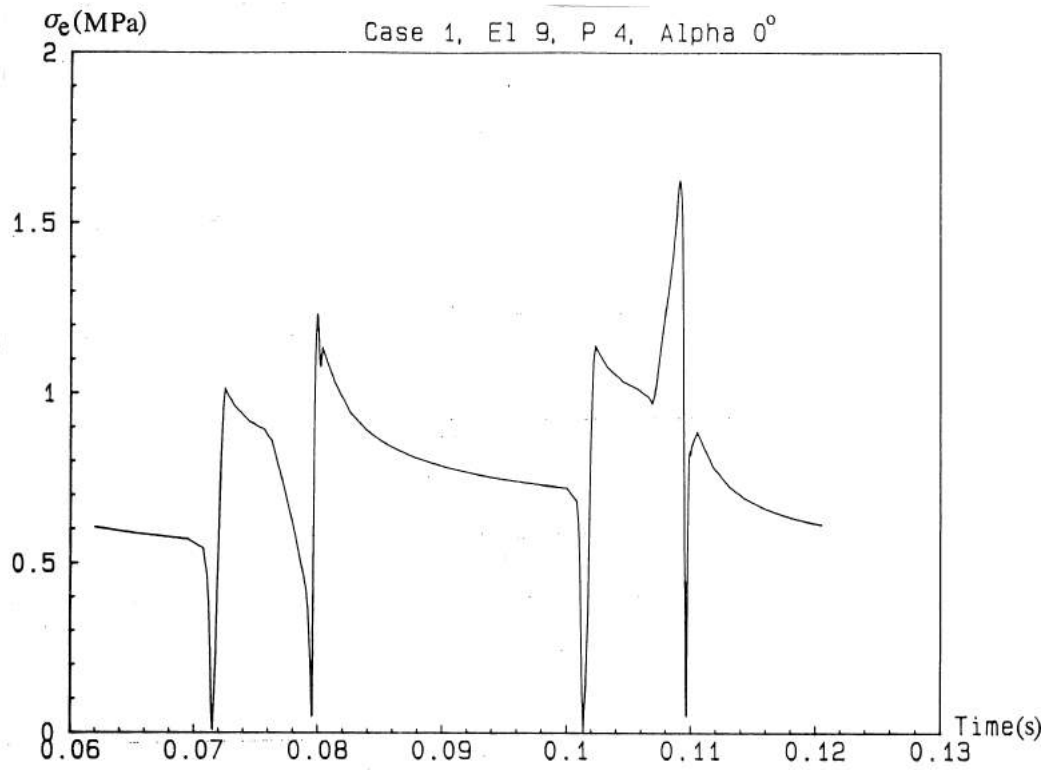

Figure 6.16 *Effective stress σ_e at element 9 point 4 in material 1. The crack propagation direction is not allowed to vary relative direction 1.*

6.5.2 Fatigue data correlation

The 11 load cases studied represent a wide range load conditions, each case different form the others. The belt type is a 0.5″ raw edge V-belt with cog shape. The loads can be classified as relatively severe as these are accelerated tests.

Of these 11 different load cases 6 had the failure mode radial crack and the rest longitudinal crack or separation. Radial cracks develop in the material labeled "material 1" at the bottom between two cogs. Longitudinal cracks develop in material 2 close to the cord layer. We chose the 1% damage level as the design level [6].

As we have two different materials in which failure can occur, two sets of fatigue material constants have to be determined. As discussed in the previous section, $\sum_{i=1}^{m} (\sigma_e)^n$ is calculated in each material point studied. In Figures 6.16, 6.17, 6.18, and 6.19 the effective stress is shown. The recognized maxima and minima are marked in Figures 6.17 and 6.19.

The areas in which failure can occur are studied and for each value of n and each load case and failure mode there is a point which has the highest value. This is the design point for that value of n, load case, and failure mode. In order to obtain the best set of values for the fatigue data constants a steepest gradient optimization technique was used. The result is shown in Figures 6.20 and 6.21.

Good correlation was obtained for both failure modes. The fatigue material con-

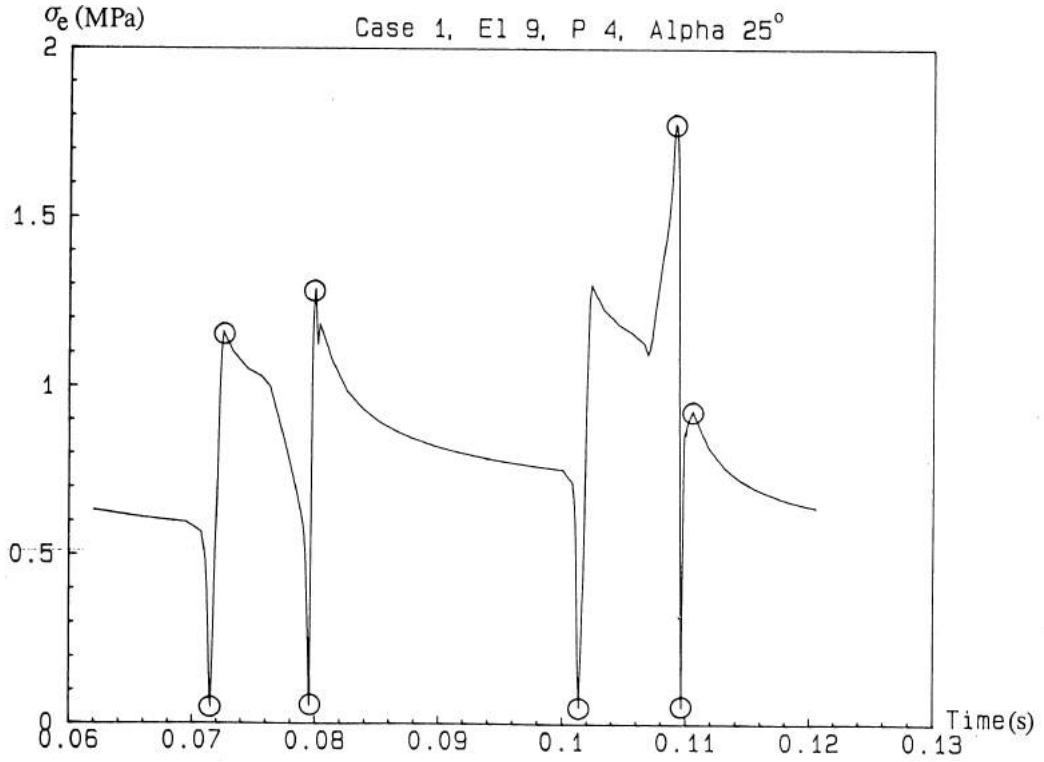

Figure 6.17 *Effective stress σ_e at element 9 point 4 in material 1. The crack propagation direction is allowed to vary at most $\pm 25°$ relative to direction 1.*

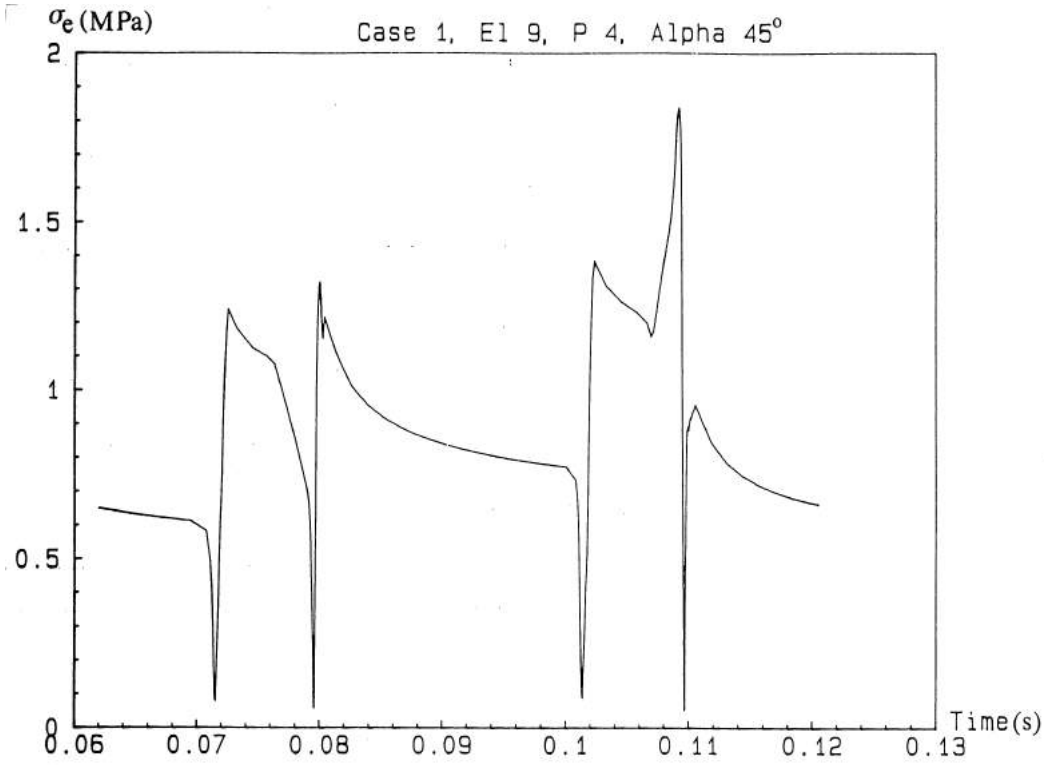

Figure 6.18 *Effective stress σ_e at element 9 point 4 in material 1. The crack propagation direction is allowed to vary at most $\pm 45°$ relative to direction 1.*

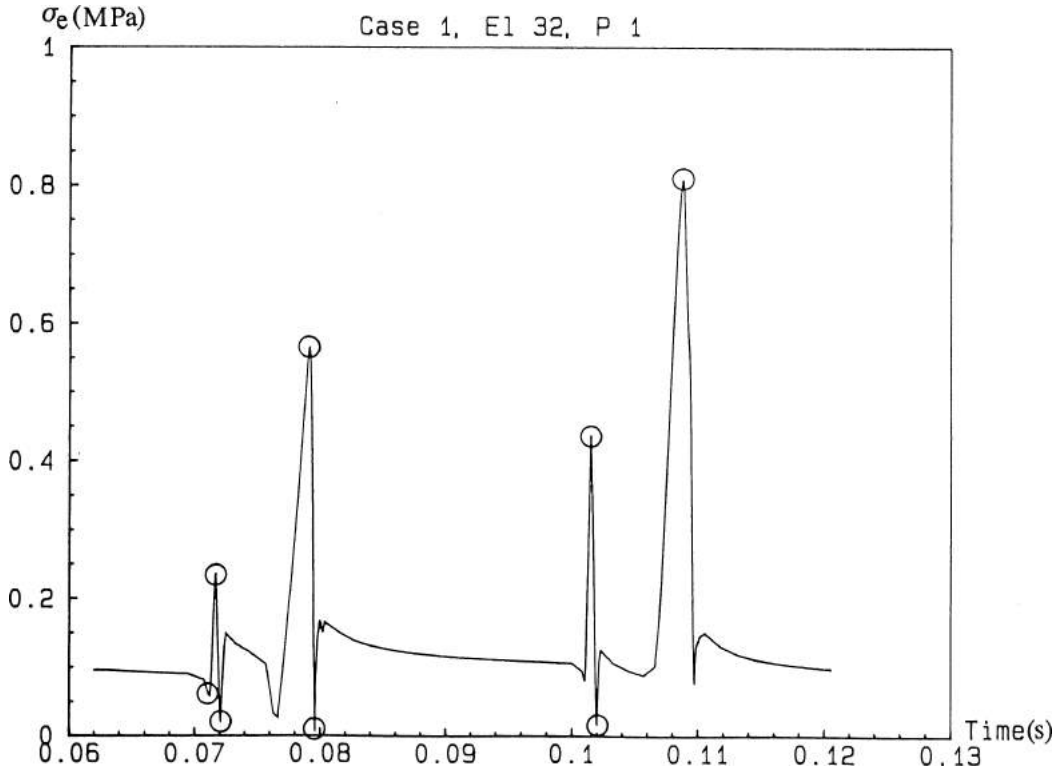

Figure 6.19 *Effective stress σ_e at element 32 point 1 in material 2. The crack propagation direction is in the longitudinal direction (2).*

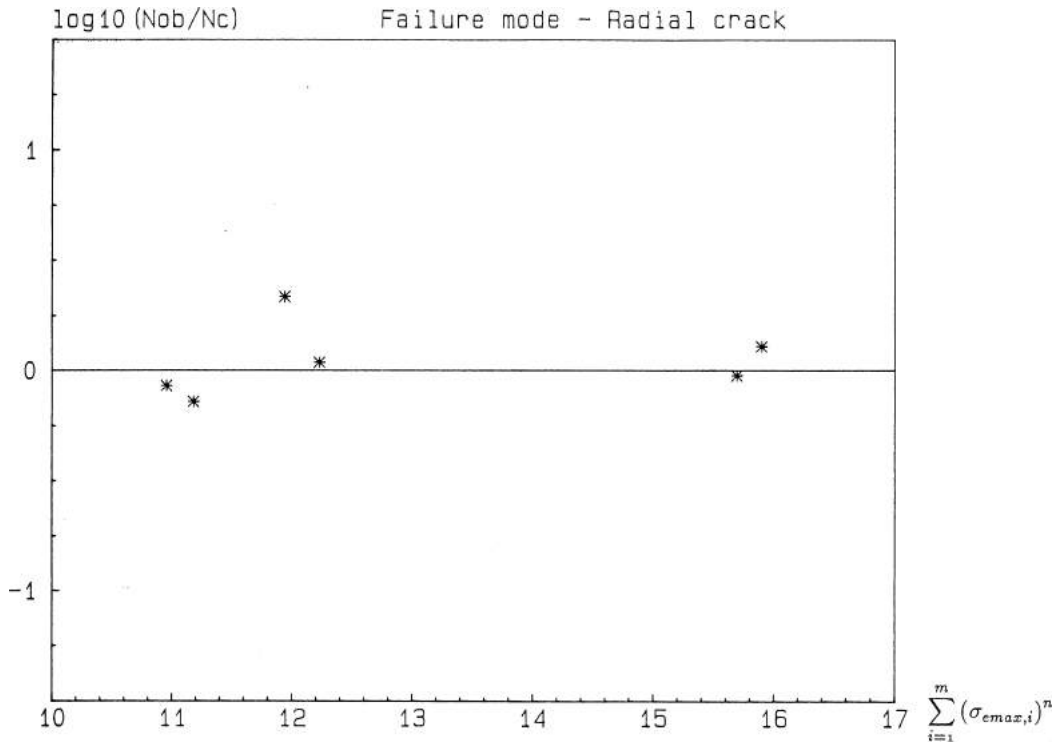

Figure 6.20 *Radial crack in material 1. Failure mode 1. The difference between observed life in load cycles N_{ob} and the calculated value N_c versus $\sum_{i=1}^{m} (\sigma_{emax,i})^n$.*

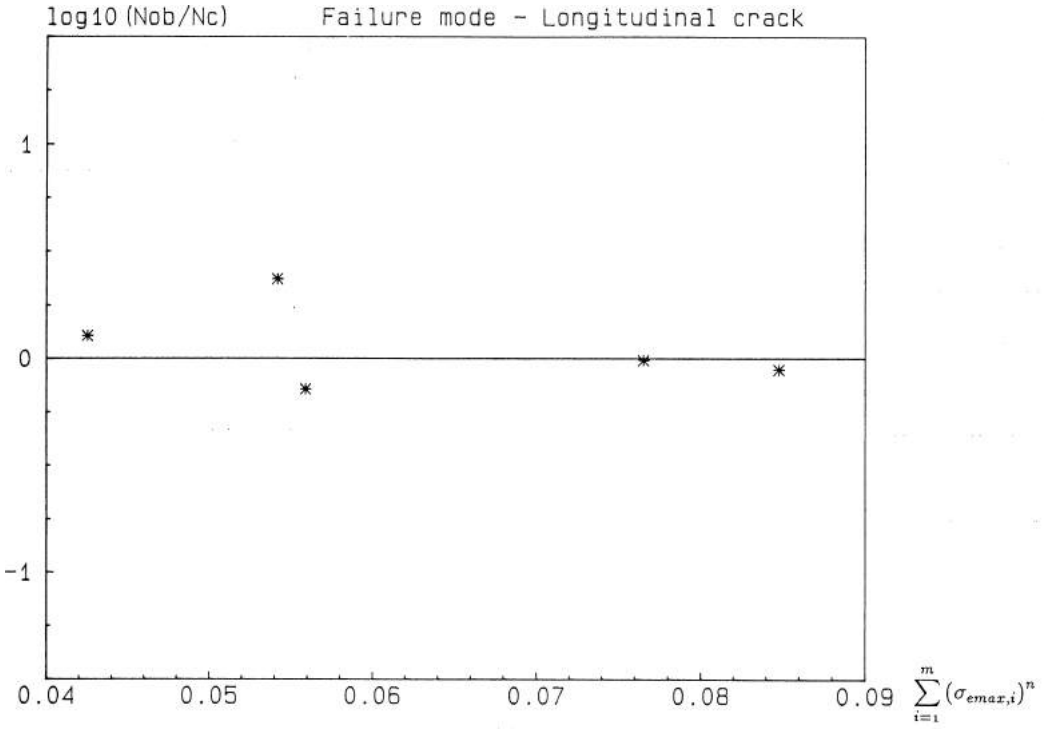

Figure 6.21 *Longitudinal crack in material 2. Failure mode 2. The difference between observed life in load cycles N_{ob} and the calculated value N_c versus $\sum_{i=1}^{m} (\sigma_{emax,i})^n$.*

stants are for the stress given in MPa:

$$\begin{aligned} \sigma_{01} &= 104.218 \quad \text{(MPa)} \\ b_1 &= 0.02897 \quad (^\circ\text{C}^{-1}) \\ n_1 &= 4.423 \quad \text{(-)} \\ \sigma_{02} &= 4.21028 \quad \text{(MPa)} \\ b_2 &= 0.1466 \quad (^\circ\text{C}^{-1}) \\ n_2 &= 11.69 \quad \text{(-)} \end{aligned}$$

So far we have treated two separable problems when determining the fatigue material constants. Now we will put the theory developed here to the test and see if it can predict the correct failure mode for all 11 cases. The result is shown in Figures 6.22 and 6.23.

As seen there is only 2 cases out of 11 that differ from what is predicted. This is a very good result, considering that there should be a stochastic variation in fatigue life among different belts. If several belts are tested under identical load conditions we can expect a distribution in fatigue life.

The fatigue material constants also agree with what can be found in the literature and empirical observations. The constant n_1 is close to what has been reported in [20, 21, 25, 24, 8]. From experimental observations [6] we know that the longitudinal crack grows faster than the radial crack. This agrees with the higher value of n_2. It seems that we are more to the right in Figure 6.3. This longitudinal crack depends

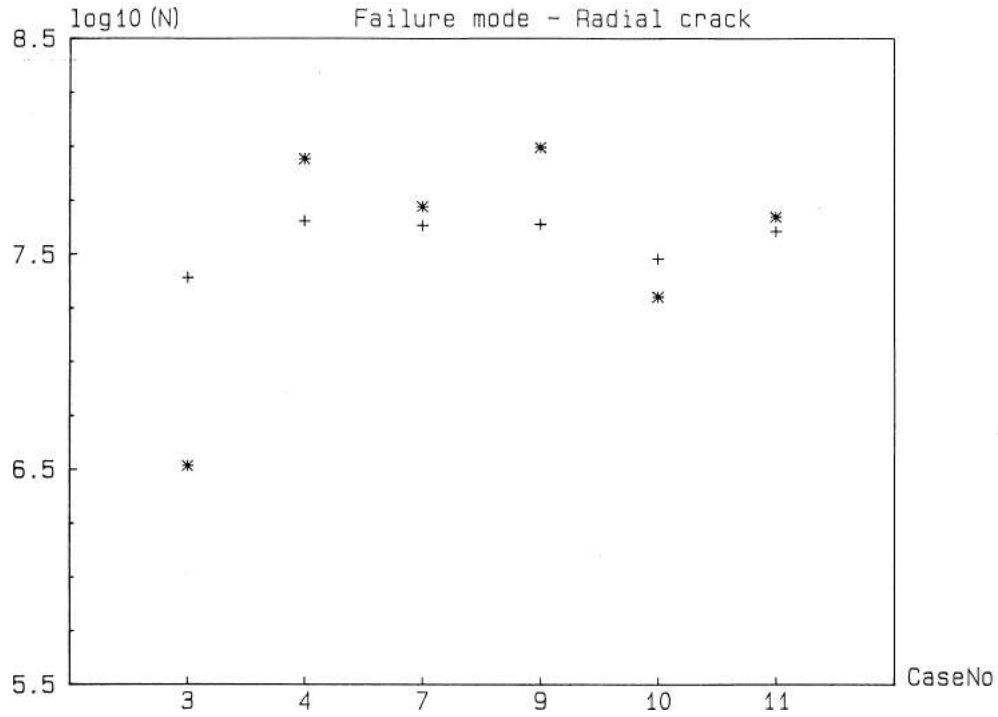

Figure 6.22 *Observed failure mode is radial crack. ∗ = predicted life for longitudinal crack. + = predicted life for radial crack.*

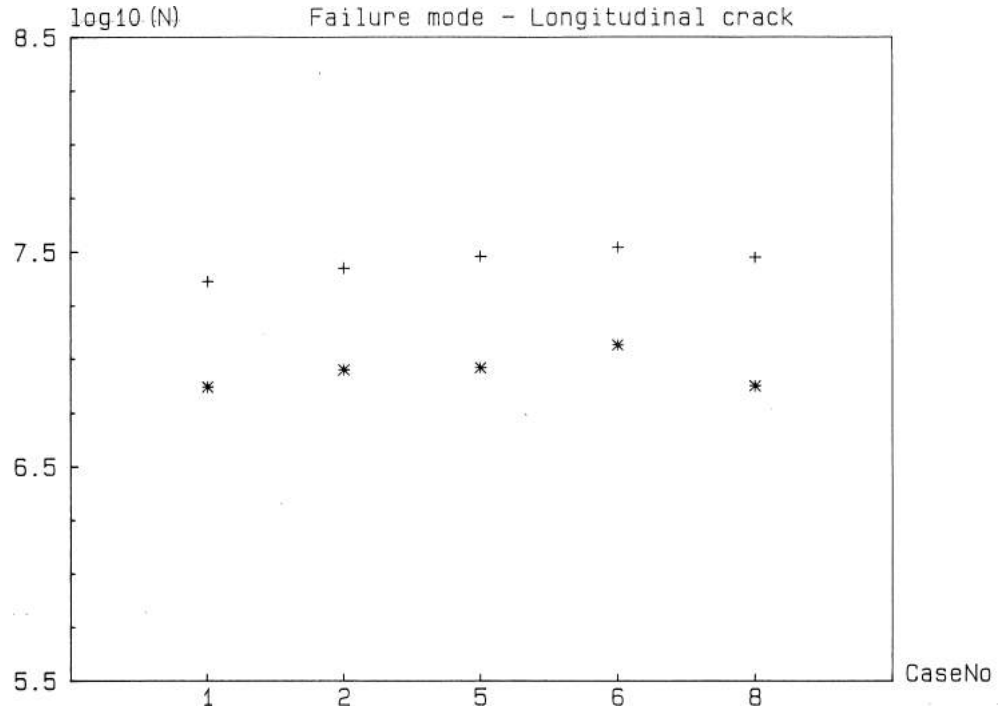

Figure 6.23 *Observed failure mode is longitudinal crack. ∗ = predicted life for longitudinal crack. + = predicted life for radial crack.*

not only on material 2 but also on the bond between this layer and the surrounding cord layer and material 1. The production methods may have a strong influence on these fatigue constants. The interval between the temperature constants determined here include the empirical value reported in [11].

6.5.3 Discussion

Our conclusion is that if material constitutive data, material fatigue data, and belt temperature are known, the belt segment model can be used to evaluate new designs of V-belts in computer simulations.

However, the fatigue data only exist in form of V-belt data today. It would be better if separate crack propagation experiments were performed to determine the material constants with good accuracy. It is very important that the materials and the loads are representative for the application. For instance, it would be best if the test pieces were cut from a real belt.

The belt temperature has been experimental determined for each studied case to date, but to allow for general simulations, it has to be calculated. This means that a heat transfer model for the V-belt drive studied has to be employed. This has been done in [13]. Such a analysis can easily be incorporated into the belt segment model, because:

- The hysteresis work is already obtained from the FEM-model.
- The belt segment model gives the pressure and the sliding conditions of the belt, and the sliding speed can also be incorporated. This makes it possible to obtain the friction loss.
- For the actual heat transfer the theory in [13] can be used, or a suitable FEM-analysis can be performed.

7
Conclusions

V-belt life prediction methods and failure mechanisms were discussed in detail in reference [6]. Our conclusion was that the methods used today correlate all kinds of failures with cord stress and do not allow prediction of the behavior of a new design as experimentally determined constants for each belt type are included in the theory.

Here "the parametric belt segment model" is developed. This approach consists of two major parts:

- A global analysis of the belt forces, displacements, slip, sliding direction, etc., in a V-belt drive is performed using the theory for the mechanics of a V-belt drive [12]. Thus, we have at each instant in time, data for all the global variables for a certain belt section.

- A local analysis of the stress - strain state of a small part of the belt is performed using a FEM-model. The model is not larger than necessary to avoid boundary effects. Input data for this model are the global forces, displacements etc., calculated above. Thus, we have, at each instant in time, the stress-strain state at any location in the belt.

There is no limitation to a certain V-belt drive configuration. Any number of pulleys, driving or driven, and different sizes can be analyzed. Also, the FEM-model used can be two or three-dimensional. The theory to date for V-belt mechanics is used, but if further results become available they can easily be incorporated into the model.

Now it is possible to monitor a certain position in the belt and study variables of interest, while simulating a running belt. From observations regarding the fatigue mechanisms the areas of interest are [6]:

- Radial crack growth towards the cord layer in the pressure section (material 1). These are normally initiated between the cogs. This is referred to as failure mode 1.

- Separation or cracking in the longitudinal direction close to the cord layer, in the cushion layer (material 2), or between the cushion and pressure section. This is referred to as failure mode 2.

The fact that it is crack propagation mechanisms that are active is recognized and a criteria for crack propagation with combined mode I and mode II is used.

While simulating a running belt, all material volume in which cracks are likely to develop, are monitored and the material point at which the crack reaches a certain length fastest is regarded as the design point. This takes into consideration that both failure modes are active simultaneously.

As a first case, we study a plane strain model of a 0.500 inch belt running on two equal size pulleys. Data are available for different loads, torques, speeds, and diameters of the pulleys. The materials used in the design of the belts are discussed in reference [7] and the constitutive equations are presented in reference [4].

The fatigue material constants are calculated. There is good correlation between experimental data and the simulations. This means that both fatigue life and failure mode can be predicted with good accuracy.

Our conclusion is that if material constitutive data, material fatigue data, and belt temperature are known, the belt segment model can be used to evaluate new designs of V-belts in computer simulations.

A

V-belt mechanics - theory and closed form approximations

A.1 Theory of V-belt mechanics

In 1972 Gerbert [12] presented a rigorous set of differential equations describing the force and slip behavior of a V-belt. The numerical solutions were obtained using a set of approximate equations. These are given below as well as in [12, 16]. The main difference from the exact theory is that the variation in the radius of curvature is assumed to be very small, and is neglected in the equilibrium equations. This simplification is applicable when the entrance and the exit regions, which are relatively small compared to the "active" arc, are excluded. Numerical solutions without the application of the approximate equations have been presented by Dolan and Worley [3].

A V-belt drive which transmits torque requires a difference between the forces F_2 on the tight side and F_1 on the slack side. For small tension ratios F_2/F_1 the contact zone is divided into a *non-sliding zone* with a constant force and a *sliding zone* with a varying force. The slip zone is placed closest to the region where the belt leaves the pulley. The traction capacity of a driving pulley is greater than that of a driven one. Therefore non-sliding zones always occur on the driving pulleys in normal applications. In the sliding zone of a driving pulley the force F decreases until it reaches the force level of the slack side F_1 at the exit point. For the driven pulley the force F increases in the sliding zone until it reaches the force of the high tension side F_2.

Basic assumptions

The theory is based on the following assumptions:

1. The belt can be considered to be a band with a certain mean width but no thickness.

2. The coefficient of friction is constant.

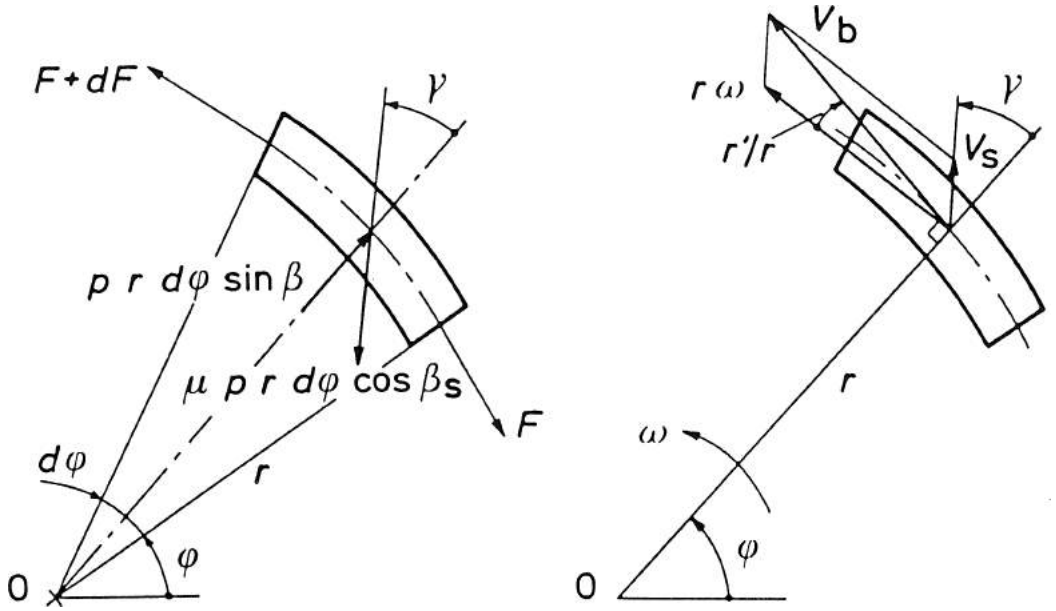

Figure A.1 *Forces and velocities acting on a belt element in contact with a pulley [16]. F = belt force. p = side pressure. γ = sliding angle in the plane of rotation. v_b = belt velocity. v_s = sliding velocity in the plane of rotation.*

3. The frictional forces are counter-directed the sliding velocity.
4. The belt has no bending stiffness, i.e. there are no bending moments.
5. The belt has no mass or the velocity is very slow, i.e. inertia forces are neglected.

Equilibrium conditions

The first assumption above means that instead of pressure on the side of the belt, the force per unit length should be used. With constant pressure it is $pH/\cos(\beta)$.

Equilibrium of the belt element in Figure A.1 in the longitudinal direction gives:

$$F' = \mu 2 \frac{pH}{\cos(\beta)} r \cos\beta_s \sin\gamma \tag{A.1}$$

Equilibrium in the radial direction gives:

$$F = 2\frac{pH}{\cos(\beta)} r \left(\sin\beta - \mu\cos\beta_s \cos\gamma\right) \tag{A.2}$$

Displacement

The belt force gives longitudinal strains. The force-strain relationship can be written as:

$$F = c\epsilon \tag{A.3}$$

where c is the strain stiffness in the longitudinal direction.

In the original presentation [12, 16] the radial displacement x not only depended on the axial compressive force $\frac{p_z H}{\cos(\beta)} = \frac{pH}{\cos(\beta)}(\cos\beta + \mu \sin\beta_s)$ but also included radial and longitudinal components. Here we simplify the relationship and only consider the dominant effect which comes from the axial load.

$$x = \frac{2}{k_1}\frac{pH}{(\cos\beta)}(\cos\beta + \mu\sin\beta_s) \tag{A.4}$$

The quantity k_1 can be referred to as radial spring stiffness.

Sliding conditions

The velocity of the sheave is $r\omega$. The belt slides relative to the sheave with the velocity v_s. The angle between the sliding velocity v_s and the radius r is the sliding angle γ. The vectorial sum of those two velocities yields the belt velocity v_b. This is shown in figure A.1. Using the assumption that the inclination of the belt is small, it can be written as r'/r, and we obtain the following equations for the velocities of the belt:

$$v_b = r\omega + v_s \sin\gamma \tag{A.5}$$

$$v_b\frac{r'}{r} = v_s\cos\gamma \tag{A.6}$$

If V is the velocity of an unloaded belt then the velocity of a loaded belt becomes:

$$v_b = V(1+\epsilon) \tag{A.7}$$

Geometric conditions

The radius R is a constant reference radius, for instance the pitch radius of the pulley. The radial displacement x describes how the belt moves radially in the grove.

$$r = R - x \tag{A.8}$$

$$r' = -x' \tag{A.9}$$

The radial displacement x is much smaller than either of the radii. In certain terms where the influence of the variable x is not significant the radius R can be used as an approximation of r.

The wedge angle, in a plane inclined with the sliding angle γ to the radius, is denoted by β_s. This angle is determined by:

$$\tan\beta_s = \tan\beta\cos\gamma \tag{A.10}$$

Non-dimensional equations

The following non-dimensional variables are introduced:

$$x_0 = x/R \tag{A.11}$$

$$F_0 = \frac{F}{R^2 k_1} \tag{A.12}$$

$$c_0 = \frac{c}{R^2 k_1} \tag{A.13}$$

In a reference point P is $F = F_P$ and we define a relative belt force:

$$\kappa = \frac{F}{F_P} = \frac{F_0}{F_{0P}} \tag{A.14}$$

Combining the two equilibrium equations results in:

$$\frac{\kappa'}{\kappa} = \frac{\mu \cos\beta_s \sin\gamma}{\sin\beta - \mu \cos\beta_s \cos\gamma} \tag{A.15}$$

If we eliminate the pressure p in Equation A.4 using the radial equilibrium Equation A.2 we obtain:

$$\frac{x}{F} = \frac{1}{rk_1} \frac{\cos\beta + \mu \sin\beta_s}{\sin\beta - \mu \cos\beta_s \cos\gamma} \tag{A.16}$$

Introduce the non-dimensional notation and replace r with the approximation R. Then the equation becomes:

$$\frac{x_0}{\kappa F_{0P}} = \frac{\cos\beta + \mu \sin\beta_s}{\sin\beta - \mu \cos\beta_s \cos\gamma} \tag{A.17}$$

The equations for the sliding conditions yield:

$$\frac{r'}{r} \tan\gamma = 1 - \frac{\omega}{V} \frac{r}{1+\epsilon} \tag{A.18}$$

Introduce the conditions at the reference point where $r = r_P$, $\gamma = \gamma_P$, and $\epsilon = \epsilon_P$. Then we can eliminate ω/V.

$$-\frac{r'}{r} \tan\gamma = \frac{r}{r_P} \frac{1+\epsilon_P}{1+\epsilon} \left(1 - \frac{r'_P}{r_P} \tan\gamma_P\right) - 1 \tag{A.19}$$

Assume that $x_0 \ll 1$ and $\epsilon \ll 1$. Then $r'/r \approx -x'_0$, and Equation A.19 is reduced to:

$$x'_0 \tan\gamma = (x_{0P} - x_0) + (\epsilon_P - \epsilon) + x'_{0P} \tan\gamma_P \tag{A.20}$$

By combining equations A.20, A.14, and A.3 using non-dimensional notation we obtain:

$$x'_0 \tan\gamma = -\left((x_0 - x_{0P}) + (\kappa - 1)\frac{F_{0P}}{c_0} - x'_{0P} \tan\gamma_P\right) \tag{A.21}$$

Initial conditions

The reference point P is chosen so that $\gamma_P = 180°$, and $x'_{0P} = 0$. Then $\beta_{sP} = -\beta$ and equation A.21 is simplified to:

$$x'_0 \tan\gamma = -\left((x_0 - x_{0P}) + (\kappa - 1)\frac{F_{0P}}{c_0}\right) \tag{A.22}$$

where

$$\frac{x_{0P}}{F_{0P}} = \frac{1 - \mu \tan\beta}{\tan\beta + \mu} = \cot(\beta + \arctan\mu) \tag{A.23}$$

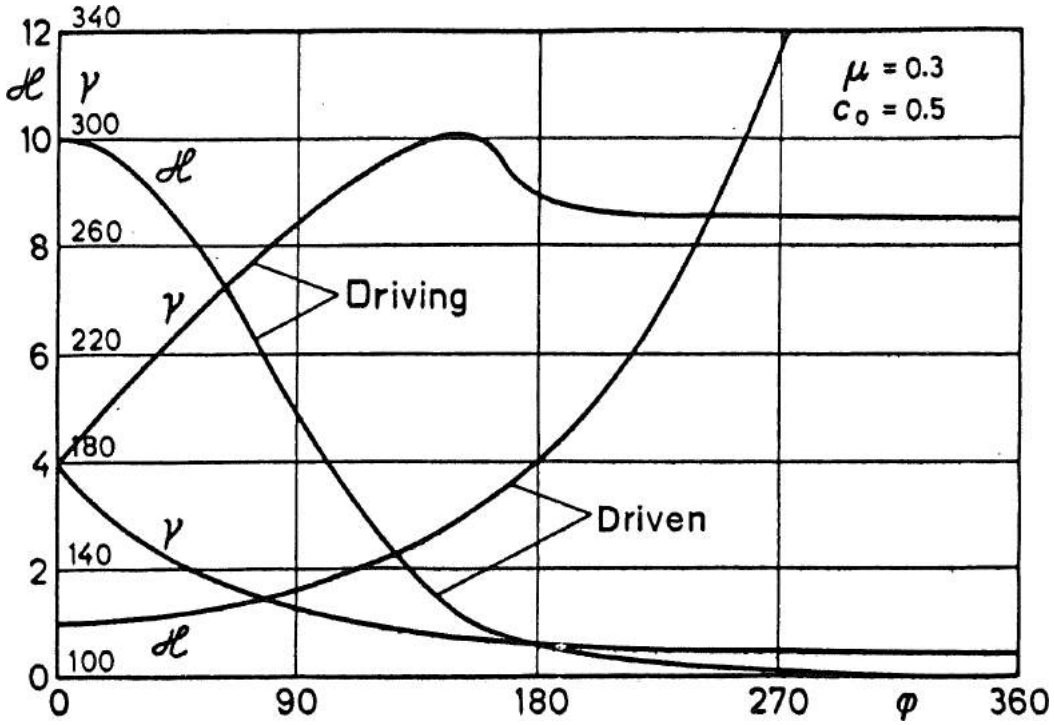

Figure A.2 *Force and slip behavior in V-belt drives [17]. κ = relative force, ratio between belt force at an angle φ and belt force at $\varphi = 0$. γ = sliding angle. c_0 a measure of the elasticity of the belt.*

The initial conditions yield zero values of the derivatives with respect to φ of the relative force and relative displacement. To start the numerical solution applying e.g. Runge-Kutta's method, a special scheme involving differentiations and series expansions around $\gamma_P = 180°$ has to be used. This is discussed in detail in [12]. From the differentiations in the starting point P the following equation in γ'_P is obtained:

$$\gamma'^{\,2}_P + \left(\frac{1}{2} - \frac{\tan\beta + \mu}{F_{0P}/x_{0P}}\right)\gamma'_P - \frac{(\tan\beta + \mu)\,(1 + c_0 x_{0P}/F_{0P})}{2c_0} = 0 \qquad \text{(A.24)}$$

From this equation we can calculate two roots for the derivative of the sliding angle. The signs of the roots determine whether it is a driven or driving pulley.

$$\begin{aligned} \gamma'_P &> 0 \quad \text{Driver} \\ \gamma'_P &< 0 \quad \text{Driven} \end{aligned}$$

This is shown in Figure A.2 where both the solution for a driven pulley and a driving pulley are presented.

A.2 Closed form approximations

The theory discussed in the previous section involves a great amount of numerical computations. When the V-belt theory is to be incorporated in software it is very

convenient if the force and slip variation of a V-belt can be approximated by some closed form equations. This simplifies the implementation and reduces the computations. The scheme described in this section has been used in various V-belt design and analysis software [15].

Driven pulley

We assume that there is a non-sliding zone, i.e. $0 < \varphi_2 < \alpha$. This is normally the case in practical applications. It has been found that the hyperbolic cosine function describes the relative belt force on the driven pulley well[3].

The belt force F increases from the low value F_1 at the low tension side until it reaches the level of the high tension side F_2.

$$\frac{F}{F_1} = \left(\cosh\left(\frac{\mu'_{fP}}{\mu_{fa}}\varphi\right)\right)^{\left(\frac{\mu_{fa}^2}{\mu'_{fP}}\right)} \quad \text{where} \tag{A.25}$$

$$\mu'_{fP} = -\frac{\gamma'_P \mu}{\tan\beta + \mu} \tag{A.26}$$

$$\varphi = 0 \Leftrightarrow F = F_1$$

$$\varphi = \varphi_2 \Leftrightarrow F = F_2$$

At the starting point P, γ'_P is obtained as the negative root $\gamma'_P < 0$ from Equation A.24. The asymptotic fictitious coefficient of friction μ_{fa} is obtained by finding the asymptotic sliding angle γ_a. This can be determined from [9]:

$$\frac{1}{c_0} + f(\gamma_a)\left(1 + \mu_{fa}\tan\gamma_a\right) = 0 \tag{A.27}$$

where

$$\mu_{fa} = \frac{\mu\cos\beta_{sa}\sin\gamma_a}{\sin\beta - \mu\cos\beta_{sa}\cos\gamma_a} \tag{A.28}$$

$$f(\gamma_a) = \frac{\cos\beta + \mu\sin\beta_{sa}}{\sin\beta - \mu\cos\beta_{sa}\cos\gamma_a} \tag{A.29}$$

$$\tan\beta_{sa} = \tan\beta\cos\gamma_a \tag{A.30}$$

The sliding angle is determined by:

$$\gamma = \pi + (\pi - \gamma_a)\tanh\left(\frac{\gamma'_P}{\pi - \gamma_a}\varphi\right) \tag{A.31}$$

Driver pulley

The belt force F decreases from level F_2 at the high tension side until it reaches the level of the low tension side F_1. An approximate expression for the force ratio of the

driver pulley has been developed [17]:

$$\frac{F}{F_2} = \left(\frac{1+\mu_e\cos(\gamma'_P\varphi)}{1+\mu_e}\right)^{1/\gamma'_P} \quad \text{where} \tag{A.32}$$

$$\mu_e = \mu/\sin\beta \tag{A.33}$$

$$\varphi = 0 \Leftrightarrow F = F_2$$

$$\varphi = \varphi_1 \Leftrightarrow F = F_1$$

At the starting point P γ'_P is obtained as the positive root $\gamma'_P > 0$ from Equation A.24.

As the cosine function is part of the formula, it cannot be used for $\gamma'_P\varphi_1 > \pi$.

The sliding angle is determined by:

$$\gamma = \gamma'_P\varphi + \pi \tag{A.34}$$

limited by:

$$\gamma \leq \gamma_{Lim} \tag{A.35}$$

For cases when self-locking does not occur we set $\gamma_{Lim} = 273°$ (see Figure 6.21 in [12]).

The belt stiffness c_o

The non-dimensional belt stiffness c_0 has to be calculated. It is defined as:

$$c_0 = \frac{c}{R^2 k_1} \tag{A.36}$$

The longitudinal strain stiffness $c = F/\epsilon$ can easily be determined from the stiffness of the cord in the belt.

The radial spring stiffness k_1 is more difficult to determine as it has to include influence both from the axial stiffness of the belt and the wedge action when the belt is seated in the pulley. In [12] a simple formula is suggested. This formula has later been modified using empirical results [15] and we have:

$$k_1 = \frac{10\tan\beta E_{33} H}{B} \tag{A.37}$$

B is the mean width of the belt. H is the height of a plain (not cog shaped) belt having the same projected area in the axial direction as the belt studied. E_{33} is an average modulus of elasticity of the belt materials of the belt section, in the axial direction. The product $E_{33}H$ can be obtained by testing complete belt sections, or E_{33} can be determined from material data. This formula could be used as a first approximation for determining k_1.

Bibliography

[1] J. Carlsson. *Brottmekanik (Fracture mechanics)*. Ingenjörsförlaget, Sweden, 1976.

[2] J. Carlsson. *Brottmekanik (Fracture mechanics)*. Division of Strength of Materials, KTH, Stockholm, Sweden, 1985.

[3] J.P. Dolan and W.S. Worley. "Closed-form approximations to the solution of V-belt force and slip equations". In: *Journal of Mechanisms* 107 (June 1985), pp. 292–300.

[4] D. Fritzson. *A three-dimensional finite strain constitutive theory for elastomer composites*. No. 1988-05-30. Department of Mechanical Engineering, Chalmers University of Technology, Göteborg, Sweden: Division of Machine Elements.

[5] D. Fritzson. *Change of V-belt geometry in a running transmission*. No. 1988-05-24. Department of Mechanical Engineering, Chalmers University of Technology, Göteborg, Sweden: Division of Machine Elements.

[6] D. Fritzson. *Fatigue mechanisms of V-belts*. No. 1988-05-27. Department of Mechanical Engineering, Chalmers University of Technology, Göteborg, Sweden: Division of Machine Elements.

[7] D. Fritzson. *Material properties of elastomer composites in mechanical transmissions with special reference to V-belts*. No. 1988-05-25. Department of Mechanical Engineering, Chalmers University of Technology, Göteborg, Sweden: Division of Machine Elements.

[8] A.N. Gent et al. "Cut growth and fatigue of rubbers. 1 The relationship between cut growth and fatigue". In: *Journal of applied Polymer Science* 8 (1964), pp. 455–466.

[9] G. Gerbert. "A complementary large slip solution in V-belt mechanics". In: *Proceedings of the Design Engineering Technical Conference, Chicago, Illinois, September 26-30, 1977*. United engineering center, New York, N.Y.: The American Society of Mechanical Engineers, 1977.

[10] G. Gerbert. *Dishing of V-belts*. Department of Mechanical Engineering, Lund Technical University, Lund, Sweden: Divison of Machine Elements, Apr. 1979.

[11] G. Gerbert. *Fatigue characteristics of V-belts*. Department of Mechanical Engineering, Lund Technical University, Lund, Sweden: Divison of Machine Elements, 1980.

[12] G. Gerbert. *Force and slip behaviour in V-belt drives*. Acta Polytechnica Scandinavica, Mech. Eng. Series No. 67. The Finnish Academy of Technical Sciences, Helsinki, Finland, 1972.

[13] G. Gerbert. *Heat in V-belt drives*. Department of Mechanical Engineering, Lund Technical University, Lund, Sweden: Division of Machine Elements, 1981.

[14] G. Gerbert. "Power loss and optimum tensioning of V-belt drives". In: *Journal of Engineering for Industry* 96.3, Series B (Aug. 1974), pp. 877–885.

[15] G. Gerbert. "Private communication". 1988.

[16] G. Gerbert. "Scheibenspreizkräfte in Breitkeilriemengetrieben". In: *Antriebstechnik* 13.1 (Jan. 1974).

[17] G. Gerbert. "Tensile stress distribution in the cord of V-belts". In: *Journal of Engineering for Industry* 97 series B.1 (Feb. 1975).

[18] H.M. Hakeem and L.E. Culver. "Environmental dynamic fatigue crack propagation in high density polyethylene: an emperical modelling approach". In: *Int. J. Fatigue* (Jan. 1981), pp. 3–7.

[19] G. Hedner. *Formelsamling i hållfasthetslära (Formulas in Strength of Materials)*. Division of Strength of Materials, KTH, Stockholm, Sweden, 1978.

[20] G.J. Lake and P.B. Lindley. "Fatigue of rubber at low strains". In: *Journal of Applied Polymer Science* 10 (1966), pp. 343–351.

[21] G.J. Lake and P.B. Lindley. "Ozone cracking, flex cracking and fatigue of rubber, Part I: Cut growth mechanisms and how they result in fatigue failure". In: *Rubber Journal* (Oct. 1964).

[22] G.J. Lake and P.B. Lindley. "Ozone cracking, flex cracking and fatigue of rubber, Part II: Technological aspects". In: *Rubber Journal* (Nov. 1964).

[23] J.C. Radon. "Cyclic crack propagation and molecular kinetics of polymers". In: *Journal of Polymer Science* 13 (1975), pp. 383–400.

[24] J.A. Sauer and G.C. Richardson. "Fatigue of polymers". In: *International Journal of Fracture* 16.6 (Dec. 1980), pp. 499–532.

[25] B. Stenberg. *Gummimaterialets dynamisk-mekaniska egenskaper - Hysteres och Utmattning (The dynamic-mechanical properties of rubber material - Hysteresis and Fatigue*. Report from PGI no. 19. Sundsvall, Sweden: PGI, 1981.

Part II

A three-dimensional finite strain constitutive theory for elastomer composites

Report II

A three-dimensional finite strain constitutive theory for elastomer composites

Dag Fritzson

Report No. 1988-05-30
Division of Machine Elements
Department of Mechanical Engineering
Chalmers University of Technology
Göteborg, S-412 96 Sweden

Abstract

A fully three-dimensional finite strain constitutive model has been developed, and is characterized by:

- Anisotropic elasticity, anisotropic "rate independent dynamic elasticity", and anisotropic viscoelastic response.
- Uncoupled bulk and deviatoric response.
- Decomposition of the deviatoric response into isotropic and anisotropic parts.
- Separable anisotropic damage mechanisms for mechanical degradation and temperature degradation. The mechanical damage is irreversible, the temperature damage is reversible.
- Separable damage mechanisms for the elastic response and the viscous (hysteresis) response.

The constitutive model can be employed in both rate formulations and total formulations, which provide a co-rotational coordinate system defined in the anisotropic material directions. Thus, the constitutive model can be used in today's commercially available FEM-software.

Contents

1
Introduction

A large class of machine elements is designed of elastomer composites. These materials are anisotropic owing to the reinforcement of fibers, and they yield hysteresis work when loaded dynamically. They are also subject to damage mechanisms which depend on the strain history, and are very sensitive to temperature. In many applications, such as belt transmission, these mechanisms are highly significant and cannot be neglected.

Generally speaking, the tools of analysis available today are hyperelastic models of rubber based on invariants of the material deformation gradient. None of the mechanisms mentioned above is included in such formulations.

A brief description of the contents of this report is given below:

Stress and strain analysis of machine elements built from these materials quite often involves large strains and rotations. In Chapter 3 some aspects of stress and strain formulations suitable to this kind of materials are discussed.

In Chapter 4 a constitutive theory is developed for this class of materials.

One analysis goal for machine elements made of such materials is to be able to calculate fatigue life. This is discussed with special reference to V-belts in Chapter 5.

The constitutive theory is verified against experiments in Chapter 6.

If the constitutive model is to be of any practical use it must be possible to use it together with a general tool for analysis. In Chapter 7 a description is given of how the constitutive model is implemented within a commercially available FEM software package.

2
Notation

The basic concepts of continuum mechanics including strain and stress are given in Appendix A following the exposition in [1]. This is for the benefit of those who are not normally using such concepts. For further reading we refer to [56, 25, 23, 47, 30] or other well-known standard publications in this field. This text is intended to be read by people who work with solving engineering problems using elastomer composites.

The notation used here is both the *direct matrix notation* of vectors and tensors, and the *vector-dyadic notation*. Therefore, the basic quantities and some formulas are given in both notations. The orthonormal right rectangular Cartesian coordinate system is used. Time derivatives are material time derivatives, i.e. the change in a variable with respect to time whilst looking at a particular material particle, unless otherwise explicitly stated.

In those cases where confusion can occur between superscript and exponents we use additional parenthesis. Example, a^2 means superscript 2, and $(a)^2$ means exponent 2.

For the notation of the material constants in the constitutive theory here developed, we refer to Chapter 4.

a	A scalar
$\hat{\mathbf{e}}_i$	Unit base vector in a rectangular Cartesian axis system
$\vec{\boldsymbol{a}}$	$a_i\hat{\mathbf{e}}_i$ a vector or first-order tensor
$\boldsymbol{a}$, $[a]$	$a_{ij}\hat{\mathbf{e}}_i\hat{\mathbf{e}}_j$ a second-order tensor or matrix
$\vec{\boldsymbol{a}}^T$	Transpose of $\vec{\boldsymbol{a}}$
$a = \vec{\boldsymbol{b}}^T \cdot \vec{\boldsymbol{c}}$	Dot product of two vectors
$\vec{\boldsymbol{a}} = \vec{\boldsymbol{b}} \times \vec{\boldsymbol{c}}$	Cross product of two vectors
$\boldsymbol{a}^T$, $[a]^T$	Transpose of $\boldsymbol{a}$
$\vec{\boldsymbol{a}} = \boldsymbol{b} \cdot \vec{\boldsymbol{c}}$	$b_{ij}c_j\hat{\mathbf{e}}_i$
$\boldsymbol{a} = \boldsymbol{b} \cdot \boldsymbol{C}$	$b_{ij}c_{jk}\hat{\mathbf{e}}_i\hat{\mathbf{e}}_k$ dot product of two second-order tensors
$\boldsymbol{a} : \boldsymbol{b}$	$a_{ij}b_{ij}$ scalar product of two second-order tensors
$\boldsymbol{I}$, I_{ij}	$\hat{\mathbf{e}}_i \cdot \hat{\mathbf{e}}_j$ unit tensor or matrix
∇_0	$\hat{\mathbf{e}}_i \frac{\partial}{\partial X_i}$ gradient operator referred to initial configuration
∇	$\hat{\mathbf{e}}_i \frac{\partial}{\partial x_i}$ gradient operator referred to current configuration
$\vec{\boldsymbol{x}}$, x_i	$x_i\hat{\mathbf{e}}_i$ spatial coordinates, current configuration
$\vec{\boldsymbol{X}}$, X_i	$X_i\hat{\mathbf{e}}_i$ material coordinates, initial configuration

$\vec{\boldsymbol{u}}$, u_i	$u_i\hat{\mathbf{e}}_i$ total displacement
$\vec{\boldsymbol{v}}$	$\frac{\partial\vec{\boldsymbol{x}}}{\partial t}$ velocity vector of a material particle
$\boldsymbol{D}$, D_{ij}	$D_{ij}\hat{\mathbf{e}}_i\hat{\mathbf{e}}_j$ rate of deformation tensor
$\boldsymbol{L}$, L_{ij}	$L_{ij}\hat{\mathbf{e}}_i\hat{\mathbf{e}}_j$ velocity gradient tensor
$\boldsymbol{W}$, W_{ij}	$W_{ij}\hat{\mathbf{e}}_i\hat{\mathbf{e}}_j$ spin tensor
$\boldsymbol{F}$	$\frac{\partial\vec{\boldsymbol{x}}}{\partial\vec{\boldsymbol{X}}}$ the material deformation gradient tensor
$\boldsymbol{H}$	$\frac{\partial\vec{\boldsymbol{X}}}{\partial\vec{\boldsymbol{x}}}$ the spatial deformation gradient tensor
$\boldsymbol{R}$, R_{ij}	$R_{ij}\hat{\mathbf{e}}_i\hat{\mathbf{e}}_j$ orthogonal rigid rotation tensor
$\boldsymbol{U}$	Right stretch tensor where $\boldsymbol{F} = \boldsymbol{R}\cdot\boldsymbol{U}$
$\boldsymbol{V}$	Left stretch tensor where $\boldsymbol{F} = \boldsymbol{V}\cdot\boldsymbol{R}$
$\boldsymbol{G}$	Lagrangian or Green's finite strain tensor
$\boldsymbol{E}$	Eulerian or Almansi's finite strain tensor
W^0	Work per unit reference volume
$\boldsymbol{\epsilon}$, $\boldsymbol{e}$	Total and deviatoric strain respectively
$\boldsymbol{\sigma}$, $\boldsymbol{s}$	Total and deviatoric conjugate stress respectively
β, α, ν	Material constants (Lubliner)
$\underline{\boldsymbol{C}}$, $\boldsymbol{C}$	Constitutive tensor
G, G', G''	Shear moduli
E, E', E''	Young's moduli
σ_p, ϵ_p	Volumetric stress (pressure) and strain respectively
$\boldsymbol{e}^m$	Mean deviatoric strain
$\boldsymbol{e}^o$	Oscillating deviatoric strain
e^m	Scalar measure for mean deviatoric strain
e^o_I, e^o_{A1}, e^o_{A2}	Scalar measures for oscillating deviatoric strain
s^{Im}_{ij}, s^{Am}_{ij}	"Mean" deviatoric stress components
s^{Id}_{ij}, s^{Ad}_{ij}	"Dynamic" deviatoric stress components
s^{Iv}_{ij}, s^{Av}_{ij}	"Viscous" deviatoric stress components
h^I_1, h^{A1}_1, h^{A2}_1	Elastic strain damage functions
h^I_2, h^{A1}_2, h^{A2}_2	Viscous strain damage functions
g^I_1, g^{A1}_1, g^{A2}_1	Elastic temperature damage functions
g^I_2, g^{A1}_2, g^{A2}_2	Viscous temperature damage functions
e^a_I, e^a_{A1}, e^a_{A2}	Scalar measures representing the irreversible strain damage
F	Force
A, A_0	Current and original area respectively
L_0	Original length
$\sigma^\star$, $s^\star$	Complex stress and complex deviatoric stress respectively
$\epsilon^\star$, $E^\star$	Complex strain and complex deviatoric strain respectively
E_m	Young's "Mean" or static modulus
E_d	Young's Dynamic elastic modulus
E_l	Young's Loss modulus

3

Strain and stress formulations suitable for elastomer composites

Elastomer composites are anisotropic. Their behavior depends on the strain and stress history, and the strain rate. This means that the analysis has to follow the actual load/deformation history to which the studied body is subject. How closely this has to be done, i.e. in how many increments the analysis should be done, depends entirely on the problem being studied and the material characteristics in question.

Anisotropy demands that the constitutive model be able to be defined at every time instant in the anisotropic material directions of the material. This requires a corotational coordinate system or material coordinates. The strain and stress should be given in the anisotropic material directions.

The strain measure should have properties such that dilatation and deviatoric components can be separated, thus allowing for proper treatment of the nearly incompressible characteristics of the material. If correct energies are to be integrated the strain and stress pair has to be work conjugate. The hysteresis work of the material is, for instance, of interest in this respect. Possible methods for calculating stress and strain can be divided into two main groups: rate formulations and total formulations.

Rate formulations are common in commercially available FEM-software today. They are, for example, used for plasticity and for material that flows. The velocity gradient in the current configuration is decomposed into the tensor for rate of deformation and the spin tensor.

$$\boldsymbol{L} = \frac{\partial \vec{\boldsymbol{v}}}{\partial \vec{\boldsymbol{x}}} \tag{3.1}$$

$$\boldsymbol{D} = \frac{1}{2}\left(\boldsymbol{L} + \boldsymbol{L}^T\right) \tag{3.2}$$

$$\boldsymbol{W} = \frac{1}{2}\left(\boldsymbol{L} - \boldsymbol{L}^T\right) \tag{3.3}$$

The Kirchoff stress is work conjugate with the rate of deformation [2, 1]. The corotational strain rate is obtained after transforming the strain rate using the material

rotation of that time instant.

$$\dot{\boldsymbol{\epsilon}} = \boldsymbol{R}^T \cdot \boldsymbol{D} \cdot \boldsymbol{R} \tag{3.4}$$

The constitutive model is defined in terms of strain rate, strain (integrated strain rate), and stress. These kinds of formulations are implemented with the help of operators such as those presented by Hughes-Winget [31, 38], making it possible to integrate the strain and rotations. Rate formulations have problems with accumulated residual strain, as they employ an approximate numerical algorithm. There are also errors built into the theory [40]. These errors are normally only noticed for closed deformation paths with pure elastic materials. They are also present for other types of analysis, but cannot be separated from the material response. The magnitude of the errors depends on the problems studied, the quality of the numerical algorithm, and the increment size. For cases with repeated cyclic deformation, and when an important part of the material response is elastic, this represents a very severe limitation on the rate formulation.

The second approach is the total formulation, when the strain can be directly calculated from the deformation gradient at every time instant. This involves no integration error. It is common with implementation of a hyperelastic material model such as the Money-Rivlin model as a function of strain invariants, but this allows no anisotropy. The stretching motion has to be separated from the material rotation.

Polar decomposition can be employed [2, 1, 28, 63]. First the stretch is calculated and then a strain definition, for instance logarithmic strain, can be introduced.

$$\boldsymbol{F} = \boldsymbol{R} \cdot \boldsymbol{U} \tag{3.5}$$

$$\boldsymbol{U} = \boldsymbol{Q} \cdot \boldsymbol{\lambda} \cdot \boldsymbol{Q}^T \tag{3.6}$$

$$\ln \boldsymbol{U} = \boldsymbol{Q} \cdot \ln \boldsymbol{\lambda} \cdot \boldsymbol{Q}^T \tag{3.7}$$

$\boldsymbol{\lambda}$ is the diagonal matrix of $\boldsymbol{U}$ whose components are the principal stretch values (eigenvalues). The entity $\boldsymbol{Q}$ is an orthogonal tensor with the unit eigenvectors (principal directions) of $\boldsymbol{U}$ as columns of the matrix. The strain is then transformed to anisotropic material directions.

Compared to the rate formulation, this involves more calculations. However, for problems with cyclic load/deformation when the numerical integration error is significant, it results in much shorter total calculation time. The increment size is only determined by how accurately strain rates, energies, etc. are to be calculated, and depends on the material model used.

For pure stretch, such as uniaxial load/deformation, the rate formulation and the logarithmic strain formulation are identical, because the integral of rate of deformation is logarithmic strain. For a general case they are not identical and research is in progress to define suitable conjugate stress to logarithmic strain [28, 63].

In the next Chapter 4 when constitutive models are discussed, we assume that strain, strain rate, stress, and stress rate can be calculated accurately enough, and that these quantities are given in the corotational anisotropic material directions.

4

Constitutive equations for elastomer composites

4.1 Introduction

The materials considered here are composites reinforced by a large number of fibers oriented in one material direction. The matrices are highly filled elastomers. In V-belt design several types of this kind of material are used in different parts of the belt. The orientation is also different.

When a V-belt is running, it is subject to cyclic deformation. The largest strains are induced by the bending over the pulleys. It carries a normal load in the reinforced material direction and transmits friction forces through the rubber material over to the cord. As the belt is subjected to a large number of deformation cycles, it is steady state conditions and not initial effects that are of interest.

The actual material is anisotropic with one reinforced material direction. The mechanical properties are highly dependent on the strain history and temperature. The damage due to strain can be regarded as irreversible because the recovery process is very slow. The material also exhibits hysteresis which can easily be observed in cyclic loading. These mechanisms and other effects are discussed in [22] where the results of an experimental investigation of this material is also presented. If not otherwise stated, the materials and their properties as discussed in this report refer to that investigation [22]. The results from [69], which are valid for V-belt materials, are also considered. For non-fiber reinforced filled elastomers some well-known results are presented in [19, 53, 54, 65].

4.2 Previous theoretical work

In [50] Morman presented the results of an extensive review of rubber viscoelasticity. He wrote, “Filled systems do not fall into the mathematical framework of materials with fading memory, special damage parameters have to be introduced and Farris [17] has produced the only three-dimensional theory to treat filled polymers”. This was in 1984.

Farris [17] presented isotropic constitutive equations, which incorporate a time dependent Mullin's effect. He applied them to composite propellants. It was demonstrated that p^{th} order Lebesgue norms $\|f\|_p = \left(\int_0^t \mid f(\tau) \mid^p d\tau\right)^{1/p}$ of the deformation history can be used to develop time dependent constitutive equations, yet they need not contain any internal viscosity contributions. However, for the cyclic deformation cases it was necessary to introduce terms including a fading memory portion $\int_0^t (t-\tau)^n \dot{\epsilon}_{ij}(\tau) d\tau$ since compressive stresses from the state of positive tensile strain cannot come from the permanent memory portion of the constitutive equation. This shows that viscous mechanisms are active as well, at least for cyclic deformation.

In 1986 Simo and Lubliner [61] presented a three-dimensional finite-strain viscoelastic model which also incorporated a damage mechanism. In the damage mechanism, which was isotropic, the assumption was that the maximum strain attained by the specimen up to the present time completely controls the damage process. The strain energy of the undamaged material was used as a scalar measure of the maximum strain. The damage function

$$\bar{g}(x) = \beta + (1-\beta)\frac{1-e^{-x/\alpha}}{x/\alpha} \qquad \beta \in [0,1] \quad \alpha \in [0,\infty] \tag{4.1}$$

reaches, asymptotically, a level of damage equal to β at large strains and no damage for low strains. Viscoelasticity accounts for all hysteresis if the maximum strain and therefore the damage has reached a constant level. The viscoelasticity is modeled by a function $K(t)$ which has an elastic part and one or several Maxwell elements in parallel.

$$K(t) = \beta_0 + \sum_{\alpha=1}^{N} \beta_\alpha e^{-t/\nu_\alpha} \tag{4.2}$$

Since both the damage function and the viscous function are isotropic, this restricts the use of this model to isotropic materials.

No doubt research is in progress to develop constitutive models for filled systems, but most efforts are being devoted to unfilled materials or to a class of problems where stress softening, for example, is assumed not to be of major importance or is just neglected. Examples are: static or quasi-static analysis at very large strains where the reinforcement effect of the filler has deteriorated and the material is thus treated as isotropic hyperelastic, or problems involving unfilled, cross-linked polymers.

Much research work is being devoted to developing better numerical algorithms for the FEM-method, to improve the robustness of the method, and to widen the field of applications in which the method can be used.

From the front lines of research there is a time lag of several years before methods developed become available in commercial FEM software. Generally speaking, one can obtain FEM software today that includes hyperelastic formulations for isotropic material. In some programs the possibility of superimposing a small viscoelastic vibration on a large static deformation exists.

4.3 Aims and strategy

As discussed above, the materials in V-belts have very complex behavior as they are elastomer composites and subject to dynamic loading. Most of the mechanisms that strongly affect the mechanical characteristics of the material are active for this kind of deformation history. Still, we want to study this machine element and be able to calculate stresses and strains with some degree of approximation. Using an isotropic hyperelastic model, which is available today, the dynamic analysis yields errors of probably several hundred percent and sometimes the wrong sign of the stress at certain parts of the deformation cycle. We need a better method, but developing new FEM software is outside the scope of this work.

The following strategy is adopted here for the development of constitutive equations:

- The constitutive equations should account for effects due to anisotropy, damage, viscoelasticity, and temperature with acceptable accuracy. These equations should approximate the experimental data available for this material [22].

- The constitutive equations should be implementable in some existing commercially available FEM software, without major modifications to the software. This is a very severe limitation, as we have to rely on the interfaces provided, and accept whatever this implies. For instance, all implementations of hyperelasticity which use invariants of the deformation gradient are ruled out, because this allows no anisotropy.

- We restrict the validity of the model to applications similar to the V-belts one. This means that cyclic deformation loading is of greatest interest. The steady state conditions are more important than what happens during the first few deformation cycles. The largest part of the cyclic strain, which governs the damage, is due to the bending of the V-belt and therefore induced by deformation and not by forces. We consider the temperature as a given quantity of each material point. It is not coupled directly to the hysteresis work in the constitutive equations. Coupled thermal and stress/strain analysis can be done if the actual FEM software allows for that type of analysis when the loss energy is calculated.

- The simplicity of the constitutive model has higher priority than very good correlation to the experimental data. The experiments available always represent a limited number of the infinite number of possible strain and stress histories for which the model is meant to give a realistic response. Higher complexity of the constitutive model and more constants to be determined increase the possibility that the model will give erroneous result for a strain history which was not among the available experiments. The experiments should as closely as possibly represent the cases for which the model will be used. The model should be simple enough to make it possible to predict its response for different strain and stress histories.

4.4 Elasticity and anisotropy

4.4.1 Isotropy, anisotropy and elastic symmetry

Assume that the constitutive law is employed in a corotational framework. This means that strain, strain rate, stress, and stress rate can be calculated accurately enough, and that these quantities are given in the corotational anisotropic material directions. The strain measure should have properties such that dilatation and deviatoric components can be separated.

Then the rate formulation for a pure elastic material is:

$$\dot{\sigma}_{ij} = C_{ijkl}\dot{\epsilon}_{kl} \tag{4.3}$$

where $\dot{\epsilon}_{kl}$ is the corotational strain rate and $\dot{\sigma}_{ij}$ is a suitable corotational stress rate.

Since $\dot{\epsilon}_{kl}$ is a symmetric second order tensor, the concepts of principal axes, principal values, invariants, a rate of deformation quadric, and a rate of deformation deviator tensor may be associated with it. Also, equations of compatibility for the components of the rate of deformation tensor, analogous to those presented for the linear strain tensors may be developed. This rate formulation, or the use of infinitesimal strain increments, are analogous.

Thus, the theoretical framework of linear elasticity can be used to determine the fourth order tensor $\underline{\boldsymbol{C}}$ in Equation 4.3 above. It is known as the *generalized Hooke's law*. Due to symmetry of the strain rate and stress rate, there are at most 36 distinct constants. A single indexing system is often used. It is shown below for stresses and strains.

$$\begin{array}{lllllll}
\sigma_{11} & = & \sigma_1 & & & & \\
\sigma_{22} & = & \sigma_2 & & & & \\
\sigma_{33} & = & \sigma_3 & & & & \\
\sigma_{23} & = & \sigma_{32} & = & \sigma_4 & = & \tau_{23} \\
\sigma_{13} & = & \sigma_{31} & = & \sigma_5 & = & \tau_{13} \\
\sigma_{12} & = & \sigma_{21} & = & \sigma_6 & = & \tau_{12}
\end{array}$$

$$\begin{array}{lllllll}
\epsilon_{11} & = & \epsilon_1 & & & & \\
\epsilon_{22} & = & \epsilon_2 & & & & \\
\epsilon_{33} & = & \epsilon_3 & & & & \\
\epsilon_{23} & = & \epsilon_{32} & = & \frac{1}{2}\epsilon_4 & = & \frac{1}{2}\gamma_{23} \\
\epsilon_{13} & = & \epsilon_{31} & = & \frac{1}{2}\epsilon_5 & = & \frac{1}{2}\gamma_{13} \\
\epsilon_{12} & = & \epsilon_{21} & = & \frac{1}{2}\epsilon_6 & = & \frac{1}{2}\gamma_{12}
\end{array}$$

Thus, we obtain

$$\dot{\sigma}_K = C_{KM}\dot{\epsilon}_M \qquad {\scriptstyle K,M\in[1,2,3,4,5,6]} \tag{4.4}$$

If a strain energy function exists, then $C_{KM} = C_{MK}$ and the number of constants is reduced to 21.

A plane of elastic symmetry exists at a point where the elastic constants have the same values for every pair of coordinate systems which are reflected images of one another with respect to the plane.

If a material posesses three mutually perpendicular planes of elastic symmetry, the material is called orthotropic and its elasticity matrix is of the form

$$C_{KM} = \begin{bmatrix} C_{11} & C_{12} & C_{13} & 0 & 0 & 0 \\ C_{12} & C_{22} & C_{23} & 0 & 0 & 0 \\ C_{13} & C_{23} & C_{33} & 0 & 0 & 0 \\ 0 & 0 & 0 & C_{44} & 0 & 0 \\ 0 & 0 & 0 & 0 & C_{55} & 0 \\ 0 & 0 & 0 & 0 & 0 & C_{66} \end{bmatrix} \tag{4.5}$$

which contains nine constants.

If the material properties are equal in a discrete number of directions which are obtained by a rotation $2\pi/N$ around a certain axis, then this axis is an axis of symmetry of the order N.

Let the axis be that which is indicated by the index 3, and for $N = 4$ we obtain for the orthotropic material

$$C_{KM} = \begin{bmatrix} C_{11} & C_{12} & C_{13} & 0 & 0 & 0 \\ C_{12} & C_{11} & C_{13} & 0 & 0 & 0 \\ C_{13} & C_{13} & C_{33} & 0 & 0 & 0 \\ 0 & 0 & 0 & C_{44} & 0 & 0 \\ 0 & 0 & 0 & 0 & C_{44} & 0 \\ 0 & 0 & 0 & 0 & 0 & C_{66} \end{bmatrix} \tag{4.6}$$

which contains six constants.

If $N \geq 6$ then we get a plane of isotropy and the material is called *transversal isotropic.*

$$\begin{aligned} C_{KM} &= \begin{bmatrix} C_{11} & C_{12} & C_{13} & 0 & 0 & 0 \\ C_{12} & C_{11} & C_{13} & 0 & 0 & 0 \\ C_{13} & C_{13} & C_{33} & 0 & 0 & 0 \\ 0 & 0 & 0 & C_{44} & 0 & 0 \\ 0 & 0 & 0 & 0 & C_{44} & 0 \\ 0 & 0 & 0 & 0 & 0 & \frac{1}{2}(C_{11} - C_{12}) \end{bmatrix} \\ &= \begin{bmatrix} (C_{12} + 2C_{66}) & C_{12} & C_{13} & 0 & 0 & 0 \\ C_{12} & (C_{12} + 2C_{66}) & C_{13} & 0 & 0 & 0 \\ C_{13} & C_{13} & C_{33} & 0 & 0 & 0 \\ 0 & 0 & 0 & C_{44} & 0 & 0 \\ 0 & 0 & 0 & 0 & C_{44} & 0 \\ 0 & 0 & 0 & 0 & 0 & C_{66} \end{bmatrix} \end{aligned} \tag{4.7}$$

This material description has five constants.

Bodies which are elastically equivalent in all directions possess complete symmetry and are termed isotropic. The number of independent elastic constants reduces to

two:

$$C_{KM} = \begin{bmatrix} (C_{12}+2C_{44}) & C_{12} & C_{12} & 0 & 0 & 0 \\ C_{12} & (C_{12}+2C_{44}) & C_{12} & 0 & 0 & 0 \\ C_{12} & C_{12} & (C_{12}+2C_{44}) & 0 & 0 & 0 \\ 0 & 0 & 0 & C_{44} & 0 & 0 \\ 0 & 0 & 0 & 0 & C_{44} & 0 \\ 0 & 0 & 0 & 0 & 0 & C_{44} \end{bmatrix} \tag{4.8}$$

where the $\lambda = C_{12}$, $\mu = C_{44}$ are the well known *Lame's constants*.

4.4.2 Separation into volumetric and deviatoric components

The stress rate and the strain rate can be separated into deviatoric and volumetric/hydrostatic parts.

$$\dot{\sigma}_{ij} = \dot{s}_{ij} + \delta_{ij}\frac{\dot{\sigma}_{kk}}{3} = \dot{s}_{ij} + \delta_{ij}\dot{\sigma}_p \tag{4.9}$$

$$\dot{\epsilon}_{ij} = \dot{e}_{ij} + \delta_{ij}\frac{\dot{\epsilon}_{kk}}{3} = \dot{e}_{ij} + \delta_{ij}\dot{\epsilon}_p \tag{4.10}$$

The class of materials studied has in many cases been regarded as incompressible. The material is however compressible, but with a bulk modulus about three orders of magnitude greater than the shear modulus, i.e. the ratio of bulk modulus to Young's modulus is typically about 250.

Assume that the bulk modulus is finite, that is compressible, and does not vary with time. Impose the following restriction on the elastic constitutive equations:

$$\dot{\epsilon}_{kk} = 0 \Leftrightarrow \dot{\sigma}_{kk} = 0 \tag{4.11}$$

This means that, for a compressible material, a pure deviatoric strain should result in pure deviatoric stress and vice versa.

The orthotropic matrix was

$$C_{KM} = \begin{bmatrix} C_{11} & C_{12} & C_{13} & 0 & 0 & 0 \\ C_{12} & C_{22} & C_{23} & 0 & 0 & 0 \\ C_{13} & C_{23} & C_{33} & 0 & 0 & 0 \\ 0 & 0 & 0 & C_{44} & 0 & 0 \\ 0 & 0 & 0 & 0 & C_{55} & 0 \\ 0 & 0 & 0 & 0 & 0 & C_{66} \end{bmatrix} \tag{4.12}$$

and for this case the restriction results in the equations below.

$$\begin{aligned} C_{22} + C_{23} - C_{11} - C_{13} &= 0 \\ C_{23} + C_{33} - C_{11} - C_{12} &= 0 \end{aligned} \tag{4.13}$$

For the transversal isotropic material this reduces to one equation because $C_{22} = C_{11}$ and $C_{23} = C_{13}$.

$$C_{13} + C_{33} - C_{11} - C_{12} = 0 \tag{4.14}$$

For the isotropic material the restriction discussed is no new constraint, it is already there.

One of the advantages of this constraint is that it is just as easy to separate deviatoric and volumetric parts for anisotropic matrices as it is for the isotropic case. The following examples are valid for the transversal isotropic case, but there is no difference in principle compared, for instance, to the orthotropic case.

The matrix $\boldsymbol{C}$ for transversal isotropic elasticity incorporating the developed constraint is then:

$$\begin{bmatrix} (C_{12}+2C_{66}) & C_{12} & (2C_{12}+2C_{66}-C_{33}) & 0 & 0 & 0 \\ C_{12} & (C_{12}+2C_{66}) & (2C_{12}+2C_{66}-C_{33}) & 0 & 0 & 0 \\ (2C_{12}+2C_{66}-C_{33}) & (2C_{12}+2C_{66}-C_{33}) & C_{33} & 0 & 0 & 0 \\ 0 & 0 & 0 & C_{44} & 0 & 0 \\ 0 & 0 & 0 & 0 & C_{44} & 0 \\ 0 & 0 & 0 & 0 & 0 & C_{66} \end{bmatrix} \tag{4.15}$$

or using the engineering constants:

K	Bulk modulus
E_{33}	Young's in the reinforced direction 3
G_{13}	Shear modulus in direction 13
G	Shear modulus in direction 12, the isotrophic plane

$$\boldsymbol{C} = \begin{bmatrix} \left(\frac{K}{1-\frac{E_{33}}{9K}}+G\right) & \left(\frac{K}{1-\frac{E_{33}}{9K}}-G\right) & \frac{K-\frac{E_{33}}{3}}{1-\frac{E_{33}}{9K}} & 0 & 0 & 0 \\ \left(\frac{K}{1-\frac{E_{33}}{9K}}-G\right) & \left(\frac{K}{1-\frac{E_{33}}{9K}}+G\right) & \frac{K-\frac{E_{33}}{3}}{1-\frac{E_{33}}{9K}} & 0 & 0 & 0 \\ \frac{K-\frac{E_{33}}{3}}{1-\frac{E_{33}}{9K}} & \frac{K-\frac{E_{33}}{3}}{1-\frac{E_{33}}{9K}} & \frac{K+\frac{E_{33}}{3}}{1-\frac{E_{33}}{9K}} & 0 & 0 & 0 \\ 0 & 0 & 0 & G_{13} & 0 & 0 \\ 0 & 0 & 0 & 0 & G_{13} & 0 \\ 0 & 0 & 0 & 0 & 0 & G \end{bmatrix} \tag{4.16}$$

Introduction of the bulk modulus and the constraint made it possible to eliminate the two *Poisson's constants*.

The inverse $\boldsymbol{C}^{-1}$ of the matrix is.

$$\begin{bmatrix} \frac{1}{4}\left(\frac{1}{G}+\frac{1}{E_{33}}+\frac{1}{3K}\right) & -\frac{1}{4}\left(\frac{1}{G}-\frac{1}{E_{33}}-\frac{1}{3K}\right) & -\frac{1}{2}\left(\frac{1}{E_{33}}-\frac{1}{3K}\right) & 0 & 0 & 0 \\ -\frac{1}{4}\left(\frac{1}{G}-\frac{1}{E_{33}}-\frac{1}{3K}\right) & \frac{1}{4}\left(\frac{1}{G}+\frac{1}{E_{33}}+\frac{1}{3K}\right) & -\frac{1}{2}\left(\frac{1}{E_{33}}-\frac{1}{3K}\right) & 0 & 0 & 0 \\ -\frac{1}{2}\left(\frac{1}{E_{33}}-\frac{1}{3K}\right) & -\frac{1}{2}\left(\frac{1}{E_{33}}-\frac{1}{3K}\right) & \frac{1}{E_{33}} & 0 & 0 & 0 \\ 0 & 0 & 0 & \frac{1}{G_{13}} & 0 & 0 \\ 0 & 0 & 0 & 0 & \frac{1}{G_{13}} & 0 \\ 0 & 0 & 0 & 0 & 0 & \frac{1}{G} \end{bmatrix} \tag{4.17}$$

Application of a hydrostatic stress $\dot{\sigma}_p = \dot{\sigma}_1 = \dot{\sigma}_2 = \dot{\sigma}_3$ results in a strain $\dot{\epsilon}_p = \dot{\epsilon}_1 = \dot{\epsilon}_2 = \dot{\epsilon}_3$.

$$\dot{\sigma}_p = (4C_{12} + 4C_{66} - C_{33})\dot{\epsilon}_p = 3K\dot{\epsilon}_p \tag{4.18}$$

Thus we have separated the dilatation from the deviatoric response.

The matrix $\boldsymbol{C}$ can be decomposed into two parts that represent the isotropic and anisotropic responses. Here we adopt the additive decomposition shown below.

$$\boldsymbol{C} = \boldsymbol{C}_I + \boldsymbol{C}_A \tag{4.19}$$

$$\boldsymbol{C}_I = \begin{bmatrix} C'_{11} & C_{12} & C_{12} & 0 & 0 & 0 \\ C_{12} & C'_{11} & C_{12} & 0 & 0 & 0 \\ C_{12} & C_{12} & C'_{11} & 0 & 0 & 0 \\ 0 & 0 & 0 & C_{66} & 0 & 0 \\ 0 & 0 & 0 & 0 & C_{66} & 0 \\ 0 & 0 & 0 & 0 & 0 & C_{66} \end{bmatrix} \tag{4.20}$$

$$\boldsymbol{C}_A = \begin{bmatrix} 0 & 0 & -C'_{33} & 0 & 0 & 0 \\ 0 & 0 & -C'_{33} & 0 & 0 & 0 \\ -C'_{33} & -C'_{33} & C'_{33} & 0 & 0 & 0 \\ 0 & 0 & 0 & C'_{44} & 0 & 0 \\ 0 & 0 & 0 & 0 & C'_{44} & 0 \\ 0 & 0 & 0 & 0 & 0 & 0 \end{bmatrix} \tag{4.21}$$

$$C'_{11} = (C_{12} + 2C_{66}) \tag{4.22}$$

$$C'_{33} = (C_{33} - (C_{12} + 2C_{66})) \tag{4.23}$$

$$C'_{44} = (C_{44} - C_{66}) \tag{4.24}$$

Using the tensor notation we can write

$$\dot{s}_{ij} = 2G\dot{e}_{ij} + C^A_{ijkl}\dot{e}_{kl} \tag{4.25}$$

$$\dot{\sigma}_{ij} = \delta_{ij}\dot{\sigma}_p + \dot{s}_{ij} \tag{4.26}$$

$$\dot{\sigma}_p = 3K\dot{\epsilon}_p \tag{4.27}$$

$$\dot{\epsilon}_{ij} = \delta_{ij}\dot{\epsilon}_p + \dot{e}_{ij} \tag{4.28}$$

where $G = C_{66}$ and $K = (3C_{12}+2C_{66})/3+(C_{12}+2C_{66}-C_{33})/3 = (4C_{12}+4C_{66}-C_{33})/3$.

Thus, the total elastic response is divided into volumetric, isotropic, and anisotropic parts.

4.5 Damage

4.5.1 The damage mechanism

The physical concept underlying damage is that crack initiation is preceded by a progressive internal deterioration of the material, which induces a loss of strength in terms of strain as well as in remaining life. A parameter, on a macroscopic scale, takes into account the microscopic deteriorations such as voids, microcracks, etc. The damage parameter can represent a loss of effective area in the material. This concept of continuous damage mechanics has been developed and applied to metals for several years [13, 44, 45, 43, 64].

Material damage in elastomer composites is a complex process which may involve microstructural damage, microvoid damage, breakage of reinforcement fibers, separation of fiber matrix etc. Influence on the mechanical properties of different variables such as strain, frequency of cyclic deformation, and temperature have been determined experimentally but no theoretical explanation has been given [54, 19, 53, 22, 69].

Let us apply the concept of a continuous damage mechanism for the purpose of being able to calculate the mechanical behavior (i.e. stress and strain) for the class of materials studied here. It is proposed that the most important quantities affecting the damage are strain history, temperature, and number of deformation cycles.

The dynamic material properties of elastomer composites used in V-belt applications have been experimentally determined as functions of strain, temperature, and frequency [22, 69]. The result suggests that we should introduce separate isotropic and anisotropic damage parameters, as the damage develops in different ways in different material directions.

4.5.2 Isotropic damage from strain

The destruction of the elastomer, the filler (i.e. carbon black), and the elastomer-filler aggregate are the dominant effects. The type of filler is more important than the elastomer. Normally, nearly all damage occurs during the first few deformation cycles during a cyclic strain history. The most common assumption is that a scalar strain measure, which more or less reflects the maximum total strain, governs the damage [17, 61, 11, 26]. However, experimental investigations performed for cyclic deformation with different mean levels of strain and a constant strain amplitude gave the result that the maximum strain amplitude is the important variable. Experiments with the strain mean level equal to zero, one strain amplitude, and two strain amplitudes gave no significant difference [22]. It is clear that a large enough static strain will give damage, but in cyclic deformation with a mean level less than two amplitudes, a good assumption is that the damage is governed by the amplitude. In V-belts, the largest strain does result from bending, which means that normally the mean strain level is less than one strain amplitude.

We need a scalar measure for the strain amplitude. This is more difficult to obtain for the strain amplitude than for the total strain where the second invariant of strain is normally used.

The deviatoric strain at any instant in time is e_{ij}. Then the mean deviatoric strain tensor over the time interval $[0-t]$ is defined as:

$$e_{ij}^m = \frac{1}{t}\int_0^t e_{ij}\,d\tau \tag{4.29}$$

Define the oscillating deviatoric strain about the mean level as:

$$e_{ij}^o = e_{ij} - e_{ij}^m \tag{4.30}$$

Thus we have at any time t:

$$e_{ij} = e_{ij}^m + e_{ij}^o \tag{4.31}$$

Let us define the scalar measure for both the mean strain level and the deviation from this level:

$$e_I^o = \sqrt{e_{ij}^o e_{ij}^o} \qquad e^m = \sqrt{e_{ij}^m e_{ij}^m} \tag{4.32}$$

Assuming a deformation or strain cycle with one mean level and one amplitude, one example is sinusoidal variation, then e_I^o will have a cyclic variation with two maxima

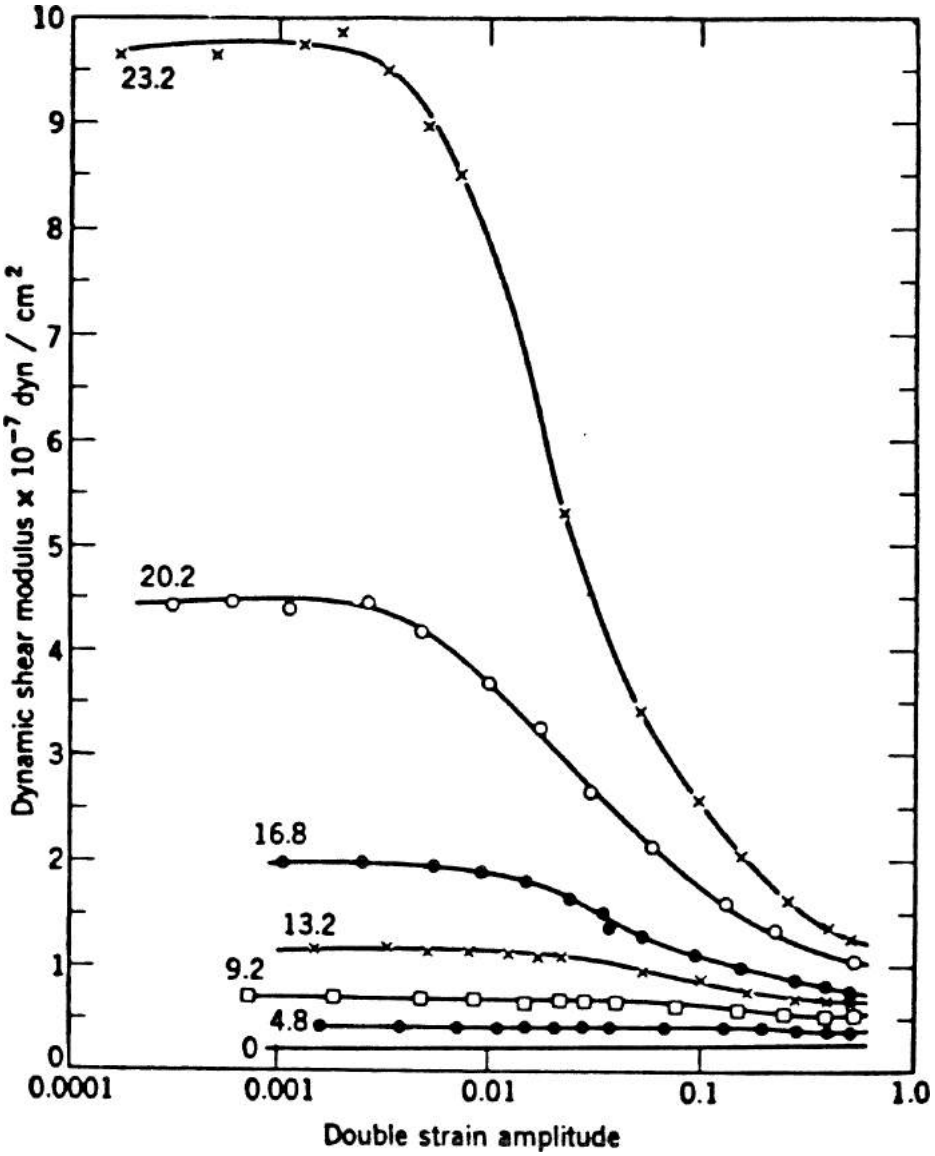

Figure 4.1 *Dependency of elastic shear modulus, G' on the double strain amplitude at 0.1 Hz for a butyl rubber containing various concentrations of HAF carbon black [57].*

during every deformation cycle, one maximum in tension and one in compression. The scalar e^m represents the integral of the strain divided by time and will approach a stable value, with continuously smaller oscillations.

How the elastic modulus and the loss modulus depend on the strain amplitude has been investigated in [54, 19, 53, 22]. Typical graphs are shown in Figures 4.1 and 4.2 where the modulus is plotted versus the logarithm of the double strain amplitude. The data represents the steady state damage level which occurs after a number of deformation cycles.

The elastic shear modulus can be characterized by $G_o^{'}$ and $G_\infty^{'}$ for very small strains and large strains, respectively. Payne showed that similar behavior was obtained for

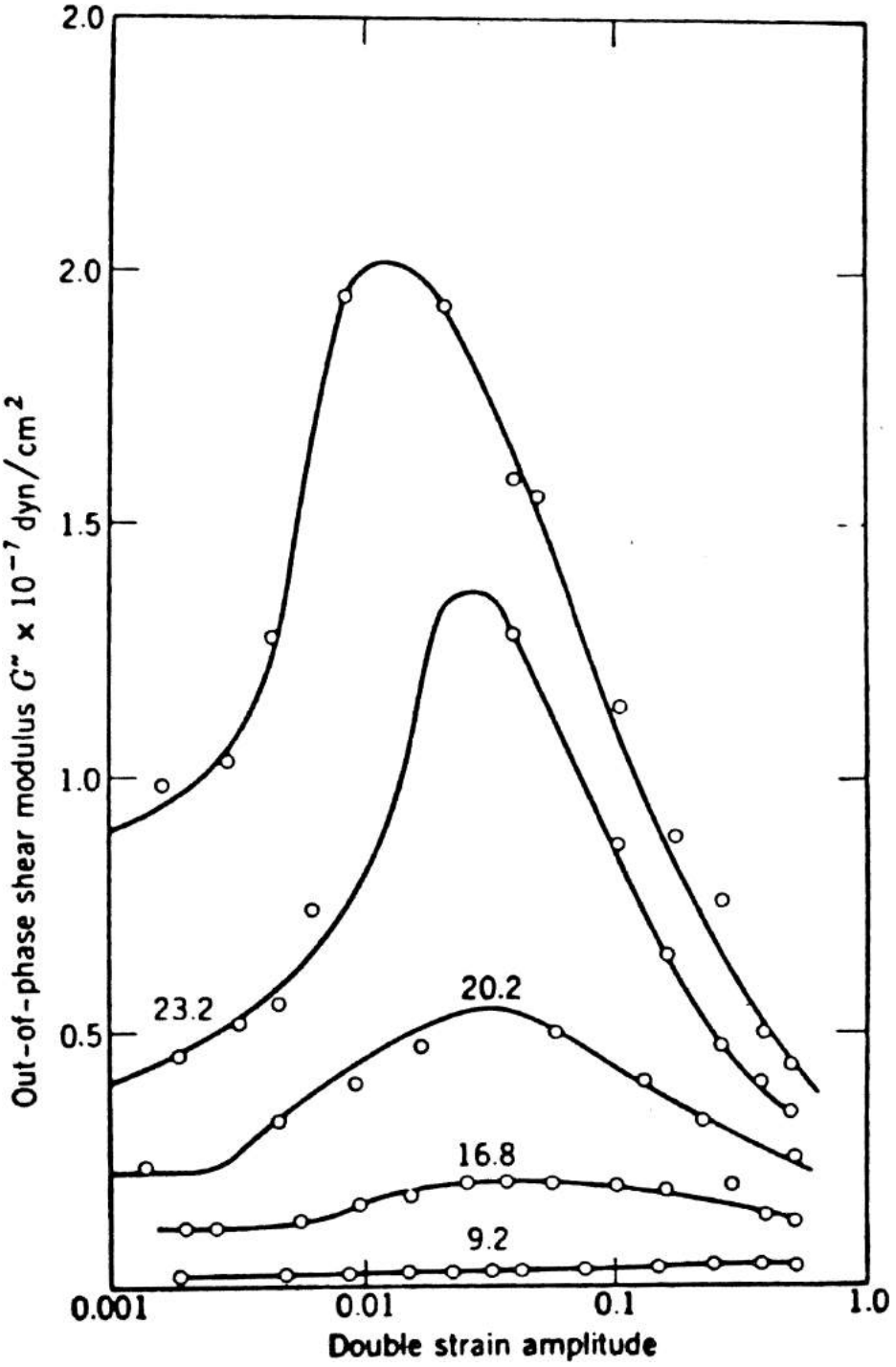

Figure 4.2 *Dependency of shear loss modulus, G'' on the double strain amplitude at 0.1 Hz for a butyl rubber containing various concentrations of HAF carbon black [57].*

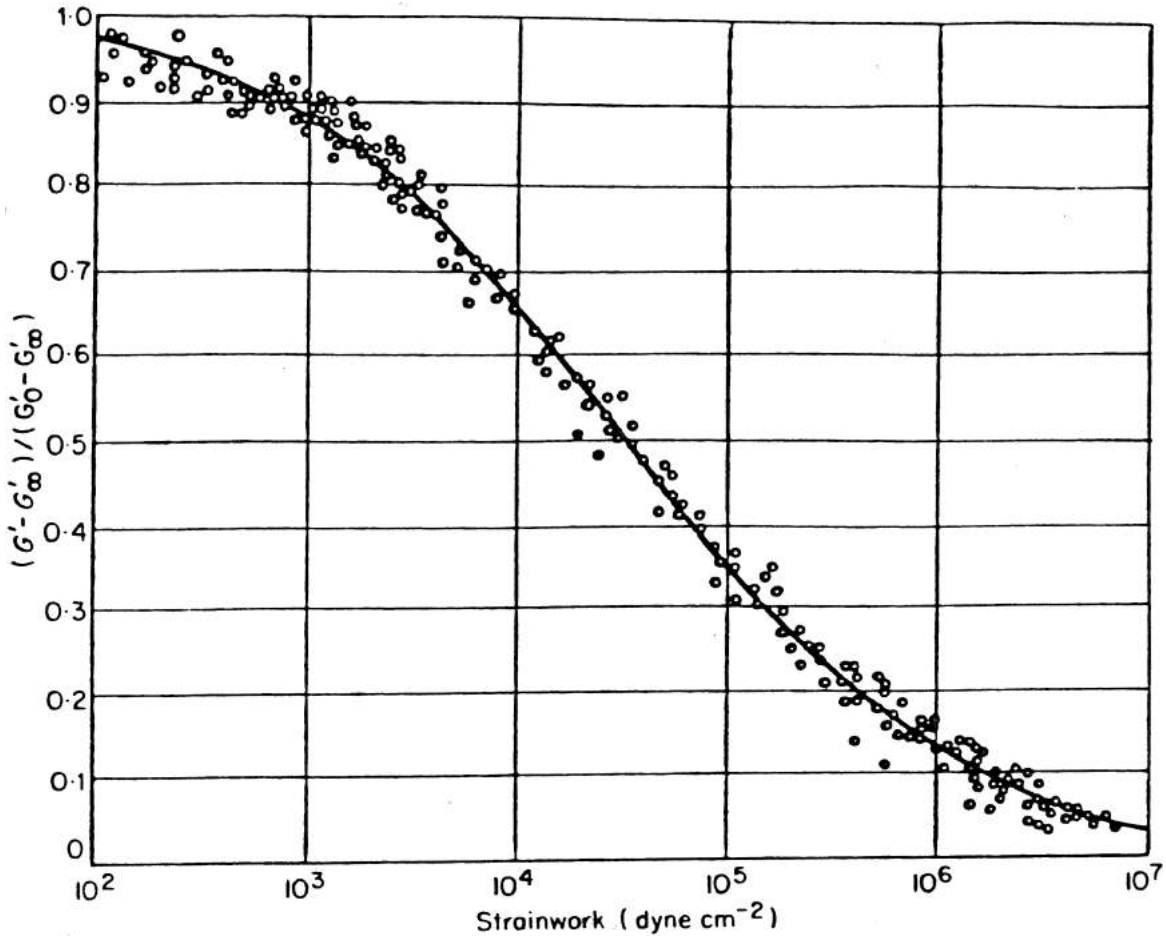

Figure 4.3 *Master curve of the change in* $(G' - G'_\infty) / (G'_o - G'_\infty)$ *with strain work (product of stress and strain) for a wide range of filled vulcanizates [53].*

different types and different concentrations of fillers and for different rubbers. He used a ratio $(G' - G'_\infty) / (G'_o - G'_\infty)$ when plotting against the logarithmic strain amplitude or the product of stress and strain.

The following characteristics for steady state damage can be deduced from the data available. There is a lower limit of strain amplitude for which no significant damage is observed. There is also an upper limit of strain amplitude for which the damage has almost reached the asymptotic value for large strains. In Figure 4.1 the lower limit of shear strain amplitude is between 0.001 and 0.002, and the upper limit between 0.1 and 0.2 . The damage takes place within an interval of two orders of magnitude of strain amplitude which is proportional to the square root of strainwork (see Figure 4.3). For the middle region with an interval of about one order of magnitude in strain, the damage is nearly linear in the logarithm of the strain amplitude. Most of the damage occurs in this region.

The loss modulus appears to be a function of the gradient of the damage on the elastic modulus. Thus, a peak in loss modulus is obtained at about 50 percent damage where the steepest gradient of the damage function is located.

Functions that can represent the behavior discussed above are needed. Here an

approximation of the normal probability function is used to represent the damage. It is suggested that the normal density function has the properties needed to account for the influence of hysteresis due to damage on the loss modulus.

$$P\left(\tfrac{x-\mu}{\alpha}\right) \approx \frac{1}{2}\left[1+\left(1-e^{-\frac{2}{\pi}\left(\frac{x-\mu}{\alpha}\right)^2}\right)^{\frac{1}{2}} sgn\left(\tfrac{x-\mu}{\alpha}\right)\right] \tag{4.33}$$

$$sgn\,(y) = \begin{cases} 1 & \text{if } y>0 \\ 0 & \text{if } y=0 \\ -1 & \text{if } y<0 \end{cases} \tag{4.34}$$

$$\frac{\partial P\left(\frac{x-\mu}{\alpha}\right)}{\partial x} = \frac{1}{\alpha\sqrt{2\pi}} e^{-\frac{1}{2}\left(\frac{x-\mu}{\alpha}\right)^2}$$

The variable x and the parameters μ, and α are expressed as logarithms (base 10) of the strain. The variable x represents the actual strain amplitude that governs the damage level, μ is a mean level for which 50 percent of the damage has occurred and is also the location of the peak in strain induced hysteresis. The variance α^2 is a measure of the interval in strain amplitude in which the damage mechanism is active.

When choosing the modulus of the undamaged material as the reference level we have to introduce a variable which controls the modulus at very large strains. Thus, the complete damage function h_1^I for the elastic modulus is as follows, assuming that we have a scalar e_I^a that represents the strain amplitude governing the damage:

$$h_1^I\left(e_I^a\right) = \beta_1^I + \left(1-\beta_1^I\right)\frac{1}{2}\left[1-\left(1-e^{-\frac{2}{\pi}\left(\frac{\log e_I^a-\mu_I}{\alpha_I}\right)^2}\right)^{\frac{1}{2}} sgn\left(\frac{\log e_I^a-\mu_I}{\alpha_I}\right)\right] \tag{4.35}$$

The damage function that governs the effect on hysteresis work due to strain becomes:

$$h_2^I\left(e_I^a\right) = \beta_2^I + \left(1-\beta_2^I\right)\frac{1}{\alpha_I\sqrt{2\pi}} e^{-\frac{1}{2}\left(\frac{e_I^a-\mu_I}{\alpha_I}\right)^2} \tag{4.36}$$

The next step is obviously to discuss how the variable e_I^a should be calculated. By following the discussion above, we conclude that it should be a function that asymptotically reaches the peak values of e_I^o during the deformation cycles. There are two extreme cases which can be discussed.

- The first one assumes no damage when calculating stresses and strains during one or more deformation cycles. Then, using the maximum values of e_I^o, the damage can be calculated and the damage value thus obtained will be used in the rest of the analysis. In fact, this case means solving two separate problems using the first solution for the next one. Whether or not this simple method is useful depends on the problem being studied. One condition should be that strains mainly come from imposed deformations attributable to geometry changes, etc. and not from loads. If the body has a uniform state of strain and is subject to imposed deformations, then this is an exact solution.

- The second extreme case is that the damage governing variable is, at every instant in time, a function of stress, strain, time, etc, making it possible to calculate the evolution of the damage. Such formulations are necessary if the stress and strain state during the few first deformation cycles are to be studied in detail, or if the constitutive equations are to be used in solving other types of problems such as creep, etc.

Different approaches have been suggested. Farris [17] studied a time dependent Mullin's Effect, when the damage increased with time at different rates at each strain level, and an accumulated damage was calculated. This formulation cannot be used for the material studied here, since we obtain a steady state level of damage after a few cycles.

Simo and Lubliner [61] used the theoretical framework from the theory of plasticity to calculate a damage surface. The square root of the elastically stored energy of the undamaged material was the governing variable. As we assume that a strain amplitude is the governing variable, this formulation cannot be used in its present form. Also, we know that the damage develops over a few deformation cycles and not only during the first deformation cycle.

Here, we restrict ourselves to cyclic deformation and are interested in the steady state level of damage, and not the initial effects. Since the main strain in V-belts are induced by bending governed by a geometrical change, an evaluation of the simple method described as the first extreme case above is motivated. However, it is not difficult to formulate an algorithm that allows the damage to develop successively over a few deformation cycles and thus accounts for some changes in the strain distribution in the body due to damage. Also, values of strain amplitudes can only be obtained after complete deformation cycles, and it takes some time before the mean level of the strain stabilizes.

The following algorithm for the irreversible damage increase is suggested. The oscillating strain e_I^o defined previously is used as the scalar value that governs the evolution of the variable e_I^a.

$$\dot{e_I^a} = \begin{cases} C_d \left(1 - e_I^a / e_I^o\right) |\dot{e}_I^o| & \text{if } e_I^o > e_I^a \\ 0 & \text{if } e_I^o \leq e_I^a \end{cases} \tag{4.37}$$

Using this definition the irreversible damage increases only when e_I^o is greater then the value of e_I^a accumulated so far. Also, the damage increase is proportional to the strain rate and to the difference in strain. At cyclic load/deformation there is no frequency dependency of the evolution of damage. These properties reflect the behavior that has been experimentally observed. The constant C_d governs how fast the damage develops. A value of 0.6 means that more than 95 percent of the damage has developed within 10 deformation cycles for cyclic deformation, and about 50 percent during the first deformation cycle.

4.5.3 Anisotropic damage from strain

The anisotropic properties come from the reinforcement of the material by fibers. They represent about 20 percent of the material and are oriented in one material

direction. Here, we consider the anisotropic part of the elastic response as defined in Section 4.4. It is reasonable to assume that the major damage mechanisms are fiber breakage and separation of fiber from the elastomer matrix. This is totally different from the damage mechanisms discussed for the isotropic response in the previous section.

The available data which can be used are presented in references [22, 69]. There is uniaxial compression in the fiber direction and simple shear along the fibers. In the uniaxial tests, only data with relatively low strain levels are available, which also is the case in real V-belt applications. Test data in shear at different mean strain levels indicate that the strain amplitude is the governing variable here, too. However in the uniaxial direction no such data are available. It may be necessary to introduce different damage functions for the two cases. However, any suggested model has to be evaluated together with the isotropic response.

As an initial model it is reasonable to suggest a damage function of the same type as for the isotropic response, but with independent variables and other strain measures.

Assume that the damage of the anisotropic parts of material response is governed by scalars representing the oscillatory part of the deviatoric strain, as for the isotropic case. However, here only strains which give contributions in the reinforced material directions are considered. For transversal isotropic material this will be the uniaxial strain in the reinforced direction and shear strain along the reinforced direction. More complex anisotropy can be treated analogously.

Thus, the complete damage function h_1^A for one anisotropic contribution to the elastic modulus becomes a function of the same type as for the isotropic case, assuming we have a scalar e_A^a that represents the strain amplitude governing the damage of this part of the anisotropy. The same function is used for damage evolution as for the isotropic contribution. Other anisotropic parts of the material response are treated analogously.

As discussed for the isotropic response, a function is used which represents the peak in hysteresis due to strain damage effects. However, here an independent parameter β_2^A will be used for each anisotropic contribution.

4.6 Influence of temperature on the mechanical properties

The material properties are strongly affected by temperature. However, within a reasonable temperature range the change is not irreversible, as opposed to damage caused by strain in continuous cyclic tests.

The temperature range of interest is determined by the applications for which the material is used. A lower temperature limit for the material in V-belts could be that of the outdoor environment plus the temperature increase due to hysteresis work. Often the transmission is also mounted close to heat radiating machinery. Thus, room temperature level is unrealistic as a lower limit. The upper temperature limit is not determined by the problems encountered in testing material properties i laboratories, but rather by the temperature limit for which realistic fatigue life is obtained for the

application studied. As the fatigue life is strongly reduced by temperature increase, the upper practical limit is quite low. For the V-belt types of interest made of the present materials, we suggest an upper limit of 100 to 150 $^{\circ}C$. This is of course, very much dependent on the acceptable fatigue life for a certain application.

Our conclusion is that any function that reflects the experimental response over this limited temperature interval can be considered. It is not necessary to develop more complex theories involving glass transition temperatures, etc. Of course, the function thus developed can only be used for the temperature range for which there is experimental data.

These experimental data [22, 69] suggest that as a first approximation influence from temperature on the mechanical response could be multiplicative with other effects, i.e. strain and frequency. The mechanical deterioration seems to be nearly linear with temperature increase. The loss modulus is more affected than the elastic response. This simple algorithm is suggested to model the influence of temperature. Separate reversible linear temperature damage functions g_1^I,g_2^I,g_1^A,g_2^A, etc. are developed for the isotropic and anisotropic parts of the material response.

4.7 Viscoelasticity

It is clear that hysteresis and other time dependent effects in filled elastomers cannot be explained successfully using only viscoelastic models. However, it is also true that part of the response can be explained using viscoelasticity, and for special cases close agreement can be obtained between experiments and viscoelastic models. Farris [17] developed a time dependent damage model which successfully explained hysteresis and other effects for the material studied. However, in cyclic deformation it was necessary to add viscoelastic terms to explain how negative stress could be obtained for pure positive strain.

The steady state for cyclic sinusoidal deformation at a certain frequency and strain amplitude can be represented by a simple viscoelastic model, such as a spring in parallel with a Maxwell element. The typical response observed from tests is a hysteresis loop from which the following moduli can be calculated: loss modulus, dynamic elastic modulus, and mean or static modulus defined as the mean stress divided by the mean strain. The test data presented in the experimental investigation for the material studied here have been expressed in such quantities [22].

The Maxwell type of viscoelastic model combined with pure elastic elements has the properties which causes primarily elastic response for very fast or slow processes, and has a peak in hysteresis work in between. This behavior is desired and corresponds to the available experiments.

If the model is to approximate the material behavior within a certain frequency range, then it needs to be expanded. This can be done either by using more Maxwell elements and elastic elements, or by introducing nonlinear dashpots in the Maxwell model [37]. Thus, the model can be expanded to cover the interval of frequencies that is of interest. It is important to be very thorough in order to obtain a realistic response, both for dynamic elastic response, maximum in hysteresis work over the

frequency domain, and the static response. The test data indicate that the slight increase in elastic modulus is linear with frequency, and that a maximum in loss modulus is within the frequency range for which tests have been performed.

If the material model was known a prior to be pure viscoelastic, tests could have been done either in relaxation or creep to give the values of the parameters in the model. However, this is normally not the case. Values obtained from relaxation tests fail to predict the creep response and vice versa. This is, of course, an indication of the fact that the theoretical model is not complete enough to be able to predict a wide range of responses. Here, we use dynamic cyclic tests that approximate the deformation cycles in the real application. The aim, and the critical assumption, are that the model should reflect the real response so well that the amplitudes of strain and stress, the mean values of stress and strain, and the hysteresis work will be correct to a certain degree of approximation even for a non-sinusoidal deformation cycle. Accurate response for creep or relaxation is secondary.

In the previous sections it has been discussed how mechanical behavior changes with variations in strain and temperature. In that discussion the need arises to be able to change the loss modulus independent of the elastic and the mean (or static) modulus as the hysteresis work has a peak for a certain strain amplitude and deteriorates with temperature slightly faster than other moduli. This can be accomplished by nonlinear dashpots or by several linear interrelated dashpots and separate elastic elements. Both these approaches have been evaluated. The nonlinear viscous model can easily model behavior from pure friction to linear viscous response. However, when implemented numerically this approach involves iterative calculations. Thus, a model having several linear Maxwell elements is much more efficient from a computational standpoint. To ensure that the hysteresis only has one maximum, a model has been developed involving several elements that have the same elastic component but different interrelated relaxation times. This model has the properties of a single Maxwell model but with an extra degree of freedom which allows variation of the width of the hysteresis peak, and thus the slope of the elastic part of the response. This makes it possible to represent experimental data observed without undesired properties outside the frequency domain for which there are data available.

To represent properly the elastic response both statically and dynamically, two separate elastic models have to be included in parallel with the Maxwell models. The Maxwell models represent only the viscous component and the small frequency dependent component of the dynamic elastic response.

The static component is only modeled elastically. The dynamic elasticity is modeled using a function that is independent of frequency. For noncyclic loading or in the initial phase of cyclic loading this model yields hysteresis work. For the isotropic case, omitting the damage functions, we have:

$$s_{ij}^{I} = 2G^{Id}(e_{ij} - e_{ij}^{m}) \tag{4.38}$$

This formulation is rate independent and thus has some of the properties of the theory presented by Farris [17], which yields permanent hysteresis.

4.8 The complete constitutive equation

Combining the equations formulated above yields the following constitutive equations for the transversal isotropic case. (As discussed previously, stress, strain, and their time derivatives are in the corotational anisotropic material directions.)

The volumetric and deviatoric responses have been separated. For the volumetric change we have a pure elastic response:

$$\sigma_p = 3K\epsilon_p \tag{4.39}$$

For the deviatoric isotropic material response we obtain the following three contributions:

- Mean or static elasticity:

$$s_{ij}^{Im} = h_1^I g_1^I 2G^{Im} e_{ij} \quad \text{where} \tag{4.40}$$

$$e_{ij} = \int_0^t \dot{e}_{ij}\, d\tau \tag{4.41}$$

- Rate independent dynamic elasticity:

$$s_{ij}^{Id} = h_1^I g_1^I 2G^{Id} e_{ij}^o \quad \text{where} \tag{4.42}$$

$$e_{ij}^o = e_{ij} - \frac{1}{t}\int_0^t e_{ij}\, d\tau \tag{4.43}$$

- Hysteresis and rate dependent dynamic elasticity:

  Any number of Maxwell functions can be considered. Here five is used:

$$s_{ij}^1 + \tau_I \dot{s}_{ij}^1 = h_2^I g_2^I 2G^{Iv} \tau_I \dot{e}_{ij} \tag{4.44}$$

$$s_{ij}^2 + \tau_I k_I \dot{s}_{ij}^2 = h_2^I g_2^I 2G^{Iv} \tau_I k_I \dot{e}_{ij} \tag{4.45}$$

$$s_{ij}^3 + \tau_I (k_I)^{-1} \dot{s}_{ij}^3 = h_2^I g_2^I 2G^{Iv} \tau_I (k_I)^{-1} \dot{e}_{ij} \tag{4.46}$$

$$s_{ij}^4 + \tau_I (k_I)^2 \dot{s}_{ij}^4 = h_2^I g_2^I 2G^{Iv} \tau_I (k_I)^2 \dot{e}_{ij} \tag{4.47}$$

$$s_{ij}^5 + \tau_I (k_I)^{-2} \dot{s}_{ij}^5 = h_2^I g_2^I 2G^{Iv} \tau_I (k_I)^{-2} \dot{e}_{ij} \tag{4.48}$$

$$\text{where} \quad \tau_I = \frac{2\eta^I}{2G^{Iv}} \tag{4.49}$$

  The components are added:

$$s_{ij}^{Iv} = s_{ij}^1 + s_{ij}^2 + s_{ij}^2 + s_{ij}^4 + s_{ij}^5 \tag{4.50}$$

The total contribution from the isotropic part of the material response will, at every instant in time, be $s_{ij}^I = s_{ij}^{Im} + s_{ij}^{Id} + s_{ij}^{Iv}$. The scalar deviatoric strain that governs the increase in strain amplitude for the damage evolution equations will be, for all three cases, the second invariant $e_I^o = \sqrt{e_{ij}^o e_{ij}^o}$.

The materials studied here as examples are transversal isotropic and have at most two independent anisotropic contributions. One is the uniaxial response in the fiber direction and the other is the shear along the fiber direction. Assume that these are independent. The same method of developing the equations as for the isotropic case are used. Material direction 3 is the reinforced one. The following equations are obtained:

- Mean or static elasticity:

$$
\begin{aligned}
s_3^{Am} &= h_1^{A1} g_1^{A1} 2C_{33}'^{Am} e_3 && (4.51)\\
s_1^{Am} &= s_2^{Am} = -\frac{1}{2} s_3^{Am} && (4.52)\\
s_{13}^{Am} &= h_1^{A2} g_1^{A2} C_{44}'^{Am} \gamma_{13} && (4.53)\\
s_{23}^{Am} &= h_1^{A2} g_1^{A2} C_{44}'^{Am} \gamma_{23} && (4.54)\\
s_{12}^{Am} &= 0 && (4.55)
\end{aligned}
$$

- Rate independent dynamic elasticity:

$$
\begin{aligned}
s_3^{Ad} &= h_1^{A1} g_1^{A1} 2C_{33}'^{Ad} e_3^o && (4.56)\\
s_1^{Ad} &= s_2^{Ad} = -\frac{1}{2} s_3^{Ad} && (4.57)\\
s_{13}^{Ad} &= h_1^{A2} g_1^{A2} C_{44}'^{Ad} \gamma_{13}^o && (4.58)\\
s_{23}^{Ad} &= h_1^{A2} g_1^{A2} C_{44}'^{Ad} \gamma_{23}^o && (4.59)\\
s_{12}^{Ad} &= 0 && (4.60)\\
e_{ij}^o &= e_{ij} - \frac{1}{t} \int_0^t e_{ij}\, d\tau && (4.61)
\end{aligned}
$$

- Hysteresis and rate dependent dynamic elasticity:

  In material direction 33 we obtain:

$$
\begin{aligned}
s_3^1 + \tau_{A1} \dot{s}_3^1 &= h_2^{A1} g_2^{A1} 2C_{33}'^{Av} \tau_{A1} \dot{e}_3 && (4.62)\\
s_3^2 + \tau_{A1} k_{A1} \dot{s}_3^2 &= h_2^{A1} g_2^{A1} 2C_{33}'^{Av} \tau_{A1} k_{A1} \dot{e}_3 && (4.63)\\
s_3^3 + \tau_{A1} (k_{A1})^{-1} \dot{s}_3^3 &= h_2^{A1} g_2^{A1} 2C_{33}'^{Av} \tau_{A1} (k_{A1})^{-1} \dot{e}_3 && (4.64)\\
s_3^4 + \tau_{A1} (k_{A1})^{2} \dot{s}_3^4 &= h_2^{A1} g_2^{A1} 2C_{33}'^{Av} \tau_{A1} (k_{A1})^{2} \dot{e}_3 && (4.65)\\
s_3^5 + \tau_{A1} (k_{A1})^{-2} \dot{s}_3^5 &= h_2^{A1} g_2^{A1} 2C_{33}'^{Av} \tau_{A1} (k_{A1})^{-2} \dot{e}_3 && (4.66)\\
\text{where} \quad \tau_{A1} &= \frac{2\eta^{A1}}{2C_{33}'^{Av}} && (4.67)
\end{aligned}
$$

  These components are added and the responses in material directions 11 and 22 are calculated:

$$
\begin{aligned}
s_3^{Av} &= s_3^1 + s_3^2 + s_3^2 + s_3^4 + s_3^5 && (4.68)\\
s_1^{Av} &= s_2^{Av} = -\frac{1}{2} s_3^{Av} && (4.69)
\end{aligned}
$$

In material direction 13 we obtain:

$$\begin{aligned} s^1_{13} + \tau_{A2}\dot{s}^1_{13} &= h^{A2}_2 g^{A2}_2 C'^{Av}_{44} \tau_{A2}\dot{\gamma}_{13} && (4.70)\\ s^2_{13} + \tau_{A2}k_{A2}\dot{s}^2_{13} &= h^{A2}_2 g^{A2}_2 C'^{Av}_{44} \tau_{A2}k_{A2}\dot{\gamma}_{13} && (4.71)\\ s^3_{13} + \tau_{A2}(k_{A2})^{-1}\dot{s}^3_{13} &= h^{A2}_2 g^{A2}_2 C'^{Av}_{44} \tau_{A2}(k_{A2})^{-1}\dot{\gamma}_{13} && (4.72)\\ s^4_{13} + \tau_{A2}(k_{A2})^{2}\dot{s}^4_{13} &= h^{A2}_2 g^{A2}_2 C'^{Av}_{44} \tau_{A2}(k_{A2})^{2}\dot{\gamma}_{13} && (4.73)\\ s^5_{13} + \tau_{A2}(k_{A2})^{-2}\dot{s}^5_{13} &= h^{A2}_2 g^{A2}_2 C'^{Av}_{44} \tau_{A2}(k_{A2})^{-2}\dot{\gamma}_{13} && (4.74)\\ \text{where} \quad \tau_{A2} &= \frac{2\eta^{A2}}{2C'^{Av}_{44}} && (4.75) \end{aligned}$$

The components are added.

$$s^{Av}_{13} = s^1_{13} + s^2_{13} + s^2_{13} + s^4_{13} + s^5_{13} \tag{4.76}$$

The equations in direction 23 are identical with the ones above using the index 23 instead of 13. For the direction 12 there is no contribution, i.e. $s^{Av}_{12} = 0$.

The total contribution from the anisotropic part of the material response will, at every instant in time, be $s^A_{ij} = s^{Am}_{ij} + s^{Ad}_{ij} + s^{Av}_{ij}$. The scalar measure of strain used for the damage evolution is different for direction 33 and directions 13, 23. In orientation 33 we have,

$$e^o_{A1} = \sqrt{2e^o_{33}e^o_{33}} \tag{4.77}$$

and in orientation 13 and 23:

$$e^o_{A2} = \sqrt{2e^o_{33}e^o_{33} + 2e^o_{13}e^o_{13} + 2e^o_{23}e^o_{23}} \tag{4.78}$$

This means that damage due to uniaxial straining in the fiber direction will affect the shear modulus but not vice versa.

The total deviatoric stresses from all parts of the constitutive model are:

$$\begin{aligned} s_{11} &= s^I_{11} - \frac{1}{2}s^A_{33} && (4.79)\\ s_{22} &= s^I_{22} - \frac{1}{2}s^A_{33} && (4.80)\\ s_{33} &= s^I_{33} + s^A_{33} && (4.81)\\ s_{13} &= s^I_{13} + s^A_{13} && (4.82)\\ s_{23} &= s^I_{23} + s^A_{23} && (4.83)\\ s_{12} &= s^I_{12} && (4.84) \end{aligned}$$

This algorithm includes effects of anisotropy, damage, temperature, and hysteresis.

The complete set of material constants for the transversal isotropic case to which numerical values should be determined, is:

Volumetric response.

- Elastic response. K Bulk modulus (Pa)

Deviatoric response.

- Mean or static elasticity:

G^{Im}	Isotropic modulus (Pa)
β_1^I, α_1^I, μ_I	Isotropic strain damage constants (-)
c_1^I	Isotropic temperature constant ($^\circ\mathrm{C}^{-1}$)
C'^{Am}_{33}, C'^{Am}_{44}	Anisotropic moduli (Pa)
β_1^{A1}, α_1^{A1}, μ_{A1}, β_1^{A2}, α_1^{A2}, μ_{A2}	Anisotropic strain damage constants (-)
c_1^{A1}, c_1^{A2}	Anisotropic temperature constants ($^\circ\mathrm{C}^{-1}$)

- Rate independent dynamic elasticity:

G^{Id}	Isotropic modulus (Pa)
C'^{Ad}_{33}, C'^{Ad}_{44}	Anisotropic moduli (Pa)

- Viscous response and rate dependent dynamic elasticity:

G^{Iv}	Isotropic modulus (Pa)
τ_I	Isotropic relaxation time (s)
k_I	Isotropic relaxation time constant (-)
β_2^I, α_2^I	Isotropic strain damage constants (-)
c_2^I	Isotropic temperature constant ($^\circ\mathrm{C}^{-1}$)
C'^{Av}_{33}, C'^{Av}_{44}	Anisotropic moduli (Pa)
τ_{A1}, τ_{A2}	Anisotropic relaxation times (s)
k_{A1}, k_{A2}	Anisotropic relaxation time constant (-)
β_2^{A1}, α_2^{A1}, β_2^{A2}, α_2^{A2}	Anisotropic strain damage constants (-)
c_2^{A1}, c_2^{A2}	Anisotropic temperature constants ($^\circ\mathrm{C}^{-1}$)

- Evolution of strain damage:

C_d	Damage evolution constant (-)

In the most complex form all constants will have different values. However, the model can also represent very simple material descriptions such as isotropic elasticity by setting most of the parameters to zero.

When fitting to test data, no more complex material description than necessary should be introduced in order to describe the material characteristics with acceptable accuracy.

5
Fatigue of elastomer composites

Constitutive models for elastomer composites are used in analysis and design of machine elements built of such materials. For V-belts and other types of belts it is of interest to be able to predict the fatigue life for different designs and materials.

Today, the only fatigue data available is in the form of data for complete V-belts and not the material itself [20]. This means that the V-belt has to be modeled and analyzed simulating a running V-belt drive under various driving conditions. The stress and strain state as well as other variables of interest can be studied and correlation to failure modes and fatigue life can be determined.

From experimental investigations it is known how V-belt fatigue develops, i.e. where the damage occurs and how it develops for different working conditions [20]. Three major failure modes have been identified. In the elastomer material cracks propagate and different material layers separate. Thus, it is possible to study a certain part of the belt which is related to a specific failure mode and calculate stresses, strains, etc. for a running belt.

To follow a crack when it propagates involves a great amount of computation. However, instead of studying the 100 percent damage level one can choose another level of damage, for instance 1 percent or lower, and thus reduce the calculations. This does not reduce the usefulness of the method to design V-belts. It is also in agreement with the concept of material damage which is said to develop before cracks are observed.

When calculating variables to be correlated to fatigue life for different failure mechanisms, several approaches can be evaluated. As fatigue data exists only for real applications it cannot be deduced in this report which approach is the best, but the following methods are suggested and can be evaluated separately or in combination.

- Cracks only develop for tensile stress normal to the crack orientation or for shear stress in the plane of the crack. As the probable location and orientation of the cracks for each failure mode are known, those tensile stresses and shear stresses could be studied and some algorithm for fatigue life prediction based on those stresses could be developed.

- The material damage concept has so far only been used for changes in the mechanical material properties, but its original use was for fatigue life prediction.

The assumption was that a crack was preceded by microdamage which reflected the level of the damage parameter. We have already calculated damage parameters both for damage due to strain and for temperature. It is well known that the fatigue life for this kind of material is very sensitive to the temperature level. The damage parameters already developed can be used or new ones can be defined. The area of interest or the whole belt section can be studied for each failure mode and correlated to fatigue life.

- The rate of the crack growth is related to the amount of strain energy released during the process. The areas of interest and different measures of energy can be studied, such as the total energy provided by the implementation of the constitutive model. The J-integral can be calculated if the used FEM-software offers that possibility.

The best method will be evaluated by correlating to existing experimental data. The material constants that represent the fatigue properties of the materials used can be calculated. It is then possible to predict fatigue life for different new V-belt designs and other loading conditions with no new experiments. If new materials or new methods of joining different materials are of interest, then the fatigue properties of the materials and production methods should be tested in special experiments. Fatigue properties are material data, and result from production methods and not V-belt properties. Thus, extensive V-belt fatigue testing can be avoided.

It can be observed that everything discussed above is based on the assumption that stresses and strains can be calculated accurately enough. This means that a proper constitutive model is necessary.

6
Correlation to experiments

6.1 Fitting to the test data

When comparing a constitutive model to experimental data, data from a few of all possible strain and stress histories are used. To increase the ability of the constitutive model to give realistic response, data from experiments that have the same characteristics as the application should be used. Also, there should be an overdetermined system of equations. This can be accomplished by many independent tests combined with tests in different material orientations. If the model describes the material correctly the same values for the material constants of the constitutive model are obtained for the different tests.

The following scheme has been used to determine the material constants in the constitutive model. Each type of load case is discussed in detail in the ensuing sections.

- Guess start values for the parameters in the constitutive model.
- Calculate static modulus, dynamic elastic modulus, and dynamic loss modulus for each individual test case. This is done both using the experimental data and using the response of the constitutive model with the same strain history. Input data are orientation and type of test, forces per unit area, deformations per unit length, frequency, loss energy per cycle, and temperature.
- The relative error is calculated for each modulus defined above and also the average relative error for one test data point.
- A new set of values for the material constants are calculated using a steepest gradient optimization technique. The total sum of the square relative error is minimized.

This scheme is repeated until a global minimum is found. Using nonlinear regression or optimization techniques is not as straightforward as the linear regression case. There are no guarantees that a global minimum will be found directly. Experience from this study shows that the best method is to perform several suboptimizations

locking some variables each time, i.e. analyzing a certain aspect of the material response separately. Finally, a global optimization can be performed.

When calculating the response for a certain test case we have to simulate a sinusoidal deformation cycle superimposed on a static deformation. This calculation/integration can be done numerically. However, since we have a linear viscoelastic model and a sinusoidal deformation, it can be accomplished analytically using complex forms. Both methods have been implemented. The numerical approach has no restrictions on the type of function used. However, the other method is between 100 and 1000 times faster computationally, and is therefore used. The numerical method was mainly used to study different types of constitutive equations and damage evolution.

6.2 Dilatation or volume compression

The actual material is nearly incompressible. The bulk modulus is about three orders of magnitude greater than the shear modulus. The constitutive theory suggests that the modulus is counted as pure elastic and not subjected to damage due to strain or temperature. Thus, the bulk modulus can be obtained directly from the experiments [22].

6.3 Uniaxial compression

The logarithmic strain, which is equal to the integral of rate of deformation for the uniaxial case, and Kirchoff stress are calculated using the approximation that the volume is constant. This approximation is valid for nearly incompressible material in uniaxial deformation. Assuming that orientation 3 is the loaded direction we have:

$$\begin{aligned}
\sigma_3 &= \frac{F}{A} = \frac{F}{A_0}\left(1 + \frac{u(t)}{L_0}\right) && (6.1)\\
\sigma_1 &= \sigma_2 = 0 && (6.2)\\
s_3 &= \frac{2}{3}\sigma_3 && (6.3)\\
s_1 &= s_2 = -\frac{1}{3}\sigma_3 && (6.4)\\
e_1 &= \epsilon_1 && (6.5)\\
e_2 &= \epsilon_2 && (6.6)\\
e_3 &= \epsilon_3 = \ln\left(1 + \frac{u(t)}{L_0}\right) && (6.7)\\
e_1 + e_2 + e_3 &= 0 && (6.8)
\end{aligned}$$

where $u(t)$ is the displacement in direction 3.

The static or mean modulus is defined as the mean level of stress divided by the mean strain:

$$E_m = \frac{(\sigma_3^{max} + \sigma_3^{min})/2}{(\epsilon_3^{max} + \epsilon_3^{min})/2} \qquad (6.9)$$

The dynamic elastic modulus and the loss modulus are defined as the real and the imaginary parts of the complex stress amplitude divided by the complex strain amplitude:

$$E_d = Re\left(\frac{\sigma_3^*}{\epsilon_3^*}\right) \tag{6.10}$$

$$E_l = Im\left(\frac{\sigma_3^*}{\epsilon_3^*}\right) \tag{6.11}$$

The procedure is analogous to the cases with deformation in orientation 1 or 2. However, the strain state in the non-loaded material directions has to be solved by iterative calculations due to anisotropy. If loaded in direction 2, we have $s_1^* = s_3^* = -\frac{1}{2}s_2^*$ which gives the strains e_1^* and e_3^*, knowing e_2^*.

6.4 Simple shear

Simple shear involves rotation as well as shear strain. This test case is often referred to in the literature and has been solved both analytically and numerically.

In our case the shear strain is always less than 0.1. For this case the following approximations to the corotational shear strain and stress are acceptable, and are therefore used here. Below we present these for shear in material direction 12. This is analogous to straining in orientations 13 and 23.

$$\sigma_{12} = \frac{F}{A_0} \tag{6.12}$$

$$\gamma_{12} = \frac{u(t)}{L_0} \tag{6.13}$$

Displacement $u(t)$ is in direction 2 and length L_0 in direction 1. As shear involves no volume change there are no differences between deviatoric components and the total strain and stress.

The static modulus, the dynamic elastic modulus, and the dynamic loss modulus are calculated analogous to the uniaxial case.

6.5 Discussion and results

The constitutive material constants have been evaluated for two different elastomer composites. The first, which is labeled material 1 in reference [22], is heavily reinforced, using about 20 percent fibers. For this material, data from 137 individual tests were used. This incorporates a wide range of variations in temperature, deformation amplitude, and frequency. Each test yielded three different moduli as discussed in the previous sections. Thus, a total of 411 data values were used when calculating the material constants of the constitutive model. An average relative error of 16 percent was obtained when comparing the response from the constitutive model and test data. Nearly the whole error is accounted for by the fact that the plane orthogonal to the

fiber direction is found to be slightly orthotropic and not isotropic as assumed using the transversal isotropic constitutive model. Tests in orientation 11 and 22 yielded the same result but the shear tests in orientation 12 gave lower values than expected of an isotropic model. More complex forms of anisotropy can be evaluated. There are no limitations in the theoretical framework of the constitutive model to only transversal isotropy. However, the deviation from isotropy can probably be explained by the fact that the test material is built up of three layers of material to obtain the thickness needed to cut test samples. In a real belt there are normally fewer layers, depending on the belt type. The material will also be deformed in the plane orthogonal to the fibers, as a cog shape is often used. These facts predict that the orthotropy will be less pronounced, and may be difficult to identify in a real belt. Moreover, the observed anisotropy, in the plane that was assumed to be isotropic, is very small compared to the anisotropy in the reinforced material direction. The label transversal isotropy is therefore a good description of this material.

The second material is labeled material 2 in the experimental investigation. It has a very small amount of short fibers. They are not as well oriented in one direction (for this material direction 22) as in the case for material 1. Therefore the material has less anisotropy. It is only about 20 percent stiffer in orientation 22 than in orientation 33. This material is used in a very thin layer (0.5 mm) surrounding the cord. To build test samples 30 layers were used, and an orthotropy is thus obtained which is not present in a single layer. This latter anisotropy is difficult to separate from the anisotropy caused by the fibers because the two different anisotropies are of the same order of magnitude for this material, as opposed to the previous case. However, following the strategy developed, we do not introduce a more complex material description than is necessary. The anisotropy is slight and therefore we use an isotropic model and accept larger errors when correlating to test data. The number of data values used was 354. The average relative error was 21 percent when correlating to the isotropic model.

7

Numerical implementation of the constitutive model

7.1 Implementation and integration within FEM-software

If more complex problems than can be analyzed using analytical methods are to be studied, the constitutive model has to be implemented within a tool that allows for general stress and strain analysis. Here the FEM-program Abaqus is used [2, 1]. It is a general FEM-software with emphasis on nonlinear analysis.

Stress analysis contains three sources of non-linearity:

- Material non-linearity. The constitutive model discussed in previous chapters is non-linear.
- Geometric non-linearity. We have large rotations and strains.
- Boundary non-linearity. If the friction contact of a belt and a pulley are to be studied we have a boundary non-linearity.

The program allows for a user-provided subroutine to define material behavior. The strain type is integrated rate of deformation and the stress type is Kirchoff stress, which form a work conjugate pair. However, Cauchy stress is used in postprocessing. The conjugate stress and strain pair is given in a corotational coordinate system, which means that anisotropy can be introduced. The Hughes-Winget operator is employed for the integration of strain and rotation [31] .

The main disadvantage of this rate formulation is the residual error in the strain, due to the approximate integration.

The constitutive model is implemented using the backward difference operator which is unconditionally stable. The four main parts of the constitutive model discussed in the previous chapters are implemented separately. Solution dependent variables are only updated after the final iteration during an increment. Examples are the stress tensors from different parts of the constitutive model, the mean deviatoric strain

tensor, and the variables governing the evolution of the anisotropic damage. The procedure returns the Kirchoff stress at the end of the increment and also the matrix of partial derivatives of the stress with respect to the strain. This matrix $\frac{\partial \sigma_i}{\partial \epsilon_j}$, called the Jacobian matrix of the constitutive model, must be defined accurately if rapid convergence of the overall Newton scheme is desired. In most cases the accuracy of this definition is the most important factor governing the convergence rate [2].

The numerical implementation of the constitutive model is tested both in simulations outside Abaqus and in tests using Abaqus. The result is verified against the analytical implementation used to calculate the constitutive material constants, and also the original experimental data.

7.2 Some test cases

In Figures 7.1, 7.2, 7.3, 7.4, and 7.5 some test cases are presented for material 1 which is the one of the two materials with the most pronounced anisotropy. First, there are four cases of cyclic deformation with the mean deformation level equal to minus one deformation amplitude. Ten deformation cycles are calculated in each case. In all cases the model consists of one C3D8 (8 node, linear displacement, 8 integration points) element.

Secondly, we have a case with an interrupted ramp function.

These were just a few cases. However, the damage and viscous characteristics of the material can easily be observed. For a discussion of the material properties in detail we refer to the experimental investigation [22].

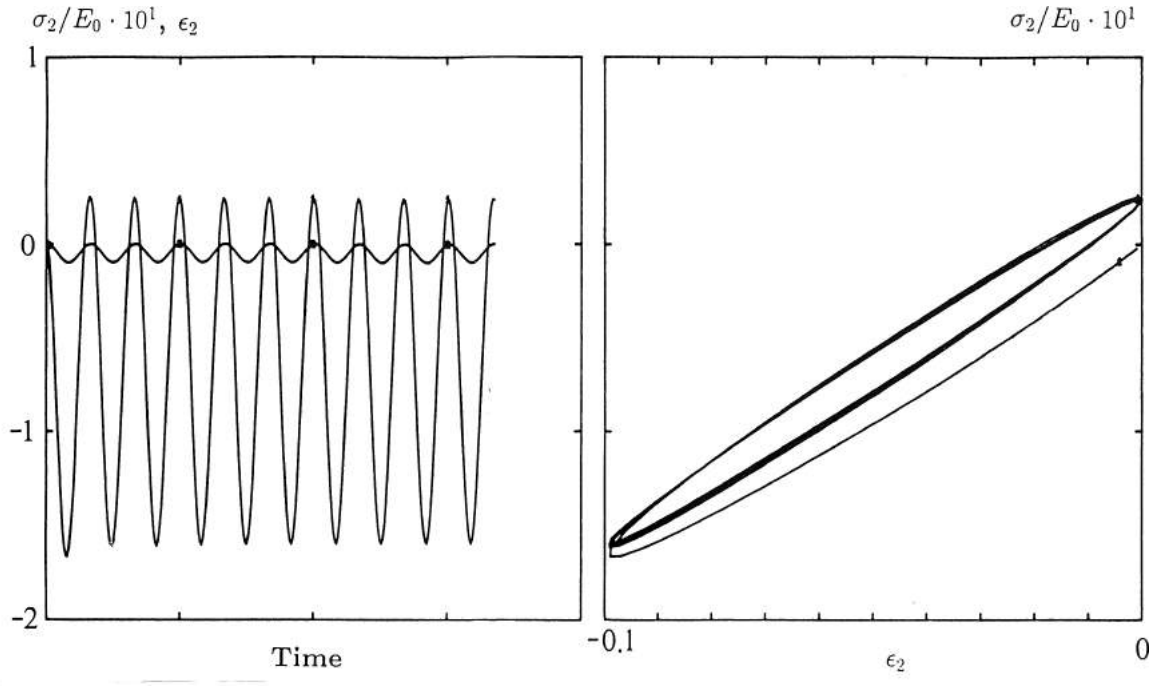

Figure 7.1 *Uniaxial deformation in orientation 22. The relative displacement amplitude is 0.0472, the frequency of deformation is 2.98 Hz, and the temperature is* $43.3°C$.

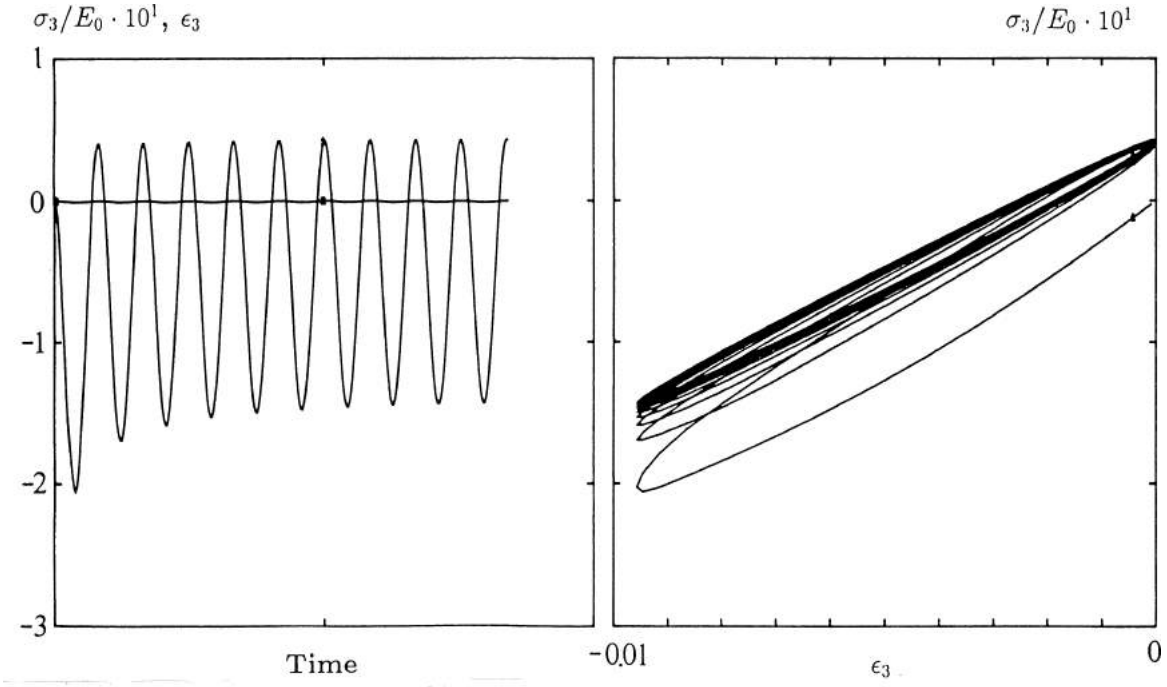

Figure 7.2 *Uniaxial deformation in orientation 33. The relative displacement amplitude is 0.00476, the frequency of deformation is 59.5 Hz, and the temperature is* $36.1°C$.

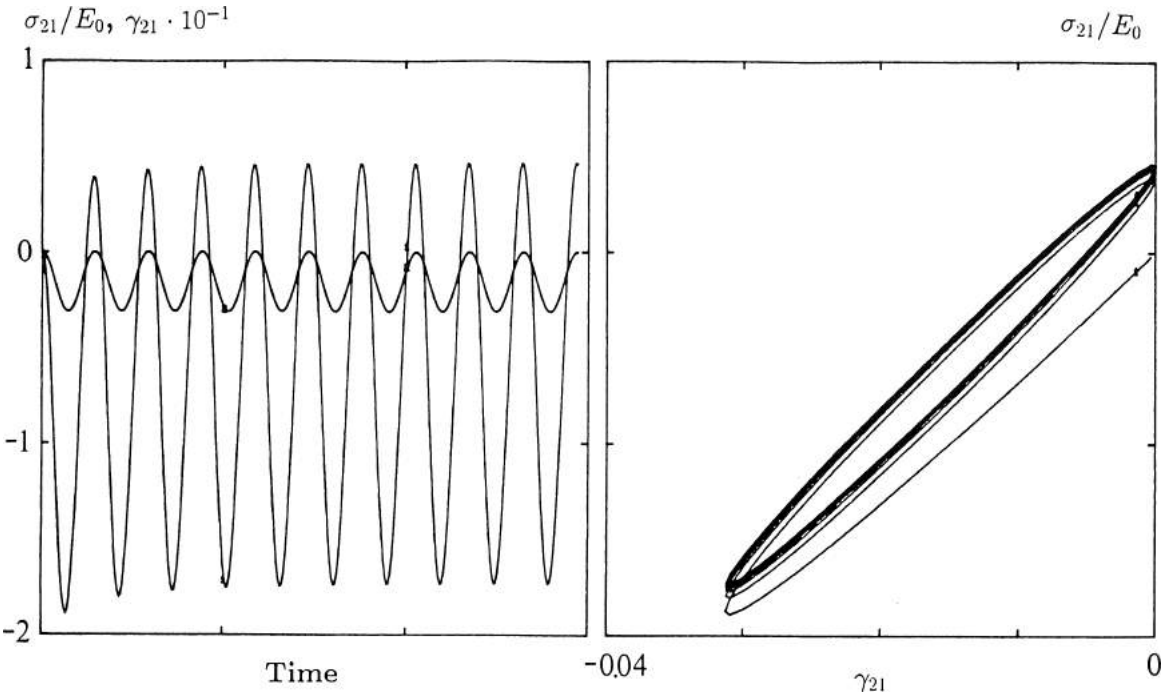

Figure 7.3 *Simple shear deformation in orientation 21. The relative displacement amplitude is 0.0156, the frequency of deformation is 34.0 Hz, and the temperature is* $27.2°C$.

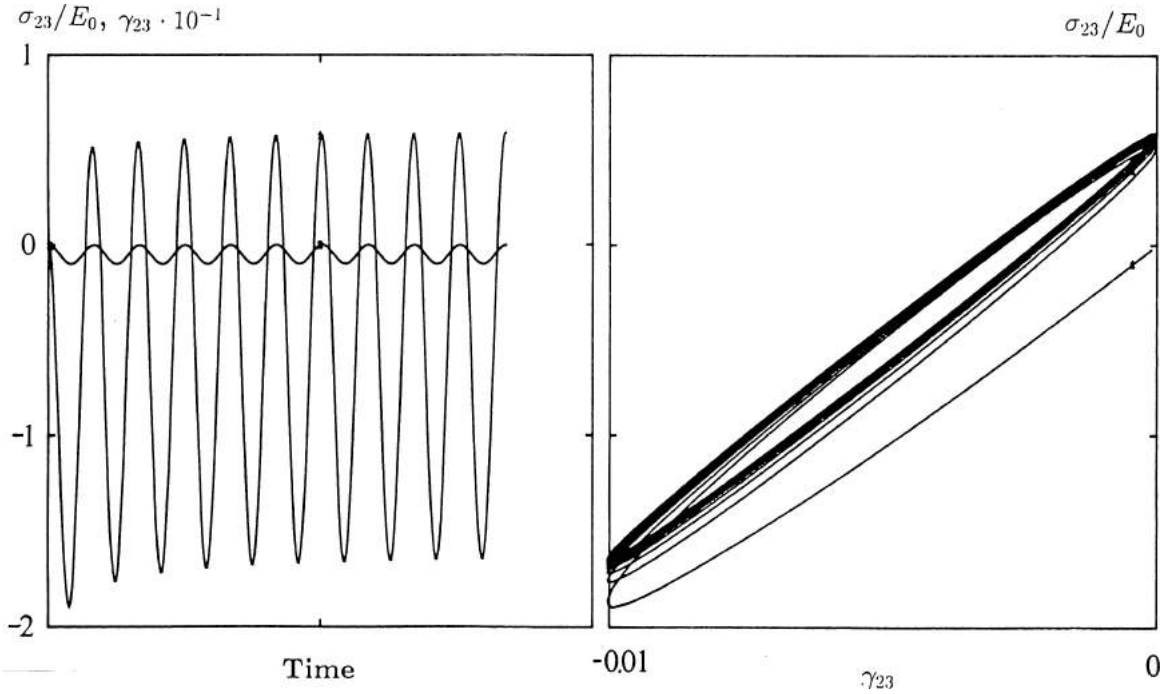

Figure 7.4 *Simple shear deformation in orientation 23. The relative displacement amplitude is 0.00502, the frequency of deformation is 59.4 Hz, and the temperature is* $25.0°C$.

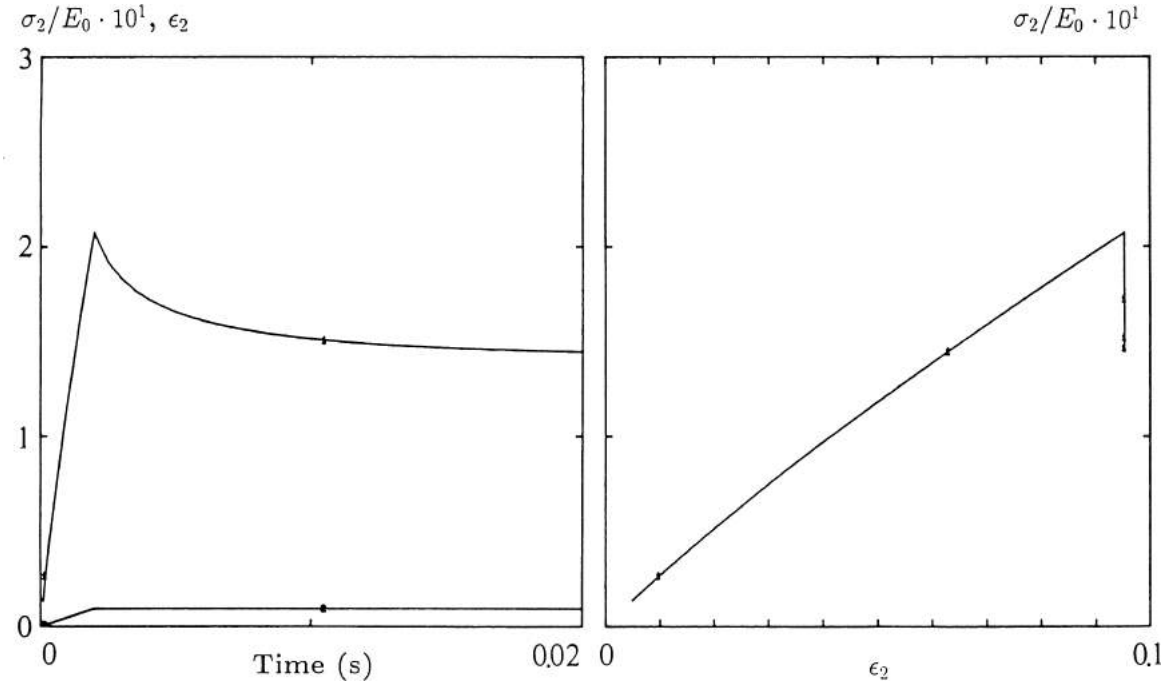

Figure 7.5 *Uniaxial deformation in orientation 22. Interrupted ramp function with a deformation rate of* $5.00(s^{-1})$ *. The strain level reached is* $\ln 1.1 = 0.0953$ *which corresponds to a relative displacement of* 0.1. *The temperature is* $30.0°C$.

8
Conclusions

A fully three-dimensional finite strain constitutive model has been developed, characterized by:

- Anisotropic elasticity, anisotropic rate independent dynamic elasticity, and anisotropic viscoelastic response.
- Uncoupled bulk and deviatoric response.
- Decomposition of the deviatoric response into isotropic and anisotropic parts.
- Separable anisotropic damage mechanisms for mechanical degradation and temperature degradation. The mechanical damage is irreversible, while the temperature damage is reversible.
- Separable damage mechanisms for the elastic response and the viscous (hysteresis) response.

The constitutive model can be employed in both rate formulations and total formulations, providing a corotational coordinate system is defined in the anisotropic material directions.

The constitutive theory is evaluated against experimental material data for two elastomer composites used in V-belt applications [22]. These materials can be described as transversal isotropic, and the values of the constitutive material constants are determined.

The constitutive model has been implemented into the FEM-software ABAQUS. Thus, it is now possible to do general stress and strain analysis of machine elements designed of elastomer composites. Examples are different types of belts.

A

Notation and basic concepts

A.1 Introduction

The basic concepts of continuum mechanics, including strain and stress, are given below, following the exposition in [1]. This is for the benefit of those who do not normally use such concepts. For further reading we refer to [56, 25, 23, 47, 30] or other well-known standard publications in this field.

This text is intended to be read by people who work with solving engineering problems using elastomer composites.

A.2 Definitions

The notation used here is both the *direct matrix notation* of vectors and tensors, and the *vector-dyadic notation*. Therefore, the basic quantities and some formulas are given in both notations below. The orthonormal right rectangular Cartesian coordinate system is used.

A vector or first order tensor $\vec{\boldsymbol{a}}$ means:

$$a_i\hat{\mathbf{e}}_i = a_1\hat{\mathbf{e}}_1 + a_2\hat{\mathbf{e}}_2 + a_3\hat{\mathbf{e}}_3 \quad \text{or} \quad a_i \quad \text{or} \quad \begin{bmatrix} a_1 \\ a_2 \\ a_3 \end{bmatrix} \tag{A.1}$$

where $\hat{\mathbf{e}}_i$ are orthonormal base vectors.

A dyadic may be considered as a second order tensor or matrix. The dyadic $\boldsymbol{a}$ is

$$a_{ij}\hat{\mathbf{e}}_i\hat{\mathbf{e}}_j \quad \text{or} \quad a_{ij} \quad \text{or} \quad \begin{bmatrix} a_{11} & a_{12} & a_{13} \\ a_{21} & a_{22} & a_{23} \\ a_{31} & a_{32} & a_{33} \end{bmatrix} \tag{A.2}$$

A fourth order tensor $\underline{\boldsymbol{a}}$ is most easily represented in tensor notation.

$$a_{ijkl} \tag{A.3}$$

The scalar product or dot product of two vectors $\vec{\boldsymbol{a}}$ and $\vec{\boldsymbol{b}}$ can be written in direct matrix notation as:

$$\begin{aligned}\lambda &= \vec{\boldsymbol{a}}^T \cdot \vec{\boldsymbol{b}} = [a_1, a_2, a_3] \begin{bmatrix} b_1 \\ b_2 \\ b_3 \end{bmatrix} = \vec{\boldsymbol{b}}^T \cdot \vec{\boldsymbol{a}} = [b_1, b_2, b_3] \begin{bmatrix} a_1 \\ a_2 \\ a_3 \end{bmatrix} = \\ & a_1 b_1 + a_2 b_2 + a_3 b_3 \end{aligned} \tag{A.4}$$

and in vector notation and tensor notation as:

$$\begin{aligned}\lambda &= \vec{\boldsymbol{a}} \cdot \vec{\boldsymbol{b}} = \vec{\boldsymbol{b}} \cdot \vec{\boldsymbol{a}} \\ \lambda &= a_i b_i = b_i a_i \end{aligned} \tag{A.5}$$

Here λ is a scalar and the superscript ^{T} means transpose. The tensor product of two vectors $\vec{\boldsymbol{a}}$ and $\vec{\boldsymbol{b}}$ can be written in direct matrix notation as:

$$\boldsymbol{A} = \vec{\boldsymbol{a}} \cdot \vec{\boldsymbol{b}}^T = \begin{bmatrix} a_1 \\ a_2 \\ a_3 \end{bmatrix} [b_1, b_2, b_3] = \begin{bmatrix} a_1 b_1 & a_1 b_2 & a_1 b_3 \\ a_2 b_1 & a_2 b_2 & a_2 b_3 \\ a_3 b_1 & a_3 b_2 & a_3 b_3 \end{bmatrix} \tag{A.6}$$

and in vector-dyadic notation and tensor notation as:

$$\boldsymbol{A} = \vec{\boldsymbol{a}}\vec{\boldsymbol{b}} = a_i b_j \hat{\mathbf{e}}_i \hat{\mathbf{e}}_j \qquad A_{ij} = a_i b_j \tag{A.7}$$

The vector-dyadic dot product of $\vec{\boldsymbol{a}}$ and $\boldsymbol{B}$ can be written in direct matrix notation as:

$$\begin{aligned}\vec{\boldsymbol{b}} &= \vec{\boldsymbol{a}}^T \cdot \boldsymbol{B} = [a_1, a_2, a_3] \begin{bmatrix} B_{11} & B_{12} & B_{13} \\ B_{21} & B_{22} & B_{23} \\ B_{31} & B_{32} & B_{33} \end{bmatrix} = \\ & a_1 B_{11} + a_2 B_{21} + a_3 B_{31} + a_1 B_{12} + a_2 B_{22} + a_3 B_{32} + a_1 B_{13} + a_2 B_{23} + a_3 B_{33} \end{aligned} \tag{A.8}$$

and in vector-dyadic notation and tensor notation as:

$$\vec{\boldsymbol{b}} = \vec{\boldsymbol{a}}\boldsymbol{B} = a_i B_{ij} \hat{\mathbf{e}}_j \qquad b_j = a_i B_{ij} \tag{A.9}$$

The dyadic-vector dot product of $\boldsymbol{B}$ and $\vec{\boldsymbol{a}}$ can be written in direct matrix notation as:

$$\begin{aligned}\vec{\boldsymbol{b}} = \boldsymbol{B} \cdot \vec{\boldsymbol{a}} &= \begin{bmatrix} B_{11} & B_{12} & B_{13} \\ B_{21} & B_{22} & B_{23} \\ B_{31} & B_{32} & B_{33} \end{bmatrix} [a_1, a_2, a_3] = \\ & \begin{bmatrix} a_1 B_{11} + a_2 B_{12} + a_3 B_{13} \\ a_1 B_{21} + a_2 B_{22} + a_3 B_{23} \\ a_1 B_{31} + a_2 B_{32} + a_3 B_{33} \end{bmatrix} \end{aligned} \tag{A.10}$$

and in vector-dyadic notation and tensor notation as:

$$\vec{\boldsymbol{b}} = \boldsymbol{B}\vec{\boldsymbol{a}} = B_{ij} a_j \hat{\mathbf{e}}_i \qquad b_i = B_{ij} a_j \tag{A.11}$$

The dot product of two second-order tensors $\boldsymbol{A}$ and $\boldsymbol{B}$ results in a second-order tensor and is given by

$$\boldsymbol{A} \cdot \boldsymbol{B} \quad \text{or} \quad A_{ij}B_{jk} \quad \text{or} \quad \begin{bmatrix} A_{11} & A_{12} & A_{13} \\ A_{21} & A_{22} & A_{23} \\ A_{31} & A_{32} & A_{33} \end{bmatrix} \begin{bmatrix} B_{11} & B_{12} & B_{13} \\ B_{21} & B_{22} & B_{23} \\ B_{31} & B_{32} & B_{33} \end{bmatrix} \tag{A.12}$$

while the trace of this product is represented as

$$\boldsymbol{A} : \boldsymbol{B} \quad \text{or} \quad A_{ij}B_{ij} \tag{A.13}$$

which is the contradiction of a second order tensor $\boldsymbol{B}$ with a second order tensor $\boldsymbol{A}$.

The contradiction of a second order tensor $\boldsymbol{B}$ with a fourth order tensor $\underline{\boldsymbol{A}}$ is given by

$$\underline{\boldsymbol{A}} : \boldsymbol{B} \quad \text{or} \quad A_{ijkl}B_{kl} \tag{A.14}$$

The partial derivatives defined as

$$\frac{\partial \vec{\boldsymbol{a}}}{\partial \vec{\boldsymbol{b}}} \quad \text{or} \quad \frac{\partial a_i}{\partial b_j} \tag{A.15}$$

can be thought of as a matrix of derivatives.

$$\begin{bmatrix} \frac{\partial a_1}{\partial b_1} & \frac{\partial a_1}{\partial b_2} & \frac{\partial a_1}{\partial b_3} \\ \frac{\partial a_2}{\partial b_1} & \frac{\partial a_2}{\partial b_2} & \frac{\partial a_2}{\partial b_3} \\ \frac{\partial a_3}{\partial b_1} & \frac{\partial a_3}{\partial b_2} & \frac{\partial a_3}{\partial b_3} \end{bmatrix} \tag{A.16}$$

The differential operator $\nabla_{\vec{\boldsymbol{b}}}$ applied from the right yields the same result. Here, the operator can be represented by the vector

$$\nabla_{\vec{\boldsymbol{b}}} = \hat{\mathbf{e}}_i \frac{\partial}{\partial \vec{\boldsymbol{b}}} \tag{A.17}$$

and the matrix is obtained by the tensor product

$$\vec{\boldsymbol{a}} \nabla_{\vec{\boldsymbol{b}}} \quad \text{or} \quad \begin{bmatrix} a_1 \\ a_2 \\ a_3 \end{bmatrix} \begin{bmatrix} \frac{\partial}{\partial b_1} & \frac{\partial}{\partial b_2} & \frac{\partial}{\partial b_3} \end{bmatrix} \tag{A.18}$$

which results in the same matrix of derivatives as above. The transponate of the matrix is obtained by applying the operator from the left $\nabla_{\vec{\boldsymbol{b}}} \vec{\boldsymbol{a}}$. In the notation, two special cases using the operator are defined. No subscript means derivative with respect to *spatial coordinates* $\vec{\boldsymbol{x}}$ and the subscript 0 means derivative with respect to *material coordinates* $\vec{\boldsymbol{X}}$. For the definitions, see Section A.3. Time derivatives are material time derivatives, i.e. the change in a variable with respect to time whilst looking at a particular material particle, unless otherwise explicitly stated.

A.3 Deformation and strain

A.3.1 Definitions, deformation and flow concepts

In the kinematics of continua, it must be clearly understood whether one is referring to a "point" in space or to a "point" of a continuum. Here, *point* is used exclusively to designate a location in fixed space. *Particle* denotes a small volumetric element, or *material point*, of a continuum.

At any instant of time t, a continuum which has a volume V and a bounding surface S occupies a certain region R of the physical space. The identification of the particles of the continuum with the points of the space it occupies at time t by referring to a suitable set of coordinate axes is the *configuration* of the continuum at that instant.

The term *deformation* refers to a change in shape of the continuum between some initial (undeformed) configuration and a subsequent (deformed) configuration. No attention is paid to the intermediate configurations or to the particular sequence of configurations by which the deformation occurs. By contrast, the word *flow* is used to designate the continuing state of motion of a continuum. A configuration history is inherent in flow investigations for which the specification of a time-dependent field is given.

A.3.2 Position vector, displacement vector

In a structural problem the initial configuration at time $t = 0$ of a structure and its deformed configuration at a later time t , has to be described. Accordingly, in the initial configuration a representative particle of the continuum occupies a point P_0 in space and has the *position vector*

$$\vec{\boldsymbol{X}} = X_1\hat{\mathbf{I}}_1 + X_2\hat{\mathbf{I}}_2 + X_3\hat{\mathbf{I}}_3 = X_K\hat{\mathbf{I}}_K \tag{A.19}$$

with respect to the rectangular Cartesian axes $OX_1X_2X_3$. The coordinates are called *material coordinates* and upper case subscripts or superscripts are used to indicate this. In the deformed configuration the particle has moved to a position P and has the position vector

$$\vec{\boldsymbol{x}} = x_1\hat{\mathbf{e}}_1 + x_2\hat{\mathbf{e}}_2 + x_3\hat{\mathbf{e}}_3 = x_K\hat{\mathbf{e}}_K \tag{A.20}$$

with respect to the rectangular Cartesian axes $ox_1x_2x_3$. The coordinates are called *spatial coordinates* and lower case subscripts or superscripts are used to indicate this.

The relative orientation of the material axes and the spatial axes obeys the law of transformation of first-order Cartesian tensors. However, it is very common in continuum mechanics that the two coordinate systems are *superimposed*. This is assumed implicitly in the other sections of this text if not stated otherwise. Then there is no difference between upper and lower case indices. If the upper case indices are still used they serve as labels to indicate the connection to material coordinates.

The *displacement vector* is then defined as.

$$\vec{\boldsymbol{u}} = \vec{\boldsymbol{x}} - \vec{\boldsymbol{X}} \tag{A.21}$$

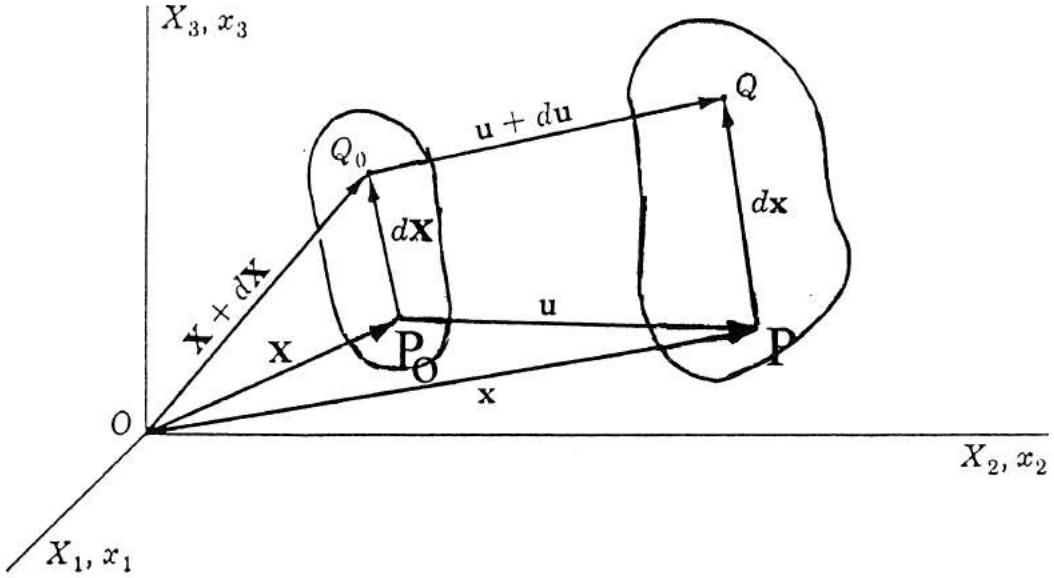

Figure A.1 *The initial and the final configurations of a continuum, referred to in the superimposed Cartesian coordinate axes for material coordinates and spatial coordinates. The two neighboring particles which occupy points P_o and Q_o before deformation, move to points P and Q respectively in the deformed configuration.*

When a continuum undergoes deformation or flow, the particles of the continuum move along various paths in space. Assume that $\vec{\boldsymbol{x}}$ contains single-valued functions of $\vec{\boldsymbol{X}}$ and t which are continuously differentiable as many times as necessary. Then

$$\vec{\boldsymbol{x}} = \vec{\boldsymbol{x}}(\vec{\boldsymbol{X}}, t) \tag{A.22}$$

which gives the present location $\vec{\boldsymbol{x}}$ of a particle that occupied the point $\vec{\boldsymbol{X}}$ at time $t = 0$, i.e. a mapping of the initial configuration into the current configuration. This description is known as the *Lagrangian* formulation. If the *Jacobian*

$$J = det\left(\frac{\partial x_i}{\partial X_j}\right) > 0 \tag{A.23}$$

then the inverse mapping exists, assuming the same conditions as above.

$$\vec{\boldsymbol{X}} = \vec{\boldsymbol{X}}(\vec{\boldsymbol{x}}, t) \tag{A.24}$$

This description is known as the *Eulerian* description.

A.3.3 Deformation gradients, displacement gradients

Consider two neighboring particles, located at $\vec{\boldsymbol{X}}$ and $\vec{\boldsymbol{X}} + d\vec{\boldsymbol{X}}$ in the reference configuration, which are $\vec{\boldsymbol{x}}$ and $\vec{\boldsymbol{x}} + d\vec{\boldsymbol{x}}$ in the current configuration.

Since $d\vec{\boldsymbol{X}}$ and $d\vec{\boldsymbol{x}}$ refer to the same two material points, we can write.

$$d\vec{\boldsymbol{x}} = \frac{\partial \vec{\boldsymbol{x}}}{\partial \vec{\boldsymbol{X}}} \cdot d\vec{\boldsymbol{X}} \quad \text{where} \quad \boldsymbol{F} = \frac{\partial \vec{\boldsymbol{x}}}{\partial \vec{\boldsymbol{X}}} = \vec{\boldsymbol{x}}\nabla_0 \tag{A.25}$$

$$d\vec{\boldsymbol{X}} = \frac{\partial \vec{\boldsymbol{X}}}{\partial \vec{\boldsymbol{x}}} \cdot d\vec{\boldsymbol{x}} \quad \text{where} \quad \boldsymbol{H} = \frac{\partial \vec{\boldsymbol{X}}}{\partial \vec{\boldsymbol{x}}} = \vec{\boldsymbol{X}} \nabla \tag{A.26}$$

$$d\vec{\boldsymbol{x}} = \boldsymbol{F} \cdot d\vec{\boldsymbol{X}} \qquad d\vec{\boldsymbol{X}} = \boldsymbol{H} \cdot d\vec{\boldsymbol{x}} \tag{A.27}$$

The matrix $\boldsymbol{F}$ is called the *material deformation gradient* or the *deformation gradient*. By definition it is the matrix which multiplies any vector joining neighboring points in the reference configuration, to give the vector joining the same two points in the current configuration. $\boldsymbol{H}$ is the *spatial deformation gradient*. The material and spatial deformation tensors are interrelated through the well-known chain rule for partial differentiation.

$$\frac{\partial x_i}{\partial X_j}\frac{\partial X_j}{\partial x_k} = \frac{\partial X_i}{\partial x_j}\frac{\partial x_j}{\partial X_k} = \delta_{ik} \tag{A.28}$$

The volume change is represented by the *Jacobian*.

$$J = det(\boldsymbol{F}) \tag{A.29}$$

Thus, the deformation gradient with the volume change eliminated is defined as:

$$\bar{\boldsymbol{F}} = J^{-\frac{1}{3}} \boldsymbol{F} \tag{A.30}$$

The *material displacement gradient* is defined as the partial differentiation of the displacement vector $\vec{\boldsymbol{u}}$ with respect to the material coordinates

$$\frac{\partial u_i}{\partial X_j} \quad \text{or} \quad \vec{\boldsymbol{u}} \nabla_0 \tag{A.31}$$

The transpose is shown below, as is the expression using the material deformation gradient.

$$\vec{\boldsymbol{u}} \nabla_0 = \boldsymbol{F} - \boldsymbol{I} \quad \text{and} \quad [\nabla_0 \vec{\boldsymbol{u}}]^T = \vec{\boldsymbol{u}} \nabla_0 \tag{A.32}$$

Similarly, we have the formulations for the *spatial displacement gradient*

$$\frac{\partial u_i}{\partial x_j} \quad \text{or} \quad \vec{\boldsymbol{u}} \nabla \tag{A.33}$$

$$\vec{\boldsymbol{u}} \nabla = \boldsymbol{I} - \boldsymbol{H} \quad \text{and} \quad [\nabla \vec{\boldsymbol{u}}]^T = \vec{\boldsymbol{u}} \nabla \tag{A.34}$$

A.3.4 Stretch tensors, rotation tensors

It is important to distinguish rigid body motion and straining motion. Looking at the *differential element* or infinitesimal *gauge length*, the initial length L and current length l can be defined as

$$dL^2 = d\vec{\boldsymbol{X}}^T \cdot d\vec{\boldsymbol{X}} \quad \text{and} \quad dl^2 = d\vec{\boldsymbol{x}}^T \cdot d\vec{\boldsymbol{x}} \tag{A.35}$$

The stretch λ of the differential element is then

$$\lambda^2 = \frac{dl^2}{dL^2} = \frac{d\vec{\boldsymbol{X}}^T}{(d\boldsymbol{X}^T \cdot d\boldsymbol{X})^{1/2}} \cdot \boldsymbol{F}^T \cdot \boldsymbol{F} \cdot \frac{d\vec{\boldsymbol{X}}}{(d\boldsymbol{X}^T \cdot d\boldsymbol{X})^{1/2}} = \vec{\boldsymbol{N}}^T \cdot \boldsymbol{F}^T \cdot \boldsymbol{F} \cdot \vec{\boldsymbol{N}} \tag{A.36}$$

where $\vec{\boldsymbol{N}}$ is a unit vector in the direction of the gauge length $d\vec{\boldsymbol{X}}$. This equation shows how to measure the stretch associated with any direction $\vec{\boldsymbol{N}}$, at any material point defined by $\vec{\boldsymbol{X}}$ or $\vec{\boldsymbol{x}}$. The direction $\vec{\boldsymbol{N}}$ can be varied to obtain stationary values of λ by solving the eigenvalue problem

$$(\boldsymbol{F}^T \cdot \boldsymbol{F} - \lambda^2 \boldsymbol{I}) \cdot \vec{\boldsymbol{N}} = \boldsymbol{0} \tag{A.37}$$

which gives the three principal stretches $\lambda_I, \lambda_{II}, \lambda_{III}$, and its corresponding orthogonal unit vectors $\vec{\boldsymbol{N}}_I, \vec{\boldsymbol{N}}_{II}, \vec{\boldsymbol{N}}_{III}$. These three orthogonal directions undergoes pure rotation and stretch, when going from the reference to the current configuration. Let $\vec{\boldsymbol{n}}_I, \vec{\boldsymbol{n}}_{II}, \vec{\boldsymbol{n}}_{III}$ be the unit vectors corresponding to $\vec{\boldsymbol{N}}_I, \vec{\boldsymbol{N}}_{II}, \vec{\boldsymbol{N}}_{III}$, but in the current configuration.

$$\begin{aligned} \vec{\boldsymbol{n}}_I &= \boldsymbol{R} \cdot \vec{\boldsymbol{N}}_I \\ \vec{\boldsymbol{n}}_{II} &= \boldsymbol{R} \cdot \vec{\boldsymbol{N}}_{II} \\ \vec{\boldsymbol{n}}_{III} &= \boldsymbol{R} \cdot \vec{\boldsymbol{N}}_{III} \end{aligned} \tag{A.38}$$

The orthogonal matrix $\boldsymbol{R}$ describes pure rigid body rotation, which means that $\boldsymbol{R}^T = \boldsymbol{R}^{-1}$. Consider a gauge length in the reference configuration $d\vec{\boldsymbol{X}}$ along $\vec{\boldsymbol{N}}_I$. The same material line in the current configuration will be $\vec{\boldsymbol{n}}_I$ and stretched by λ_I. The same can be said for the other material directions.

$$\begin{aligned} d\vec{\boldsymbol{x}}_I &= \boldsymbol{R} \cdot \lambda_I d\vec{\boldsymbol{X}}_I \\ d\vec{\boldsymbol{x}}_{II} &= \boldsymbol{R} \cdot \lambda_{II} d\vec{\boldsymbol{X}}_{II} \\ d\vec{\boldsymbol{x}}_{III} &= \boldsymbol{R} \cdot \lambda_I d\vec{\boldsymbol{X}}_{III} \end{aligned} \tag{A.39}$$

As the base vectors are orthonormal, any infinitesimal material line $d\vec{\boldsymbol{X}}$ can be written in terms of its components in this basis

$$d\vec{\boldsymbol{X}} = d\vec{\boldsymbol{X}}_I + d\vec{\boldsymbol{X}}_{II} + d\vec{\boldsymbol{X}}_{III} \tag{A.40}$$

where

$$\begin{aligned} d\vec{\boldsymbol{X}}_I &= \vec{\boldsymbol{N}}_I \cdot \vec{\boldsymbol{N}}_I{}^T \cdot d\vec{\boldsymbol{X}} \\ d\vec{\boldsymbol{X}}_{II} &= \vec{\boldsymbol{N}}_{II} \cdot \vec{\boldsymbol{N}}_{II}{}^T \cdot d\vec{\boldsymbol{X}} \\ d\vec{\boldsymbol{X}}_{III} &= \vec{\boldsymbol{N}}_{III} \cdot \vec{\boldsymbol{N}}_{III}{}^T \cdot d\vec{\boldsymbol{X}} \end{aligned} \tag{A.41}$$

The current differential element is then

$$\begin{aligned} d\vec{\boldsymbol{x}} &= d\vec{\boldsymbol{x}}_I + d\vec{\boldsymbol{x}}_{II} + d\vec{\boldsymbol{x}}_{II} = \\ &\quad \boldsymbol{R} \cdot (\lambda_I \vec{\boldsymbol{N}}_I \cdot \vec{\boldsymbol{N}}_I{}^T + \lambda_{II} \vec{\boldsymbol{N}}_{II} \cdot \vec{\boldsymbol{N}}_{II}{}^T + \lambda_{III} \vec{\boldsymbol{N}}_{III} \cdot \vec{\boldsymbol{N}}_{III}{}^T) \cdot d\vec{\boldsymbol{X}} \end{aligned} \tag{A.42}$$

which can be written

$$d\vec{\boldsymbol{x}} = \boldsymbol{R} \cdot \boldsymbol{U} \cdot d\vec{\boldsymbol{X}} \tag{A.43}$$

Here

$$\boldsymbol{U} = \lambda_I \vec{\boldsymbol{N}}_I \cdot \vec{\boldsymbol{N}}_I{}^T + \lambda_{II} \vec{\boldsymbol{N}}_{II} \cdot \vec{\boldsymbol{N}}_{II}{}^T + \lambda_{III} \vec{\boldsymbol{N}}_{III} \cdot \vec{\boldsymbol{N}}_{III}{}^T \tag{A.44}$$

is the stretching matrix.

Taking the definition of the deformation gradient, we obtain

$$\boldsymbol{F} = \boldsymbol{R} \cdot \boldsymbol{U} \tag{A.45}$$

where

$$\boldsymbol{R}^{-1} = \boldsymbol{R}^T \qquad \boldsymbol{U} = \boldsymbol{U}^T \tag{A.46}$$

This is the *polar decomposition theorem of Cauchy*: "any motion of a body in the vicinity of a material particle can be written as pure stretch along three orthogonal principal directions in the original configuration, followed by pure rigid body rotation." There is also rigid body translation, but this is not important because relative motion of neighboring points is studied.

Similarly, the rotation can be done first

$$\boldsymbol{F} = \boldsymbol{V} \cdot \boldsymbol{R} \tag{A.47}$$

The tensors $\boldsymbol{U}$ and $\boldsymbol{V}$ are the right and left stretch tensors, respectively. They are symmetrical and positive definite.

$$\boldsymbol{U}^2 = \boldsymbol{F}^T \cdot \boldsymbol{F} \qquad \boldsymbol{V}^2 = \boldsymbol{F} \cdot \boldsymbol{F}^T \tag{A.48}$$

A.3.5 Strain measure

Strain can be studied in one dimension and then be generalized to three dimensions using the polar decomposition theorem. Define the strain ϵ in one dimension, i.e. along some differential element $d\vec{\boldsymbol{X}}$, as a function of the stretch ratio λ of that differential element.

$$\epsilon = f(\lambda) \tag{A.49}$$

Introduce the restrictions $f(1) = 0$, $\frac{df(1)}{d\lambda} = 1$, $\frac{df}{d\lambda} > 0$ for $\lambda > 0$, which ensure that strain increases monotonically with stretch and at small strain we obtain the definition "change in length per unit length".

As shown in the previous section the deforming part of the motion in the neighborhood of a material point is completely described by the three principal stretch ratios and their orientation in the reference or current configuration. Let $\epsilon_i = f(\lambda_i)$ be the strain along the first principal direction, etc. Then the strain in three dimensions at the material point is

$$\boldsymbol{\epsilon} = \epsilon_I \vec{\boldsymbol{N}}_I \cdot \vec{\boldsymbol{N}}_I{}^T + \epsilon_{II} \vec{\boldsymbol{N}}_{II} \cdot \vec{\boldsymbol{N}}_{II}{}^T + \epsilon_{III} \vec{\boldsymbol{N}}_{III} \cdot \vec{\boldsymbol{N}}_{III}{}^T \tag{A.50}$$

where it is written using the reference configuration. This has the advantage that any anisotropy in the material is conveniently included in the description.

The choice of strain definition should be made considering the appropriateness of the strain measure with respect to the constitutive model and the ease with which the strain can be computed from the displacements, as the latter are usually the basic variables in the finite element model. Two examples are discussed below.

The formulation $f(\lambda) = \ln(\lambda)$ is called logarithmic strain. It is appropriate in materials which flow. True stress (force per current area) is plotted against logarithmic strain.

The definition $f(\lambda) = \frac{1}{2}(\lambda^2 - 1)$ is known as the *Lagrangian or Green strain.* It is generally useful in problems involving large motions but small strain. Its usefulness for large strain depends on the constitutive model used. The strain measure can be calculated directly from the deformation gradient without solving the eigenvalue problem described above. This will be discussed in Section A.3.6 below.

A.3.6 Eulerian and Lagrangian finite strain tensors

The general algorithm discussed above involves computing eigenvectors and eigenvalues. There are two well-known formulations of finite strain which avoids this.

The *Lagrangian or Green's finite strain tensor* is defined as

$$\boldsymbol{G} = \frac{1}{2}\left(\boldsymbol{F}^T \cdot \boldsymbol{F} - \boldsymbol{I}\right) \tag{A.51}$$

where $\boldsymbol{F}$ is the material deformation gradient. This can also be expressed using material displacements gradients

$$\boldsymbol{G} = \frac{1}{2}\left(\vec{\boldsymbol{u}}\nabla_0 + \nabla_0\vec{\boldsymbol{u}} + \vec{\boldsymbol{u}}\nabla_0 \cdot \nabla_0\vec{\boldsymbol{u}}\right) \tag{A.52}$$

The *Eulerian or Almansi's finite strain tensor* is defined as

$$\boldsymbol{E} = \frac{1}{2}\left(\boldsymbol{I} - \boldsymbol{H}^T \cdot \boldsymbol{H}\right) \tag{A.53}$$

where $\boldsymbol{H} = \vec{\boldsymbol{X}}\nabla$ is the spatial deformation gradient. It can also be expressed in spatial displacements gradients.

$$\boldsymbol{E} = \frac{1}{2}\left(\vec{\boldsymbol{u}}\nabla + \nabla\vec{\boldsymbol{u}} - \vec{\boldsymbol{u}}\nabla \cdot \nabla\vec{\boldsymbol{u}}\right) \tag{A.54}$$

A.3.7 Rate of deformation

The velocity of a material particle is

$$\vec{\boldsymbol{v}} = \frac{\partial\vec{\boldsymbol{x}}}{\partial t} \tag{A.55}$$

The velocity difference between two neighboring particles in the current configuration is:

$$d\vec{\boldsymbol{v}} = \boldsymbol{L}d\vec{\boldsymbol{x}} \quad \text{where} \tag{A.56}$$

$$\boldsymbol{L} = \frac{\partial\vec{\boldsymbol{v}}}{\partial\vec{\boldsymbol{x}}} \tag{A.57}$$

$$\boldsymbol{L} \cdot \boldsymbol{F} = \dot{\boldsymbol{F}} \tag{A.58}$$

The velocity gradient $\boldsymbol{L}$ in the current configuration is decomposed into the rate of deformation tensor and the spin tensor.

$$\boldsymbol{D} = \frac{1}{2}\left(\boldsymbol{L} + \boldsymbol{L}^T\right) \tag{A.59}$$

$$\boldsymbol{W} = \frac{1}{2}\left(\boldsymbol{L} - \boldsymbol{L}^T\right) \tag{A.60}$$

The strain is obtained by integrating the rate of deformation. For cases with pure stretch the integrated rate of deformation is identical to logarithmic strain.

The strain rate in the corotational coordinate system or the corotational strain rate is obtained after transforming the rate of deformation using the material rotation at that time instant.

$$\dot{\boldsymbol{\epsilon}} = \boldsymbol{R}^T \cdot \boldsymbol{D} \cdot \boldsymbol{R} \tag{A.61}$$

A.4 Stress

For problems involving finite strain the choice of stress measure is important. It should be natural for the problem studied and the constitutive theory used. Cauchy stress is defined as force per current area and is therefore widely used.

A stress and strain pair is work conjugate if the work rate per unit reference volume can be written as:

$$dW^0 = \boldsymbol{\sigma} : d\boldsymbol{\epsilon} \tag{A.62}$$

The stress work conjugate to the rate of deformation is the Kirchoff stress which is equal to Cauchy stress multiplied with the Jacobian of the volume change [2, 1].

Bibliography

[1] *Abaqus Theory Manual*. Version 4-5. Hibbit, Karlsson, and Sorensen Inc. 100 Medway Street, Providence, Rhode Island, 1984.

[2] *Abaqus User's Manual*. Version 4-5. Hibbit, Karlsson, and Sorensen Inc. 100 Medway Street, Providence, Rhode Island, 1984.

[3] S. Abrate. "The mechanics of short-fiber-reinforced composites: A review". In: *Rubber Chemistry and Technology* 59 (1986), pp. 384–404.

[4] J. Bäcklund. "Fracture analysis of notched composites". In: *Computers & Structures* 13 (1981), pp. 145–154.

[5] J. Bäcklund. *Kompositmekanik (Composite mechanics)*. 82–10. KTH, Stockholm, Sweden: Dept. of strength of materials, 1982.

[6] K-J. Bathe et al. "Finite element formulations for large deformation dynamic analysis". In: *Int. J. for Numerical Methods in Engineering* 9 (1975), pp. 353–386.

[7] Y. Benveniste and J. Aboudi. "A continuum model for fiber reinforced materials with debonding". In: *Int. J. Solids Structures* 20.11/12 (1984), pp. 935–951.

[8] A.K. Bhowmick and A.N. Gent. "Strength of neoprene compounds and the effect of salt solutions". In: *Rubber Chemistry and Technology* 56 (1983), pp. 845–854.

[9] S.F. Borg. *Matrix-tensor methods in continuum mechanics*. Princeton, New Jersey: D. van Nostrand company Inc., 1963.

[10] H. Broberg. "A new criterion for brittle creep rupture". In: *Journal of Applied Mechanics* 41.3 (Sept. 1974), pp. 809–811.

[11] R.V. Browning. "A one-dimensional viscoplastic constitutive theory for filled polymers". In: *Int. J. Solids Structures* 20.11/12 (1984), pp. 921–934.

[12] J. Carlsson. *Brottmekanik (Fracture mechanics)*. Ingenjörsförlaget, Sweden, 1976.

[13] J-L. Chaboche. "Continuous damage mechanics - a tool to describe phenomena before crack initiation". In: *Nuclear engineering and design* 64 (1981), pp. 233–247.

[14] R.M. Christensen. "A nonlinear theory of viscoelasticity for application to elastomers". In: *Journal of Applied Mechanics* 47 (Dec. 1980), pp. 732–768.

[15] S.K. Clark. "Theory of the elastic net applied to cord-rubber composites". In: *Rubber Chemistry and Technology* 56 (1983), pp. 372–389.

[16] P. Ekström et al. *Beräkning och provning av gummikomponenter (Analysis and testing of rubber components)*. Report to the Swedish Board of Technical Development 84-4271. Västerås, Sweden: Asea research and innovation, May 1987.

[17] R.J. Farris. "The stress-strain behavior of mechanically degradable polymers". In: *Proceedings of the ACS Symposium on Highly Cross-Linked Polymer Networks, held in Chicago, Illinois, September 14-15, 1970*. New York: Plenum Press, 1970, pp. 341–394.

[18] G.S. Fielding-Russel and R.L. Rongone. "Fatiguing of rubber-rubber interfaces". In: *Rubber Chemistry and Technology* 56 (1983), pp. 838–844.

[19] P.K. Freakley and A.R. Payne. *Theory and practice of engineering with rubber*. Ripple Road, Barking, Essex, England: Applied Science Publishers Ltd, 1978.

[20] D. Fritzson. *Fatigue mechanisms of V-belts*. No. 1988-05-27. Department of Mechanical Engineering, Chalmers University of Technology, Göteborg, Sweden: Division of Machine Elements.

[21] D. Fritzson. *Friction of elastomer composites - influence of surface temperature, sliding speed, and pressure*. No. 1988-05-26. Department of Mechanical Engineering, Chalmers University of Technology, Göteborg, Sweden: Divison of Machine Elements.

[22] D. Fritzson. *Material properties of elastomer composites in mechanical transmissions with special reference to V-belts*. No. 1988-05-25. Department of Mechanical Engineering, Chalmers University of Technology, Göteborg, Sweden: Division of Machine Elements.

[23] Y.C. Fung. *Foundations of solid mechanics*. Int. series in dynamics. Englewood Cliffs, New Jersey: Prentice-Hall Inc., 1965.

[24] A.N. Gent. "Fracture mechanics applied to elastomeric composites". In: *Rubber Chemistry and Technology* 56 (1983), pp. 1011–1018.

[25] A.E. Green and W. Zerna. *Theoretical elasticity*. London: Oxford University Press, Amen House, 1954.

[26] M.E. Gurtin. "Simple rate-independent model for damage". In: *J. Spacecraft* 18.3 (May 1981), pp. 285–286.

[27] B. Häggblad and K-J. Bathe. *Finite element analysis of rubber-like solids*. Västerås, Sweden: Asea research and innovation, 1988.

[28] A. Hoger. "The stress conjugate to logarithmic strain". In: *Int. J. Solids Structures* 23.12 (1987), pp. 1645–1656.

[29] T.J.R. Hughes. "Generalization of selective integration procedures to anisotropic and nonlinear media". In: *Int. J. for Numerical Methods in Engineering* 15.9 (1980), pp. 1413–1418.

[30] T.J.R Hughes. *The finite element method - linear static and dynamics analysis*. Englewood Cliffs, New Jersey: Prentice-Hall Inc., 1987.

[31] T.J.R. Hughes and J. Winget. “Finite rotation effects in numerical integration of rate constitutive equations arising in large-deformation analysis”. In: *Int. J. for Numerical Methods in Engineering* 15.12 (1980), pp. 1862–1867.

[32] A.G. James et al. “Strain energy functions of rubber. I. Characterization of gum vulcanizates”. In: *Journal of applied polymer science* 19 (1975), pp. 2033–2058.

[33] A.G. James et al. “Strain energy functions of rubber. II. Characterization of filled vulcanizates”. In: *Journal of applied polymer science* 19 (1975), pp. 2319–2330.

[34] Jankovich-81 et al. “A finite element method for the analysis of rubber parts, experimental and analytical assessment”. In: *Computers & Structures* 14.5–6 (1981), pp. 385–391.

[35] Ashton J.E. et al. *Primer on composite materials: Analysis*. 750 Summer street, Stamford, Conn.: Technomic Publishing Company, Inc., 1969.

[36] R.M. Jones. *Mechanics of composite materials*. Washington, D.C.: Scripta book company, 1975.

[37] B. Keren et al. “Nonlinear viscoelastic response in two dimensions - numerical modelling and experimental verification”. In: *Polymer engineering and science* 24.18 (1984), pp. 1409–1416.

[38] S.W. Key and R.D. Krieg. “On the numerical implementation of inelastic time dependent and time independent, finite strain constitutive equations in structural mechanics”. In: *Computer methods in applied mechanics and engineering* 33 (1982), pp. 439–452.

[39] B.V. Kiefer and P.D. Hilton. “Combined viscous and plastic deformations in two-dimensional large strain finite element analysis”. In: *Journal of engineering materials and technology* 107 (Jan. 1985), pp. 13–18.

[40] M. Kojic and K-J. Bathe. “Studies of finite element procedures - stress solutions of a closed elastic strain path with stretching and shearing using the updated Lagrangian Jauman formulation”. In: *Computers & Structures* 26.1/2 (1987), pp. 175–179.

[41] G.J. Lake and P.B. Lindley. “Ozone cracking, flex cracking and fatigue of rubber, Part I: Cut growth mechanisms and how they result in fatigue failure”. In: *Rubber Journal* (Oct. 1964).

[42] G.J. Lake and P.B. Lindley. “Ozone cracking, flex cracking and fatigue of rubber, Part II: Technological aspects”. In: *Rubber Journal* (Nov. 1964).

[43] J. Lemaitre. “A continuous damage mechanics model for ductile fracture”. In: *Journal of engineering materials and technology* 107 (Jan. 1985), pp. 83–89.

[44] J. Lemaitre. “Coupled elasto-plasticity and damage constitutive equations”. In: *Computer methods in applied mechanics and engineering* 51 (1985), pp. 31–49.

[45] J. Lemaitre. “How to use damage mechanics”. In: *Nuclear engineering and design* 80 (1984), pp. 233–245.

[46] J. Lubliner. "A model of rubber viscoelasticity". In: *Mechanics research communications* 12.2 (1985), pp. 93–99.

[47] G. Mase. *Continuum mechanics*. Schaum's outline series. New York: McGraw-Hill Inc, 1970.

[48] E.A. Meinecke. "Comparing the time and rate dependent mechanical properties of elastomers". In: *Rubber Chemistry and Technology* 53 (1983), pp. 1145–1159.

[49] K.N. Morman. "Finite element analysis of sinusodial small-amplitude vibrations in deformed viscoelastic solids. Part I: Theoretical development". In: *Int. J. for Numerical Methods in Engineering* 19 (1983), pp. 1079–1103.

[50] K.N. Morman. *Rubber viscoelasticity - a review of current understanding*. Dearborn, Michigan, USA: Ford Motor Company, June 1984.

[51] K.N. Morman and B.G. Kao. "Finite element analysis of viscoelastic elastomeric structures vibrating about non-linear statically stressed configurations". In: *Proceedings of the fourth international conference on vehicle structural mechanics, held in Detroit, Michigan, November 18-20, 1981*. 400 Commonwealth Drive, Warrendale, PA: Society of Automotive Engineers Inc., 1986, pp. 83–92.

[52] J.S. Mshana and A.S. Krausz. "Constitutive equation of cyclic softening". In: *Journal of engineering materials and technology* 107 (Jan. 1985), pp. 7–12.

[53] L. Mullins. "Mechanical behaviour of polymers - accomplishments and problems". In: *Elastomers: Criteria for engineering design*. Ed. by C. Hepburn and R.J.W. Reynolds. Ripple Road, Barking, Essex, England: Applied Science Publishers, 1979. Chap. 1, pp. 1–6.

[54] L. Mullins. "Softening of rubber by deformation". In: *Rubber Chemistry and Technology* 42 (1969), pp. 339–362.

[55] J.C. Nagtegaal and N. Rebelo. "On the development of a general purpose finite element program for analysis of forming processes". In: *Int. J. for Numerical Methods in Engineering* 25 (1988), pp. 113–131.

[56] J.T. Oden. *Finite elements of nonlinear continua*. Advanced engineering series. New York: McGraw-Hill Inc., 1972.

[57] A.R. Payne and R.E. Whittaker. In: *Rubber Chemistry and Technology* 44 (1971), pp. 340–.

[58] B.E. Read and G.D. Dean. *The determination of dynamic properties of polymers and composites*. New York: John Wiley and Sons, 1978.

[59] D.K. Setua and S.K. De. "Short silk fiber reinforced natural rubber composites". In: *Rubber Chemistry and Technology* 56 (1983), pp. 808–826.

[60] J.C. Simo. "A framework for finite strain elastoplasticity based on maximum plastic dissipation and the multiplicative decomposition: Part I. Continuum formulation". In: *Computer methods in applied mechanics and engineering* 66.2 (Feb. 1988), pp. 199–219.

[61] J.C. Simo and J. Lubliner. “Formulation and computation aspects of a three-dimensional finite strain viscoelastic damage model”. In: *Proceedings of the sixth international conference on vehicle structural mechanics, held in Detroit, Michigan, April 22-24, 1986*. 400 Commonwealth drive, Warrendale, PA: Society of Automotive Engineers Inc., 1986, pp. 155–167.

[62] G.D Smith. *Numerical solution of partial differential equations: Finite difference methods*. Second. Oxford applied mathematics and computing science series. Walton street, Oxford, England: Oxford University Press, 1978.

[63] R. Sowerby and E. Chu. “Rotations, stress rates and strain measures in homogeneous deformation processes”. In: *Int. J. Solids Structures* 20.11/12 (1984), pp. 1037–1048.

[64] U. Stigh. “Material damage and constitutive properties”. PhD thesis. Division of Solid Mechanics, Chalmers University of Technology, Göteborg, Sweden, Dec. 1985.

[65] J.L. Sullivan and V.C. Demery. “The nonlinear viscoelastic behavior of a carbon-black-filled elastomer”. In: *Journal of Polymer Science* 20.11 (Nov. 1982), pp. 2083–2101.

[66] K.N. Sullivan et al. “A non-linear viscoelastic characterization of a natural rubber gum vulcanizate”. In: *Rubber Chemistry and Technology* 53 (1979), pp. 805–821.

[67] L.R.G. Treloar. “The mechanics of rubber elasticity”. In: *Journal of applied polymer science* 48 (1974), pp. 107–123.

[68] S.W. Tsai et al. *Composite materials workshop*. 750 Summer Street, Stamford, Conn. 06902, USA: Technomic publishing company, Inc., 1968.

[69] C. Van Ho. *Internal test report - material properties*. Denver, Colorado, USA: The Gates Rubber Company, 1987.

[70] M.L. Williams and F.N. Kelley. “The interaction between polymeric structure, deformation and fracture”. In: *Proceedings of the ACS Symposium on Highly Cross-Linked Polymer Networks, held in Chicago, Illinois, september 14-15, 1970*. New York: Plenum Press, Sept. 1970, pp. 193–218.

[71] Y. Yamada. “Nonlinear matrices, their implications and applications in plastic large deformation analysis”. In: *Computer methods in applied mechanics and engineering* 33 (1982), pp. 417–437.

[72] A.B. Zdunek and M. Bercovier. “Numerical evaluation of finite element methods for rubber parts”. In: *Reprint from P-178 - Proceedings of the sixth international conference on vehicle structural mechanics, held in Detroit, Michigan, April 22-24, 1986*. 400 Commonwealth Drive, Warrendale, PA: Society of Automotive Engineers Inc., 1986, pp. 155–167.

Part III

Fatigue mechanisms of V-belts

Report III

Fatigue mechanisms of V-belts

Dag Fritzson

Report No. 1988-05-27
Division of Machine Elements
Department of Mechanical Engineering
Chalmers University of Technology
Göteborg, S-412 96 Sweden

1 st version completed 1987

Abstract

Knowledge of the failure characteristics of V-belts is important for a number of reasons. It is necessary for development of theoretical methods for predicting the life of V-belt transmissions and also product development.

Together with previous work, this experimental investigation of V-belt fatigue characteristics, shows how different failure modes in V-belt fatigue can be identified. It is shown that the failure modes defined here occur for test conditions such that long life can be associated with radial cracks, medium life with separation, and cord break with short life.

These failure modes have not been recognized in fatigue life prediction theory to date, which has, instead, been based on cord stress. However, if we want to avoid including experimentally determined constants for different belt types in the theory, it will have to be further developed to account for the different failure mechanisms.

Contents

1
Introduction

Knowledge of the failure characteristics of V-belts is important for several reasons, including development of theoretical methods for predicting the life of V-belt transmissions and in product development.

Today, belt manufacturer's primary feedback on V-belt designs comes from extensive fatigue tests of V-belts in the product development process. For each design modification, an extensive fatigue test program has to be carried out. Thus, there is a large amount of experimental data, accumulated over the years, in addition to practical "know how". Fatigue tests are expensive. This is because a large number of tests have to be performed to achieve statistically significant results. Also, there are many parameters which influence V-belt fatigue, and each test takes a long time (10 - 2000 hours). And of course the necessary testing equipment costs a lot of money.

There is a need for theory development and design support systems. This would allow simulation for prediction and optimization of fatigue life. Material fatigue life, given a certain stress, strain and environment history, should be an intrinsic material property, and should not depend on the design in which it is used.

In this report the fatigue characteristics of V-belts are investigated from the experimental point of view, i.e. from fatigue life experiments. However, first we survey already published results and theories.

2
Notation

σ_m	Stress mean value (Pa, MPa)
σ_o, σ_a	Oscillating stress or stress amplitude (Pa,MPa)
σ	Design stress level (MPa)
σ_A	Alternating fatigue strength (MPa)
σ_U	Ultimate strength (MPa)
τ	Shear stress (MPa)
p	Pressure (MPa)
T_1	Tight-side tension excluding centrifugal component (N)
T_2	Slack-side tension excluding centrifugal component (N)
T_{1e}	Edge cord component of T_1 (N)
T_{2e}	Edge cord component of T_2 (N)
T_{be}	Edge cord tension due to bending (N)
T_{ce}	Edge cord tension due to centrifugal force (N)
k, K_i	Experimental individual belt constants (-)
K_o, K_m	Experimental individual belt constants (Pa)
N	Belt life in cycles attributed to a single pulley (-)
V	Belt speed (m/s)
L	Belt pitch length (cm)
A	Nominal area of each cord (m^2)
a	A constant, different for each failure mode (-)
b	A constant, different for each failure mode (MPa^{-1})
N_T	Life in cycles at temperature difference of ΔT (-)
N_O	Life in cycles at a reference temperature (-)

3
Previous work

3.1 Experiments

Fatigue tests of V-belts can be classified into three groups.

First, we have real applications which are monitored, such as V-belts in automotive applications [8, 6, 7, 13]. In these tests operating conditions are not really controlled, and no influence of various V-belt drive data such as force, speed, etc. can be investigated. The belt life failure distribution incorporates the variation in these data. However, important information about real failure behavior is obtained. Such results are valuable because they come from real applications with realistic belt life. This makes them different from accelerated laboratory tests, which may give different distribution of failure modes.

Fatigue data from Tetsue Orito at Japan's Bando Chemical Industries are presented below [8]. This is a road car test with self-tensioning belts. The polyester cord of these belts shrinks when subjected to heat.

Belt damage was classfied as presented in Figure 3.1. Different levels of damage are marked with labels A to E.

The cumulative failure distribution for the different damage levels is plotted against belt life. See Figure 3.2.

These results show that belt failure is a continuous damage mechanism in which crack damage and separation have about the same importance. The slope of the cumulative failure increases at more serious damage levels. This means that the failure distribution is narrower at more serious damage levels.

The second group of tests are "standard" tests in laboratories [12, 11]. Examples are the dead weight test and tests for certain applications like the SAE 3-pulley test for automotive applications. The main purpose of these tests is to compare life and failure modes for different belts and check if they pass a certain quality standard. Here to, the failure modes of radial cracking and separation are common. However, as the tests are normally accelerated to give a life of around 300 hours, disastrous failures such as cord breakage are not uncommon. As these tests are performed in laboratories, no influence from variation in loads, temperatures, etc. should be expected, as is the case in real applications, as mentioned above. However, the question of how well accelerated test can represent the failure characteristics observed in real applications

Conventional auto belt failure

Level	Mode of failure			
	Sepa-ration	Cracking Bottom	Top	Abrasion, wgt. loss
A	To 10 mm	In 1st bot. canvas layer	In 1st top canvas layer	To 3%
B	10 mm - 50 mm	To 3rd bot. canvas layer	To 2nd top canvas layer	To 5%
MDTF*	(44,600)	(37,800)		(43,400)
C	50 mm - ½L**	To under-cord rubber	Through to cord	To 7%
MDTF*	(53,000)	(41,500)		(49,000)
D	Over ½L**	Through to cord	Crack space below 30mm	To 10%
E	Break	Break: cord separates	Top canvas separates	Over 10%

*MDTF = mean dist. to failure, mi. **L = belt length

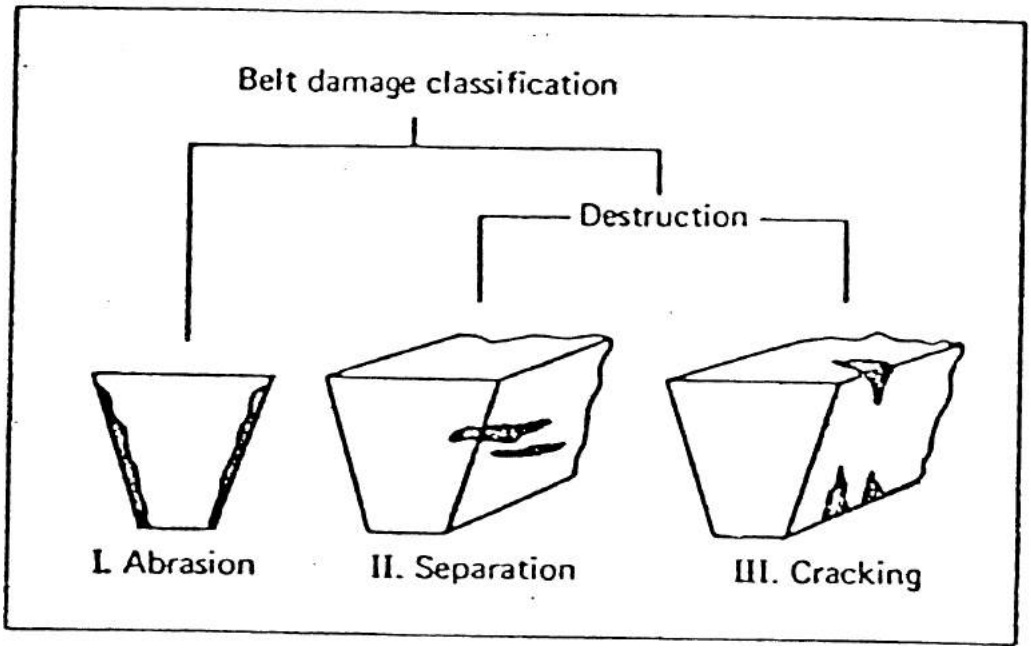

Figure 3.1 *Belt damage classification [8].*

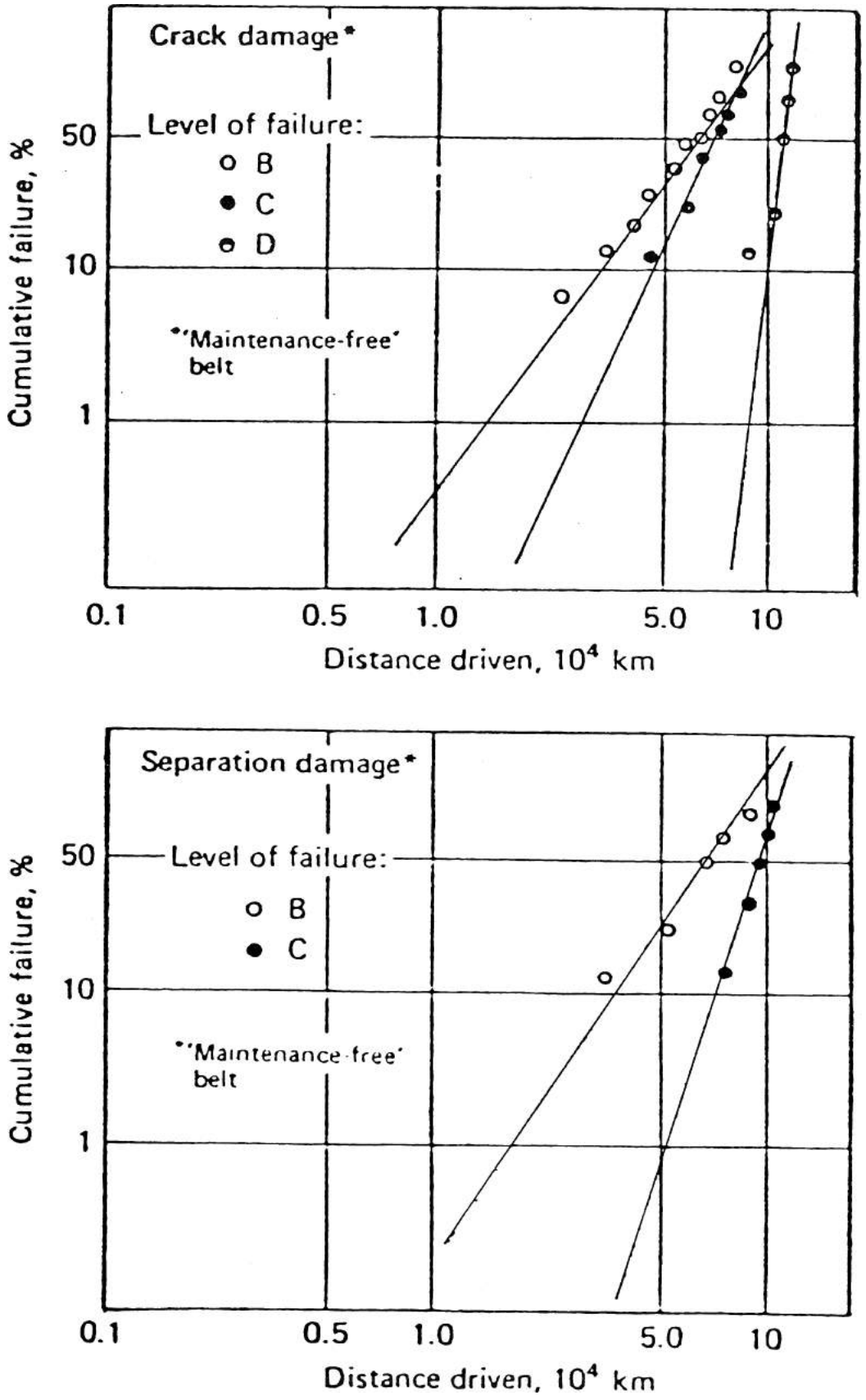

Figure 3.2 *Cumulative cracking and separation from a 15-month road test. Test cars covered an average of 112400 km each. Mean distance to failure, both cracking and separation, was 92000 km [8].*

should be taken into consideration.

The third group includes tests made to study the influence of V-belt drive operating conditions and design parameters [10, 9, 5]. Results from these tests are presented as means of calculating fatigue life for V-belt drives with arbitrary loads and speeds.

In reference [10], a service-life prediction and rating formula is presented for use in the design of V-belt transmission drives. When the supporting experiments were performed the following variables, which could be varied independently, were included: belt type, pulley diameter, tight-side tension, slack-side tension, belt length, and belt speed. In each test two equal diameter pulleys were used, and a fixed torque was applied. There were also constant belt tension, constant speed, and controlled environment temperature. The failure criteria were belt breakage, component separation extending across the width of belt, or radial cracks extending from the bottom of the belt to the cord. In this case accelerated tests were used. Thus the question arises as to whether these failure modes are representative for a real application, which has a ten to one hundred times longer expected life.

3.2 Theory

In this section we discuss methods for predicting the expected life of V-belts.

First, there are pure statistical methods which are based on experimental data for a certain application [8, 6, 7, 13]. When these methods are used a large number of fatigue life tests are performed. Failure is defined as damage exceeding a certain predefined level. This definition is used for each failure mode. The experimental data are then used to calculate the parameters of a chosen distribution for the probability of failure. Thus, predictions of a belt life with a certain probability can be done for the same application and V-belt type. The Weibull distribution function is normally found very useful for such applications. One exception is results from references [6, 7] where the normal distribution function is preferred.

Second, there are methods based on the assumption that edge cord stress governs V-belt fatigue for all failure modes. In these tests only maximum stress was used at first, but later both minimum and maximum edge cord stresses were incorporated into the theory [10]. The formula presented in reference [10], has been derived from statistically designed and analyzed life tests, in addition to cord bending stress measurements, and calculations of cord stress distribution. The variables are the mean and oscillating edge cord stresses, belt length, and belt speed. Belt life in cycles is obtained from:

$$N = K_i(K_o - \sigma_o)^2(K_m - \sigma_m)^2 L^{1.75} V^k \tag{3.1}$$

$$\sigma_m = \frac{1}{2A}\left(T_{1e} + T_{be} + 2T_{ce} + T_{2e}\right) \tag{3.2}$$

$$\sigma_o = \frac{1}{2A}\left(T_{1e} + T_{be} - T_{2e}\right) \tag{3.3}$$

T_1 = Tight-side tension excluding centrifugal component
T_2 = Slack-side tension excluding centrifugal component
T_{1e} = Edge cord component of T_1
T_{2e} = Edge cord component of T_2
T_{be} = Edge cord tension due to bending
T_{ce} = Edge cord tension due to centrifugal force
k, K_i, K_o, K_m = Experimental individual belt constants
N = Belt life in cycles attributed to a single pulley
V = Belt speed
L = Belt pitch length
A = Nominal area of each cord

In a drive with unequal pulley diameters, the total life is calculated using Miner's theory for cumulative damage.

However, there is a set of constants that have to be determined experimentally and are unique for each belt type. Edge cord criteria are used to analyze failure modes where cord does not break. This is also pointed out by the authors. The formula should be recognized for what it is, namely an advanced method based on experimental data from V-belt drive tests and edge cord stress calculations, used to predict life for V-belt drives. Only V-belts for which there is a complete set of experimental constants can be analyzed using it, but for such an application this method works well. It is not intended to be used for the design of new V-belts. Neither does it contribute to the understanding of belt failure, except at high loads where the cord breaks. Compared with the "pure" statistical methods discussed above, this method allows for the study of the response of the V-belt drive variables listed above.

The next step is to study each failure mode separately and try to correlate a design quantity to each such case. This has been done by Gerbert [4]. He recognizes three main failure modes and suggests the following theory.

Analytical methods are used to calculate stresses for the different failure modes. The design stress for each failure mode is then correlated to fatigue data using the equation given below:

$$N = 10^{(a-b\sigma)} \tag{3.4}$$

N = Number of deformation/load cycles
σ = Design stress
a, b = Constants, different for each failure mode

The aim is not to correlate the constants thus obtained to a certain belt type and size, but to parameters such as:

- Cord material
- Kind of rubber material, etc.

Thus a V-belt drive can be designed to satisfy the power and life-time requirements with minimum pulley diameters and the desired failure mode.
Thermal influence on fatigue life is expressed using the following equation:

$$\frac{N_T}{N_O} = 2^{(-0.1\Delta T)} \tag{3.5}$$

N_T = Life in cycles at a temperature difference of ΔT
N_O = Life in cycles at a reference temperature

This suggests that a 10 °C reduction in temperature will double the belt life. This is reasonable within a temperature range of, say, 60 - 140 °C. The following three failure modes are recognized, and theoretical models for them are presented:

1. Cord breakage. This is a rare failure mode associated with high torques and short life. The tensile stress in the cord is the design parameter, referred to as "tensile fatigue". Analytical expressions yield terms on the basis of belt tension, friction forces, dishing, bending around the pulley, and centrifugal load.

   Both a mean stress and an alternating component are defined. A simple linear relationship between alternating fatigue strength and ultimate strength is used.

$$\sigma_a = \sigma_A \left(1 - \frac{\sigma_m}{\sigma_U}\right) \tag{3.6}$$

σ_a = Stress amplitude
σ_m = Stress mean value
σ_A = Alternating fatigue strength
σ_U = Ultimate strength

Equations 3.4 and 3.5 give:

$$N = 10^{(a-b\sigma_A)}2^{(-0.1\Delta T)} \tag{3.7}$$

2. Cord separation. This is separation of the cord from the cushion or the cushion from the compression layer. This failure mode is associated with moderate torque and moderate life. The design parameter is the shear stress between the layers, which is referred to as "shear fatigue".

   Analytical expressions yield terms due to friction forces, dishing, bending around the pulley, and transferring the side pressure to the cord. Effective shear stress is calculated, and is used in the fatigue life formula below.

$$N = 10^{(a-b\tau)}2^{(-0.1\Delta T)} \tag{3.8}$$

$$\tau = \text{Shear stress}$$

3. Radial cracks. This failure mode is associated with long life and low torques. This is the desired failure mode. Radial cracks grow towards the cord which ultimately causes rubber parts to degrade from the belt. The compressive stress is the design parameter, and is referred to as "pressure fatigue".

   Side pressure and pressure due to bending are discussed. A combined pressure is calculated by applying von Mieses' theorem, and is used in the following fatigue formula.

$$N = 10^{(a-bp)}2^{(-0.1\Delta T)} \tag{3.9}$$

$$p = \text{Pressure}$$

Figure 3.3 shows how the different failure modes combine.

The method [4] presented above recognizes the different failure modes and incorporates this recognition. The major mechanisms that contribute to forces and deformations of the belt are probably identified. In reference [5], the importance of "pressure fatigue" is also recognized.

The tensile fatigue model for cord breakage is probably the best developed of the three failure modes. In the other two cases it has to be verified that the relatively simple analytical expressions for stresses and strains are sufficiently accurate. They should ideally correlate so well with the fatigue mechanism of the materials that the constants of the equations are independent of V-belt type and V-belt design. In fact, they should be intrinsic material constants.

It is probable that more complex models have to be suggested to account for the damage mechanisms in elastomer composites. Such theories have to include the following aspects:

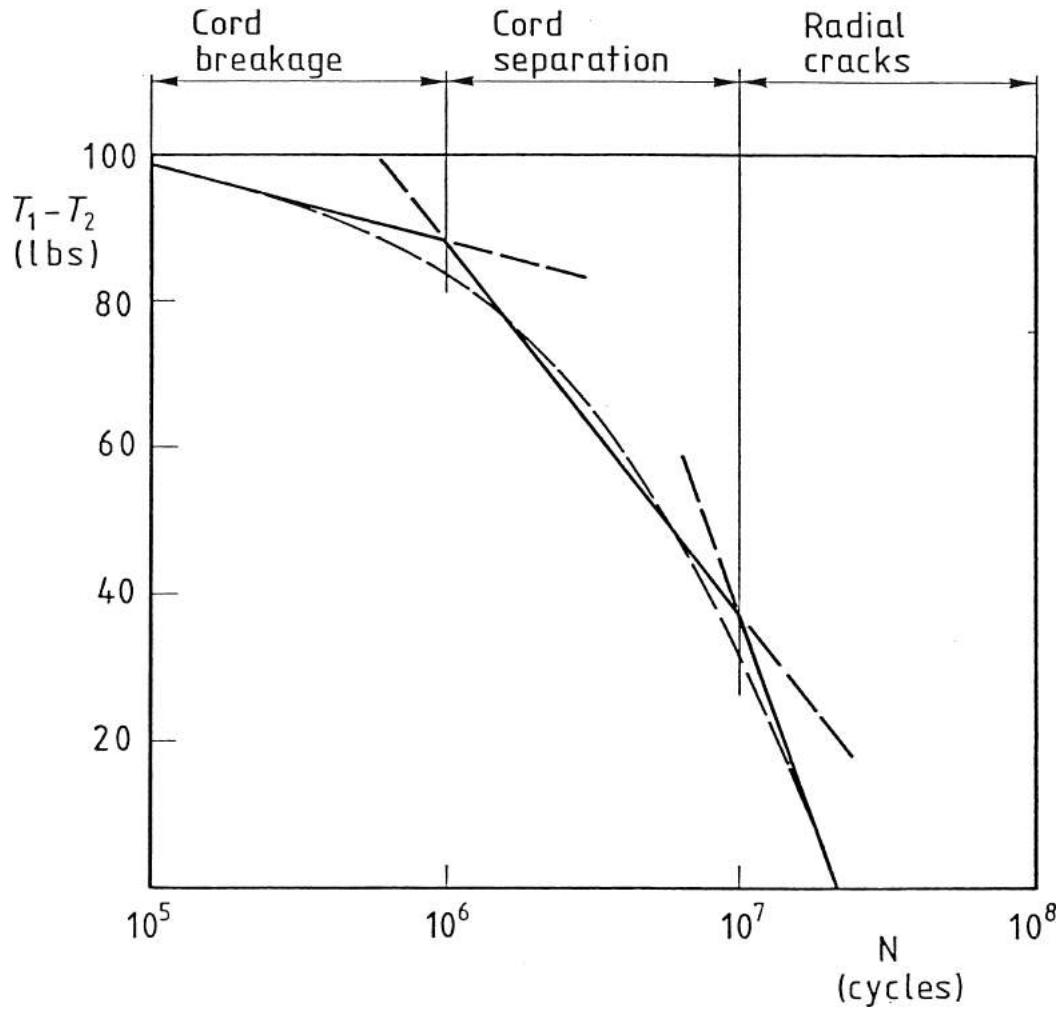

Figure 3.3 *How an effective pull-life diagram can be constructed by combining the formulas of different failure modes [4].*

- A proper material model or constitutive model that can handle viscoelasticity, material breakdown, anisotropy, etc.
- A parameter that can be correlated with the crack propagating mechanism, i.e. fatigue mechanism, for this kind of materials.
- A theory and numerical methods that can calculate these parameters for the complex geometry and loads, i.e. simulate a V-belt drive. They must be able to handle non-linearities from large deformations, large rotations, large strain, and material nonlinerities.

4
Fatigue characteristics

4.1 Introduction

This experimental investigation is based on raw data from belt-fatigue tests made by the Dayco Corporation [1] and the Gates Corporation [2]. The material represents accelerated laboratory tests with life-times ranging from 1 to 2000 hours. Independent V-belt drive variables include belt type, tight-side tension, slack-side tension, belt length, pulley diameter, belt speed, and environment temperature. The drive conditions in each belt test were two equal pulleys, constant belt tension, fixed applied torque, constant speed, and controlled environment temperature. Belt temperature, slip, elongation, damage, and wear were monitored throughout the tests. Normally the belt was inspected for damage and wear at least daily. A large number of different damage identifications with associated severity ratings were defined and used in the data sheets.

4.2 Data interpretation - failure modes

The data from the belt fatigue tests on the data sheets should be condensed to a few major failure mechanisms. The failure mechanisms so defined should represent the most important belt fatigue mechanisms. They should also be defined with the purpose in mind of being able to correlate them with certain calculated quantities such as stress, strain, energy or other quantities in the local area of the belt where the damage occurs. A severity rating must be introduced which is used when correlating to belt life. This severity rating, different for each failure mode, should be realistic and not diverge from the general definition: "a belt has failed when it cannot transmit power with good functionality". A 100% rating should not be too far from this definition in the number of deformation cycles. However, major damage cannot be ignored even if in some applications the belt can be run for longer, thanks to the attention of service personnel.

Many difficulties are encountered when interpreting the data. The greatest source of errors is differences in interpretation of the belt damage. The subjective interpretation of damage by various technicians and their classification of damage may differ from our understanding of the information available on the data-sheets. As the two companies

represented here use different damage classification methods and routines, different algorithms were developed for the same failure mode in each case. For this reason it is not meaningful to make any absolute comparisons, nor is this meaningful even for a theoretical case when all the V-belt drive variables are the same, which they are not here.

The methods and algorithms below are the results of a study of the experimental data available. Our aim was to incorporate the most important damage mechanisms and define failure criteria to which stresses, strains or other quantities can be correlated in the local area where the damage occurs.

The following failure modes were defined:

- Radial Crack: This is crack growth in the hard rubber which carries the axial pressure. The main crack direction is radial. A 100% failure is defined as a crack running from the bottom of the belt up to the cushion rubber layer or cord layer, over the width of the belt. The cushion layer is the thin soft rubber layer that surrounds the cord.

  Design parameters could include tensile or shear stresses that govern the crack propagation in the area where the crack starts.

- Separation: Separation is classified as crack propagation along the belt or across the belt, close to the cord layer. Typical phenomena are: separation of the cord from the underlying cushion layer, separation of the cushion layer to the compression zone, crack propagation in the cushion layer, crack propagation in the upper part of the compression zone, and edge cord separation. A 100% failure is separation or cracking over the belt width or over a distance equal to a belt width along the belt except for edge cord separation where a distance of 5 times a belt width is allowed.

  Design parameters that govern crack propagation or cord separation could include shear stresses in the material layers under the cord layer.

- Cord breakage: A 100% cord break is defined as when more than 25% of the cords in the belt are broken or lost.

  Edge cord tensile stress is probably the design parameter.

Several failure modes can be active simultaneously, or one failure mode can initiate another failure mode. Here the radial crack failure mode has the highest priority. Next comes separation. This means that a radial crack can initiate a separation or cord break, and a separation can initiate a cord break. If a belt has had total tensile failure between two observations it is difficult to tell which failure mode caused it, as the belt has been completely destroyed. The following algorithm is used in such cases:

1. If, in the previous observation, radial crack damage of 75% of the actual limit has occurred, then it is classified as radial crack damage. The limit can be defined as 100% or lower.

2. If the condition above not apply and the previous separation damage has reached 50% of the limit, then it is classified as separation damage.

3. If none of those conditions apply, it is classified as cord break.

4.3 Correlation of fatigue life to failure modes

The results given below are presented for three different belt types: the .380 and .500 from Dayco Corporation [1], and the 5VX from Gates Corporation [2]. They are all raw edge V-belts with cog-shaped compression zones. For each belt type about 15 different tests have been performed at various combinations of force, pulley diameters, velocities, etc. These combinations cover a wide range of applications. However, the tests have been designed not to give too a long life. These are accelerated tests.

Four different levels of damage are presented for each failure mode. First, 100% damage as defined in the previous Section 4.2, then 50%, 10% and 1% damage. The 1% level probably represent the first recorded observation of damage for the actual failure mode in all cases .

The diagrams show that there is good correlation between belt life and different failure modes. Radial cracks dominate for belts with a long life. Separation occurs at more severe conditions and gives shorter life. Cord break happens in those cases where very short life is attained. In general this distribution has been achieved for

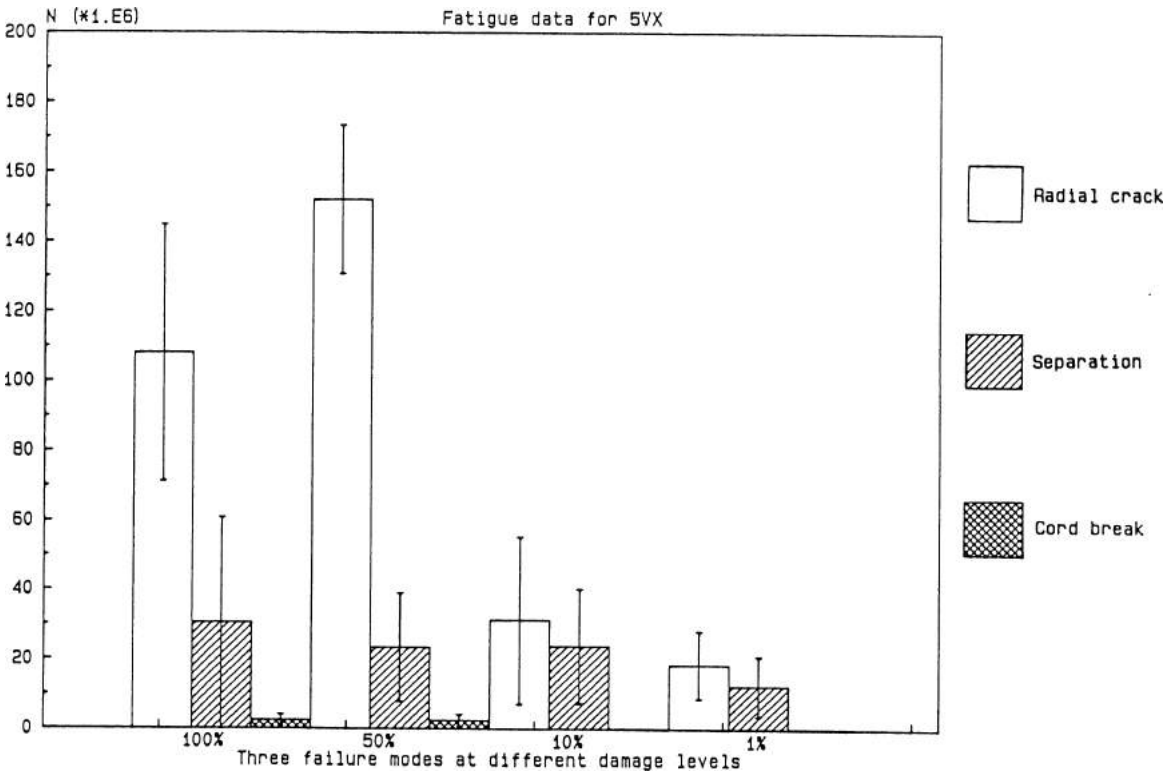

Figure 4.1 *Mean value and standard deviation of belt life for different failure modes and damage levels. Belt type 5VX [2]. Sixteen belts were tested.*

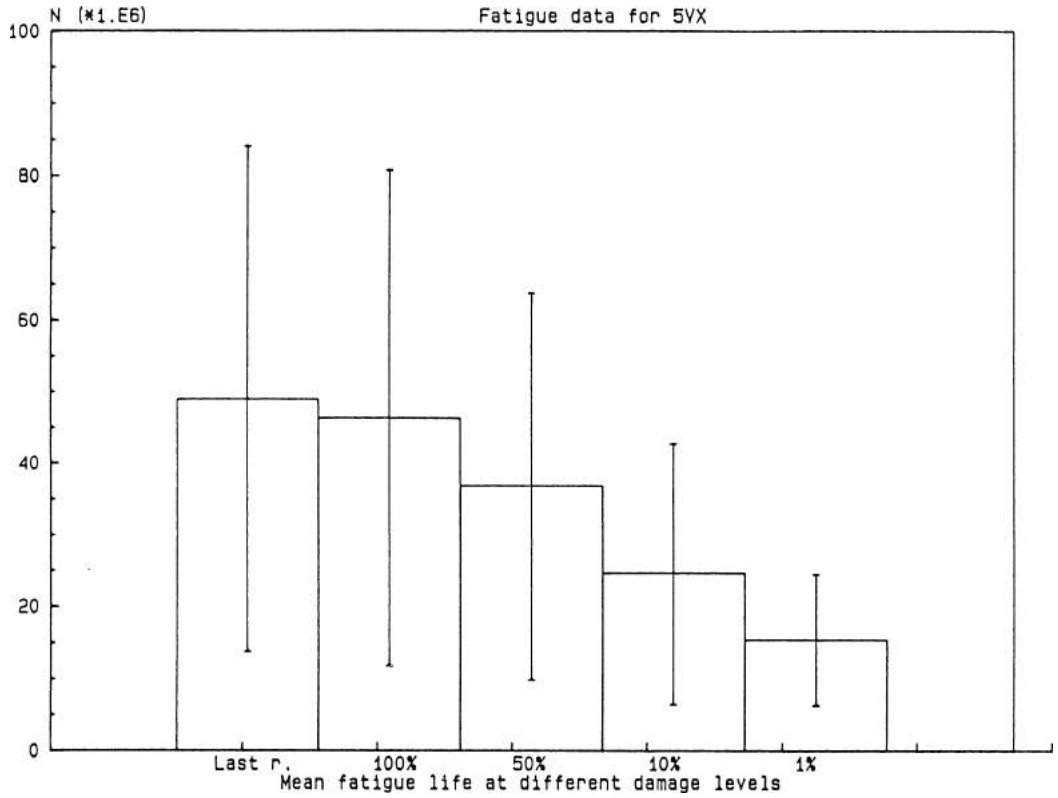

Figure 4.2 *Mean value and standard deviation of belt life for different damage levels and last recorded value. Belt type 5VX [2]. Sixteen belts were tested.*

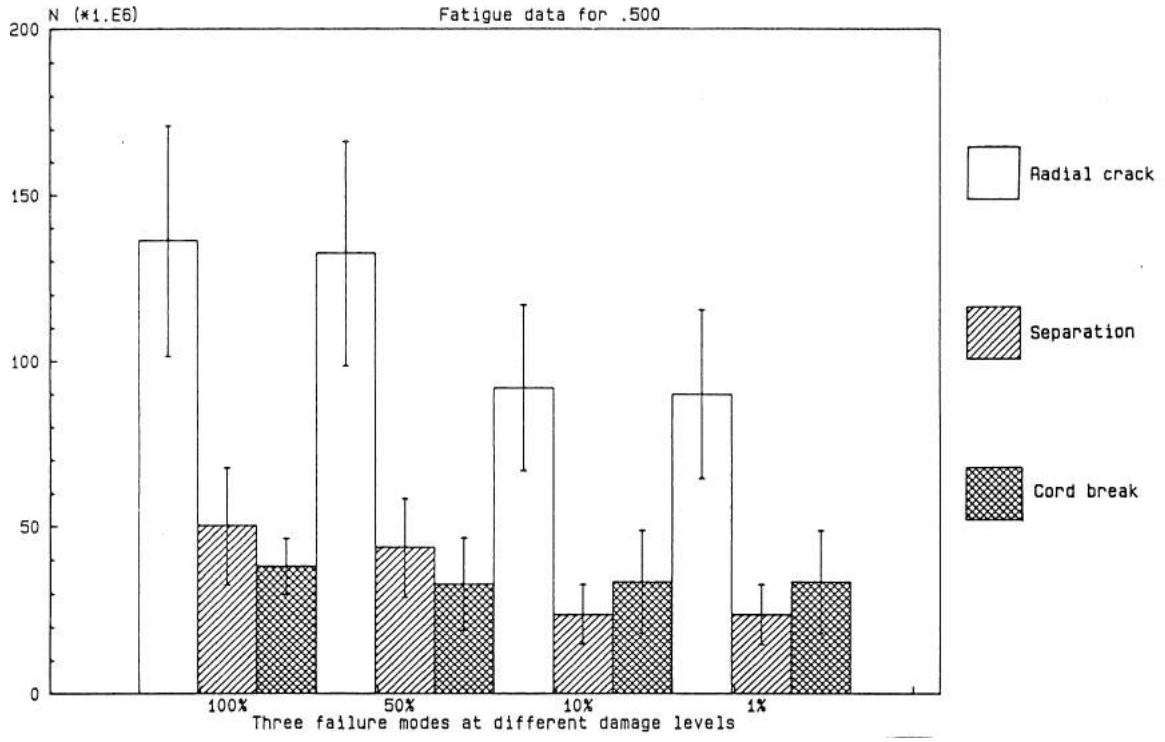

Figure 4.3 *Mean value and standard deviation of belt life for different failure modes and damage levels. Belt type .500 [1]. Sixteen belts were tested.*

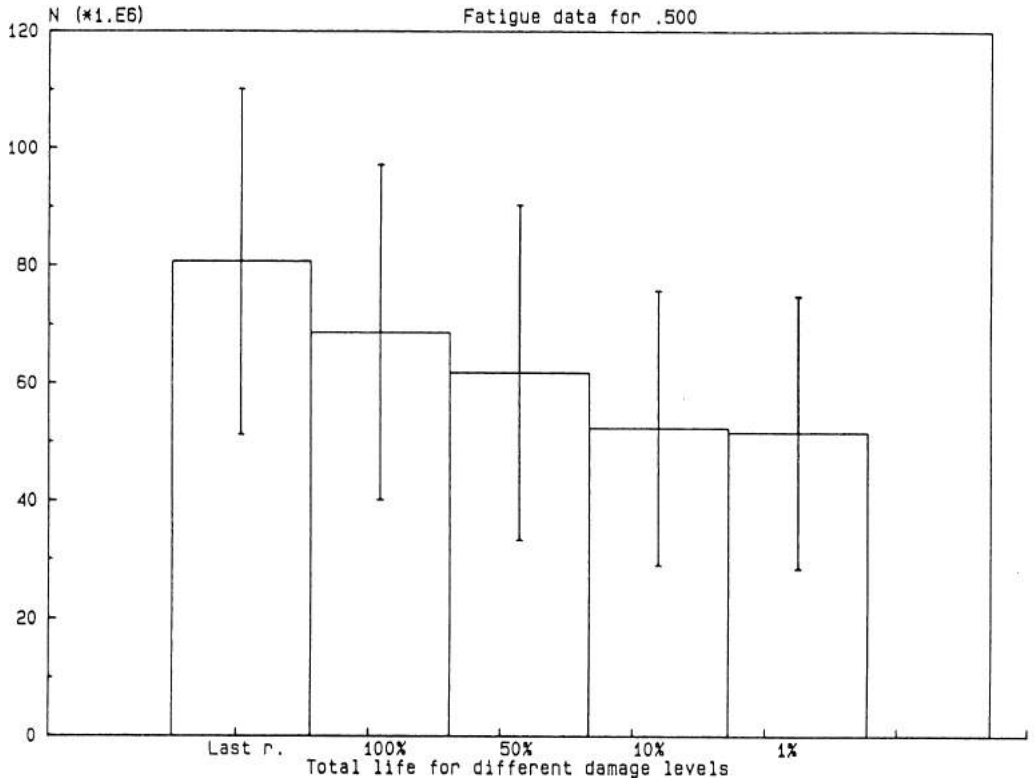

Figure 4.4 *Mean value and standard deviation of belt life for different damage levels and last recorded value. Belt type is .500 [1]. Sixteen belts were tested.*

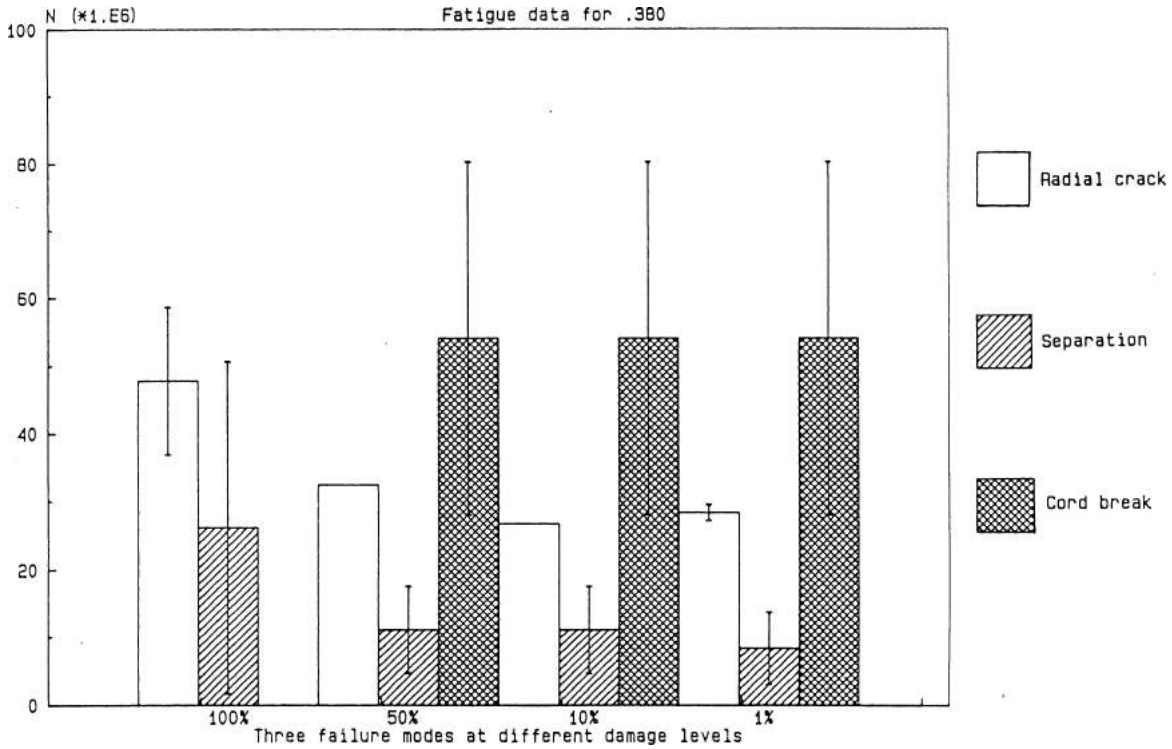

Figure 4.5 *Mean value and standard deviation of belt life for different failure modes and damage levels. Belt type .380 [1]. Thirteen belts were tested.*

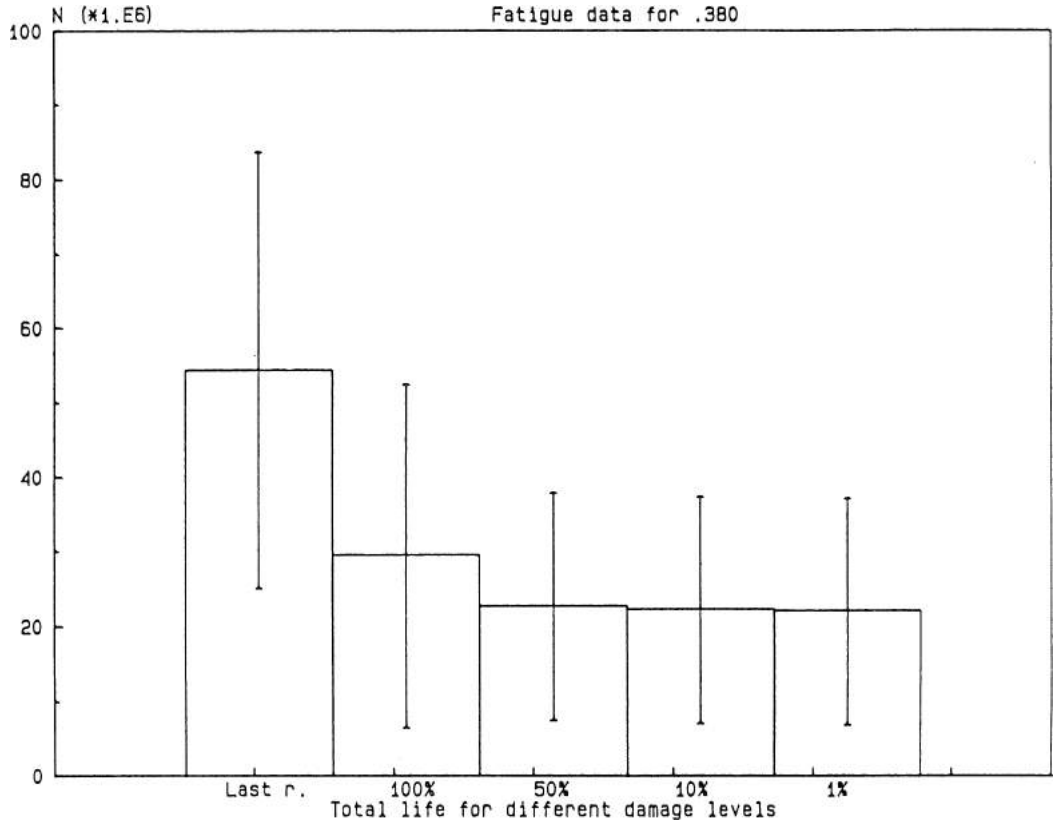

Figure 4.6 *Mean value and standard deviation of belt life for different damage levels and last recorded value. Belt type .380 [1]. Thirteen belts were tested.*

all damage levels studied. In Figures 4.2, 4.4 and 4.6 it can be seen that the 100% damage level does not differ much from the last recordings except for belt .380.

This result means that any of the four damage severity ratings can be chosen as a design level to which stresses, strains etc. may be correlated.

5
Discussion and conclusions

This experimental investigation, like previous work, shows that several different failure modes can be identified in V-belt fatigue. Here it is shown that the failure modes thus defined occur for such test conditions that long life can be associated with radial cracks, medium life with separation, and cord break with short life. Also, any damage severity level can be chosen as the design level.

These different failure modes are not recognized in the fatigue life prediction theory used to date, which is instead based on cord stress. However, if the belt type itself is not to be included in the theory as an experimentally determined constant, the theory has to be developed further in order to account for multiple failure mechanisms, etc. In reference [4] a theory is suggested that includes three failure modes.

Our aim is to have a theory in which the only experimental constants are material constants. Such a theory would make it theoretically possible to design a new belt type with a predicted life for a certain application. From the results presented in reference [3] we suggest that as a first step, much more effort should be put into modelling and understanding each failure mode and its governing parameter. From the results obtained, any simplified theory can be suggested.

6
Acknowledgements

Many thanks to the management at The Gates Corporation and The Dayco Corporation who made the experimental part of this investigation possible by giving me access to their experimental fatigue data.

Bibliography

[1] Dayco Corporation., Springfield Technical Center, Springfield, MO, USA, 1988.

[2] The Gates Rubber Company, Automotive Technical & Dev., Denver, CO, USA, 1988.

[3] D. Fritzson. *Material properties of elastomer composites in mechanical transmissions with special reference to V-belts*. No. 1988-05-25. Department of Mechanical Engineering, Chalmers University of Technology, Göteborg, Sweden: Division of Machine Elements.

[4] G. Gerbert. *Fatigue characteristics of V-belts*. Department of Mechanical Engineering, Lund Technical University, Lund, Sweden: Divison of Machine Elements, 1980.

[5] B. Horowitz. "Die zeitfestigkeit von gummi-keilriemen (The strenght of rubber V-belts)". In: *Gummi. Asbest. Kunststoffe* 23.8 (1970).

[6] O.G. Karbasov and V.Y. Menyak. *A mathematical model of the probability distribution of the failure of V-type fan belts.* RAPRA 6B221-9T. Zagorsk Branch of the Rubber Research Institute, 1968.

[7] O.G. Karbasov and V.Y. Menyak. *Prediction of the service life of V-belts.* RAPRA 6B221-95. Zagorsk Branch of the Rubber Research Institute, 1969.

[8] D. McCormick. "V-belts: stretching life and efficiency." In: *Design Engineering* (Apr. 1982).

[9] L.R. Oliver. "Contemporary methods in V-belt drive design." In: *Paper no. 76-1559*. American Society of Agricultural Engineers. St. Joseph, Michigan, 1976.

[10] L.R. Oliver et al. "V-Belt Life Prediction and Power Rating." In: *Journal of Engineering for Industry* (Feb. 1976), pp. 340–347.

[11] J.D. Shepherd. "Fundamentals of belt testing." In: *National Conf. on Power Transmission , BLLD 6021.8055, Vol 3*. 1976, pp. 78–89.

[12] J.D. Shepherd and L.L. Jackson. "V-belt Reliability - A Statistical Study of Large Sample Size Fatigue Tests." In: *SAE Technical paper Series 800446*. Society of Automotive Engineers Inc. Wallendale, Pennsylvania, 1980.

[13] V.A. Zhurov et al. "Failure of V-belts." In: *International Polymer Science and Technology* 2.1 (1975).

Part IV

Friction of elastomer composites - influence of surface temperature, sliding speed and pressure

Report IV

Friction of elastomer composites - influence of surface temperature, sliding speed and pressure

Dag Fritzson

Report No. 1988-05-26
Division of Machine Elements
Department of Mechanical Engineering
Chalmers University of Technology
Göteborg, S-412 96 Sweden

1 st version completed 1987

Abstract

The friction coefficient of elastomer composites sliding on a cast iron surface has been investigated. The parameters studied were pressure, sliding speed, and surface temperature.

The most important finding of this experimental investigation is that the friction coefficient is highly dependent on the surface structure, which is in a state of continuous change during the test. This phenomenon causes the greatest variation in friction coefficient thus dominating the other effects.

Two methods have been developed to measure the temperature of the contact surface of the rubber sample. In the parameter interval of this test program, normally no more than a 3-4 degree temperature increase over the environment is obtained for the highest speed and pressure. The loss heat generated in the friction contact is mostly conducted off through the cast iron disk and not through the rubber composite.

Contents

1
Introduction

In any method of measuring friction there are two contacting surfaces, a way of providing relative motion between them, and a means of measuring the resistant force. Static friction is a special case and occurs when the relative motion starts from a state of rest. If the static friction is greater than the dynamic friction, stick slip may occur under certain conditions. It is quite common to refer to the coefficient of friction, which is the ratio of frictional force to normal force according to practice established over the past three centuries. However, the mistake should not be made of referring to this as a "law of friction" and assuming that the coefficient of friction is a constant. The friction force between two materials in any given combination depends on the nature of the surfaces and varies with many factors such as surface temperature, environment temperature, sliding velocity, surface finish, time of contact, environment atmosphere, normal force, the physical dimensions of the contact surface, etc. The normal force is just one of the parameters and may not be the most important one. Thus, in any test program it is necessary to specify the test conditions closely and carry out measurements over a suitable range of conditions, depending on the application in which they are to be used.

It is necessary to have knowledge about the friction coefficient in order to analyze the function of a transmission based on friction. In this report, the friction coefficient between materials normally used in V-belt transmissions is experimentally investigated as a function of pressure, sliding speed, surface temperature and environment temperature.

2
Notation

T	Temperature (°C)
p	Surface pressure (MPa)
F, N	Force (N)
V	Sliding speed (m/s)
μ	Friction coefficient (-)

3
A V-belt transmission

3.1 Material properties

Today a V-belt is built out of several layers of different elastomer composites. In the longitudinal direction there is cord which carries the forces between the pulleys. A typical elastomer composite for V-belt applications consists of elastomer, carbon black and several other additives, and is reinforced with fibers in one direction. This gives the material anisotropic characteristics. Elastomers exhibit viscoelastic properties when loaded, and a hysteresis loop is obtained during cyclic deformation. Some of the additives, in particular carbon black, increase the hysteresis. In order to decrease bending losses and at the same time decrease temperature, which affects fatigue life, the belt is normally designed with a cog shape as shown in Figure 3.1.

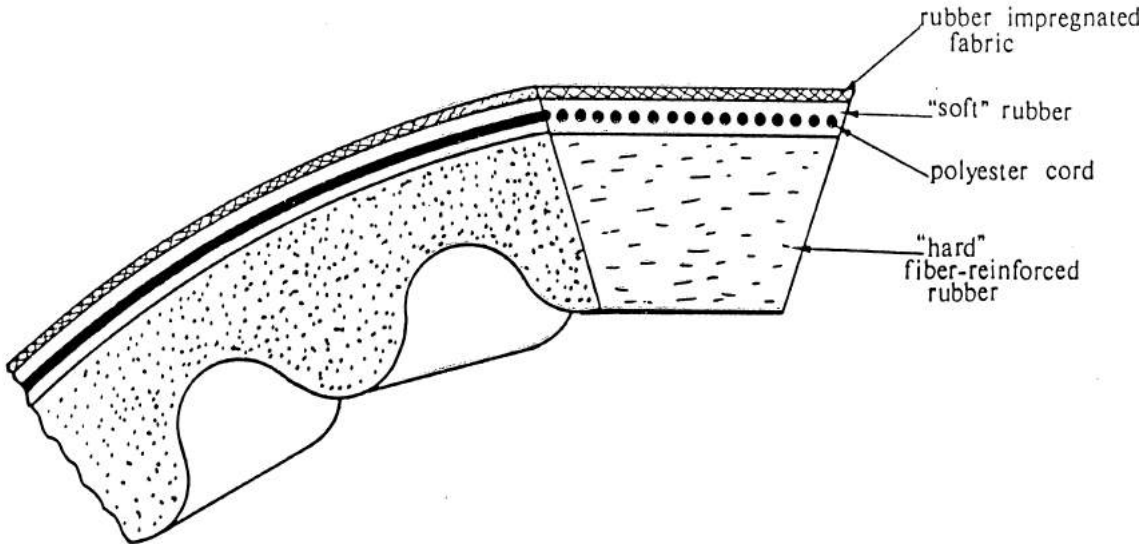

Figure 3.1 *A normal V-belt design.*

3.2 Power transmission

The mechanics of a V-belt transmission have been investigated [7] over many years. The theory explains the interaction between belt and pulley. The hard fiber reinforced rubber in the pressure zone carries all the contact forces and transmits the friction forces to the cord. The friction coefficient must be established as a function of such parameters as material combination, pressure, sliding velocity and temperature.

4
Previous work

The phenomenon of friction between, elastomers and other materials has long been subject to investigation and many theories explaining the behavior have been suggested [9, 16, 14, 4, 15, 20], [2, 1, 5, 10] [11, 3, 17, 13, 8]. This interest is quite natural, as elastomer materials are often used precisely because of their friction characteristics. The following conclusions can be drawn:

- Friction is not only an adhesive and abrasive process, viscoelasticity or hysteresis is also very important because, among other things, it causes energy losses, which arise from the deformation of the rubber by surface asperities.
- The friction characteristics are highly dependent on the actual mixture of the elastomer material. Rubber is not a well defined material group, nor to the friction coefficient well defined.
- Friction is dependent on pressure, sliding speed, temperature, environment and history.

The friction properties of all elastomers depend on velocity. However, the influence of velocity cannot be isolated from that of temperature for two reasons. First, since elastomers are bad thermal conductors, any heat developed at the interface is likely to cause local temperature changes, an effect which is bound to be more pronounced at high velocities. Secondly, in those cases where friction is dominated by a hysteresis loss mechanism, the position of the loss peaks is a function of both velocity and temperature. Therefore two temperatures should be considered: the temperature of the elastomer surface layer and the environment temperature. The tests presented in the references above were done at such low speeds that there was either no significant temperature change or only the environment temperature was presented.

The condition of both surfaces is dependent on history. It is important to start with clean surfaces. As testing proceeds both surfaces become more polished and contaminated by wear products. After some time, equilibrium conditions can be reached. For the RAPRA/Davenstest apparatus it took about fifty test runs before service equilibrium conditions could approximately be represented [9].

For V-belt applications the friction coefficient is essential for the functionality of transmitting torque and angular speed. There are experimental investigations in

which whole V-belts have been tested [6, 19]. Advantages of this method are that the conditions are very close to those of a running V-belt drive and that the belt is not destroyed. Two reports are discussed below.

In the first report the friction was investigated for whole V-belts [6]. The friction coefficient was determined as a function of pressure and sliding speed. Three different methods were developed and evaluated. In the method used, two plates of steel were used to simulate a part of a grove of a pulley. The plates were held immobile and the belt rotated in order to obtain sliding along the peripheral direction of the belt. Here the normal force has to be calculated. The sliding speeds were 8.5, 40 and 70 mm/s. The pressure was varied at three different levels from about 0.2 MPa to 5.5 MPa. These tests were done at room temperature.

In these tests, the friction coefficient generally increased both with pressure and sliding speed. The results depend very much on the type of belt or mixture of rubber used. The running time was an equally important parameter. V-belts which have been conditioned by running them for several hours have a friction coefficient at a different level. Depending on belt and rubber mixture the level is higher or lower. The variation caused by the parameters of pressure and sliding speed seem to decrease for a conditioned belt.

No temperature measurements of the belts were made, and may not have been necessary since the speed intervals were not great.

It should be pointed out that the whole belt side-wall, which consists of different kinds of elastomer materials, was tested simultaneously. Also, a variation in pressure was to be expected, as the pressure distribution was not controlled. Both of these factors mean that the design of the belt and not only the materials influenced the friction.

In the second report the radial coefficient of friction for whole V-belts was tested as a function of sliding speed [19]. The axial force was held constant and the temperature was at a room temperature level. The belt was moved down between two pieces of steel, where one was fixed and one was movable. This represents a sheave with constant axial load. Here the radial coefficient of friction has to be calculated. It is averaged for the different materials of the side-wall of the belt and also for variations in pressure over the belt side. Four positions on each belt were tested. New belts were tested as well as belts conditioned by running them in a dead weight test drive for a given load and time period, depending on belt type.

The results show that for the kinds of belts tested the friction coefficient increase a few percent for an increase in speed of a factor of two. However, the decrease of about 20 percent of the friction coefficient for the conditioned belts is much more significant.

These results agree with the results from the first report, as far they go. The same problems also occur. For example, the pressure may vary over the belt side. There is a very small variation in speed in this investigation. There is no temperature or pressure variation. The report also points out that tests have to be done on a conditioned surface.

5
The friction test apparatus

5.1 Introduction

The purpose here was to design apparatus for investigation of the friction properties of relatively soft materials like elastomers when sliding against various hard surfaces.

Of the test apparatus found in the literature the RAPRA apparatus [9, 12] seemed to be most interesting. However, it requires a tensile testing machine which allows for continuous operation. Unfortunately the sample is in contact with the surface only during half of the testing time. Due to the fact that "running in" or conditioning of the test sample is an important part of the test, a principle that allows continuous operation, i.e. a pin disk machine, was preferred.

In general, the work needed to design a test apparatus is a continuous process of design, test, evaluation and redesign. This process goes on until the desired tests can be performed with acceptable accuracy. From the experience obtained just as much can be learned as from the final test program.

5.2 Description of the test apparatus

The basic principle behind the friction test apparatus is illustrated in Figure 5.1. A thin sample is glued on to a holder which is held stationary, and a given force applied. The surface moves at a certain speed. The velocity, force and environment temperature can be varied. When changing test sample both the holder and the sample are replaced as they are an integrated part. Normally, all the integrated test samples needed are prepared before a test series is performed. Thus it is very easy to change test sample.

The complete test apparatus except for the electronic equipment is illustrated in Figures 5.2, 5.3 and 5.4. As shown it is basically a kind of pin-disk test apparatus. Both the pin and the disk can easily be changed.

The available slip velocities depend on the transmission used. Here the speed is continuously variable within an approximate ratio from 1 to 1000 . The normal force can be varied within a wide range as it is only a function of the weight and the length

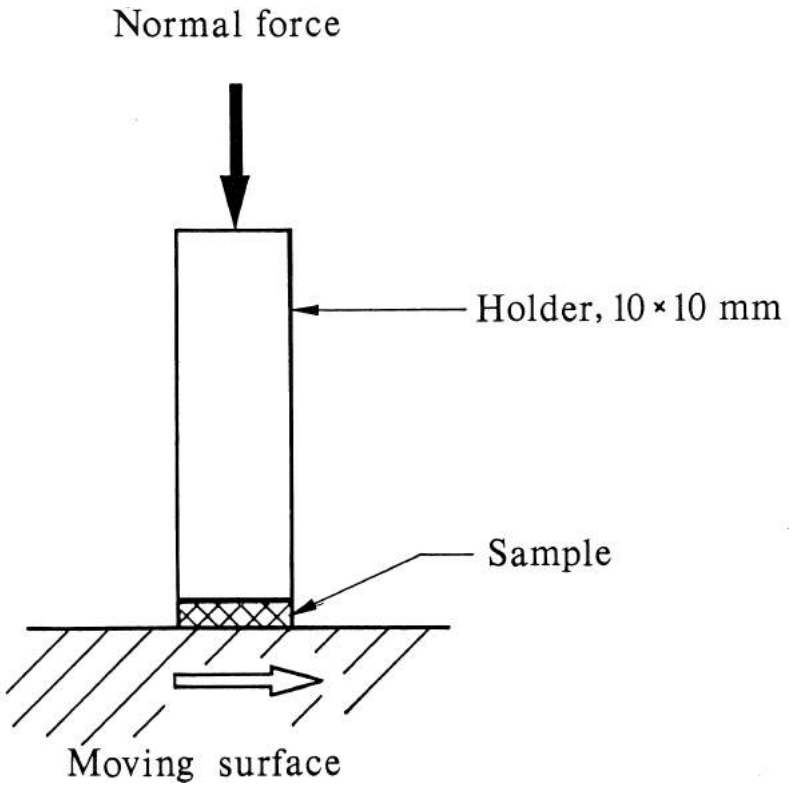

Figure 5.1 *A test sample.*

of the loading arm, which can be shortened to half its length if necessary. However, first the force transducers have to be exchanged, since these have a limited ratio for a certain accuracy. The arm with the sample and its holder is slid through a linear ball bearing, which allows axial movement but prevents rotation in all directions. In this way the sample is held 90 degrees perpendicular to the disk. The force transducer is mounted in the same plane as the disk surface, and with the ball bearings used this guarantees that no errors in force measurement are introduced. With the help of the pneumatic cylinders, which are controlled by the test computer, the sample can be lifted and moved in the radial direction on the disk or to the position of the infrared detector. A climate box with a hot air fan makes it possible to perform testing at elevated temperatures.

The angular speed of the disk is recorded using a pulse detector. The environment temperature is measured using four different thermistors placed in the climate box. The mean temperature value is used. The friction force is sampled about 100 times or more during one revolution of the disk. Here the mean force value is used in order to eliminate stochastic errors due to vibrations and varying surface structure of the disk along the circumference. The standard deviation is monitored because it acts as an important signal if something goes wrong.

The test apparatus is completely computerized. Measurements, calculations, data storage, and data presentation are done using programs running on a HP-computer connected to the necessary electronic equipment. Both calibrations and tests are run on the same program.

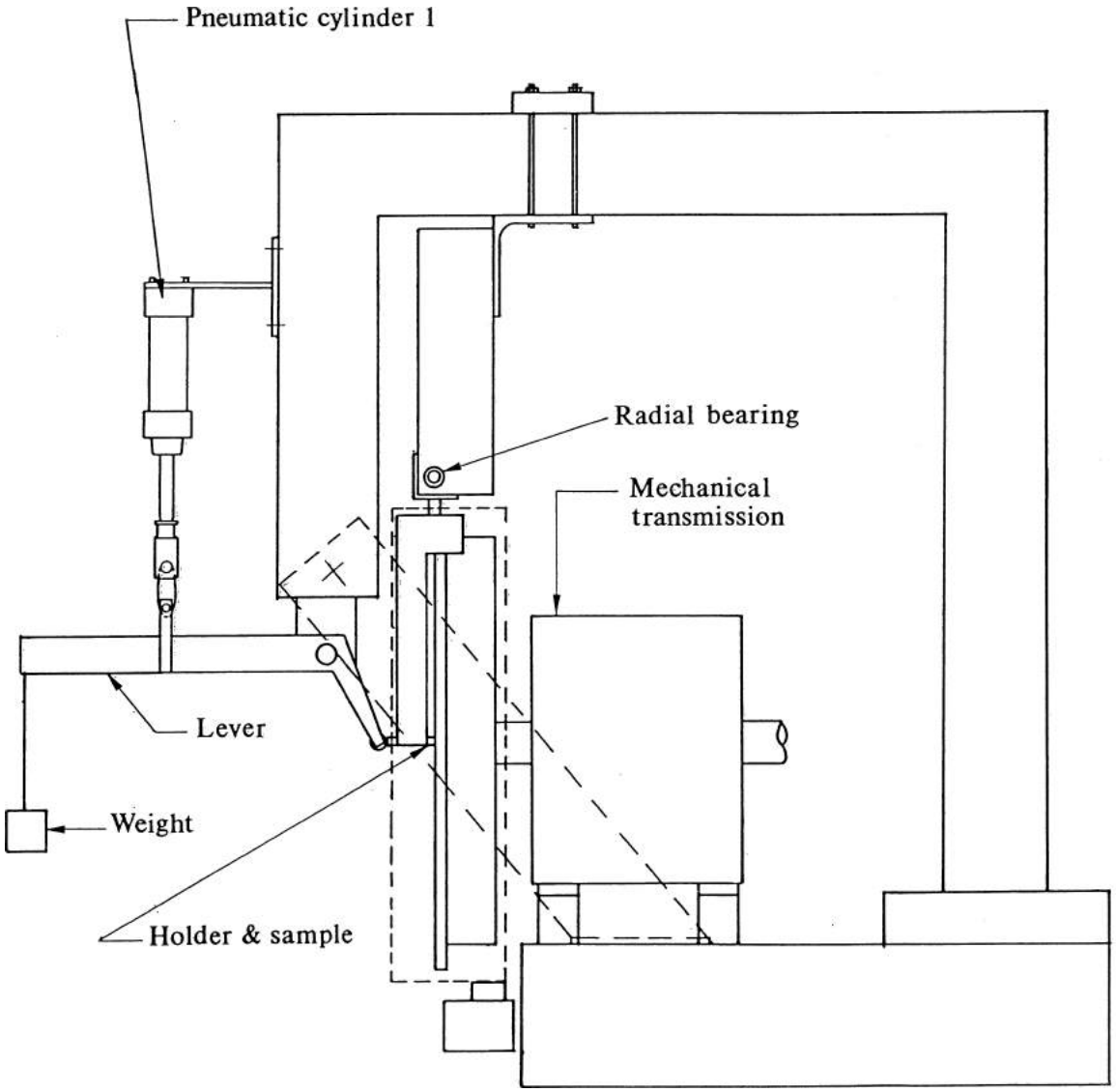

Figure 5.2 *The test apparatus. A side view.*

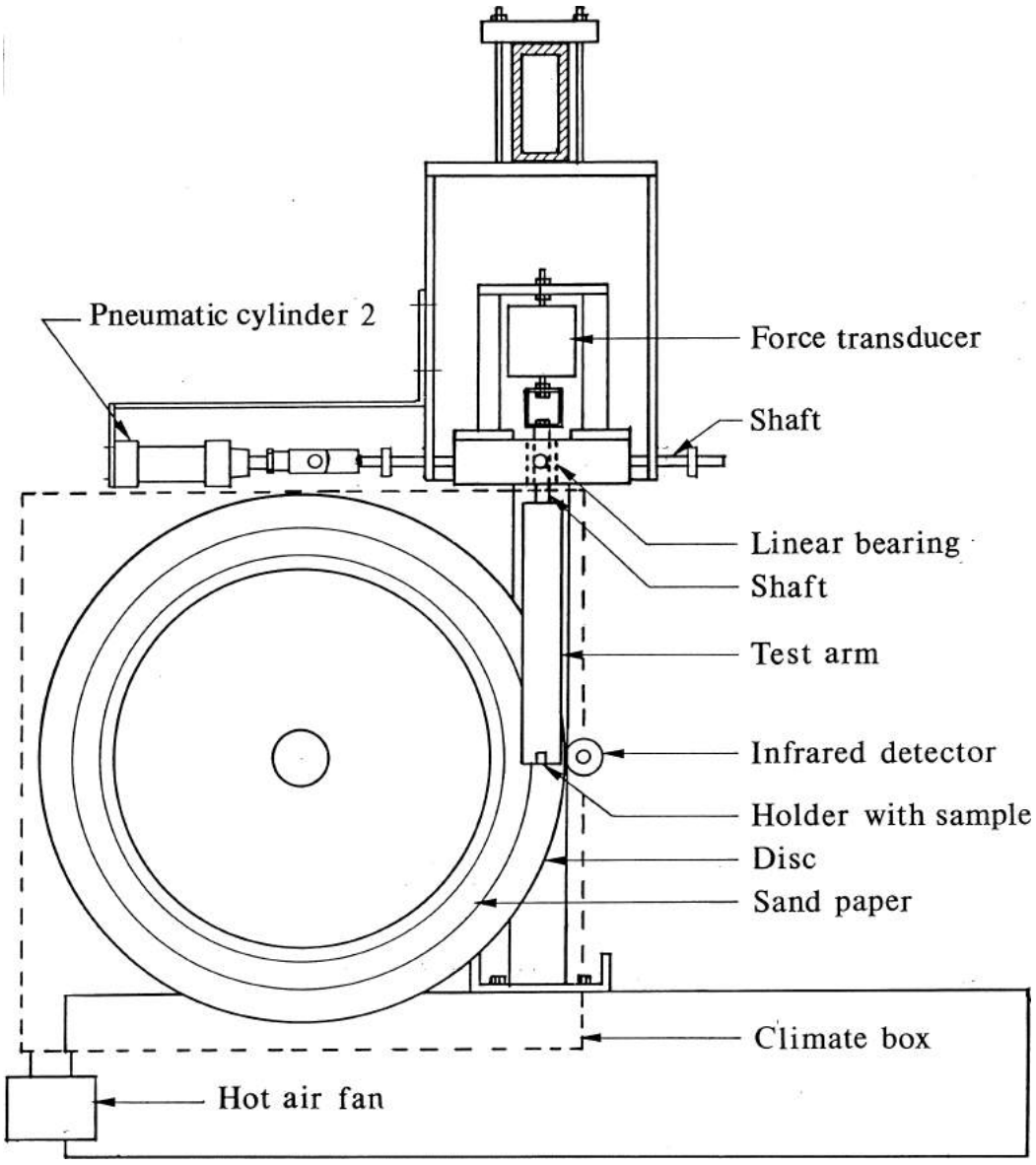

Figure 5.3 *The test apparatus. A front view.*

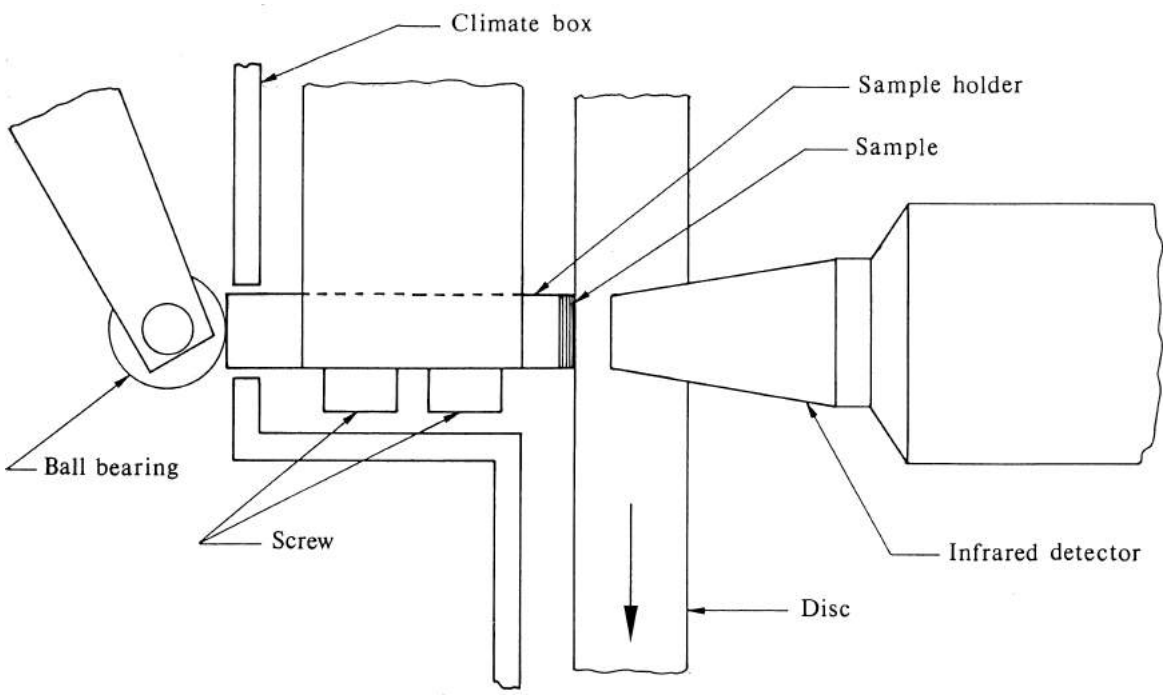

Figure 5.4 *A detail of the part where the sample and the holder are situated.*

5.3 The contact surface temperature measurement method

The important temperature to relate to the friction characteristics is the temperature of the surface layer. This is not the same as the environment temperature or the temperature in other parts of the sample. How great the difference is depends on factors such as geometry, viscoelastic properties, heat conduction of the materials, heat produced by friction, etc. This means that if test results, e.g. produced by this apparatus, are to be compared with tests subject to other geometry and conditions, for instance a V-belt drive, then the temperature of the material layer on which the friction mechanism is working should be used.

The problem of measuring contact temperature is very difficult. This is because nothing that alter the conditions can be inserted in the contact if the result should be useful. Two approximate methods were developed and used simultaneously for verification and comparison.

First, the thermocouple method, which is based on an approximation in distance. A very thin thermocouple wire (0.2 mm) is inserted at 0.5 to 1.0 mm depth into a cut in the middle of the sample. This is shown in Figure 5.5. It is assumed that there is no significant difference in temperature between the surface layer of the rubber and the wire position. The fact that the thermocouple, together with the necessary electronic equipment, correctly records temperature has been verified.

The second method is based on an approximation in time. By using an infrared detector the surface temperature of a rubber sample can be recorded with good accuracy. The detector which measures the infrared radiation must point towards the surface. This means that the sample must be moved from the disk to a certain measurement position (see Figures 5.4 and 5.3). This movement takes only 1-2 seconds as it is done using pneumatic cylinders which are controlled by the computer. This time and the measurement time needed by the infrared detector means that the temperature thus measured is a bit down on the cooling curve of the surface. In order to get a value of the original temperature, extrapolation was done backwards in time, as illustrated in Figure 5.6. The curve fitting and extrapolation were done using the computer test

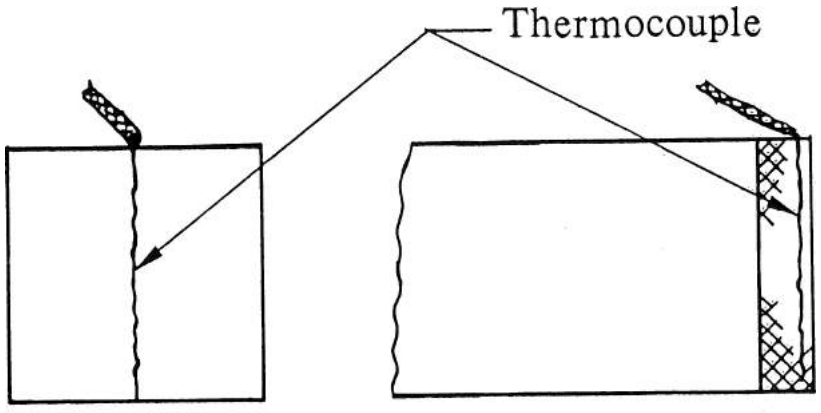

Figure 5.5 *The thermocouple inserted into the test sample.*

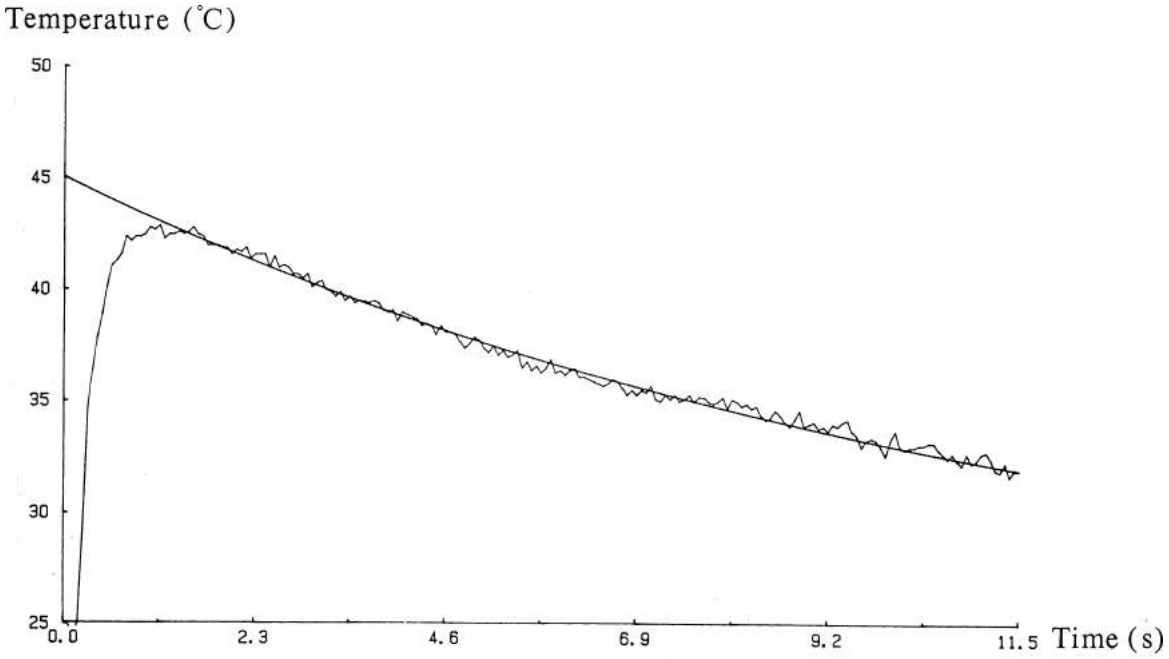

Figure 5.6 *A temperature curve form the infrared detector and the extrapolation curve.*

program.

These methods were verified by holding a sample with a holder against a surface with a known temperature. For the thermocouple method the temperature could be recorded directly, but for the other method the sample had to be moved to the infrared detector. The two methods were in good agreement but showed about 20 percent lower temperature than the surface of the disk. This result is quite natural, as the test case is heat flow from a hot disk (100 °C) to a cold environment (20 °C) through the contact and the rubber sample with the holder. The rubber surface should have a lower temperature than the disk surface, as only the asperities of the surfaces are in contact. The greatest temperature drop should be in the contact. This problem does not occur in a real case, when the heat is generated at the contact or in the surface layer of the rubber.

6

The test procedure and the tested material combination

Two different elastomer composites have been tested in this investigation. These materials are referred to as A and B and are shown in the Figure 6.1. The materials are reinforced with fibers in one material direction. Material A has more reinforcement and is harder than the other material. For material A sliding is tested orthogonal to the fiber direction, and for material B along the fibers. This represents a V-belt application as presented in the Figure 6.1.

The parameter intervals were chosen to represent conditions normal in V-belt applications. The following values were used.

Sliding velocities:	0.00033	0.0095	0.271	[m/s]
Contact pressures:	0.136	0.491	0.847	[MPa]
Environment temperatures:	25	65	95	[°C]

The disk is made of cast iron, which is the most widely used material in pulleys. The surface has been finely lathed and then polished with an emery cloth. In the radial

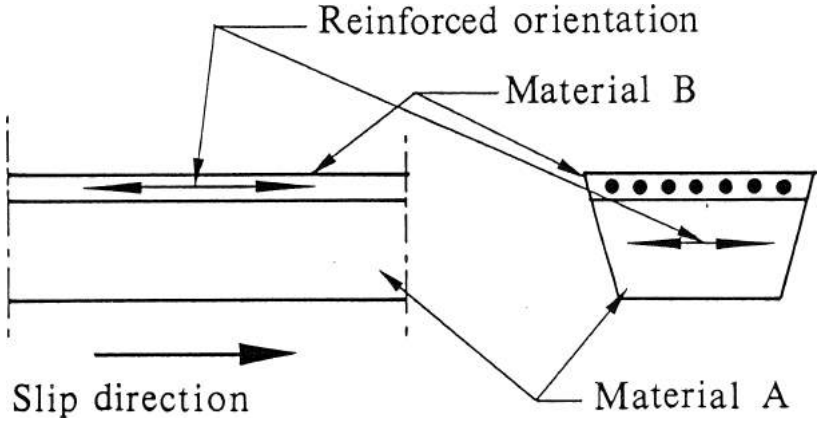

Figure 6.1 *The tested materials of a V-belt.*

direction the surface has a smoothness of R_a 1.74 μm. The circumferential direction, which is the sliding direction, is much smoother due to the machining process used.

A new sample is conditioned before any tests are run. First it is ground down about 0.3 mm in its mounted position on the arm at the test apparatus. This is done to ensure perfect contact between the disk and the rubber surface, which guarantees an even pressure distribution. It is done by allowing the sample to slide on the sandpaper-covered path of the disk for about 2 minutes. Secondly, the sample is "run in" at the highest speed (0.27 m/s) and lowest pressure (0.136 MPa) until the friction coefficient has stabilized. This takes about 3 hours.

The tests start with the highest speed, lowest pressure and lowest temperature. After tests are done at the three different speeds the pressure is increased and the process is repeated. Each separate parameter combination or test takes about one hour. The highest speed is chosen first because at each pressure level the sample has to be "run in" or conditioned for the new pressure. This is done most quickly at a high speed. After a complete set of 9 tests at each temperature level the sample is completely conditioned as has been described above for new samples. Because about 0.3 mm material has been ground away and a new surface has been exposed, there is no difference between a conditioned sample and a new one. It takes a long time to change temperature level. Therefore, this is the last parameter to be changed.

The test procedure described above is the result of experience from extensive preliminary tests series [18].

7
Test results

7.1 Introduction

Three independent test series have been run on material A and two on material B . Each one of these test series, which have 27 parameter combinations, took about one week to complete [18]. For one normal test case or parameter combination, which takes about one hour to complete, the friction coefficient presented below is the mean value of the last ten minutes of the test.

Various aspects of the test results are discussed in the different sections below. Special attention should be given to the first section where the surface and time effects are presented.

7.2 The surface of the sample and changes with time

Our results show that the surface structure of the sample has a major impact on the friction coefficient. The materials tested were composites. The fibers seems to have different friction characteristics than the matrix which consists of rubber. This means that the amount and location of the fiber in the surface layer are of importance for the friction. The surface also changes with time, as it is continuously worn down.

The surface structure is highly dependent on the applied pressure. This can be seen in Figures 7.1 to 7.6. At low pressure a smooth surface is obtained, but at high pressures the surface is covered with pits. This is caused by the fibers, which are more resistant to wear than rubber and are not evenly distributed within the surface layer. A surface section with a large amount of fiber has better resistance against wear than a section with a small amount of fiber. This means that a “hill” is created on the first surface section.

Figure 7.1 *Characteristic surface structure for material A. Environment temperature 25 °C. Sliding speed 0.27 m/s. Pressure 0.136 MPa. Sample size* 10 *mm* · 10 *mm.*

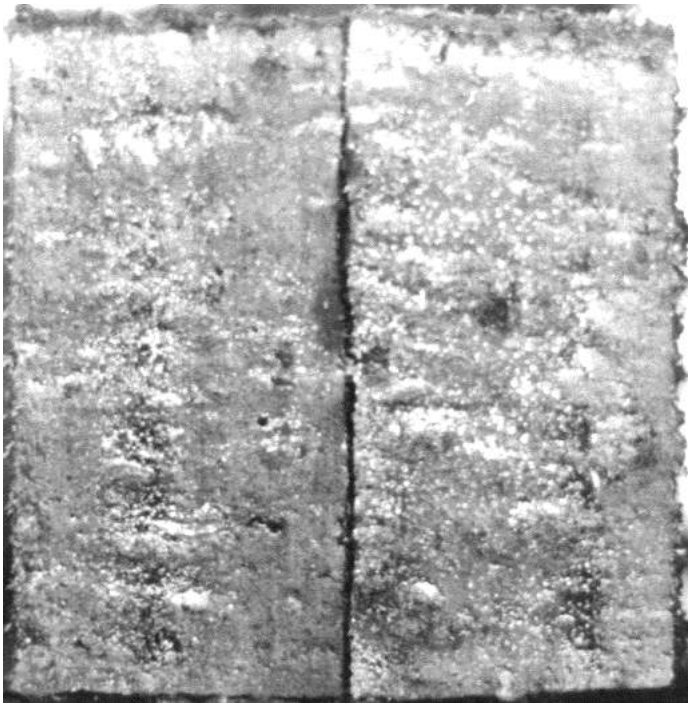

Figure 7.2 *Characteristic surface structure for material A. Environment temperature 25 °C. Sliding speed 0.27 m/s. Pressure 0.491 MPa. Sample size 10 mm · 10 mm.*

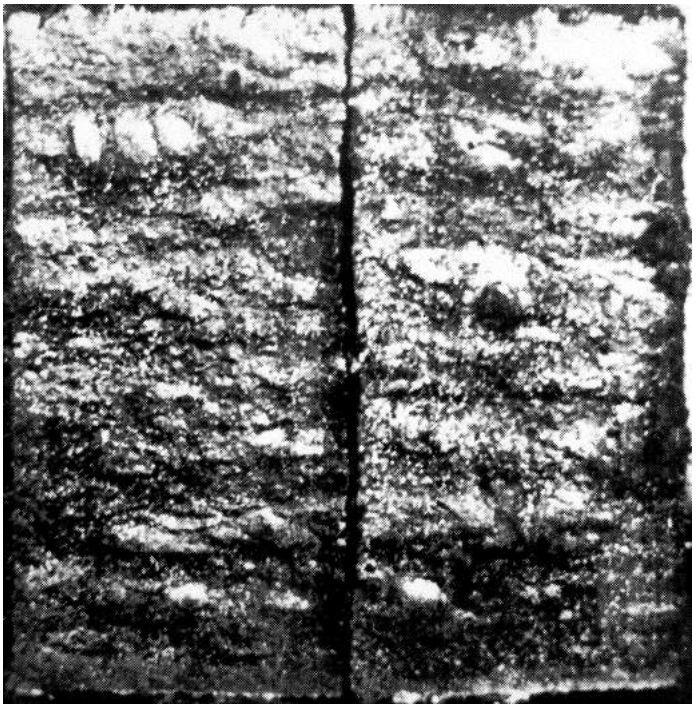

Figure 7.3 *Characteristic surface structure for material A. Environment temperature 25 °C. Sliding speed 0.27 m/s. Pressure 0.847 MPa. Sample size 10 mm · 10 mm.*

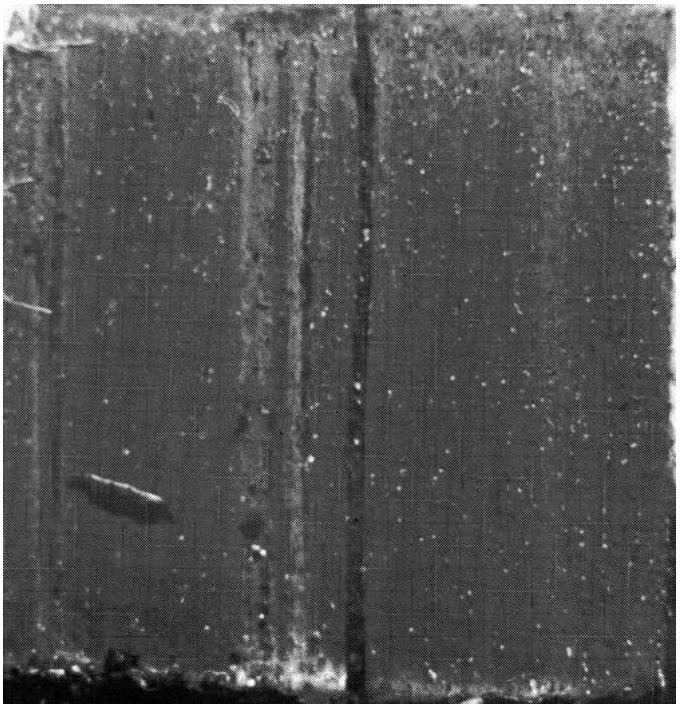

Figure 7.4 *Characteristic surface structure for material B. Environment temperature 25 °C. Sliding speed 0.27 m/s. Pressure 0.136 MPa. Sample size 10 mm · 10 mm.*

Figure 7.5 *Characteristic surface structure for material B. Environment temperature 25 °C. Sliding speed 0.27 m/s. Pressure 0.491 MPa. Sample size 10 mm · 10 mm.*

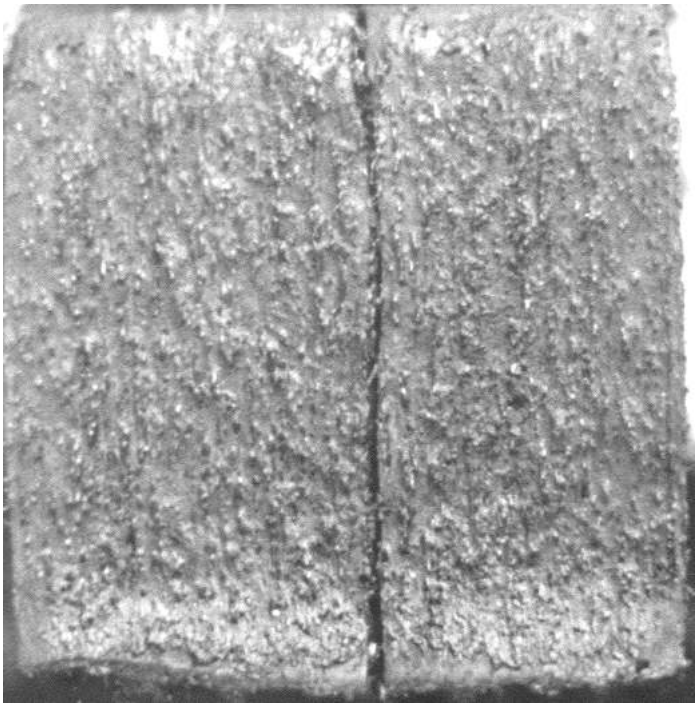

Figure 7.6 *Characteristic surface structure for material B. Environment temperature 25 °C. Sliding speed 0.27 m/s. Pressure 0.847 MPa. Sample size 10 mm · 10 mm.*

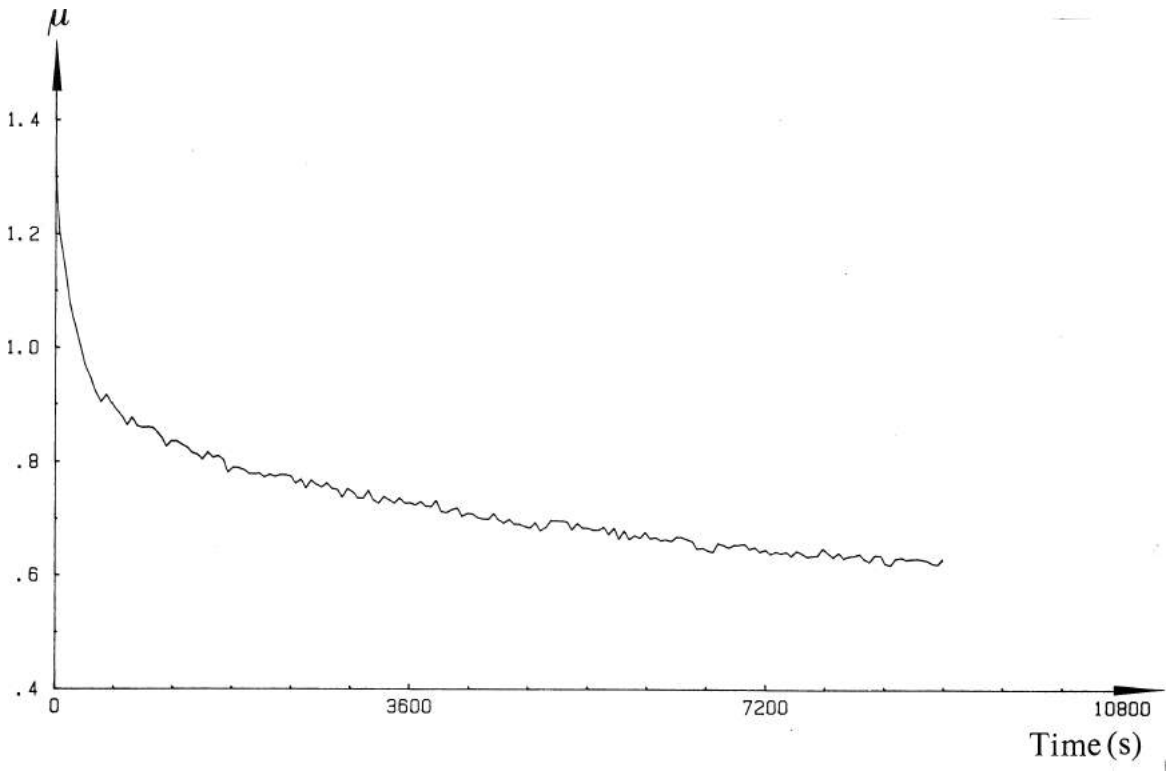

Figure 7.7 *Friction coefficient during a conditioning process for material B. Environment temperature 25 °C. Sliding speed 0.27 m/s. Pressure 0.136 MPa.*

A sample which is conditioned at a high pressure and therefore develops a pitted surface, and which is later tested at low pressure exhibits a lower friction coefficient than a sample conditioned at the same low pressure.

Because the process described above is a function of sliding distance it is also a function of time. If the material has an uneven distribution of fibers at different material depths, the friction coefficient will not stabilize. In Figure 7.7 a conditioning or "running in" process is shown for material B. Some tests are plotted in Figures 7.8 and 7.9.

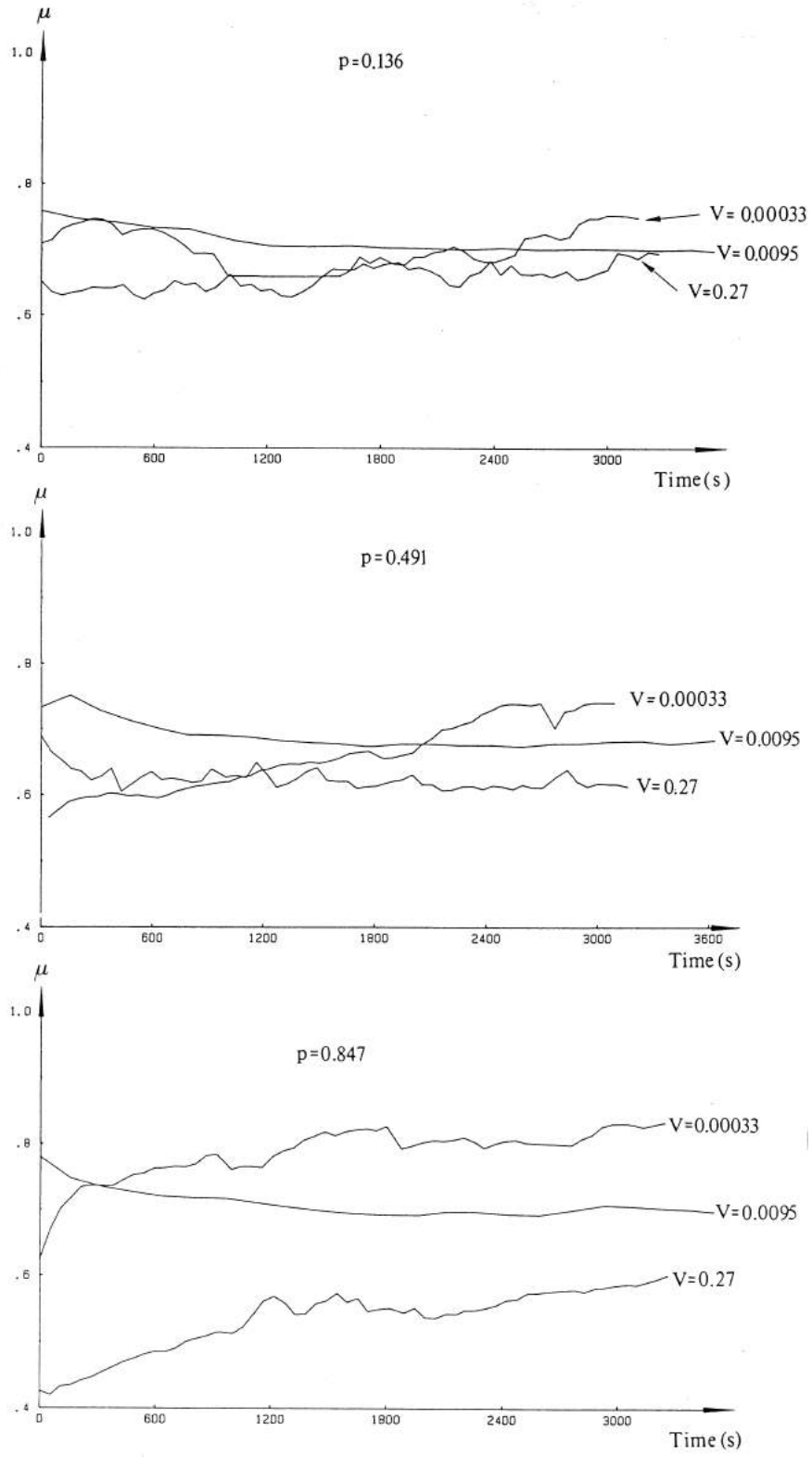

Figure 7.8 *Friction coefficient during test runs for material A. Environment temperature 25 °C. Pressure given in MPa and sliding speed in m/s.*

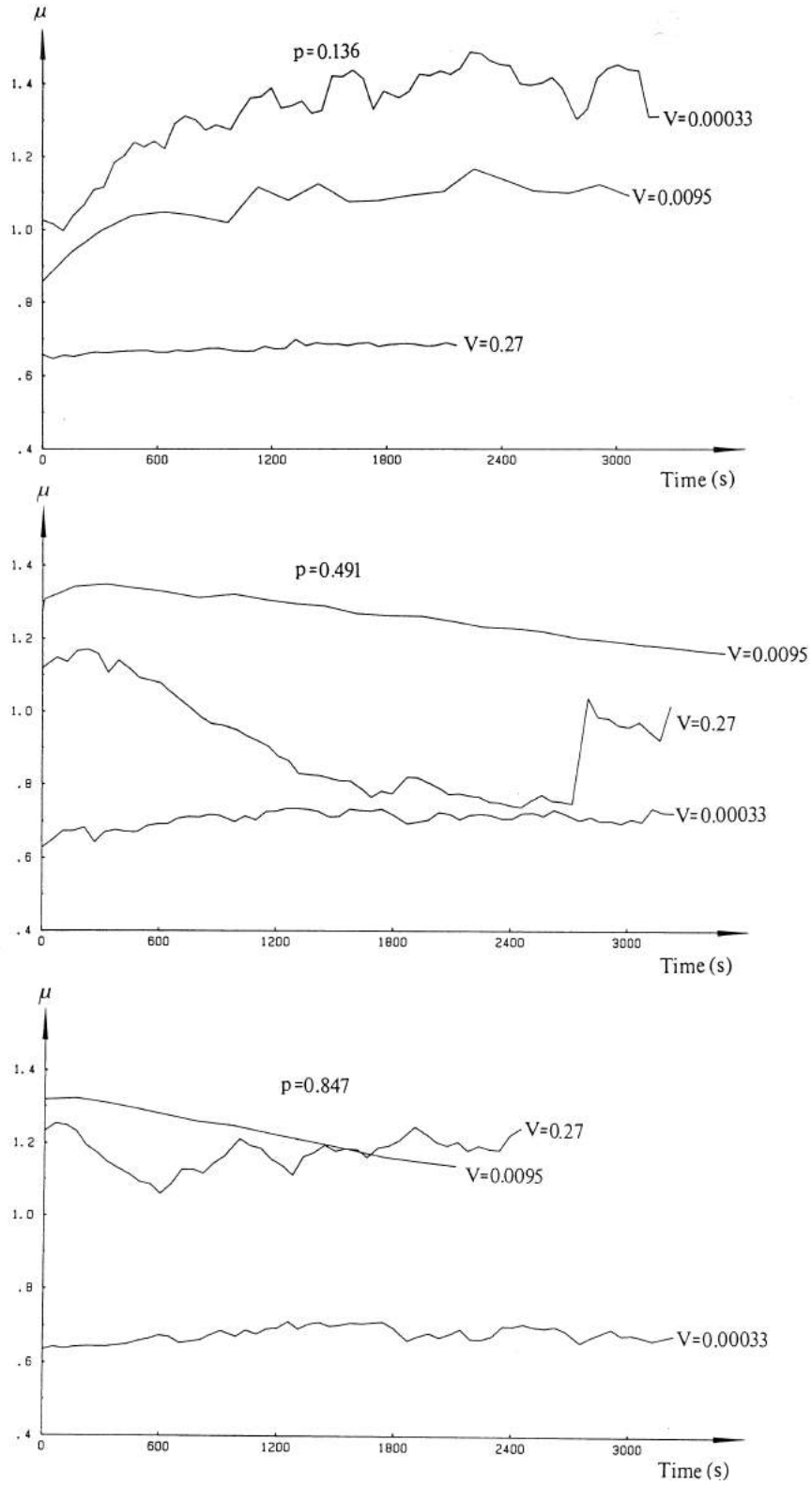

Figure 7.9 *Friction coefficient during test runs for material B. Environment temperature 25 °C. Pressure given in MPa and sliding speed in m/s. For V = 0.27 m/s and p = 0.491, 0.847 MPa, the stick slip phenomenon is observed.*

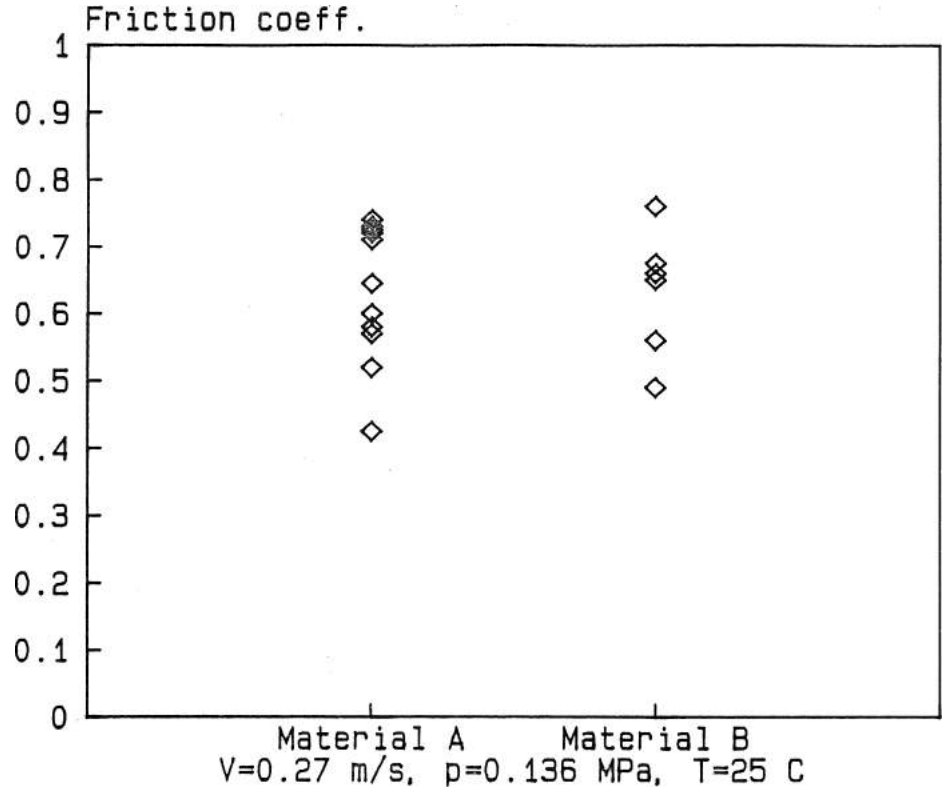

Figure 7.10 *The variation in friction coefficient due to surface structure.*

This results in large variations in friction coefficients among the separate tests. There may be a variation between 0.4 - 0.8 due to the surface structure. This is illustrated in Figure 7.10 where the total number of tests available is plotted for the parameter combination for which conditioning has been performed. More than three independent tests are necessary to get a good estimate of the absolute level of the friction coefficient.

7.3 The difference between surface and environment temperature

In Tables 7.1 and 7.2 we present the temperature differences between the rubber surface and the environment, for test cases at room temperature. As previously discussed, both of the two temperature measurement methods are used only at the room temperature level. For elevated temperatures the thermocouple method exclusively was used.

The stick slip phenomenon only occurred for four tests at the room temperature level (see Table 7.2) and for no tests at elevated temperatures. This phenomenon was further investigated in some special experiments [18]. It was demonstrated that

Table 7.1 *Temperature differences for Material A at the room environment temperature level. Maximum estimated error* $\pm 1.5\ ^{\circ}C$.

Pressure [MPa]	Sliding velocity [m/s]	ΔT [°C] Infrared	ΔT [°C] Thermocouple
0.136	0.00033	- 0.3	- 0.1
0.136	0.0095	0.3	1.3
0.136	0.271	2.1	1.5
0.491	0.00033	0.8	
0.491	0.0095	0.6	0.6
0.491	0.271	1.4	1.4
0.847	0.00033	- 0.4	- 0.7
0.847	0.0095	- 0.2	0.8
0.847	0.271	3.0	4.1

Table 7.2 *Temperature differences for Material B at the room environment temperature level. Maximum estimated error* $\pm 1\ ^{\circ}C$. * = *The stick slip phenomenon is observed.*

Pressure [MPa]	Sliding velocity [m/s]	ΔT [°C] Infrared	ΔT [°C] Thermocouple
0.136	0.00033	0.4	0.4
0.136	0.0095	- 0.9	- 0.8
0.136	0.271	0.2	0.6
0.491	0.00033	1.5	1.7
0.491	0.0095	1.1	1.2
0.491	0.271	11.5*	11.8*
0.847	0.00033	1.2	1.5
0.847	0.0095	2.1	2.5
0.847	0.271	20.3*	28.3*

for two identical tests with respect to pressure, temperature, sliding speed, and loss energy, the temperature in the rubber surface layer was much higher for the test with stick slip. There was a temperature difference of 14 °C. In the case where all heat is generated due to friction in the contact area most of the heat is conducted directly off into the cast iron disk, which conducts heat very well compared to rubber. When stick slip occurs a great deal of heat is produced inside the rubber due to hysteresis. This heat is not as easily conducted off, as it has to pass through rubber and through the contact asperities between the rubber and the disk. Therefore a higher temperature is recorded in this case. These results indicate that it is important to avoid stick slip in friction contacts between rubber and a well conducting surface, if the temperature is to be kept as low as possible in the rubber. This theory also explains why the thermocouple records a slightly higher temperature than the infrared detector, 28.3 degrees versus 20.3, see Table 7.2. This is because the the thermocouple wires have been inserted into the rubber.

Our results show that both surface temperature measurement methods give good results which verify one another. The usefulness and application potential of the infrared detector are only a function of how well it can be protected from heat.

Of the temperatures measured, the environment temperature was the most difficult to measure and control. It is important that all equipment inside the climate box have same temperature.

Our conclusion is that for normal tests without stick slip performed as in this investigation, no more than 3-5 degrees of temperature increase should be expected for the highest speed and pressure.

7.4 Dependency on sliding velocity, pressure and temperature for material A

The friction coefficient for material A is presented in Figures 7.11 and 7.12. Each test point in the diagrams represents the mean value of the last 10 minutes of the recording. The number of parameter combinations is 27 and 3 independent test series have been performed, making a total of 81 tests. The relative humidity was recorded continuously, and stayed at a level of about 50 percent during the tests.

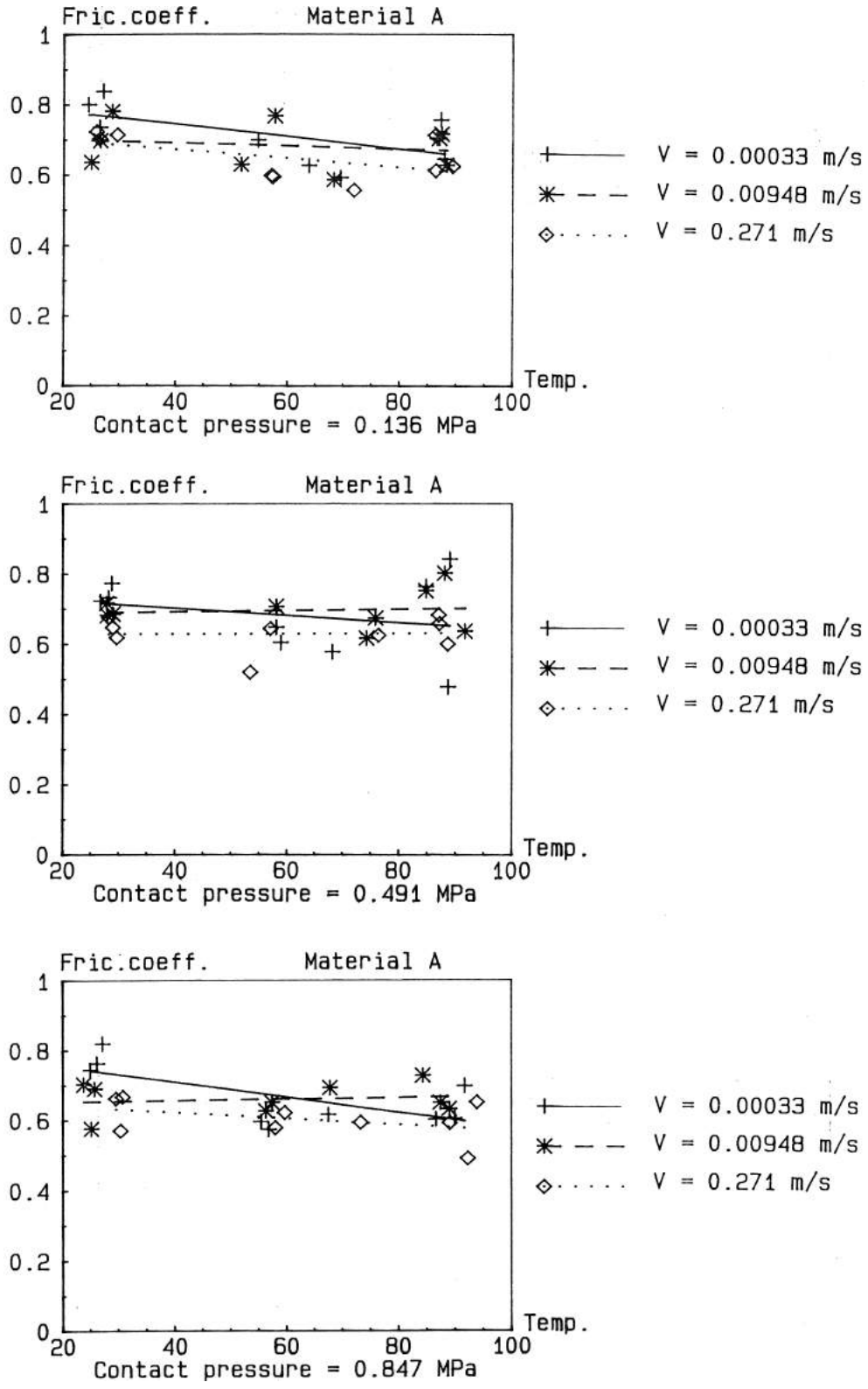

Figure 7.11 *The friction coefficient for material A versus surface temperature. The pressure is constant in each diagram.*

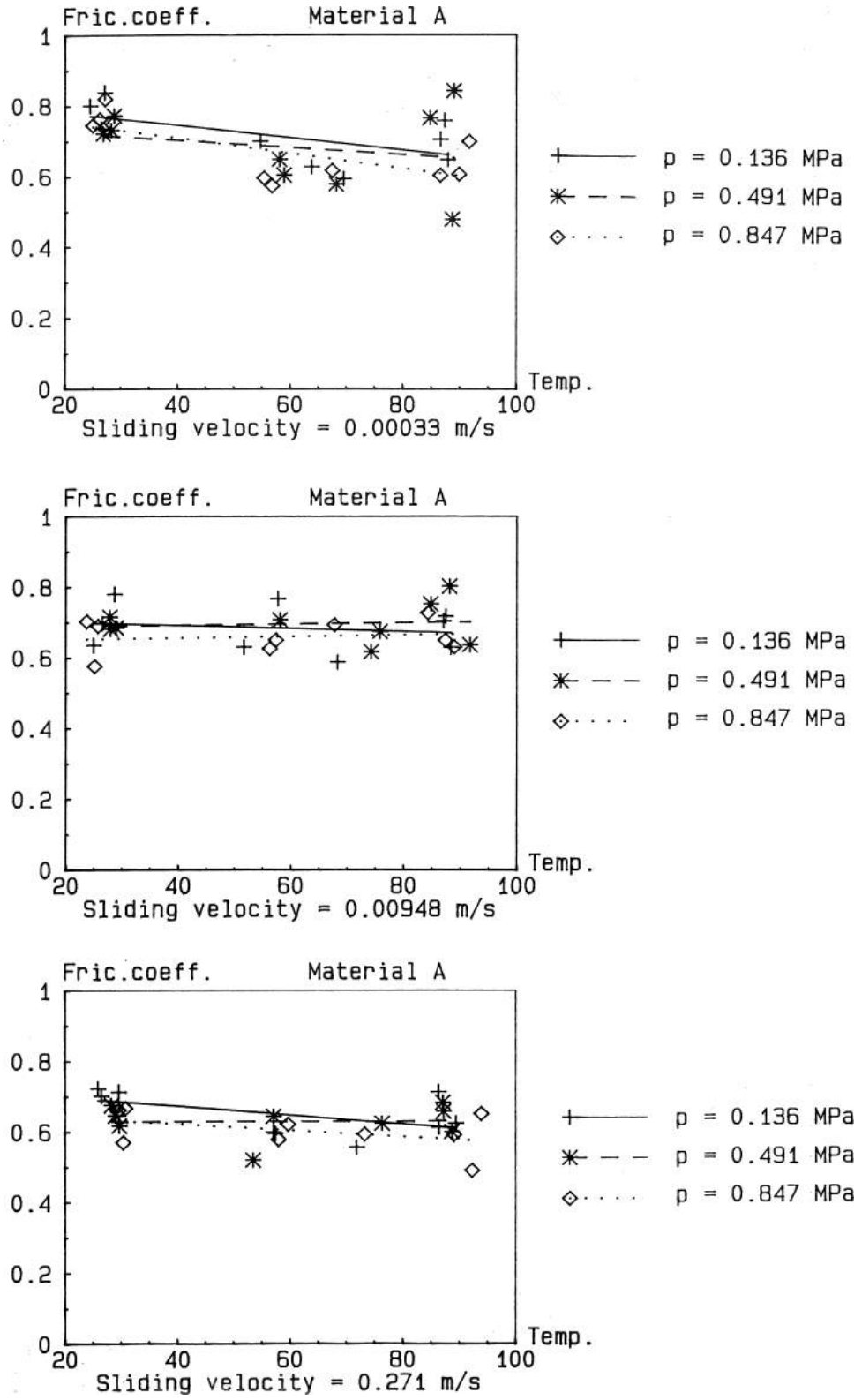

Figure 7.12 *The friction coefficient for material A versus surface temperature. The velocity is constant in each diagram.*

7.5 Dependency on sliding velocity, pressure and temperature for material B

The friction coefficient for material B is presented in Figures 7.13 and 7.14. Each test point in the diagrams represents the mean value of the last 10 minutes of the recording. The number of parameter combinations is 27, and 2 independent test series have been performed, making a total of 54 tests. The relative humidity was around 50 percent during the tests.

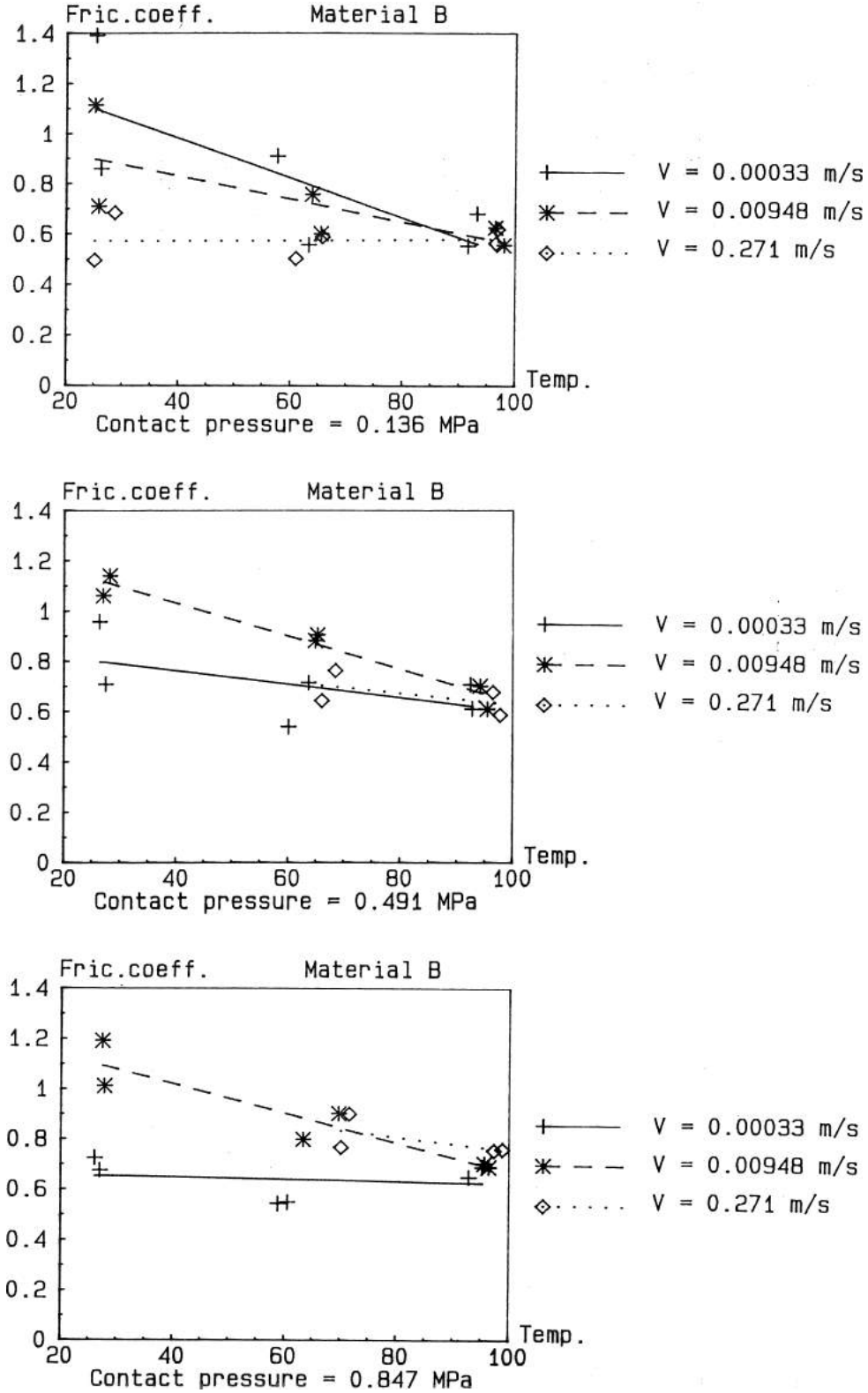

Figure 7.13 *The friction coefficient for material B versus surface temperature. The pressure is constant in each diagram.*

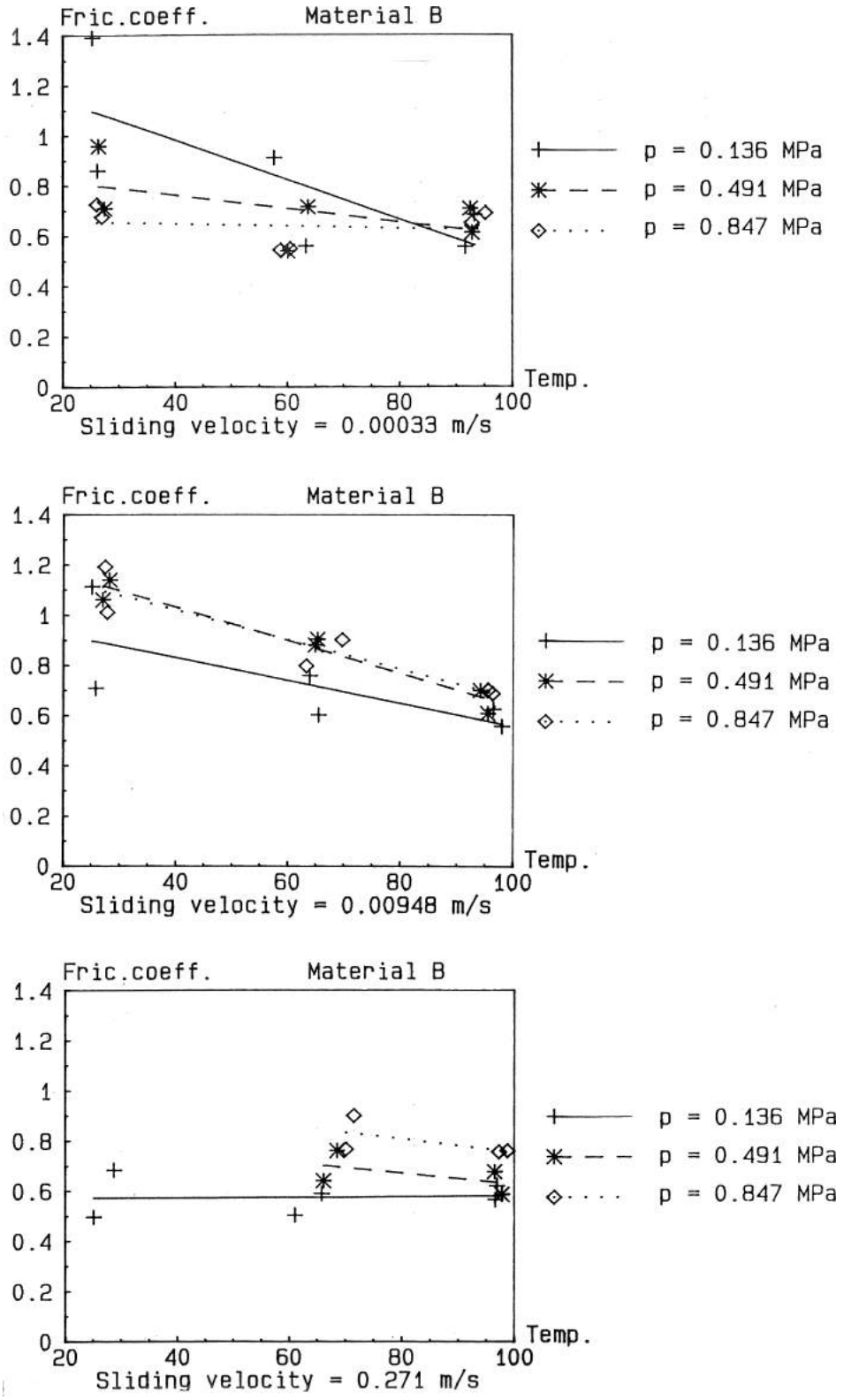

Figure 7.14 *The friction coefficient for material B versus surface temperature. The velocity is constant in each diagram.*

8

Conclusions and discussion

The most important finding of this experimental investigation is that the friction coefficient is highly dependent on the surface structure. However, this structure is continuously changing during the tests. Surface sections with a large amount of reinforcement fiber show greater resistance to wear, and display different friction characteristics. As the sample area is quite small, 10 mm times 10 mm, local variations in the surface will affect the total friction force. This phenomenon causes the greatest variation in friction coefficient, thus dominating other effects. It is difficult to conclude that there is a consistent dependency on pressure, slip velocity or surface temperature.

Both the methods developed to measure temperatures of the contact surface of rubber samples, give satisfactory results and verify one another. In the parameter interval which has been investigated in this test program, normally not more than a 3-4 °C temperature increase over the environment is obtained for the highest speed and pressure. The loss heat generated in the friction contact is mostly conducted off through the cast iron disk and not through the rubber composite. However, if stick slip occurs, heat is created inside the rubber material due to hysteresis. This gives rise to higher temperatures in the rubber.

Two reports of tests of whole V-belts are discussed in chapter 4. These reports do not investigate the variation of the friction coefficient with time at any given parameter combinations since these tests were performed over a very short time. However, both reports present test results from belts that were conditioned by being run in a normal V-belt drive. These are compared with results from new V-belts. The conditioning seems to be the most important variable, which confirms that the surface structure changes with time.

The relative high friction coefficient here obtained compared to test with whole V-belts probably comes from different surface structure. From our experience and results obtained so far, I would suggest that further studies should be done on the surface structure of V-belts in real drive configurations. From the experience thus obtained further development of test methods could be suggested.

9
Acknowledgements

I appreciate the interest and energy of Magnus Söderquist who performed the tests in our laboratory during the hot summer months.

Bibliography

[1] S. Bahadur. "Dependence of polymer sliding friction on normal load and contact pressure." In: *Wear* 29 (1974), pp. 323–336.

[2] M. Barquins and R. Courtel. "Rubber friction and the rheology of viscoelastic contact." In: *Wear* 32 (1975), pp. 133–150.

[3] G.M. Bartenev et al. "The actual contact area and friction properties of elastomers under frictional contact with solid surfaces." In: *Wear* 18 (1971), pp. 439–448.

[4] J.J. Bikerman. "Adhesion in friction." In: *Wear* 39 (1976), pp. 1–13.

[5] A.N. Gent. "Friction and wear of highly-elastic solids." In: *Wear* 29 (1974), pp. 111–116.

[6] G. Gerbert. *Experimentell bestämning av friktionskoefficienten hos kilremmar.(Experimental determination of the friction coefficient for V-belts).* Department of Mechanical Engineering, Lund Technical University, Lund, Sweden: Division of Machine Elements, Nov. 1977.

[7] G. Gerbert. "On V-belt drives with special reference to force conditions, slip, and power loss." PhD thesis. Lund, Sweden: Lund Technical University, 1973.

[8] K.A. Grosch. "The relation between the friction and visco-elastic properties of rubber." In: *Proc. Roy Soc. A. 274, No. 1356.* 25 June 1963, p. 21.

[9] D.J. James and W.G. Newell. *A new concept in friction testing.* England: Polymer Testing, Applied Science Publishers Ltd., 1980.

[10] D.F. Moore. *The friction and lubrication of elastomers.* Oxford, England: Pergamon Press LTD, 1972.

[11] D.F. Moore and W. Geyer. "A review of adhesion theories for elastomers." In: *Wear* 22 (1972).

[12] *Patent specification no. 1494 274, Improvements in friction test apparatus.* Application No. 19541/75 filed 9 May 1975. London: The Patent Office, 1977.

[13] E. Rabinowicz. *Friction and wear of materials.* New York: John Wiley & Sons Inc., 1965.

[14] A.D. Roberts. "Friction of rubber." In: *Proc. of Rubber Technol.* 41 (1978), pp. 151–158.

[15] A.D. Roberts and A.G. Thomas. “The adhesion and friction of smooth rubber surfaces.” In: *Wear* 33 (1975), pp. 45–64.

[16] T. Sakamoto et al. “A friction apparatus for measuring the normal displacement of a sliding body.” In: *J. Phys. E., Sci. Instrum.* 13 (1980).

[17] A. Schallamach. “How does rubber slide.” In: *Wear* 17 (1971), pp. 301–312.

[18] M. Söderquist. “Mätning av friktionskoefficient och yttemperatur på gummi i kontakt med gjutjärn. (Measuring of friction coefficient and surface on rubber in contact with a cast iron surface).” MA thesis. Göteborg, Sweden: Division of Machine Elements, Department of Mechanical Engineering, Chalmers University of Technology, 1986.

[19] C. Van Ho. *Coefficient of friction of the sidewall of a V-belt.* Internal test report. Denver, Colorado: The Gates Rubber Company, May 1986.

[20] G.V. Vinogradov et al. “Frictional properties of elastomers at increased sliding rates.” In: *Wear* 32 (1975), pp. 203–210.

Part V

Material properties of elastomer composites in mechanical transmissions with special reference to V-belts

Report V

Material properties of elastomer composites in mechanical transmissions with special reference to V-belts

Dag Fritzson

Report No. 1988-05-25
Division of Machine Elements
Department of Mechanical Engineering
Chalmers University of Technology
Göteborg, S-412 96 Sweden

1 st version completed 1985

Abstract

Rubber, or elastomers, is not a well-defined material group in terms of mechanical material properties. For any given material, the mechanical properties are very much dependent on what environment the material is used in, and what kind of loads, deformations, temperatures, etc, it is subjected to.

The material characteristics of elastomer composites used in V-belt applications are very much dependent on strain, temperature and, to some extent, frequency. The fiber-reinforced materials are anisotropic, with one material direction differing from the others. The label "transversal isotropic" can be used. For one of the materials, the reinforced direction is up to 4 times stiffer than the other directions.

The conclusion drawn in this study is that in any material description made for the elastomer composites for the V-belt application several variables should be studied. The order of priorities among these should be anisotropy, strain effects, temperature effects and finally, frequency effects.

For polyester cord, temperature is the most important variable.

Contents

1
Introduction

Rubber, or elastomers, is not a well-defined material group in terms of mechanical material properties. For any given material, the mechanical properties are very much dependent on what environment the material is used in, and what kind of loads, deformations, temperatures, etc, it is subject to. It is very seldom possible to find the data needed for a particular analysis in handbook or even in information from the manufacturer of the material.

Mechanical material properties are needed for any analysis or simulation of a mechanical system in which sections of rubber are important parts, essential for the functioning of the system.

This report presents a study of the application of mechanical transmissions with special reference to V-belts. A V-belt is built up of several different reinforced rubber materials and cord (see Figure 4.1), each optimized in terms of its function. Some are heavily reinforced to be able to take the load. Thus the expression "an anisotropic elastomer composite" is more descriptive than the conventional word "rubber".

In Chapter 3 theories and results found in the literature are surveyed. Applications to the problem here studied are discussed.

In Chapter 4 test methods which might be usable are presented. Design and evaluation of test equipment is discussed. What variables should be studied and in what intervals measurements should be made are also investigated.

In Chapter 5 a method is developed which makes it possible to study experimental data which is a function of several variables.

In Chapter 6 the results of the test program are evaluated and discussed.

2
Notation

Superscript

*	Complex value
$^{\prime}$	The real component of a complex value
$^{\prime\prime}$	The imaginary component of a complex value
^{1,2,3,4}	Used to indicate the different vector components

Subscript

$_{a}$	Amplitude
$_{m}$	Mean value
$_{i,j,l}$	Index used to indicate different constants
$_{0}$	Initial value
$_{c}$	Constant

Variables and constants

ϵ, γ	Strain (-)
σ, τ	Stress (MPa)
E	Young's modulus (MPa)
$E_m = \frac{\sigma_m}{\epsilon_m}$	Mean Young's modulus (MPa)
G	Shear modulus (MPa)
$G_m = \frac{\tau_m}{\gamma_m}$	Mean shear modulus (MPa)
δ	Phase or loss angle (Rad)
f	The frequency of the cyclic deformation (Hz)
$\omega = 2\pi f$	Angular speed (Rad/s)
u	Deformation (mm)
ΔV	Volume deformation (mm^3)
V	Volume (mm^3)
p	Hydrostatic pressure (MPa)
K	Bulk modulus (MPa)
$E0$, $E1$	Constants (MPa)

k	Correction factor depending of carbon black content (-)
S	Shape factor (-)
L	Length of sample (mm), or longitudinal module (MPa)
a	Side of a square cross-section (mm)
A	Area (mm^2)
c	Specific heat $\left(\frac{\text{Joule}}{\text{kg } ^\circ\text{C}}\right)$
ρ	Density $\left(\frac{\text{kg}}{\text{m}^3}\right)$
T	Temperature (Celsius or Kelvin)
u, v, w	Parameter variables (-)

3
Rubber viscoelasticity

3.1 Introduction

It is characteristic of all elastomeric (rubber-like) materials that they are viscoelastic. This behavior is manifested in different ways, including creep under constant load , damping in dynamic applications, stress relaxation under constant strain, etc. Other significant properties are the elongation to rupture, which is typically 500-1000 percent, and the virtual incompressibility of rubber due to the low Young's modulus relative to the bulk modulus.

Elastomers are often used in applications where they are subject to dynamic loads or deformations. To design a component for a specific dynamic response and adequate service life requires a good knowledge of the stress-strain properities of rubber and their dependence on frequency, temperature and amplitude of strain. In this chapter, the influence of these factors on material properities is discussed.

3.2 Some basic viscoelastic definitions

To interpret the dynamic viscoelastic behavior in a specific test, the theory of linear viscoelasticity is normally applied. Rubber in the simple shear mode of deformation shows linear behavior in a large range of deformations, but the characteristic of rubber in tension or compression is nonlinear. Approximation to linear behavior is not good, except when the deformations are small (less than a few percent [5, 4, 14]).

In a sinusoidally varying strain, the stress response will be out of phase with an angle of δ. The stress can be divided into two components, one in phase with the strain and one ninety degrees out of phase. This is shown in the following equations and Figure 3.1.

$$\epsilon = \epsilon_a \sin(\omega t) \tag{3.1}$$

$$\sigma = \sigma_a \sin(\omega t + \delta) = \sigma_a \cos(\delta) \sin(\omega t) + \sigma_a \sin(\delta) \cos(\omega t) \tag{3.2}$$

From Equations 3.1 and 3.2 an elastic modulus and a viscous modulus can be defined.

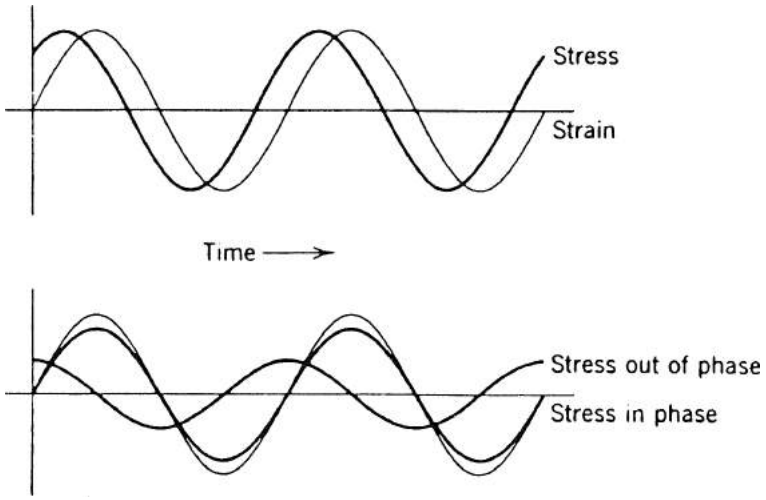

Figure 3.1 *Sinusoidally varying strain and stress. The stress decomposed into in-phase and out-of-phase components.*

$$E' = \frac{\sigma_a}{\epsilon_a}\cos(\delta) \tag{3.3}$$

$$E'' = \frac{\sigma_a}{\epsilon_a}\sin(\delta) \tag{3.4}$$

The modulus can then be expressed in complex values.

$$E^\star = E' + \imath E'' \tag{3.5}$$

$$\tan(\delta) = \frac{E''}{E'} \tag{3.6}$$

$$\sigma^\star = E^\star \epsilon^\star \tag{3.7}$$

In a stress-strain plot the hysteresis loop will be an ellipse for sinusoidally varying stress and strain.

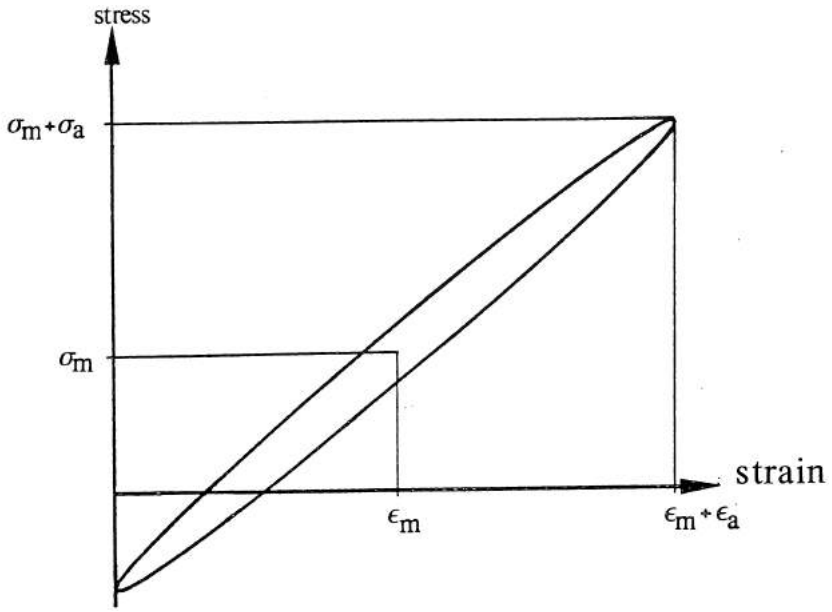

Figure 3.2 *The stress-strain loop due to a sinusoidal deformation of a rubber unit.*

3.3 Effects of strain amplitude on the dynamic material properties

Rubber is seldom used as pure gum in technical applications since the addition of reinforcing fillers improves material properties enormously [5, 11, 14]. The most important filler is carbon black which is produced by incomplete combustion of hydrocarbons or by thermal cracking. Other common fillers such as silicas do not give the same reinforcement and are not used when high strength is needed. However the structure of the elastomer reinforced by carbon black is sensitive to the magnitude of strain [5, 11, 4, 14, 18].

A typical graph, from the work of Payne and Whittaker [15], of the effects of filler content and strain on the storage shear modulus is shown in Figure 3.3.

The modulus has limiting values at very low strain, at which the "structure" is intact (G'_0), and at high strains when the "structure" is assumed to have been destroyed (G'_∞). If the strain amplitude is changed from a high value to a low value, the storage modulus very slowly recovers towards its original value [4]. Figure 3.4 shows that the loss modulus is highest when the rate of storage modulus change is greatest. An explanation theory [5] for this behavior is that at small amplitudes little of the structure breaks down, and therefore the loss modulus (G'') is small. At large amplitudes, the structure is so completely broken down that reformation is much slower than the cycle period and so the loss modulus is low again. Maximum loss modulus is achieved in the middle region where both fast reformation and large structure breakdown occur. Published test results in both shear and compression by many different authors [18] show similar strong dependence of the strain amplitude for the modules of carbon black filled elastomers. The moduli are more dependent on the structure of the carbon black than on the properties of the elastomer [18].

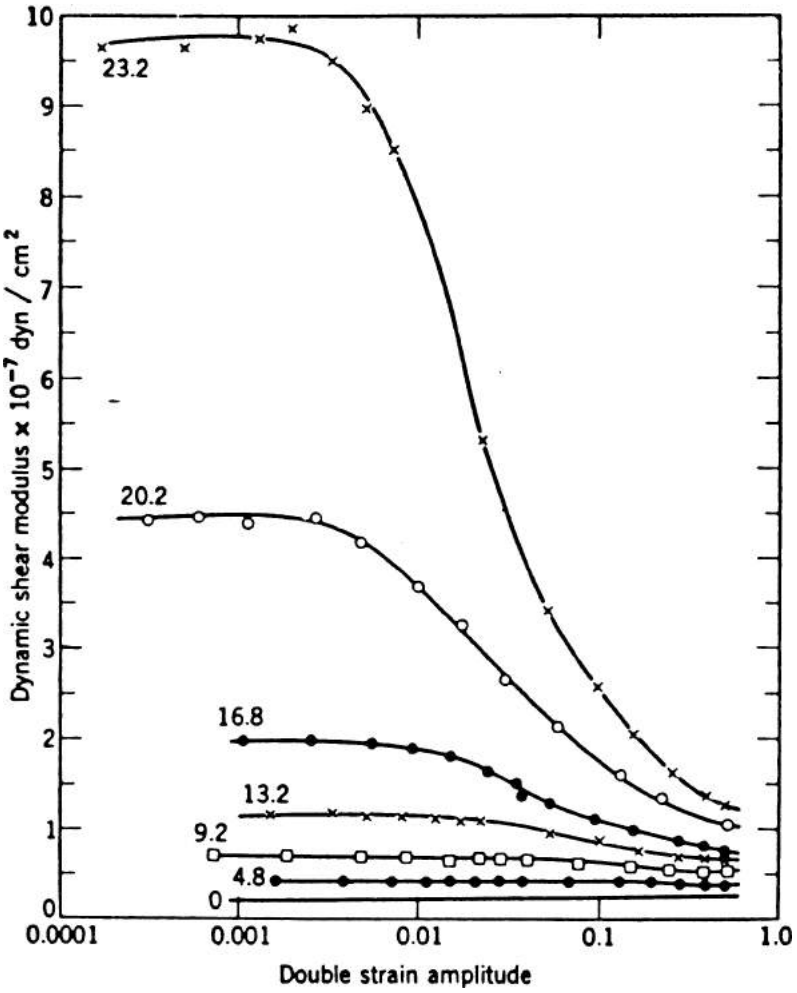

Figure 3.3 *Dependence of storage shear modulus on double strain amplitude at 0.1 Hz for butyl rubber containing varying concentrations up to 23.2 vol. percent HAF carbon black [5, 15].*

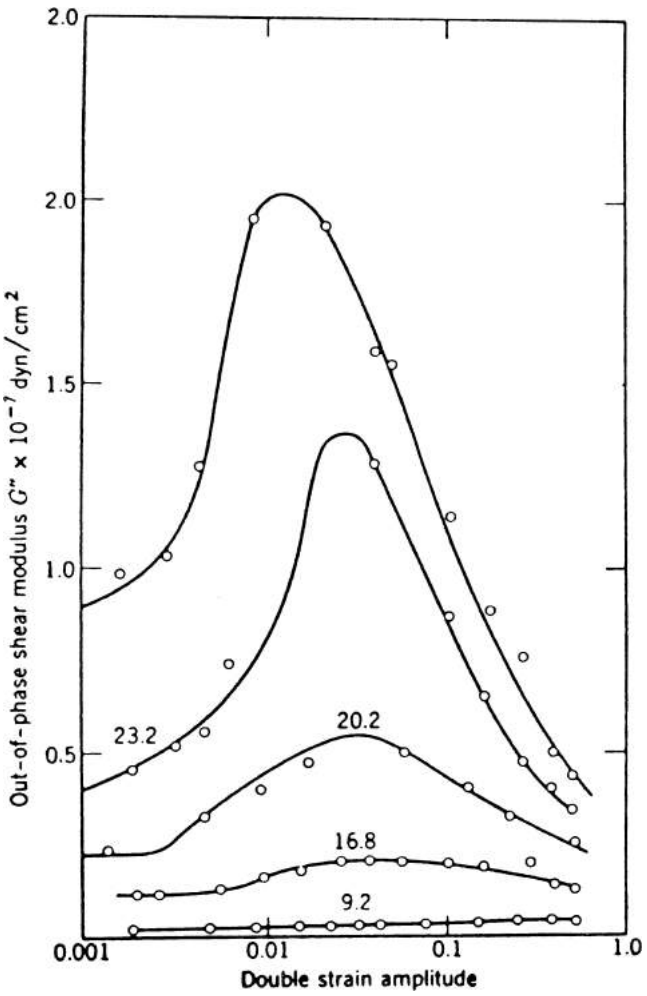

Figure 3.4 *Dependence of loss shear modulus on double strain amplitude at 0.1 Hz for butyl rubber containing varying concentrations up to 28.8 vol percent HAF carbon black [5, 15].*

3.4 Effects of temperature and frequency on the dynamic material properties

Studies [11, 4] of the variation of elastic modulus with frequency, preload and strain amplitude have indicated that the elastic and loss modulus can be expressed as separable functions of frequency and overall strain effects. A tenfold increase in frequency normally causes a small increase in elastic modulus.

The effect of temperature is more complex. There are three major effects that cause changes in storage modulus with a decrease of temperature [4]. Lower temperatures mean an increased resistance to molecular motion and therefore a higher storage modulus, although the statistical theory of rubber elasticity predicts the opposite. There are also the effects of fillers and the interaction of fillers and matrix. This last effect introduces a coupling to the strain amplitude, which is illustrated in Figure 3.5.

In this example, an increase in temperature from twenty to ninety degrees Celsius, which is not uncommon in technical applications, causes a reduction of storage modulus by fifty percent at small amplitudes, but no significant reduction of storage modules for a strain amplitude of five to ten percent.

There is an important class of viscoelastic materials which have a translational shift in various material properties, such as complex modulus, for a change in temperature. Material data obtained at different temperatures and frequencies can be superimposed on a single master curve. From this curve the material properties can be obtained for a wide range of frequencies and temperatures. This group of materials is referred to as thermorheologogically simple materials, and the principle is often called "the time - temperature superposition principle" [5, 11, 4, 14]. Experimental evidence shows that the principle holds for many rubber materials. However, the theory is valid only for linear materials and any effect of dependence on strain amplitude on material

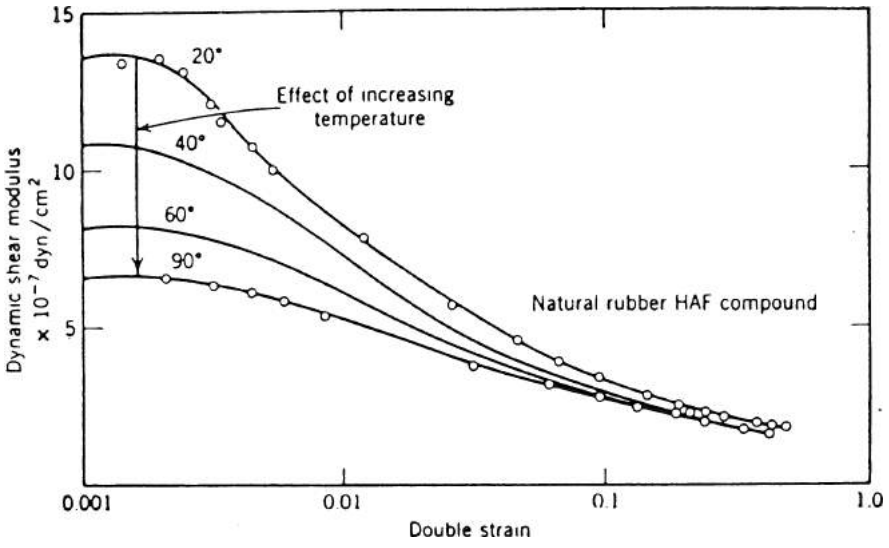

Figure 3.5 *Variation of storage shear modulus with double strain amplitude as a function of temperature at 0.1 Hz for natural rubber containing 32 vol percent HAF carbon black [5, 15].*

properties must be taken into consideration.

3.5 Stress softening

It is well known that for all kinds of rubber material, cured or non-cured, filled or non-filled, a larger stress is needed to achieve a given deformation in the first deformation cycle than in the following cycles [5, 11, 4, 14, 18]. This behavior is called stress-softening or Mullin's effect. It is illustrated in the Figure 3.6.

Mullin's effect is also significant for very large deformations, not only for strain amplitudes up to ten percent, such as for the breakdown of the carbon black rubber structure [18]. The effect has been well investigated but there are no widely accepted theories. Both viscoelastic and plastic behavior have been observed, and the properties of the particular elastomer seem to be important [18].

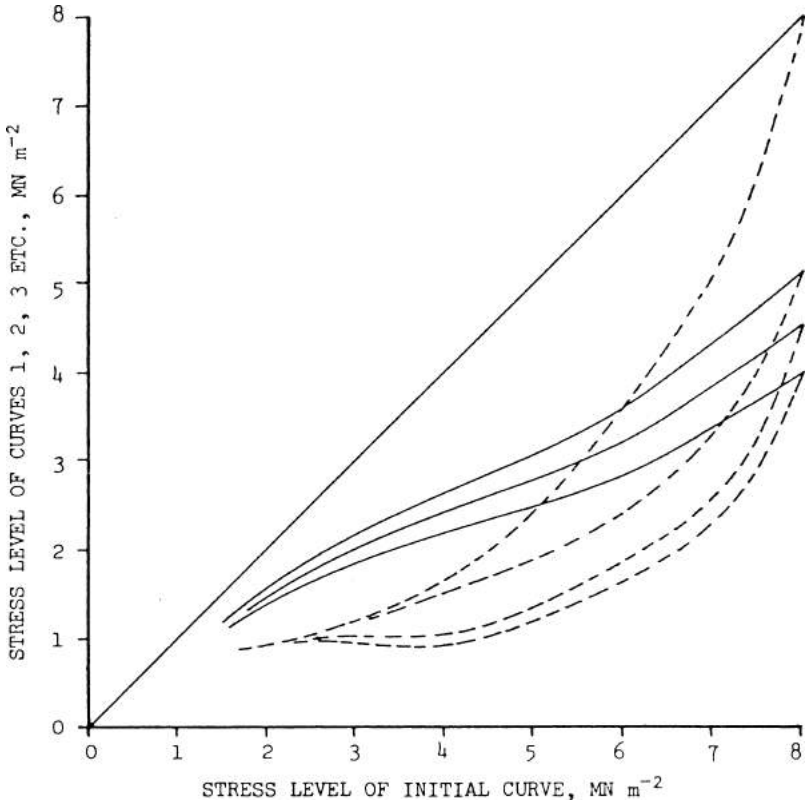

Figure 3.6 *Comparison of stress levels for repeating cycling of gum natural rubber vulcanizate [5, 8].*

3.6 Creep and stress relaxation

All rubbers exhibit the characteristics of creep and stress relaxation, even at low temperatures. The general effect of fillers is that the rate of stress relaxation increases, particularly if the filler is carbon black. The creep rate is also sensitive to the temperature and environment, as shown in the Figure 3.7 [5].

In this example a tenfold increase of creep rate is caused by an increase of the temperature from fifty to seventy degrees Celsius. It has been shown that creep under cyclic deformation is faster than static creep [18]. This is shown in Figure 3.8.

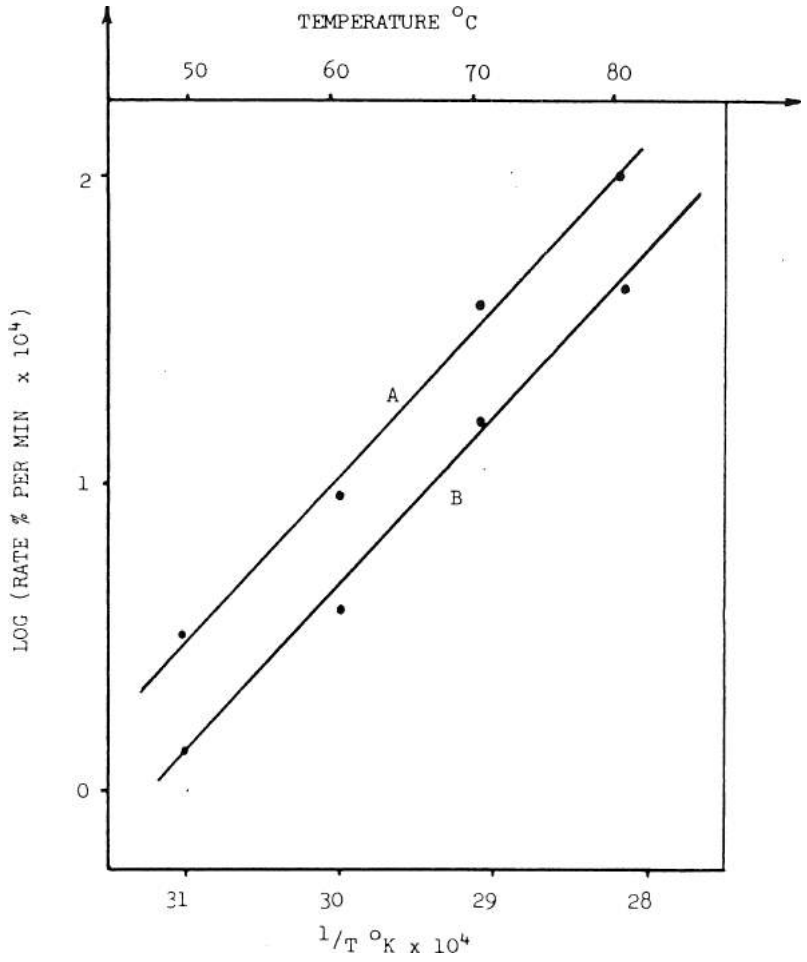

Figure 3.7 *The creep rate, at various temperatures, of a conventional accelerated sulphur vulcanizate of natural rubber. A is unprotected and B contains an antioxidant [5, 3].*

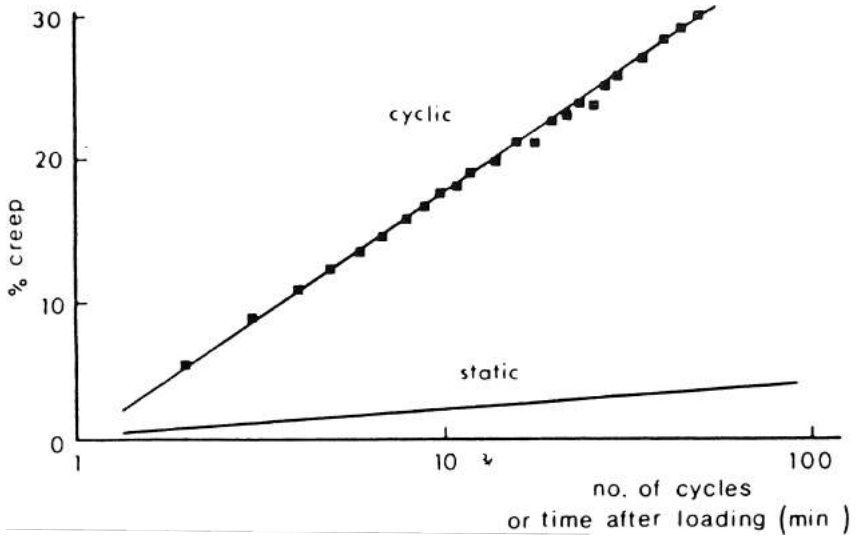

Figure 3.8 *Cyclic and static creep of natural rubber vulcanizate containing 40 phr carbon black [2, 12].*

3.7 Ageing

A typical rubber compound is a mixture of elastomers, fillers and additives. To achieve the prescribed mechanical properties, the compound is cured under pressure and a high temperature for a given period of time.

During the service life of the rubber certain chemical reactions may continue in the rubber compound. Additives may evaporate and the surface may change due to reactions with the environment (ozone, light ,oil, etc.) . In long term applications, especially at high temperatures, significant changes in material properties can occur. This process is normally referred to as the ageing process.

3.8 Anisotropy

There are applications in which different material properties are needed in different material directions. This can be accomplished using reinforcement, i.e. of dispersed fibers, fabric or cord. The anisotropy achieved by using reinforcing fibers, such as Kevlar, polyester, nylon, cotton etc., comes from the orientation of the individual fibers in the mixing process.

When using rubber impregnated fabric, the anisotropy is determined by the weave and the orientation of the fabric layers.

Cord, usually made of Kevlar, polyester, fiberglass, Rayon or steel, normally has physical dimensions which allow it to be distinguished, and subsequently treated separately from rubber.

For the other reinforcement methods, the question of how the “rubber” viscoelasticity is influenced by the reinforcement arises.

3.9 Discussion

From an engineering point of view, rubber is not a well-defined material. The most well-known effects on material properties, frequently referred to in the literature, are discussed above.

"Rubber" viscoelasticity is also influenced by the reinforcement of fibers, which should be investigated.

From the discussion above, it can be concluded that, in a given technical application, it is wise to determine the limits of temperature, strain, frequency, and time in order then to determine the material properties within these limits. From the results obtained, any simplification of the description of the material properties can be considered.

4
Experiments

4.1 Introduction

To investigate the behavior of a V-belt drive, the material properties have to be determined. The belt materials should be tested for the same variations of frequency, temperature and strain to which a running belt are subject.

A typical V-belt is a composite of highly anisotropic rubber materials and cord. The belt must be subject to high loads both in the axial and longitudinal directions to be able to transmit sufficient torque. All loads are dynamic, and the frequency of bending is normally between one and to one hundred Hz.

The temperature in the environment of the V-belt transmission varies greatly from low winter temperatures to high temperatures (close to a heat radiating machinery) in summer.

Hysteresis in the cord, hysteresis in the rubber, and slip between the belt and the pulleys cause the temperature in the belt to be higher than in the environment. In many cases there is a temperature difference of fifty degrees Celsius.

4.2 The material in the belt

The V-belts considered in this report were made of four different materials. See Figure 4.1.

The bottom layer must be able to carry most of the axial force and still be easily bent around the pulley. For this reason the fiber is reinforced in the axial direction.

The rubber compound mix consists mainly of Neoprene (polychloroprene), Carbon Black, fibers (cotton, polyester, nylon, etc.) and of different additives.

The bottom layer often has a cog shaped design to minimize bending strain and therefore hysteresis due to bending.

The reason there is a middle layer is to provide a good bond between the cord and the rest of the belt. The rubber in this layer is designed to be softer than the rubber in the bottom layer, for improved adhesion. Some of the reinforcing carbon black is replaced with silica, and a very small percentage of fiber is used. The fibers are oriented in the longitudinal direction.

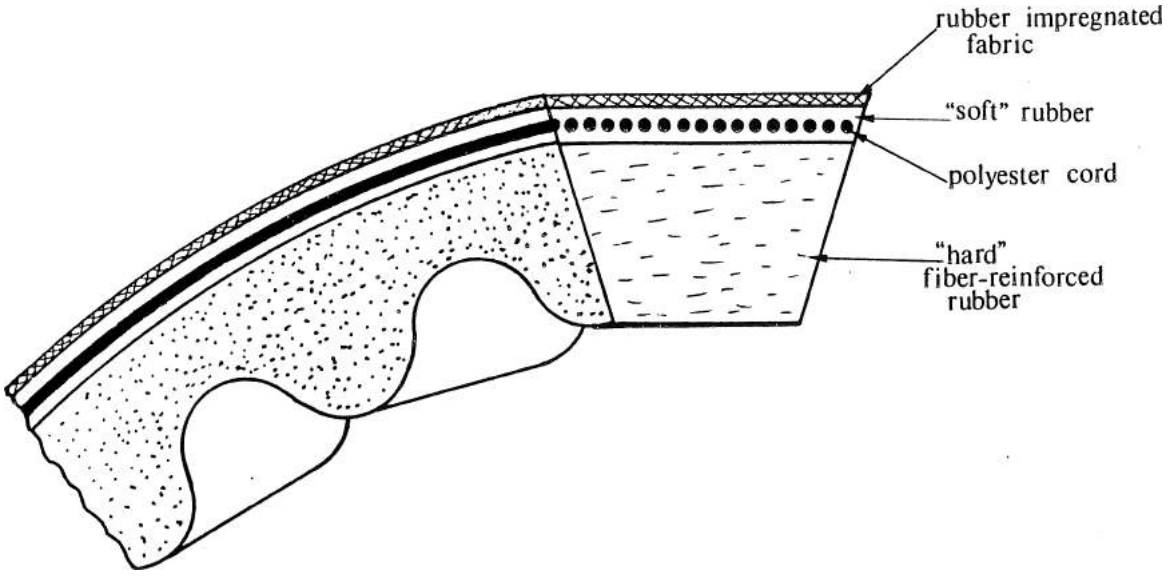

Figure 4.1 *A cross-section of a typical design of a raw edge V-belt. The different materials in various sections of the V-belt are also indicated.*

On the top of the belt there are layers of Neoprene-impregnated fabric. The weft and weave are oriented at ninety degree angles and at a forty five degree angle to the longitudinal direction of the belt. This orientation of the fabric relative to the belt ensures that the bending forces of the belt are minimized.

From what has been discussed above it may be expected that the bottom layer and the middle layer are considered transversal isotropic materials and the fabric orthotropic.

The cord is made of polyester and is subsequently treated with chemicals to improve the bond with the rubber. The stiffness in the longitudinal direction of the cord layer is about three orders of magnitude (1000 X) greater then that of the rubber and fabric layers. It can therefore be expected that nearly all of the forces and hysteresis due to tensile strain in longitudinal direction will be related to the cord. The rubber in the middle layer surrounding the cord prevents, the individual yarn plies of the cord from moving to some extent. This probably causes an increase in the stiffness of the cord layer.

The test samples needed for the different tests were of such physical dimensions that they could not be cut out of an original belt. Special test belts were therefore manufactured, for the specific pieces to be cut out and tested. The belts were produced using the same type of materials and manufacturing processes as the normal belts, to ensure similar material properties. The major difference was in the physical thickness of the layers of the belt. To confirm that the vulcanization was correct, the temperature was monitored in different layers of the belt during the curing process.

4.3 The nonresonant force-deformation method

There are many different methods for measuring the dynamic performance of materials. A good review of dynamic test methods may be found in [16].

Using the non resonant force-deformation method, a strain mean level and an oscillation at a given strain amplitude can easily be imposed on the test sample. The influence of different frequencies can be studied. With the addition of a climate box, the temperature can also be varied. The strain mean level, amplitude, frequency and the temperature can be set to represent the conditions inside a running belt.

In this investigation an "Instron 1320 Dynamic Testing System" was used [10]. It has a hydraulic actuator which means that its best performance is at low frequencies. To analyze the output signals and calculate all material parameters a "Norland 3001 Waveform Analysis System" was used [13].

The stroke signal and the load signal can be calibrated using measurement and dead weights respectively, but there are two other important sources of error that have to be considered in dynamic tests: errors due to the compliance of the different testing arrangements and errors caused by resonances in the testing equipment. A theoretical model of masses, springs and dampers can be used to calculate and design testing equipment that gives acceptable margins of error. Any remaining errors due to resonance can easily be detected with the wave form analyzer. Generally speaking the load cell should be stiff but still sensitive. The test specimen holders should be stiff and light.

Many problems are encountered in designing the test samples and their holders. Strain, stress, frequencies and temperature should be varied over a wide range that represents the condition inside the belt. Any given load cell has a limited range in which it gives accurate readings of the force. In dynamic tests, load cells with higher stiffness must be used compared to static tests, due to the problem with excitation of resonance frequencies.

As the strain will be calculated from the stroke feedback signal, there are limitations of how small the stroke can be in order to be detected with accuracy. The maximum stroke is determined by the performance of the hydraulic actuator at higher frequencies.

The compliance of the test arrangements has to be negligible compared to the test samples to give correct readings of strain and phase angle. This means that a relatively stiff load cell has to be used.

There are also some geometrical limitations imposed by the physical size of the climate box.

The performance of the load cells, stroke transducer and the hydraulic actuator were determined by tests. This gave the limits of what forces, strokes and frequencies can be used. The stresses and strains that should be studied were given, and this determined what stiffness and length the test samples could have.

Read and Dean [16] give design methods for preventing errors in phase angle and strain due to the compliance of the testing arrangements and for investigating resonance in the equipment. Basically, simple models consisting of masses, springs and dampers are used to simulate the behavior of the testing arrangements.

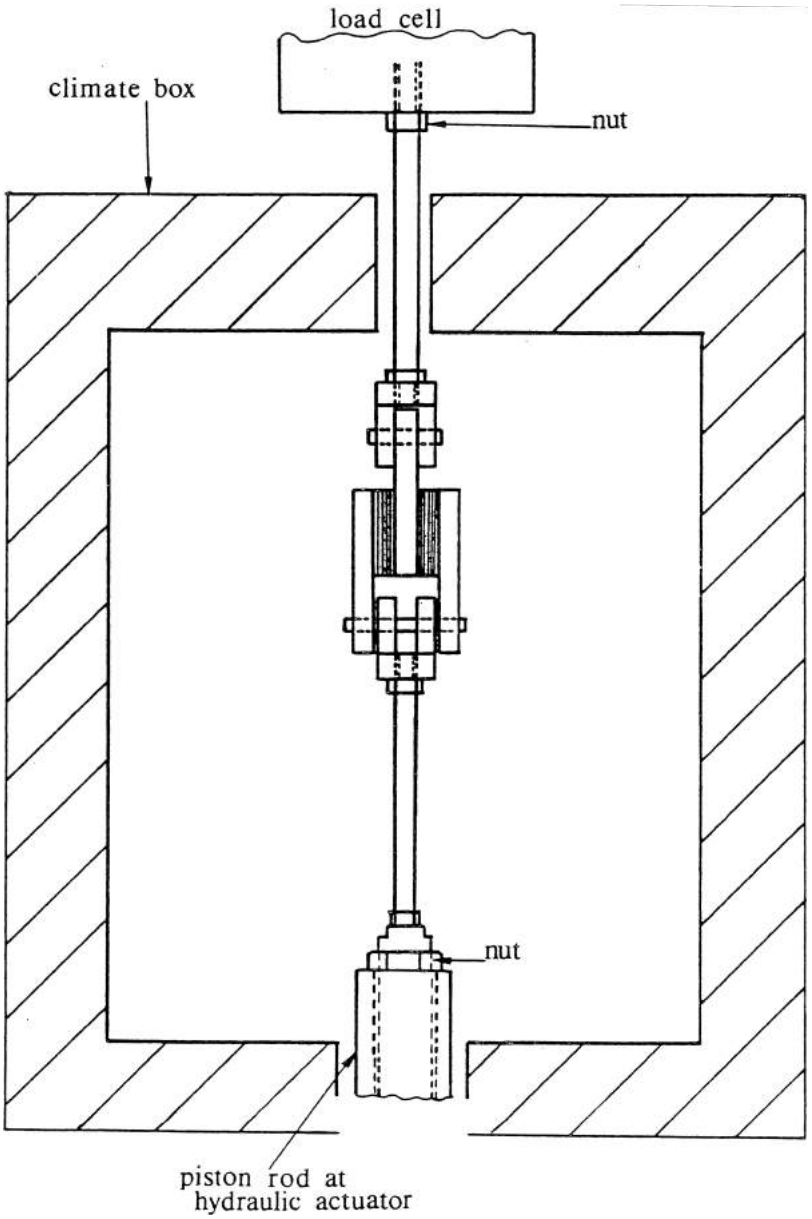

Figure 4.2 *The test arrangement for shear test including the climate box. The load cell and hydraulic actuator of the Instron Dynamic Testing System are also shown.*

The calculations of the resonance frequencies of the testing arrangements were easily verified with tests.

It is very important to realize that the testing arrangements, including the test samples, are mechanical systems that move dynamically and to deal with it accordingly, especially when it is impossible or difficult to measure the necessary parameters such as strain and stress directly on the test sample.

The testing arrangements were designed to minimize the errors discussed above. Of course, in different types of tests such as shear, compression, etc., different critical limits are encountered. This is discussed in the following sections.

The aim was to have three significant numbers and, in the worst combinations of test parameters at least two significant numbers, because of the possible sources of error as discussed above.

4.4 Tests in shear

Tests in shear involve a change in shape at a constant volume, while tests in compression and extension involve changes in both shape and volume. Shear tests have become quite a popular method for evaluating dynamic properties of elastomers, and most of the published results are of this kind.

The shape of the sample allows forces of measurable amplitude to be achieved without using a very sensitive load cell. For the load stage shown in Figure 4.3, the test-sample consists of two identical rectangular blocks of the sample material bonded to the end pieces.

The test samples were first cut from the belt with a bandsaw and then ground to the rectangular shape (50.8mm·12.7mm·12.7mm) with tolerances as small as possible. To account for any remaining geometrical variation the dimensions used in calculations were measured for each individual test piece.

Simple shear cannot be maintained unless constraints, resulting in bending, are applied to the bonded end surfaces. The specimen is loaded in the shear stage shown in Figure 4.3. Let h be the thickness of each sample, A the cross-sectional area of the bonded faces and L the length of the sample in the direction of the displacement applied . Then the components of the complex shear modulus may be obtained from the equations below [16] if the classical theory of linear viscoelasticity is applied to interpret the viscoelastic behavior.

$$G' = \frac{F_a h}{2u_a A}\left(1+\frac{h^2 G'}{L^2 E'}\right)\cos(\delta) \tag{4.1}$$

$$G'' = \frac{F_a h}{2u_a A}\left(1+\frac{h^2 G'}{L^2 E'}\right)\sin(\delta) \tag{4.2}$$

Where

$$\begin{aligned} \delta &= \text{Phase angle} \\ u_a &= \text{Displacement amplitude} \\ F_a &= \text{Force amplitude} \end{aligned}$$

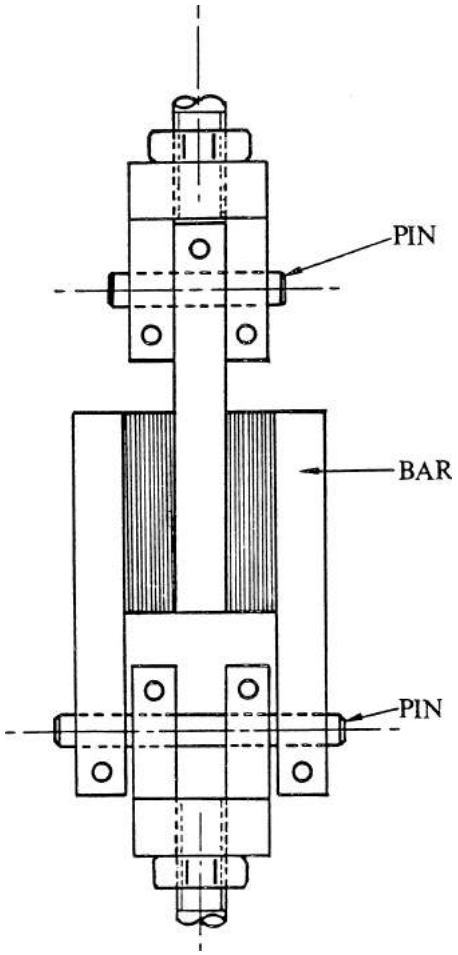

Figure 4.3 *The load stage for tests in simple shear. The dimensions of the two identical samples were:* $(50.8mm \cdot 12.7mm \cdot 12.7mm)$

For rubberlike material that exhibits a behavior close to incompressibility and for a height to length ratio of 0.25 the error is less than two percent if the second term in the bracket is neglected. The error here is considered so small that the equations given below are used in the following analysis.

$$\tau_a = \frac{F_a}{2A_m} \tag{4.3}$$

$$\gamma_a = \frac{u_a}{h_m} \tag{4.4}$$

$$G' = \frac{\tau_a}{\gamma_a}\cos(\delta) \tag{4.5}$$

$$G'' = \frac{\tau_a}{\gamma_a}\sin(\delta) \tag{4.6}$$

$$\tau_m = \frac{F_m}{2A_m} \tag{4.7}$$

$$\gamma_m = \frac{u_m}{h_m} \tag{4.8}$$

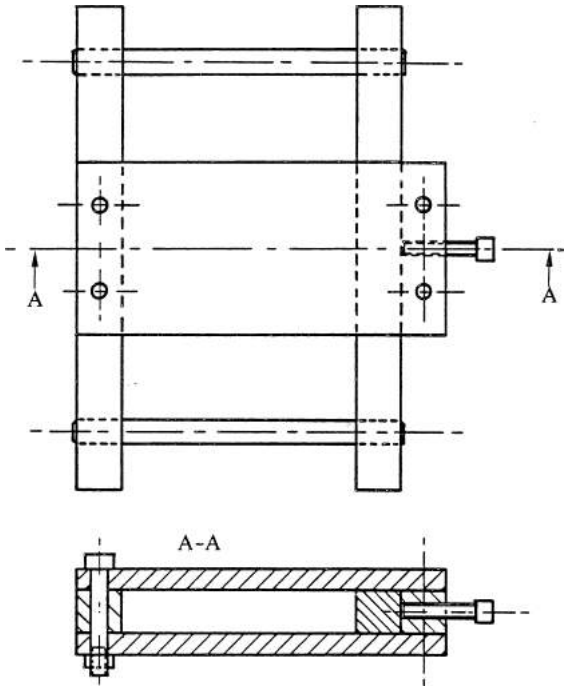

Figure 4.4 *The fixture used when bonding the rubber samples to the shear test stage.*

Where

$$A_m = \text{Mean cross-sectional area} \tag{4.9}$$
$$h_m = \text{Mean thickness} \tag{4.10}$$
$$F_m = \text{Mean force} \tag{4.11}$$
$$u_m = \text{Mean displacement} \tag{4.12}$$
$$\tau_a = \text{Stress amplitude} \tag{4.13}$$
$$\gamma_a = \text{Strain amplitude} \tag{4.14}$$

The bond between the vulcanized rubber and the steel holders have to take up all the shear forces in dynamic test, even at high temperatures.

Many different adhesives and methods for bonding vulcanized rubber to steel were evaluated in dynamic tests at various temperatures. Cyanoacrylate showed the best performance. If the loads were increased to cause failure, the rubber broke instead of the bond, except at very high temperatures when the bond between the rubber and steel broke first.

In order to achieve a perfect bond the steel has to be sand blasted and cleaned with acetone. The rubber surface, that had been ground smooth, was given a very thin layer of adhesive. This was allowed to dry completely before the final layer was applied and the surfaces put together. The fixture used to achieve good alignment and apply a slight pressure shown in Figure 4.4 was used.

To ensure that a bad bond would not influence or cause errors in the test data, all test samples were taken apart after the tests and the bond surface analyzed. All test

results were disregarded for a certain test sample if any suspicion of failure in the bonds could be detected.

4.5 Tests in compression and extension

Deformation in compression or extension involves changes in both shape and volume. This introduces a dependency of both the shear modulus and the bulk modulus which define the Young's modulus in classical small strain theory.

Rubber has a very high coefficient of friction and hence unique gripping properties. This introduces a dependence of the friction coefficient for the stiffness of a rubber block in compression. This is illustrated in Figure 4.5 where it can be seen that for rubber against metal the grip is nearly as good as a bond.

In dynamic tests the surfaces of the rubber and the metal cannot be allowed to slide against one another, as this causes losses that cannot be separated from the hysteresis work in the rubber. If the rubber slides during a certain part of the deformation cycle it might introduce nonlinear behavior of the force-deformation curve. A common way to prevent sliding is to apply preload or predeformation on the sample. This ensures that there are sufficient normal forces to prevent sliding during all parts of the deformation cycle.

From preliminary tests it was concluded that predeformation has to be three to four times larger than the deformation amplitude to eliminate the effect discussed above. This high predeformation is not surprising, considering that the minimum normal force is reduced because of the phase lag between the force and deformation curves. The phase lag occurs due to hysteresis. Creep will also cause a decrease in the preload.

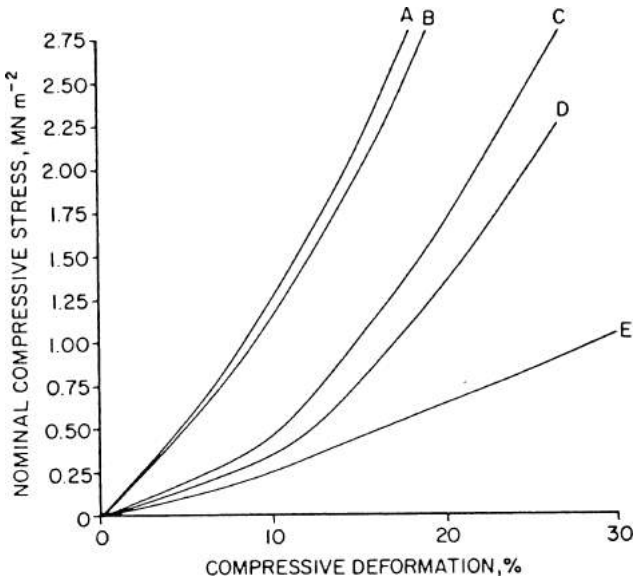

Figure 4.5 *Effect of surface condition on stress-deformation curve for a given rubber sample under compression. (A) bonded, (B) polished steel, (C) dusted with talc, (D) rubbed with graphite, (E) coated with petrolatum [5].*

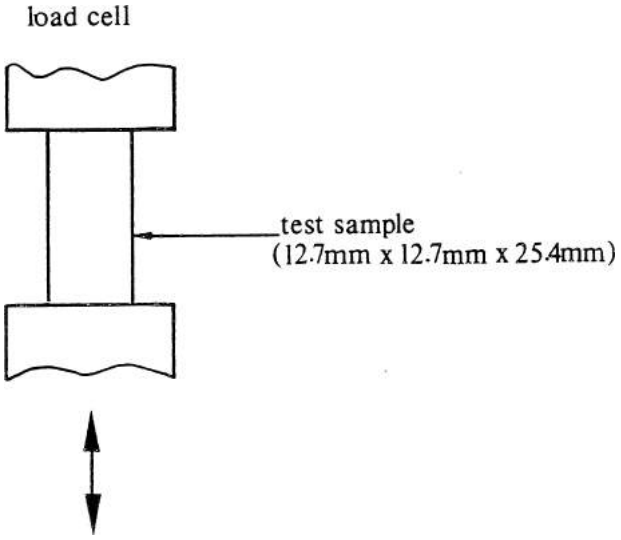

Figure 4.6 *The compression test stage. The rubber sample is bonded to the two steel holders.*

However a predeformation of such a high level, three times the magnitude of the deformation amplitude, makes the test results less interesting in terms of problems in V-belt applications. Therefore, it was decided to bond the test samples to the metal surfaces in order to circumvent the necessity of excessive preloading. The bonding technique used was identical to that used in the shear test.

Bonded test samples made it possible to test both extension and compression.

After each sample had been tested, the bonds between the rubber and steel were analyzed to make sure that no failure in the bond had caused an error in the test data.

When the ends of a test specimen are fixed, it will bulge in the middle when a compression load is applied. The stiffness is greater than for the purely uniaxial state of strain. This effect has been widely investigated [5, 14, 4], and it is known that a shape factor is introduced. The derivations for shape effect are based upon the classical small strain elasticity theory. Good agreement with experimental results can be obtained for compressive strains up to 10 percent [5] or 20 percent [4]. The strain and stress are then defined below.

$$\sigma = \frac{F}{A} \tag{4.15}$$

$$\epsilon = \frac{u}{L} \tag{4.16}$$

Which define the Young's modulus

$$E' = \frac{\sigma_a}{\epsilon_a} S\cos(\delta) = \frac{F_a L}{A u_a} S\cos(\delta) \tag{4.17}$$

$$E'' = \frac{\sigma_a}{\epsilon_a} S\sin(\delta) = \frac{F_a L}{A u_a} S\sin(\delta) \tag{4.18}$$

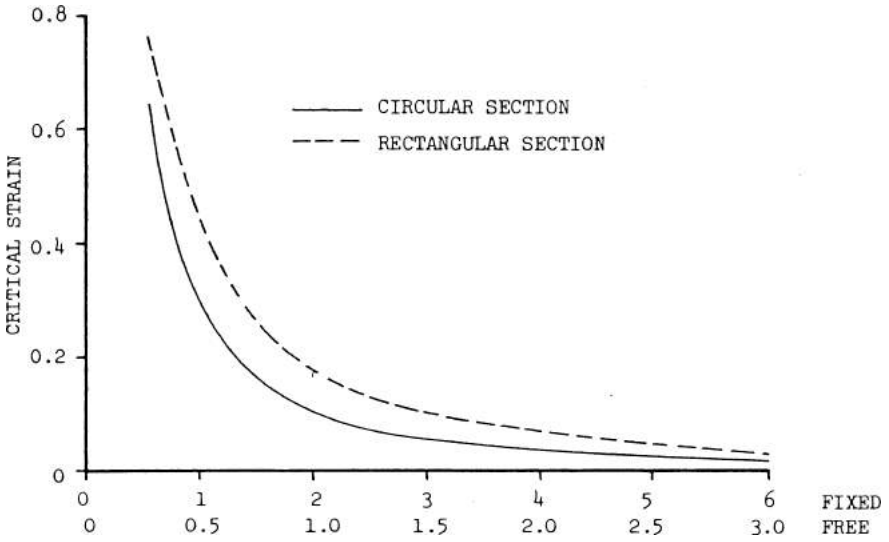

Figure 4.7 *Instability in rubber cylinders. Variation of critical compression strain with dimensions, sample with fixed or free ends. Abscissa: ratio of height to diameter or short side [5].*

Where S is the shape factor which is defined below for a test sample of square cross-section with side a and length L [5].

$$S = 1 + 2k\left(\frac{a}{2L}\right)^2 \tag{4.19}$$

The correction factor k is dependent on the carbon black content and is between 0.5 and 1.0 [5]. Using the equations above for the materials considered and the test piece of the the dimensions shown in Figure 4.6, the error will be approximately 1.6 percent (maximum 3.1 percent) if the shape factor is neglected. As the error is so small in this investigation no shape factor is used.

As discussed above a more uniaxial state of strain can be achieved if the ratio of length to width in the test sample is high. However, there is an upper limit of the ratio because of the risk for instability. Payne and Freakly [5] present a diagram ,shown in Figure 4.7, based on investigations from three different authors. With the help of this diagram it is possible to design rubber mountings to prevent instability under compressive loads.

This diagram indicates that, for a design as shown in Figure 4.6, the critical strain for instability will be approximately 18 percent.

For the highly anisotropic composite materials used in belts, the critical strain is dependent on what material direction is tested. Tests indicated that, for compression in the fiber direction of the material, instability occurred with a deformation of just a few percent. An initial phase of a collapse can easily be visually detected and also seen on the force-deformation curve. The limits were recorded for the different materials and material directions so further tests could be made well below these limits without errors in test data arising due to instability.

The test procedures described so far in this section can be applied to the various materials considered, except in the test for the cord in extension. The cord layer

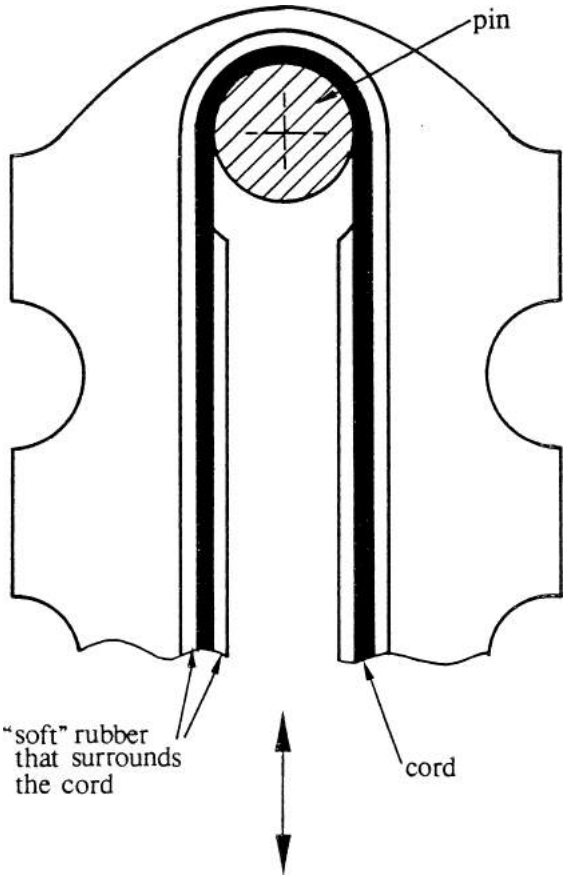

Figure 4.8 *The test arrangement for cord in extension. The cord is in direct contact with the steel pins. Only a part of the V-belt and one pin is shown above. The pins have very small dimensions compared to the length of the V-belt.*

transmits all the torque between the different pulleys in a V-belt drive and therefore has a very high tension load on both the slack and tight side. A well designed V-belt drive usually has a ratio of the forces on the tight side to the slack side of somewhere between three to one and five to one.

As discussed in Chapter 3, the surrounding rubber may have a some what restraining effect on the movement of the individual fibers in the cord, and thereby influence the stiffness of the cord layer. Here, the material properties of cord inside a belt are of interest, and therefore whole belts are tested for tension as shown in Figure 4.8.

To ensure that the force and deformation are transmitted directly to the cord without passing through a rubber layer that will act as a soft spring, the top layer is cut away down to the cord at the contact areas of the steel pin, see Figure 4.8, before the belt is mounted upside down.

The strain is calculated using the measured length of the cord layer of the individual belt. The stresses and strains in the contact area of the belt and the pins are not precisely known. However, the total length of the belts is selected in such a way that any possible error due to uncertainty of length for the strain calculations can be neglected. When calculating stress, the measured cord area from each individual belt was used.

The stiffness of the cord layer is about three orders of magnitude greater than the stiffness of the rubber layers in the belt. This indicates that any remaining error due to rubber elasticity or hysteresis can be neglected. In any case some rubber was cut away to make the belt bend more easily around the pins, and the fabric layer was also pulled off.

4.6 Test in bulk compression

The mode of deformation referred to as isotropic compression is shown in Figure 4.9.

On each face of the cube the normal or hydrostatic stress p is applied and there are no shear stresses. The sample, of the initial volume V_0, then undergoes a volume change ΔV. The bulk modulus is then defined as the ratio of applied hydrostatic stress and induced volume strain.

$$K = \frac{pV_0}{\Delta V} \tag{4.20}$$

In the case of dynamic volume deformation it is customary to specify the dynamic behavior by the complex modules and its components in the same way as, for example, in shear tests [16].

$$|K^\star| = \frac{\sigma_a V_a}{\Delta V_a} \tag{4.21}$$

$$K' = |K^\star| \cos(\delta) \tag{4.22}$$

$$K'' = |K^\star| \sin(\delta) \tag{4.23}$$

σ_a = The hydrostatic stress amplitude

ΔV_a = The volume deformation amplitude

$|K^\star|$ = The absolute bulk modulus

K' = The bulk storage modulus

K'' = The bulk loss modulus

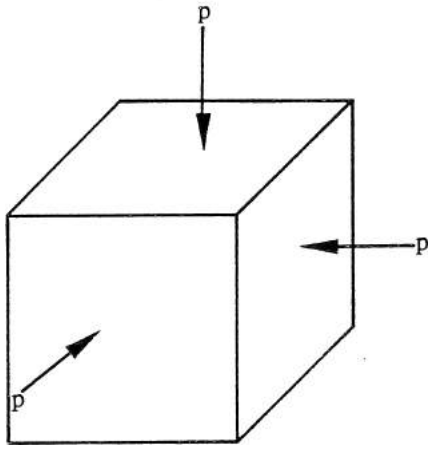

Figure 4.9 *A sample subject to a hydrostatic pressure.*

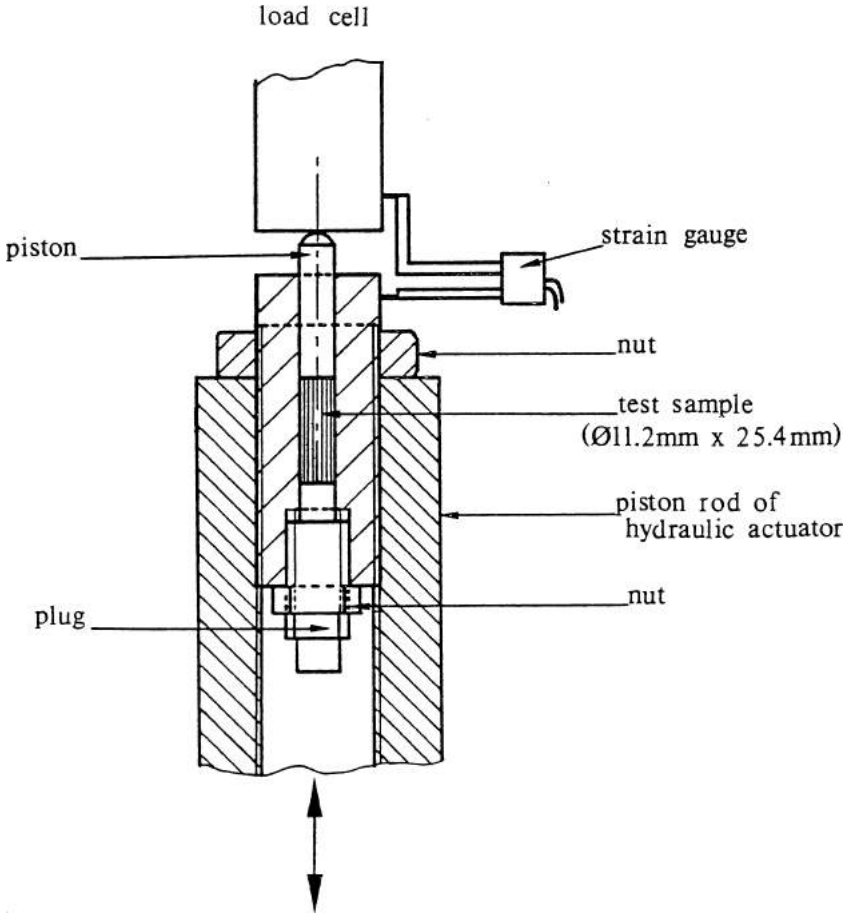

Figure 4.10 *The bulk compression test equipment. The cylindrical rubber sample is enclosed in the cylinder, which is mounted directly on the piston of the hydraulic actuator. The relative movement is detected using a strain gauge.*

Hubbard [9] points out, for bulk compression tests, that the mechanical characteristic is not dependent, at any significant level, on the number of deformation cycles.

For this report the tests were carried out by using the test apparatus shown in Figure 4.10.

The test samples have been ground cylindrically to a diameter that allows a small clearance with respect to the bore. This, in combination with the removable plug in the bottom of the bore, guarantees a good function when exchanging test samples. In dynamic bulk compression tests, when very high forces are used, it is advantageous for the cylinder to be fixed to the stroke actuator.

Before the apparatus was assembled, the test piece was lightly coated with a Teflon spray lubricant and the piston with a thin layer of an extreme pressure lubricant to ensure that the friction forces were negligible compared to the compression forces.

The top end of the piston is rounded off to ensure that the force is applied in its center. The penetration of the piston into the bore is measured by the direct method of mounting a strain gauge, as shown in the Figure 4.10, to indicate the relative movement of the piston to the cylinder. This is necessary in order to avoid errors due to the compliance in the cross-heads.

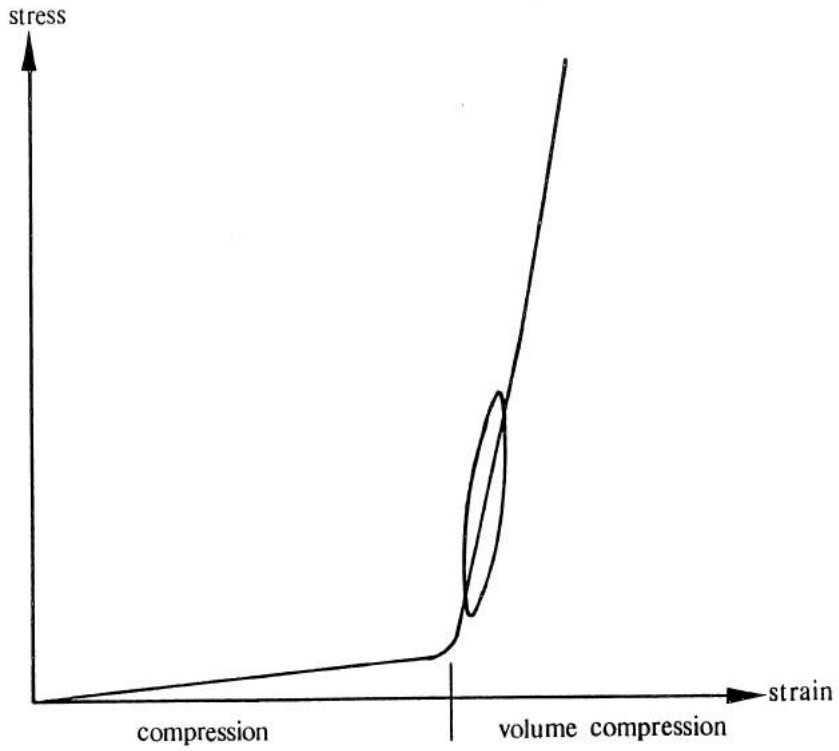

Figure 4.11 *The stress-strain curve for a rubber sample subject to compression in an enclosing cylinder. The stress-strain loop in dynamic bulk compression test is also shown.*

As indicated in Figure 4.11, it is necessary to apply a preload before any cyclic deformation can be superimposed for measuring the bulk modulus.

First, load has to be applied until the sample completely fills up the bore, then a preload of at least the size of the dynamic force amplitude has to be applied. This ensures that the deformation cycle is kept on the steep part of the curve shown above. For practical reasons some preliminary tests were run for different materials and material directions to determine what preload was needed to run all the following tests.

In a cylinder where the lateral strains are zero after the initial diametrical expansion of the test sample, the bulk modulus is not measured but the longitudinal module, due to the applied stress, is not truly hydrostatic. For the case of isotropic materials the longitudinal module is defined below.

$$L = K + \frac{4}{3}G \tag{4.24}$$

However, the correction factor is so small that it is negligible for rubber materials.

When investigating the influence of frequency on the material properties, due to machine limitations, the tests have to be run at frequencies lower than one Hz because of the very high dynamic loads.

4.7 Temperature

The conclusion that may be drawn from the previous work, discussed in Chapter 3, is that the temperature of the material is one of the most important factors regarding material properties for elastomers.

Sources of heat are the environment, friction losses on the surface of a body and hysteresis work in the body. As rubber is a very good insulator it takes a long time to achieve temperature equilibrium if the body is moved to an environment with a different temperature level. The high friction coefficient in combination with poor heat conduction can cause high local temperatures on the surfaces of a sliding body.

The hysteresis work can cause significant rises of temperature in many applications. In this case it is a combination of heat production and poor conduction that creates the extreme rise in high temperature.

If the temperature of the test sample is one of the parameters that should be recorded in dynamic tests, there are two possible methods that can be used. The first method is to do the test in such a short time that no significant temperature rises in the material can occur due to hysteresis. A worst case where no conduction is considered can be calculated with the following equation:

$$\dot{T} = \frac{\pi \gamma_a^2 G'' f}{c\rho} = \frac{\pi \gamma_a^2 |G^\star| \sin(\delta) f}{c\rho} \tag{4.25}$$

Where

$$f = \text{Frequency of cycling} \tag{4.26}$$

$$c = \text{Specific heat} \tag{4.27}$$

$$\dot{T} = \text{The rate of temperature rise} \tag{4.28}$$

For a strain amplitude of 4.5 percent, an absolute modulus of 10 MPa, a loss angle of 8 degrees, a specific heat of 1.67 (kJoule / kg°C), a density of $1.15 \cdot 10^3$ (kg / m^3) and a frequency of 60 Hz, the rate of rise in temperature would be 0.28 (°C /s). Already after fifteen seconds the temperature in the environment cannot be used as the representative temperature of the material due to the large difference.

In this investigation the initial run-in effects, discussed in Chapter 3, must be avoided. The test samples therefore have to be run in a large number of cycles so conditions stabilize. This makes the method above not usefull except for very small strain amplitudes, at which the rise in temperature is negligible.

The second method discussed here is to measure the body temperature of the sample as precisely as possibly during the dynamic test. No holes, etc. in the test sample may be made as this may change the stiffness or cause a rupture in the test sample. For this reason the temperature has to be measured on the surface of the sample.

When measuring the changing temperature on a surface, if non-conduct sensing is not practical, it is important that only a small amount of heat is used to induce correct temperature in the temperature sensor in order to achieve fast response. This means that the mass of the sensor has to be small compared to the body that generates the heat. The temperature sensor must also be well insulated against the environment so

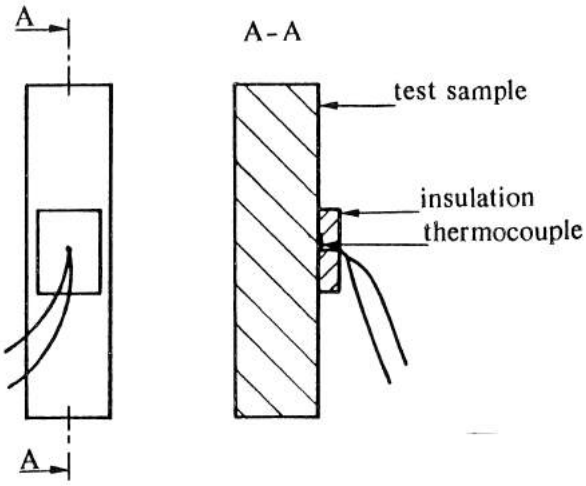

Figure 4.12 *The thermocouple with insulation mounted on a test sample for simple shear.*

that the measured temperature will be as close as possible to the body temperature. A thermocouple insulated with a piece of styrene foam plastic fulfills the requirements above. The design is illustrated in the Figure 4.12.

The temperature was continuously recorded as a time temperature graph during the whole test. This made it easy to follow the temperature rise to equilibrium for a certain test. Of course the temperature will vary inside the sample because of the heat conduction. However the method described above should show temperatures that represent the conditions a certain distance below the surface of the sample because the thermocouple is well insulated against the environment. In any case tests done on samples of the same physical dimensions and similar heat conduction properties will be comparable.

In the bulk compression test the environment temperature was used as the material temperature. Calculations with Equation 4.25 showed that no significant rises in temperature occurred, due to the small amplitudes and low frequencies. This result was obtained despite the fact that the rubber sample inside the bore is in contact with steel surfaces which conduct heat very well.

4.8 The waveform analysis

When running a test, two low voltage signals, the force signal and the stroke feedback signal, are produced from the dynamic test system. Force transducers relying on the use of strain gauges to monitor the deformation of a proof-ring under an applied load are suitable for measuring low-frequency dynamic forces. It is important that similar electronic detecting circuits be used for detecting the signals from both force and displacement-measuring transducers so that a negligible phase difference is introduced by these circuits. To verify this, test were run for a steel spring at different frequencies. Tests were run up to 70 Hz without detection of any significant phase errors.

The two signals, the stroke feedback signal and the force signal, were recorded

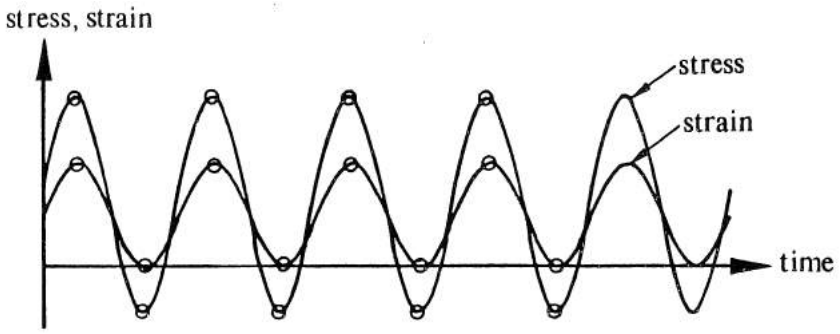

Figure 4.13 *The stress and strain signals stored in the Wave form analysis system. All the points indicated with "o" are used when calculating average values of amplitudes, etc.*

continuously of the Norland Wave form analysis system. The sampling frequency was selected so that about five periods were shown simultaneously.

When the measurement is taken the curves shown are stored in the memory. The five successive periods for each curve are stored in arrays with 1024 elements.

In all the data analyzes described below, four successive wave periods are analyzed. The parameters presented are therefore the mean values from the calculations for each of the four periods. This was done to decrease the risk of obtaining bad results due to a stochastic error in the test signals.

The arrays of the curves shown above were then multiplied by the geometric constants for the sample tested to obtain stress and strain instead of a certain voltage. A slight smoothing was then performed to decrease the influence of noise from the environment. Each data value was replaced with a mean value calculated from itself and a number of surrounding points. The selected number was low enough that no significant error was introduced.

Two new curves or arrays were then calculated, the strain rate and the strain rate multiplied by the stress. For the last curve mentioned above the maximum stored energy and energy loss per cycle were integrated.

The phase angle or loss angle can be obtained in two ways. First, by measuring the phase difference between the strain curve and the stress curve, second by calculating it from the loss energy as shown below.

$$\sin(\delta) = \frac{\text{Loss energy}}{\pi \sigma_a \epsilon_a} \tag{4.29}$$

This latter relation gives an average phase angle value and is therefore particularly useful when there is non-linearity [19, 11]. The data for the loss angle presented in this report were obtained by this method.

A program that performed the calculations discussed above and presented the results obtained was written for the Norland 3001 Waveform Analysis System. The results for a test were printed on a sheet where the stress-strain curve from the four cycles were also plotted, see figure 4.14. The temperature and the number of cycles logged were filled in as well. The strain rate divided by angular speed was plotted against strain to verify the sinusoidal motion, so that a perfect circle was obtained.

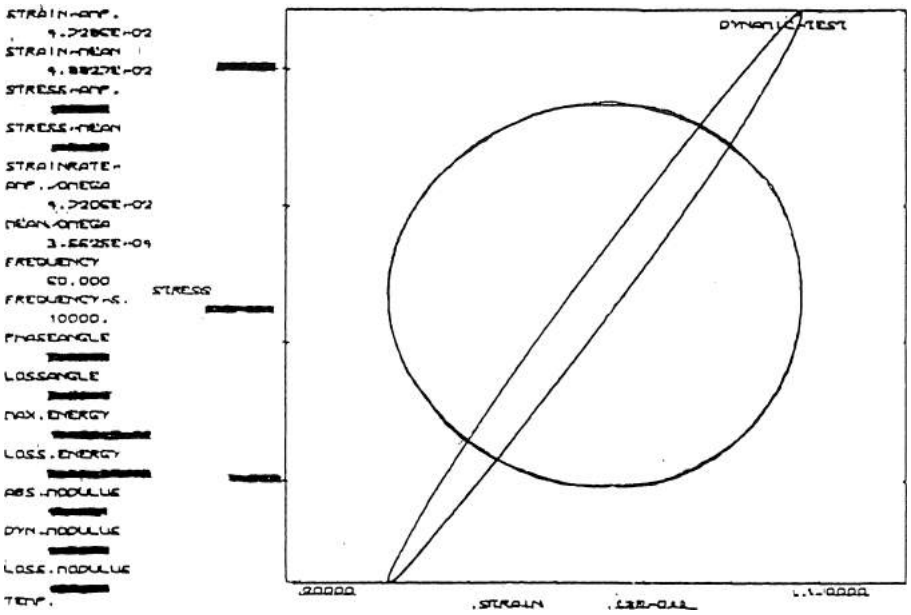

Figure 4.14 *A typical test data sheet for compression or shear test.*

4.9 The test procedure

The conclusion drawn in Chapter 3 was that the material considered shows a highly complex behavior that was dependent on temperature, frequency, strain amplitude, strain mean value, atmosphere and time. This made it necessary to limit the variation of parameters to what was needed in a certain application to be able to perform a complete test series. Otherwise the number of tests would have been too great.

The main aim of this investigation was to study the different materials in a V-belt for the conditions they are subject to in a real application. Initially, the conditions that apply for all parts of a belt will be discussed.

V-belts are typically used in long-term applications. A belt is expected to have a service life of up to several thousand hours. The frequency of bending is within the limits of 1 to 100 Hz. This means that all initial effects, such as the Mullin's effect, that are highly significant during the first cycles, are of no interest and should be avoided. The samples should be run at so many deformation cycles that no significant difference can be detected in successive tests. From the results of some preliminary tests it was decided to run all rubber samples 30000 cycles before the first measurement was made. After this, tests were done for 3 Hz, 34 Hz and 60 Hz.

The bulk compression test is an exception. In this test the frequency has to be limited to 1 Hz owing to the very high loads and machine limitations. For this case, initial effects have been reported to be no significant [9]. In these tests the samples were allowed to cycle 200 periods before tests were done and the frequencies used were 0.01 Hz and 1 Hz.

The temperature of the belt can vary greatly because of the influence from the environment and power losses. Here the environment temperature was held at two to three levels, between room temperature and 110 degrees Celsius. All common

applications should be covered by this range. The hysteresis caused the measured temperature to be higher than the temperature in the environment in some tests.

For practical reasons the bulk modulus could not be tested at elevated temperatures. This is probably not a serious limitation due to the nearly incompressible behavior of the rubber materials.

Interpolations from published experimental data [17] and approximate calculations for some sizes of the V-belt in different applications were done to obtain some approximate values on the conditions to which the different materials in different material directions are subject.

The belt is free between the pulleys, and the rubber in the belt is subject to small strains due to the high stiffness of the cord. When it passes through a pulley, the belt is bent and compressed. The compressive strains are varied approximately linearly from very small strains in the the neutral layer up to 10 - 15 percent in the bottom layer. In the axial direction the belt is relatively stiff due to the reinforcement, and the compressive strains are typically below 2 percent.

The type of deformation cycle described above is similar to a sine wave deformation cycle where the mean value of the compressive strain is about the same as the amplitude, and the frequency equals the bending frequency. For this reason, all rubber test were performed with this type of cyclic deformation at which the mean strain is equal to one amplitude. Some special tests were also made to investigate the influence of the strain mean level up to a level of twice the amplitude.

For deformation in shear it was estimated, with help of the method described above, that the strain should stay below 10 - 15 percent in all parts of the belt in most applications. For the shear test the mean strain level was also set at one amplitude. The influence of a different strain mean level was studied in some additional tests.

The stiffness of the cord layer is about three orders of magnitude above that of the rubber. Therefore it is the material properties of the cord and its longitudinal loads that dictate rubber strains close to the cord. A well designed V-belt transmission can have a ratio of up to 5 to 1 for the force on the tight side to the slack side. The longitudinal forces in the belt were easily estimated using a chosen force ratio and the design methods for the power transmission with the belt studied. The strains could be obtained from the forces, and it was concluded that a good estimation of the upper limit of the double strain amplitude can be 1 percent.

So far the limits of all the studied parameters have been discussed and the test were made for a certain number of levels inside these limits.

However, there is a another problem that must be considered. The rubber material has a “memory”. A rubber sample that has been tested first at low strain amplitude and then high strain amplitude will not give the same test result when tested at low strain again. This also applies to large temperature variations.

The mechanisms discussed in Chapter 3 cause some irreversible changes in the material. It may, in fact, take many days of recovery for the material to achieve properties close to the original values. These effects were confirmed in preliminary tests. The following conclusions can also be drawn.

A test at a low strain amplitude has no significant influence on a later test with a strain amplitude about double the level or more. Neither can any, irreversible

influence of the frequency be detected.

At a certain point inside a belt that is running under stable conditions in a power transmission, there is a unique combination of the parameters strain amplitude, temperature and frequency. The material point is not subject to a sudden change in any of these parameters. It is therefore important to study the characteristics of the material for such unique combinations where only the parameters mentioned above are held constant.

When performing tests for many combinations of these parameters which have long-term effects on material properties it is impossible to use the same sample for all test combinations. For this reason new samples were used at each temperature level. They were cut out of the same piece of material, and many samples were tested to account for stochastic variations in the test results. The main problem with this method is that so many tests have to be carried out. For example, with three temperatures, three strain amplitudes, three frequencies, four materials, four different material directions and two samples for each combination, the number of tests is 864. If the time estimated, including sample preparation for each test is 20 minutes, the test program above takes 288 hours. For practical reasons it was necessary to eliminate the least interesting combinations before carrying out the test program.

The question arises as to whether the material properties thus obtained can be used in calculations for a power transmission that are subject to changes in transmitted power and therefore changes in load and temperature. The changes considered here are so fast that a possible recovery process of the material properties cannot be counted on. The strain amplitudes in the rubber are closely related to the geometry of the belt and the pulleys and these are not usually subject to change. It is possible that it is the maximum strain amplitude during a certain time interval that is the significant value. Temperature is, however, by nature a phenomenon that does not allow very fast change due to all the stored energy. The factors discussed above may make it possible to use the material data obtained here in a wider application than just total stable conditions. However, only a few points have been discussed here and more research is needed in this field.

5

Analytical representation of an n-dimensional empirical function

5.1 Introduction

When studying experimental data which is a function of more than one or two variables or parameters, it is impossible to plot diagrams from these data directly and be able to draw conclusions. For instance, to plot a two dimensional diagram of data which depends on four variables, one must be able to fix two variables to certain values and thus make a projection. However, it is usually impossible to fix a variable to a certain value, as the available data points can have different values. There can also be stochastic variations if the data has been collected from several independent experiments. To be able to make a projection one must have all test points in a matrix of numerical values. This is normally not possible in experimental analysis. Consider, for instance, the temperature variable of rubber in this investigation, which is dependent on hysteresis and therefore very hard to control.

The solution to these problems is to fit the test data to a function and plot projections of this function in diagrams and figures. It is very important to choose a function that does not introduce any restrictions that result in loss of information from the test data. It is the characteristics of the test data that should be studied, not the function itself. Yet it is also important to have control over the degrees of freedom of this function. Otherwise the function can give a totally erroneous interpretation of the test data. It is important that there be a sufficient number of test data points for all variable combinations so that interpolation and not extrapolation is always performed.

In a physical process which is represented by the material parameters measured in this report, it could be expected that the function and its first derivative would be continuous. This is in analogy with a free form geometrical surface.

5.2 Fitting of a function

As discussed in the previous section, many of the necessary properties are common to applications in free form geometrical surfaces. Therefore it may be wise to use the theory for such surfaces and develop it further for this application.

Consider the theory for Bezier surfaces. Extend the number of parameters to be the same as the number of independent variables which are needed. Increase the dimension of the vectors which describe the geometrical space to be the same number as the total number of variables. This is the number of independent variables plus one, as there is only one dependent variable.

In theory the function thus obtained can be used directly, by letting each of the variables correspond to one dimension of the space vector. However this method is not very easy to use and understand. There is no simple way of choosing the control points or establishing the number of them, i.e. the order of the blending function, for a certain parameter. Construction of a mapping between the parameter domain and the geometrical domain is not simple and can involve iterative calculations.

For this reason the function is developed further and some restrictions are introduced. We assume that the real function which is studied here behaves well and doesn't have double points etc, as is true for all functions modelling real applications. Thus the further development introduced no restrictions on the desired functionality.

Let each of the first n-1 dimensions of the vector space correspond to an independent variable, and the last n:th dimension correspond to the dependent variable. By doing the mapping between the parameters and the vector, the restriction that each dimension of the vector should only depend on a certain parameter is introduced. This means that there is one parameter for each of the dimensions or independent variables. In order to perform such calculations it is convenient to leave the vector representation of the equation, and rewrite it into a system of equations, one for each vector dimension or variable. When a certain variable is a function of a special parameter it is quite natural to set the order of its blending function as less than or equal to the number of separate test levels of that variable minus one. Test levels are significant separate numerical values of a certain variable. The tests points should be on those different levels, at least one on each level. When choosing test levels for a certain variable, knowledge of the problem being studied is important. If the test levels are chosen badly, a stochastic variation can show through for a high order blending function. On the other hand, if too low a order of polynomial is chosen, information may be lost. The choice of control points is another important possibility for controlling the behavior of the function. This can be studied as a one-dimensional problem for each variable. A concentration of control points makes it more possible to control that part of the function. Simple rules such as equidistance can be chosen. However, the algorithm used directly influences the mapping between the parameter and the variable, since the control points are constants in the corresponding equation. This controls how easy it will be to express the equation analytically.

When fitting the function to the test data, the control points of the dependent variable, i.e. the last dimension, will be calculated. If regression techniques are used to fit the function to the test data, the multiple correlation coefficient, the residual

standard deviation and the maximum relative error can be used to judge how well the function approximates the test data.

The theory presented above does not impose any limitations on the number of variables or constraints on the test data. Here the Bezier function was chosen for its simplicity and the fact that it has only one parameter interval as the blending function can be of high order without creating a problem. However, other types of functions can be used, such as, Ferguson, B-spline etc. This will, of course, result in the actual functions and mapping functions being different than was the case for the Bezier function, but they will be developed in the same way as discussed above and using the same restrictions.

In this investigation we need a function with one dependent and three independent variables. Normally there are test data for three different levels of values of each variable in this investigation. This means that for the blending function, the second order is the highest order that can be used. The functions and equations are presented below for this case.

A Bezier surface of second order.

$$\vec{\boldsymbol{r}}(u,v) = \sum_{i=0}^{2}\sum_{j=0}^{2} \vec{\boldsymbol{rc}}_{ij} U_i(u) V_j(v) \tag{5.1}$$

The vector $\vec{\boldsymbol{r}}(u,v)$ describes the surface and the constant vectors $\vec{\boldsymbol{rc}}_{ij}$ are the control points. The functions $U(u)$ and $V(v)$ are blending functions of the type given below.

$$B_{i2}(t) = \frac{2!}{(2-i)!\cdot i!} t^i (1-t)^{(2-i)} \tag{5.2}$$

Extend the function to four dimensions and three parameters. Written as a system of equations it will be like the following one, with one equation for each dimension.

$$r^1(u,v,w) = \sum_{i=0}^{2}\sum_{j=0}^{2}\sum_{l=0}^{2} rc^1_{ijl} U_i(u) V_j(v) W_l(w) \tag{5.3}$$

$$r^2(u,v,w) = \sum_{i=0}^{2}\sum_{j=0}^{2}\sum_{l=0}^{2} rc^2_{ijl} U_i(u) V_j(v) W_l(w) \tag{5.4}$$

$$r^3(u,v,w) = \sum_{i=0}^{2}\sum_{j=0}^{2}\sum_{l=0}^{2} rc^3_{ijl} U_i(u) V_j(v) W_l(w) \tag{5.5}$$

$$r^4(u,v,w) = \sum_{i=0}^{2}\sum_{j=0}^{2}\sum_{l=0}^{2} rc^4_{ijl} U_i(u) V_j(v) W_l(w) \tag{5.6}$$

Functions r^1, r^2, and r^3 are referred to as the independent variables. Function r^4 is the dependent variable. Now the restriction is applied that variable r^1 is only a function of parameter u, variable r^2 is only a function of v, variable r^3 is only dependent of w. It will be shown for Equation 5.3. Let the control points of Equation 5.3 have the following properties:

$$rc^1_{000} = rc^1_{010} = rc^1_{011} = rc^1_{012} = rc^1_{020} = rc^1_{021} = rc^1_{022} \quad (5.7)$$
$$rc^1_{100} = rc^1_{110} = rc^1_{111} = rc^1_{112} = rc^1_{120} = rc^1_{121} = rc^1_{122} \quad (5.8)$$
$$rc^1_{200} = rc^1_{210} = rc^1_{211} = rc^1_{212} = rc^1_{220} = rc^1_{221} = rc^1_{222} \quad (5.9)$$

Equations 5.3, 5.7, 5.8 and 5.9 result in

$$r^1(u,v,w) = \sum_{i=0}^{2} rc^1_{i00} U_i(u) \sum_{j=0}^{2} V_j(v) \sum_{l=0}^{2} W_l(w) \quad (5.10)$$

According to the property of the blending function the sum of its components is equal to one.

$$\sum_{j=0}^{2} V_j(v) = 1 \quad (5.11)$$
$$\sum_{l=0}^{2} W_l(w) = 1 \quad (5.12)$$

Equations 5.10, 5.11 and 5.12 result in:

$$r^1(u,v,w) = \sum_{i=0}^{2} rc^1_{i00} U_i(u) \quad (5.13)$$

As no dependency of the parameters v and w is left the equation is written as follows:

$$r^1(u) = \sum_{i=0}^{2} rc^1_i U_i(u) \quad (5.14)$$

Now the system of equations, 5.3 - 5.6, can be replaced with the following equations:

$$r^1(u) = \sum_{i=0}^{2} rc^1_i U_i(u) \quad (5.15)$$
$$r^2(v) = \sum_{j=0}^{2} rc^2_j V_j(v) \quad (5.16)$$
$$r^3(w) = \sum_{l=0}^{2} rc^3_l W_l(w) \quad (5.17)$$
$$r^4(u,v,w) = \sum_{i=0}^{2} \sum_{j=0}^{2} \sum_{l=0}^{2} rc^4_{ijl} U_i(u) V_j(v) W_l(w) \quad (5.18)$$

What is left to do is to choose the method for distributing the control points. Here they are set as being chosen equidistant, which means for example for variable 1:

$$rc_1^1 = \frac{rc_0^1 + rc_2^1}{2} \tag{5.19}$$

The blending function used together with Equations 5.15 and 5.19 gives a very simple linear expression for the parameter u and the start and end of the variable interval for which the function has been defined.

$$\begin{aligned} rc^1(u) &= rc_0^1 + \left(rc_2^1 - rc_0^1\right)u \quad \text{or} \\ u\left(r^1\right) &= \frac{rc^1 - rc_0^1}{rc_2^1 - rc_0^1} \end{aligned} \tag{5.20}$$

Finally, the system of equations is reduced to the simple expressions below. The dependent variables are expressed directly in terms of their parameters, and are linear expressions. Therefore, the whole system can be expressed as one linear equation that is fitted to test data using linear regression techniques, and the control points in Equation 5.24 be calculated. They are the regression constants.

$$u\left(r^1\right) = \frac{rc^1 - rc_0^1}{rc_2^1 - rc_0^1} \tag{5.21}$$

$$v\left(r^2\right) = \frac{rc^2 - rc_0^2}{rc_2^2 - rc_0^2} \tag{5.22}$$

$$w\left(r^3\right) = \frac{rc^3 - rc_0^3}{rc_2^3 - rc_0^3} \tag{5.23}$$

$$r^4(u,v,w) = \sum_{i=0}^{2}\sum_{j=0}^{2}\sum_{l=0}^{2} rc_{ijl}^4 U_i(u)V_j(v)W_l(w) \tag{5.24}$$

These four functions can easily be expressed as

$$r^4\left(r^1, r^2, r^3\right) = \mathcal{F}\left(r^1, r^2, r^3\right) \tag{5.25}$$

which means that the dependent variable r^4 is a function of the independent variables r^1, r^2 and r^3.

5.3 Handling of missing values

In the example discussed in the previous section, the order of the blending functions for all independent variables were chosen so that three different test levels or values were required for each variable. That means a total of 27 different test points which correspond to the 27 constants which should be calculated. However, in practice it is quite common for it to be impossible to perform all the tests and for test data to be missing for some combinations of test variables. This means that the above function cannot be used. A function of a lower order can be constructed by using blending functions of a lower order for one or several variables. Sometimes this is a

good solution, but in other cases the high order blending function is really needed, e.g. when just a few data points are missing for a certain combination of variable values. In this case some other method must be used. Missing data points for a certain combination of independent variables cannot be replaced by extra data points in other parts of the matrix. This is a fundamental rule and violation leads to in totally useless results. There are too many degrees of freedom of the function.

The solution to this dilemma is to introduce local constraints which reduce the degrees of freedom of the function. This is not done by changing blending functions as discussed above, but by introducing constraints which give equations involving the control points.

Here we present an example which will be studied more closely. Assume that for the variable r^3's maximum value or third level of test values there are no test data points for the variable r^1's third level. This means that for a parameter which is close to 1 there is not enough information to fit a second order function of parameter u, as there are only two test points for that variable. Hence it is necessary to forcibly make the function linear, as this is the highest order function which can be fitted to two data points.

Equation 5.24 is

$$r^4(u,v,w) = \sum_{i=0}^{2}\sum_{j=0}^{2}\sum_{l=0}^{2} rc^4_{ijl} U_i(u) V_j(v) W_l(w)$$

A restriction is imposed. For $w = 1$ let

$$\frac{\partial^2 r^4(u,v,w)}{\partial u^2} = 0 \tag{5.26}$$

This means that the function will be linear in parameter u for $w = 1$, which is precisely what was discussed above. Performing the partial derivative with respect to u produce:.

$$\frac{\partial^2 r^4(u,v,w)}{\partial u^2} = \sum_{i=0}^{2}\sum_{j=0}^{2}\sum_{l=0}^{2} rc^4_{ijl} \frac{\partial^2 U_i(u)}{\partial u^2} V_j(v) W_l(w) \tag{5.27}$$

Substituting $w = 1$ and imposing the constraint, the following equation is obtained:

$$\frac{\partial^2 r^4(u,v)}{\partial u^2} = \sum_{j=0}^{2} V_j(v) \sum_{i=0}^{2} rc^4_{ij2} \frac{\partial^2 U_i(u)}{\partial u^2} = 0 \tag{5.28}$$

It is reasonable that this equation should be valid for all values of the parameter v, which results in Equation 5.29. This equation provides a reduction from 27 degrees of freedom to 24. This was needed since three data points were missing.

$$\begin{aligned} \sum_{i=0}^{2} rc^4_{ij2} \frac{\partial^2 U_i(u)}{\partial u^2} &= 0 \\ j &\in [0,1,2] \end{aligned} \tag{5.29}$$

This can be rewritten:

$$rc^4_{202} = -rc^4_{002} + 2rc^4_{102} \tag{5.30}$$
$$rc^4_{212} = -rc^4_{012} + 2rc^4_{112} \tag{5.31}$$
$$rc^4_{222} = -rc^4_{022} + 2rc^4_{122} \tag{5.32}$$

6
Test results

6.1 Introduction and some general results

In this chapter we present test results according to the method described in Chapter 5, to make it possible to evaluate the test data. For each combination of material, material direction and parameter studied, the number of test values, the multiple correlation coefficient and the residual standard deviation are presented in a diagram. The MULREG program system was used for all database and statistical analysis of the test data [6]. The diagrams are drawn using the SURRENDER graphic system [20].The most important parameters discussed are elastic modulus, loss modulus and "mean" modulus. The first two are defined from the hysteresis loop. The last parameter results from the position of the hysteresis loop, as it is the stress mean value divided by the strain mean value. Independent variables are temperature, frequency and strain amplitude. These tests have been made for combinations of three different frequences, three different strain amplitudes and three different temperatures, with a few exceptions: the compression tests were performed for two temperature levels, and no shear tests were performed for the largest amplitude at the highest temperature. This was taken into consideration when using the function fitting method described in Chapter 5. The mean strain level is equal to one strain amplitude in the diagrams, unless otherwise stated. Normally, three to four independent samples were taken at each test point to account for stochastic errors or variations of material properties. The results show that the repeatability of the test procedure is excellent. The difference between two independent test samples is usually within one to two percent. This is also shown by a typical multiple correlation coefficient of 0.99 .

The different materials are discussed in separate sections below. Due to the large size of the test program that have been carried out, only general observations will be mentioned explicitly. For details it is best to study the diagrams themselves.

The following conventions apply to material and material orientation. Material 1 is the hard rubber in the bottom layer. Material 2 is the relatively soft rubber that surrounds the cord. Material 3 is the rubber impregnated fabric at the top of the belt. Material labels which start with the digit 4 refer to the cord. The material directions are related to a V-belt drive. Orientation 1 is the radial direction outward from the axis of the pulley. Orientation 2 is along the belt i.e. in the peripheral

direction. Lastly, there is the axial direction, which is orientation 3. When referring to the tests, then example orientation label 22 means that the surface on which the stress is applied has direction 2 (the first digit) and that the stress is also in direction 2 (the last digit). Orientation 23 means that this is a shear test on a surface with normal direction 2 and shear stress in direction 3. The elastic modulus, loss modulus and mean modulus are presented nondimensionally in the diagrams by dividing them with a certain value. For the cord the constant is $E1$ used, and in the other cases $E0$ is used. To obtain those constants, I refer to Dayco Technical Center, Dayco Corp. [1].

A special test series to investigate the influence of different mean strain levels was done. Those tests were performed at room temperature level. The tests were in shear and uniaxial compression. The uniaxial test in the material directions where large strain levels could be expected, i.e. the not reinforced material directions. The strain levels were, mean strain equal to zero, mean strain equal to one strain amplitude, and mean strain equal to two strain amplitudes. The result was that no significant influence of the mean strain level could be detected. This for a mean strain within the limits specified above.

6.2 Material 1 - the "hard" rubber in the bottom layer

Test data for material 1 are shown in diagrams 6.1, 6.2, 6.3, 6.4, 6.5, 6.6, 6.7, and 6.8. By studying the Dynamic Young's Modulus and the Dynamic Shear Modulus it becomes clear that this material is really a heavily reinforced elastomer composite. One material direction (orientation 33) is different from the other directions. The material is about 4 times stiffer in this direction. Thus the material description "transversal isotropic" can be applied.

The elastic modulus shows a strong dependence on temperature and strain amplitude. An increase from room temperature to about 100 degrees Celsius typically cause a reduction by a factor 2 in elastic modulus. The strain amplitudes are 0.005, 0.015 and 0.045 except for the reinforced material direction, in which they are 0.005 and 0.01. However, the increase of strain amplitude causes a reduction of elastic modulus of the same factor 2 as for the temperature discussed above. The variation in frequency from 3 Hz to 60 Hz only typically results in an increase in modulus of 10-15 percent.

From the diagrams of the mean or static modulus and the diagrams of mean stress divided by stress amplitude it can be concluded that the mean modulus varies between 0.75 and 0.25 percent of the elastic modulus. However, the temperature is the most important parameter here, and the mean modulus decreases quickly with increasing temperature. It could be suspected that pure plastic deformation or creep causes this behavior. However unloading the test samples after the tests show that no permanent deformation has taken place and therefore this conclusion is not true. The frequency has very little influence on the mean modulus.

The loss modulus has more complicated behavior. It shows a very strong dependency on all the parameters and can vary within a factor of 3 for the parameter intervals

discussed. In general it decreases with decreasing temperature or with increasing strain amplitude, but it seems to have an optimum at a certain frequency. The anisotropic characteristic commented on above also applies to this kind of modulus.

The bulk modulus is shown in diagram 6.37. It can be seen that there is a slight frequency dependence. However, the most important result is that the bulk modulus is about three orders of magnitude higher than the shear modulus discussed above. This result means that for many applications the material can be considered incompressible.

6.3 Material 2 - the "soft" rubber that surrounds the cord

The test data for material 2 are presented in diagrams 6.9, 6.10, 6.11, 6.12, 6.13, 6.14, 6.15, and 6.16. This material shows a much less anisotropic behavior than material 1. Along direction 22 this material is about 25 percent stiffer than along the other directions. Thus the description "transverse isotropic" fits this material, too. This result correlates with the fact that the material is only reinforced with a very small amount of short fiber in the circumferential direction.

The elastic modulus shows a strong dependence on temperature and strain amplitude. An increase from room temperature to about 100 degrees Celsius typically causes a reduction by a factor of 2 or more in the elastic modulus. The strain amplitudes are 0.005, 0.015 and 0.045 in the shear test. In the other cases they are 0.005 and 0.015. The increase of strain amplitude causes a reduction of elastic modulus of the same factor (2 - 2.5) as for the temperature. The variation in frequency from 3 Hz to 60 Hz results in a typical increase in modulus typically 10-15 percent and is therefore the least interesting parameter for the chosen parameter intervals.

The diagrams of the mean modulus and the mean stress divided by the stress amplitude show that the mean modulus varies between 0.6 and 0.25 percent of the elastic modulus. The mean modulus decreases quickly with increasing temperature, and the frequency has very little influence on it. No significant residual deformation was detected, as discussed in the previous section.

The loss modulus has the same complicated behavior for material 2 as for material 1. The loss modulus shows strong dependency on all the parameters and can vary up to a factor of 3. It decreases with decreasing temperature or with increasing strain amplitude and has an optimum value at a certain frequency.

The bulk modulus is shown in diagram 6.38. The elastic bulk modulus increases with increasing volume strain amplitude. There is a small frequency increase at higher frequencies. For this material, too, the bulk modulus is about three orders of magnitude higher than the other moduli. This result means that for many applications the material may be considered incompressible.

6.4 Material 3 - the rubber impregnated fabric

This material is different from the two discussed previously. It consists of several thin layers of rubber-impregnated fabric. All the layers are oriented in the same direction. The fabric is woven with 90 degrees between the weft and the weave. Therefore the material has orthotropic characteristics in the plane of the fabric. This fabric represents a large part of the material volume. The test data for material 3 are shown in diagrams 6.17, 6.18, 6.19, 6.20, 6.21, 6.22, 6.23, 6.24, 6.25, 6.26, 6.27, and 6.28. The orthogonal directions of weft and weave do not correspond to the axial (3) or the peripheral (2) directions, but are rotated 45 degrees. Therefore tests were not only performed in combinations 11,33,13 and 23 of surface normal and stress directions, but were also made in the orthotropic directions. Combination 3232 means surface direction 45 degrees from directions 3 and 2 . This corresponds to the direction of the reinforcement, and a stress in the same direction. Similarly, combination 2332 designates a shear test on a surface with the direction between directions 2 and 3.

The elastic modulus shows a strong dependence on temperature, strain amplitude, and frequency. An increase from room temperature to about 100 degrees Celsius can result in reduction in elastic modulus by a factor of 2. The strain amplitude interval is 0.005 to 0.045 in shear test, except for the combination 23 where it is very stiff, 0.005 to 0.015, as in the other directions. The increase in strain amplitude may also cause a reduction in elastic modulus of a factor of 2. Variation of the frequency from 3 Hz to 60 Hz resulted in a typical increase in modulus of 10 - 20 percent.

The diagrams of the mean modulus and the stress mean divided by stress amplitude show that the mean module varies between 0.75 to 0.25 percent of the elastic modulus. The mean modulus decreases rapidly with increasing temperature, while frequency has very little influence. No significant residual deformation was detected, as discussed in previous sections.

The loss modulus shows strong dependency of all the parameters and may vary up to a factor of 2. It decreases with decreasing temperature or with increasing strain amplitude, and seems to increase with frequency.

The bulk moduli are shown in diagram 6.39. There was a greater increase with frequency compared with the previous materials. The bulk hysteresis was also higher than for the other materials. It should be noted that the material showed creep behavior in the bulk modulus testing. Here the bulk modulus is also about three orders of magnitude higher than the shear modulus. This result means that for many applications the material may be considered incompressible.

6.5 The cord and the cord layer

Material 4 is the cord. Two different sizes of cord were tested. The smaller diameter is refferred to as material 4.1 (see Figures 6.35 and 6.36) and the larger as 4.2 (see Figures 6.33 and 6.34). The method used for testing the material properties is described in Chapter 4. Tests were done for two different temperatures and frequencies. Due to the length of the belts only low frequencies were used. As discussed in previous chapters the variables have been chosen to represent realistic values for V-belt appli-

cations. This means that for the circumferential direction (22), which applies to the cord, the strain amplitude and strain mean value are mainly functions of the force in the belt and not of geometry. For this material direction, strain and stress are defined on the cord cross-section. Therefore the mean strain was held constant at 0.015 and the amplitude was varied between 0.0025 and 0.005 to simulate normal load cases in a V-belt drive. The modulus of the cord is about 2 to 3 orders of magnitude higher than for the rubber. No significant irreversible effects due to strain amplitude could be found, as opposed to the other materials.

Temperature was found to be the only important variable for the cord, especially for the loss module, which increased about 50 percent over the temperature interval. The elastic modulus decreased by 20 - 30 percent over the same interval. A small decrease, of about 10 percent, in elastic modulus, and an increase in loss modulus were recorded when going from the low strain amplitude to the high value. Increasing the frequency by a factor of 100 caused a typical increase in elastic modulus of 10 percent and a decrease in loss module of 10 - 20 percent.

The mean stress was also found to be a function of cycles. At room temperature no significant reduction was recorded, only a few percent. At high temperatures the stress value fell fast initially but stabilized after a few thousand cycles.

Our conclusion for the polyester cord is that temperature is the only important variable. It should also be noted that although the hysteresis of the cord is relatively low, it is a very important part of the total V-belt hysteresis as the cord transmits very large forces.

For the larger cord, additional tests were made for the whole cord layer (see Figures 6.29, 6.30, 6.31, and 6.32), i.e. the cord and the surrounding layer of soft rubber (material 2). Test samples were built out of several cord layers. Tests in compression and shear were also made. The material thus built consists of approximately equal parts of cord and rubber. The motivation for performing tests on this macroscopic material is the results might indicate that it is possible to replace the whole cord layer with one anisotropic material. As expected this material shows similar properties as material 2, except for the tensile test in direction 2. Note also that this material consists to a large extent of material 2.

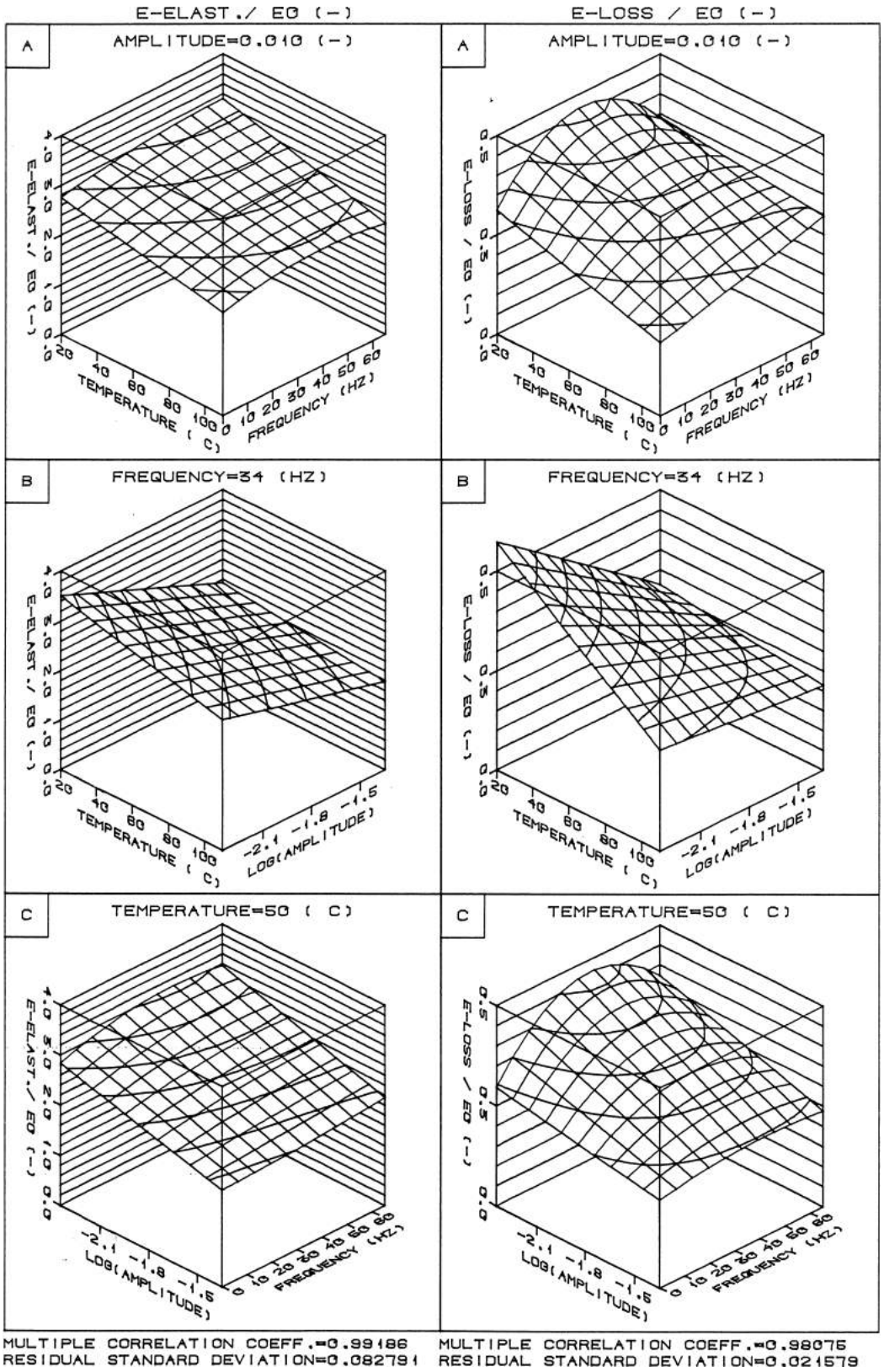

Figure 6.1 *(a) Material 1, orientation 22, 36 test values, 24 degrees of freedom.*

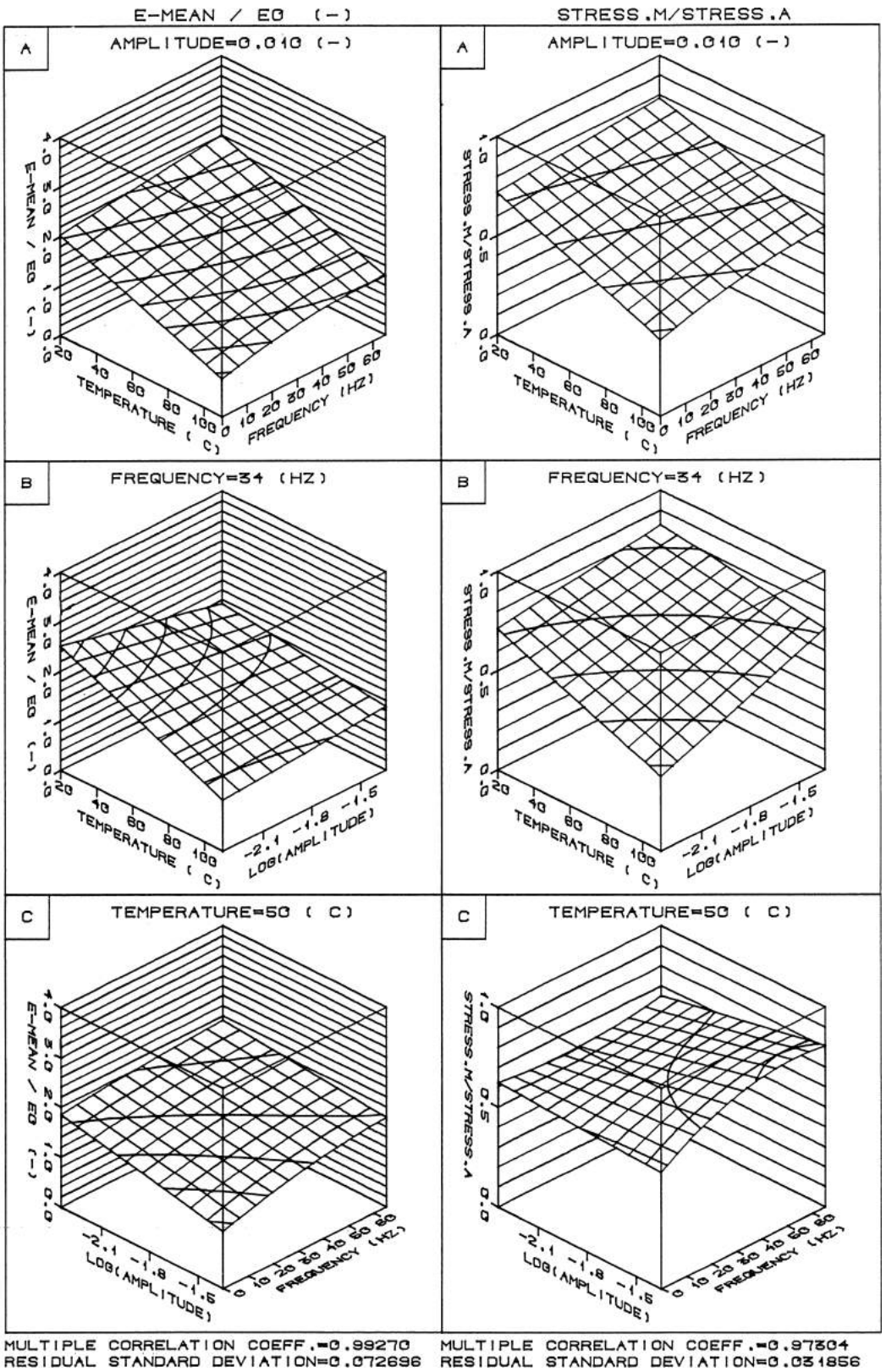

Figure 6.2 *(b) Material 1, orientation 22, 36 test values, 24 degrees of freedom.*

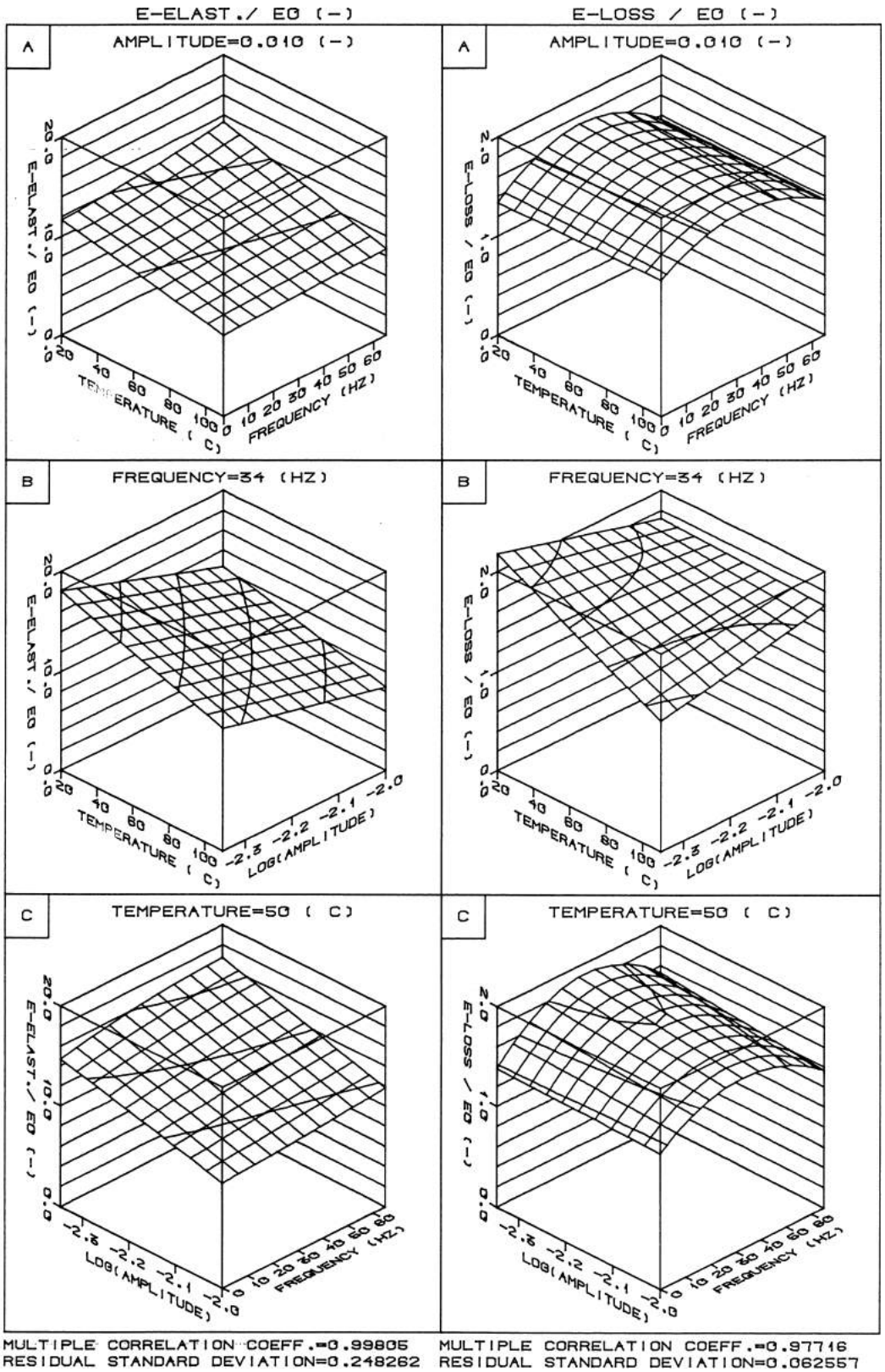

Figure 6.3 *(a) Material 1, orientation 33, 24 test values, 12 degrees of freedom.*

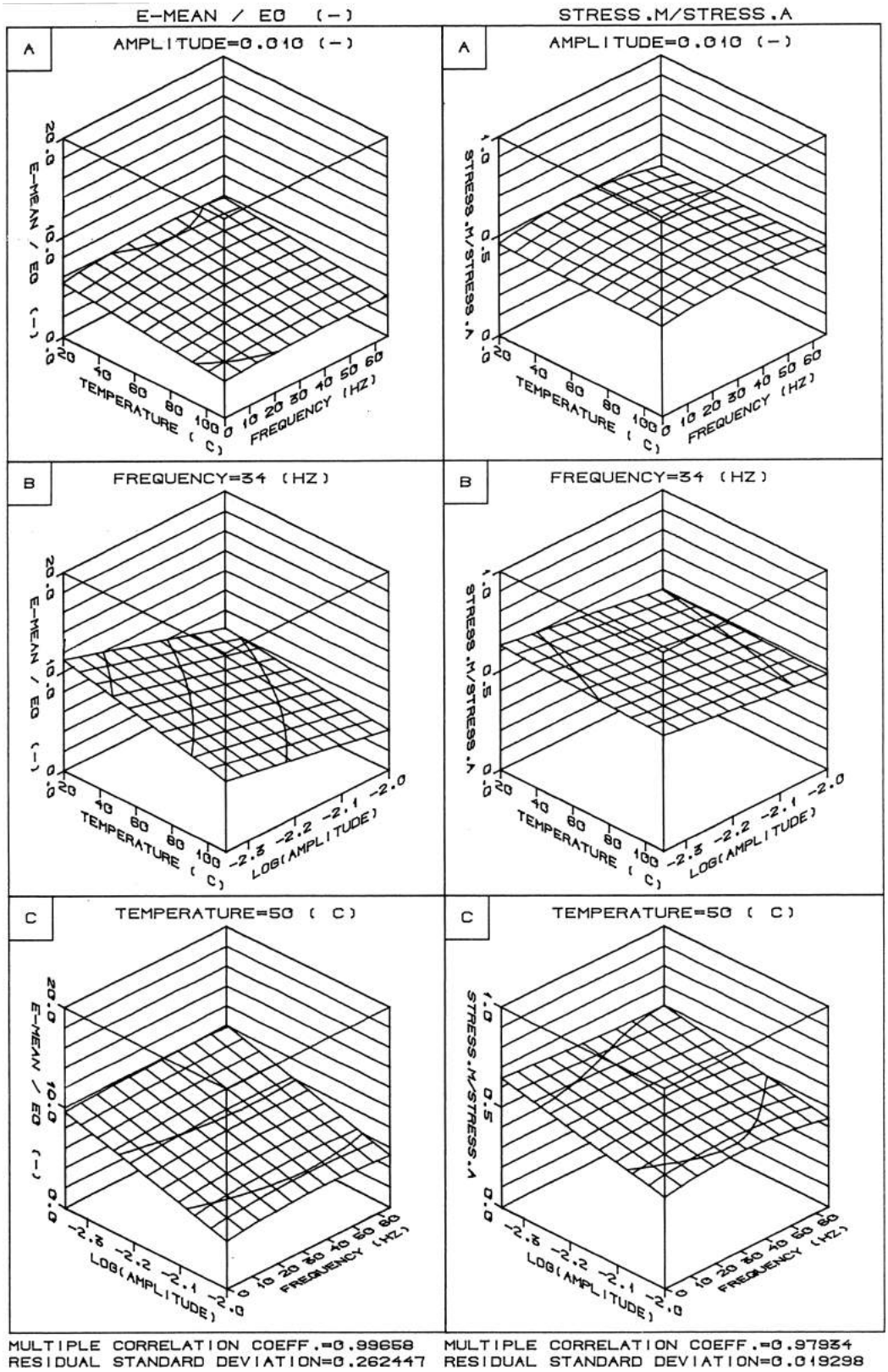

Figure 6.4 *(b) Material 1, orientation 33, 24 test values, 12 degrees of freedom.*

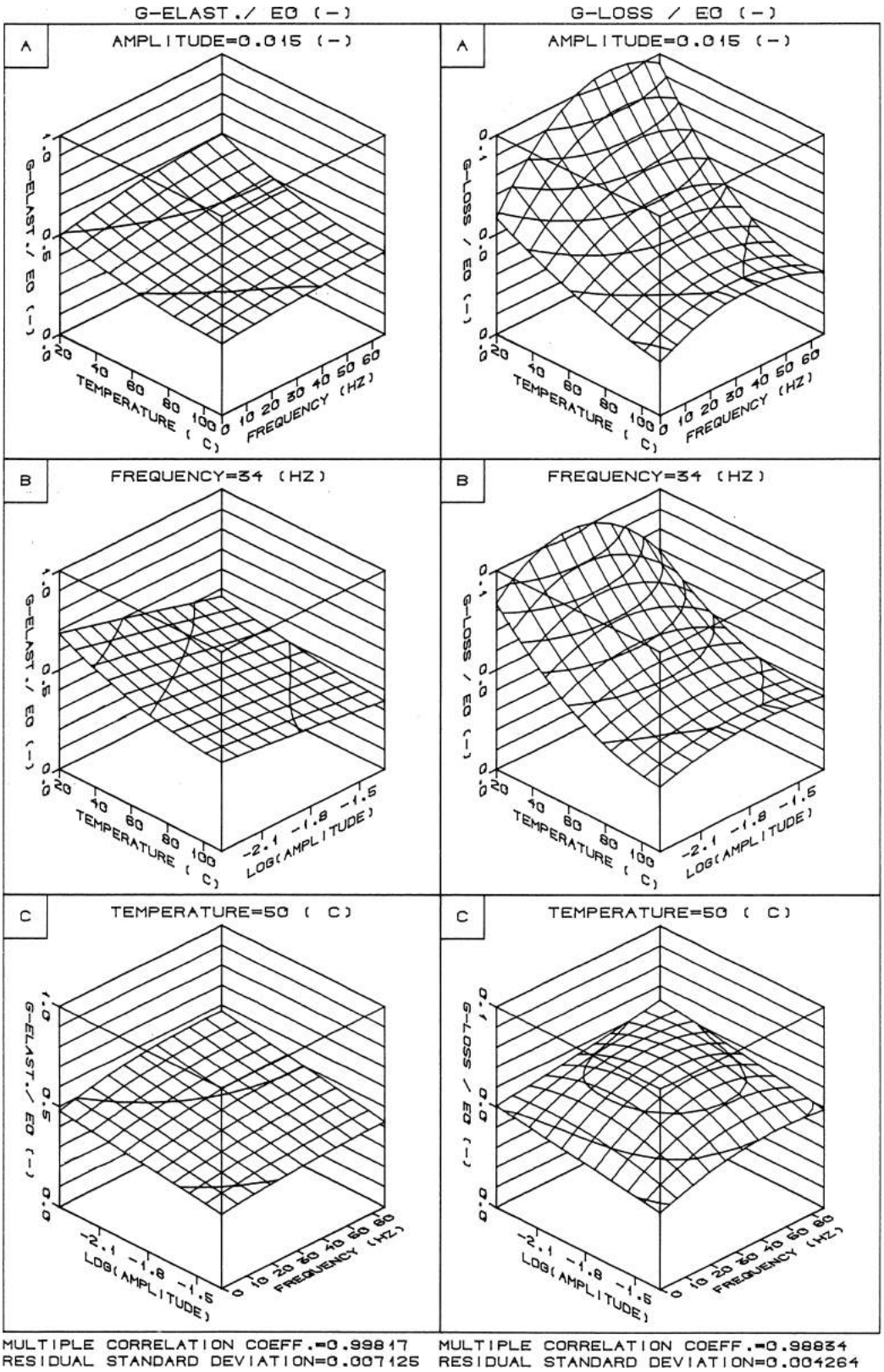

Figure 6.5 *(a) Material 1, orientation 12, 47 test values, 23 degrees of freedom.*

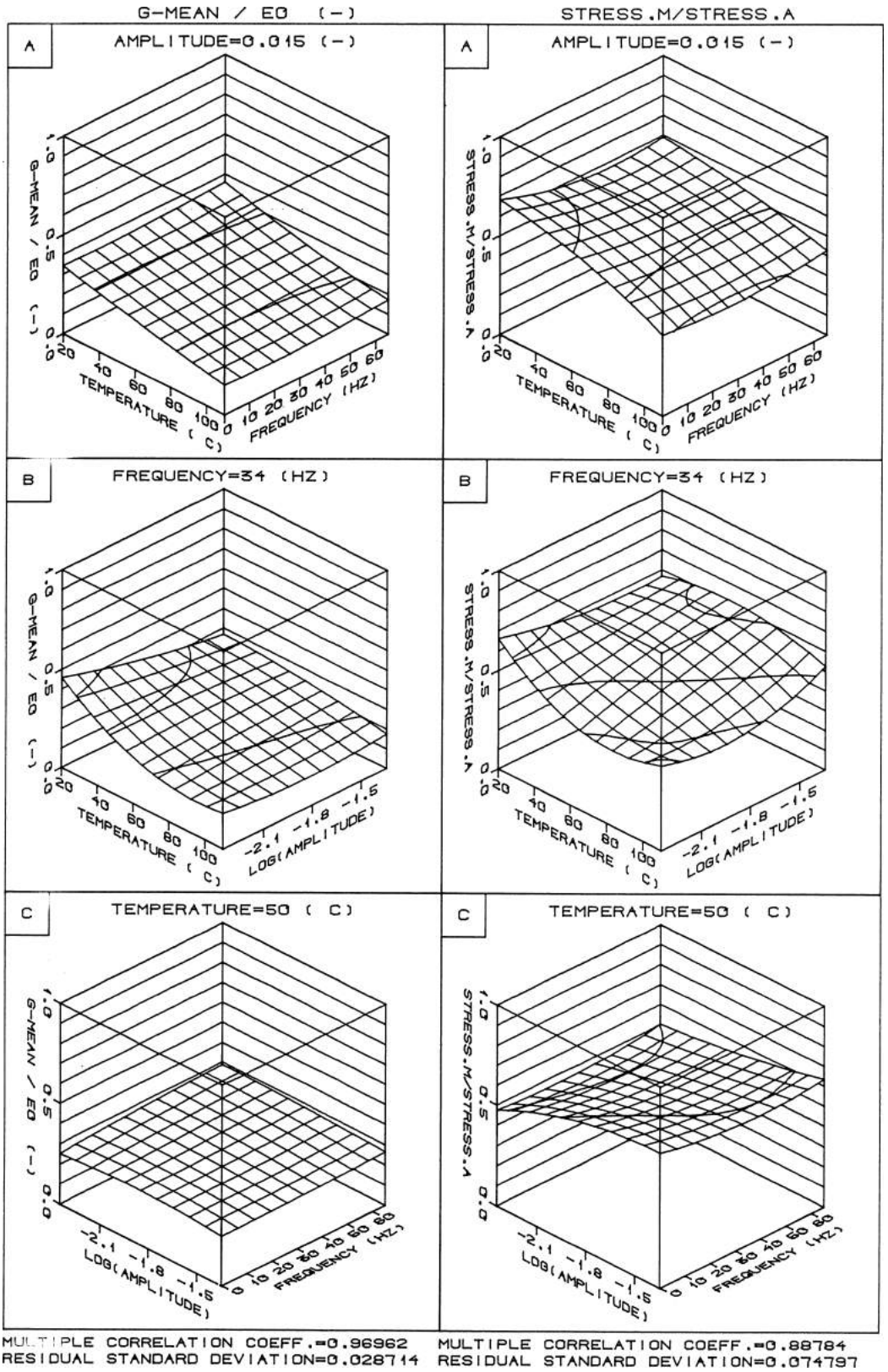

Figure 6.6 *(b) Material 1, orientation 12, 47 test values, 23 degrees of freedom.*

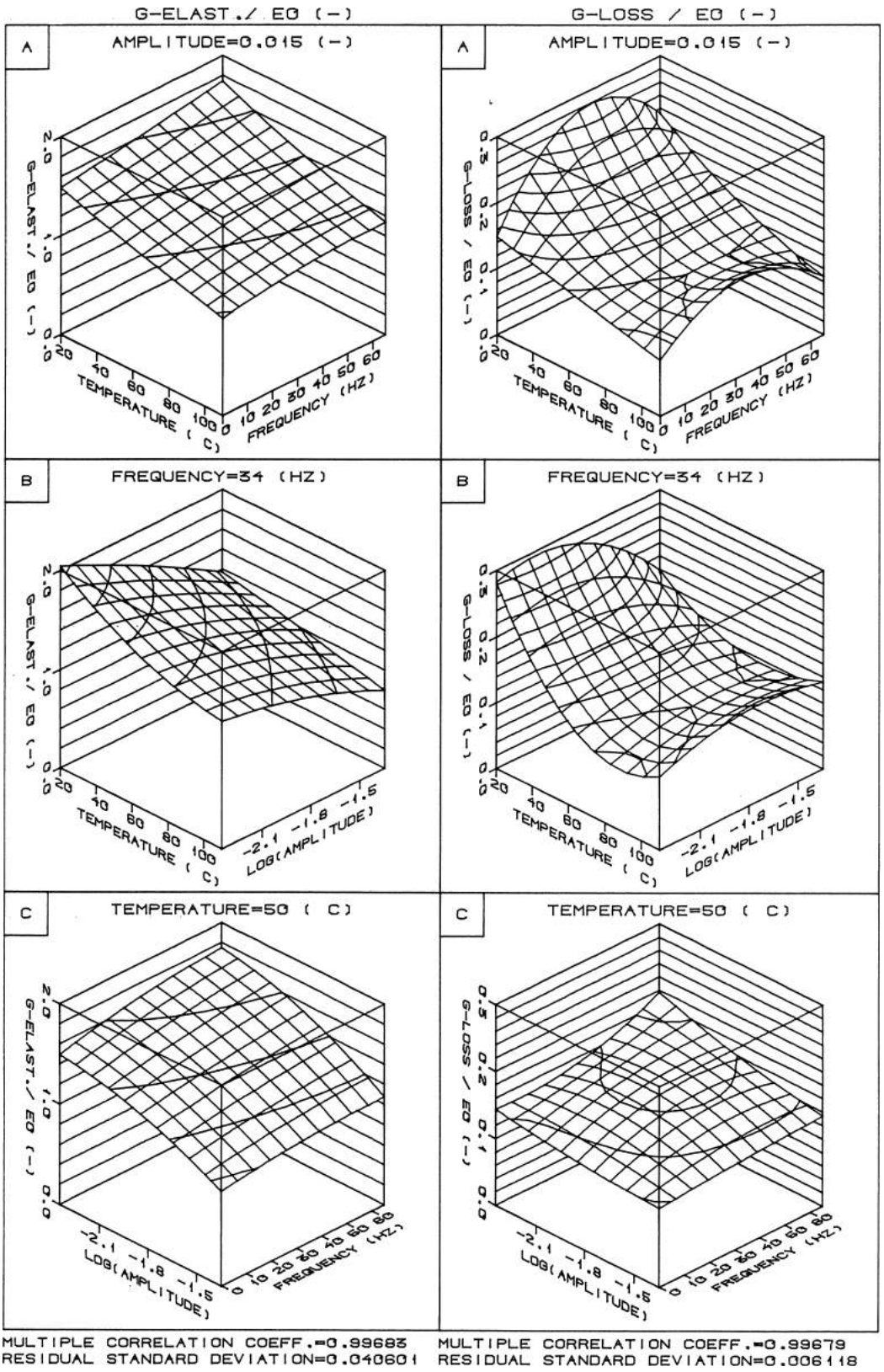

Figure 6.7 *(a) Material 1, orientation 23, 42 test values, 18 degrees of freedom.*

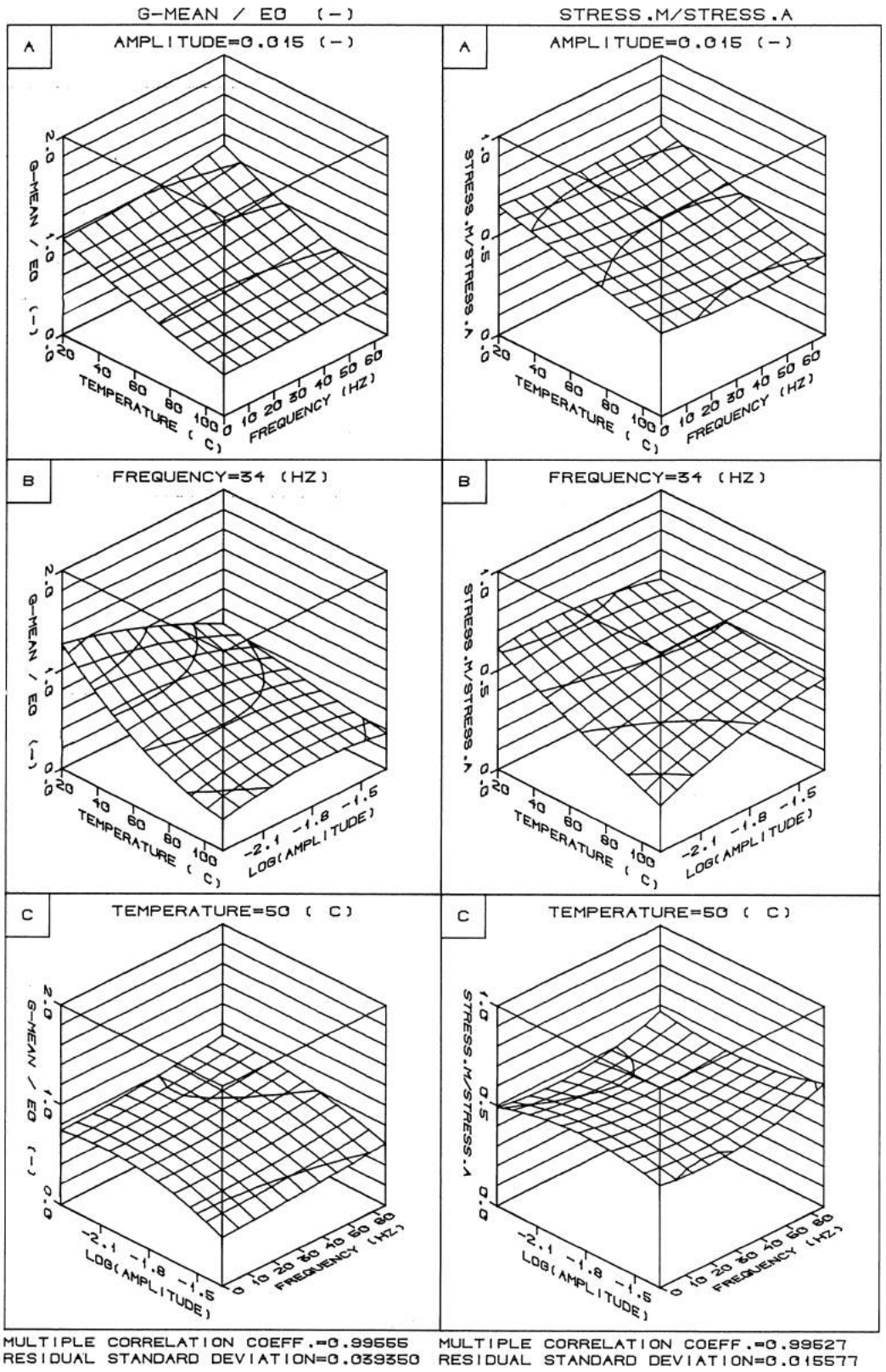

Figure 6.8 *(b) Material 1, orientation 23, 42 test values, 18 degrees of freedom.*

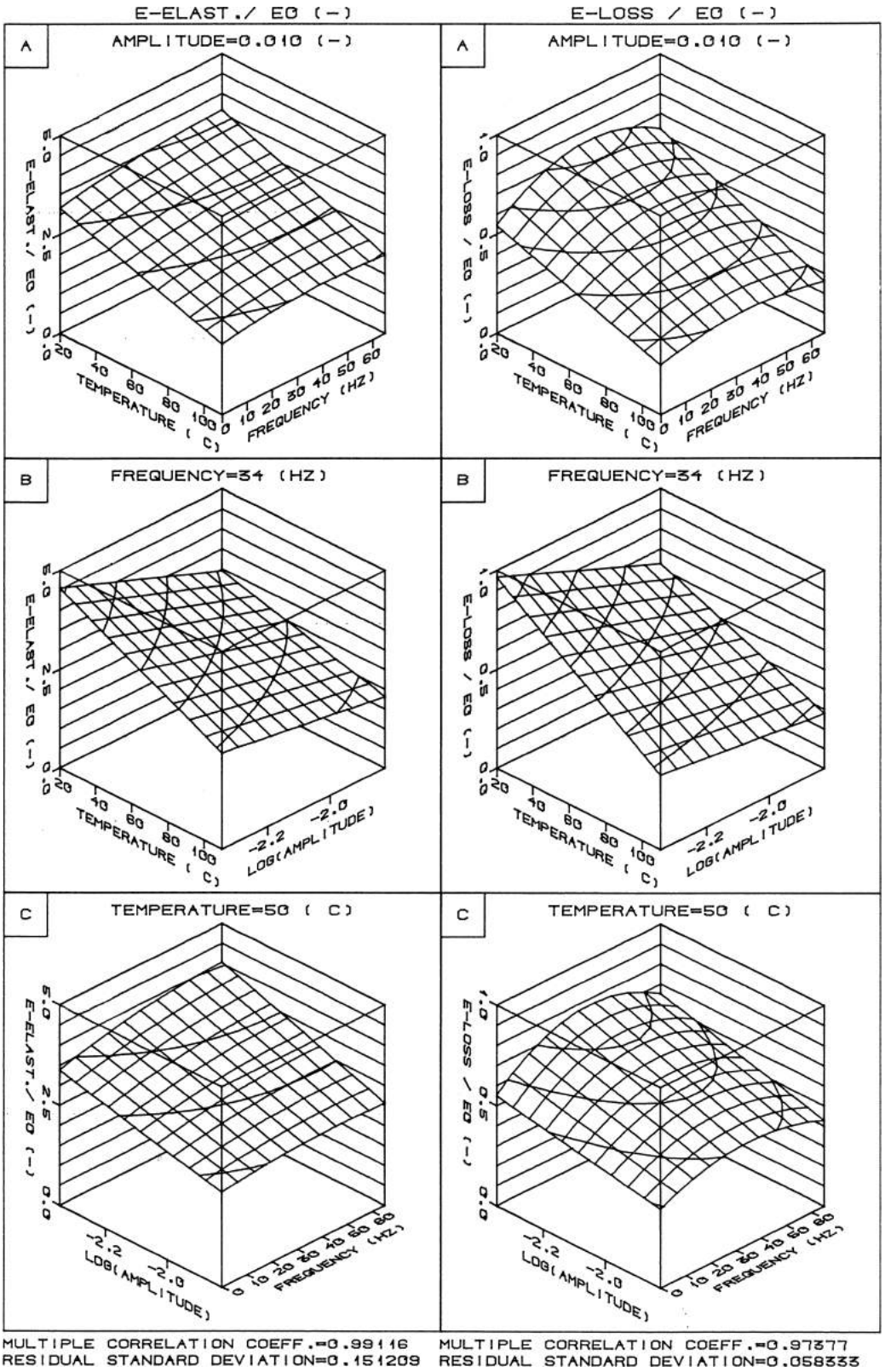

Figure 6.9 *(a) Material 2, orientation 22, 24 test values, 12 degrees of freedom.*

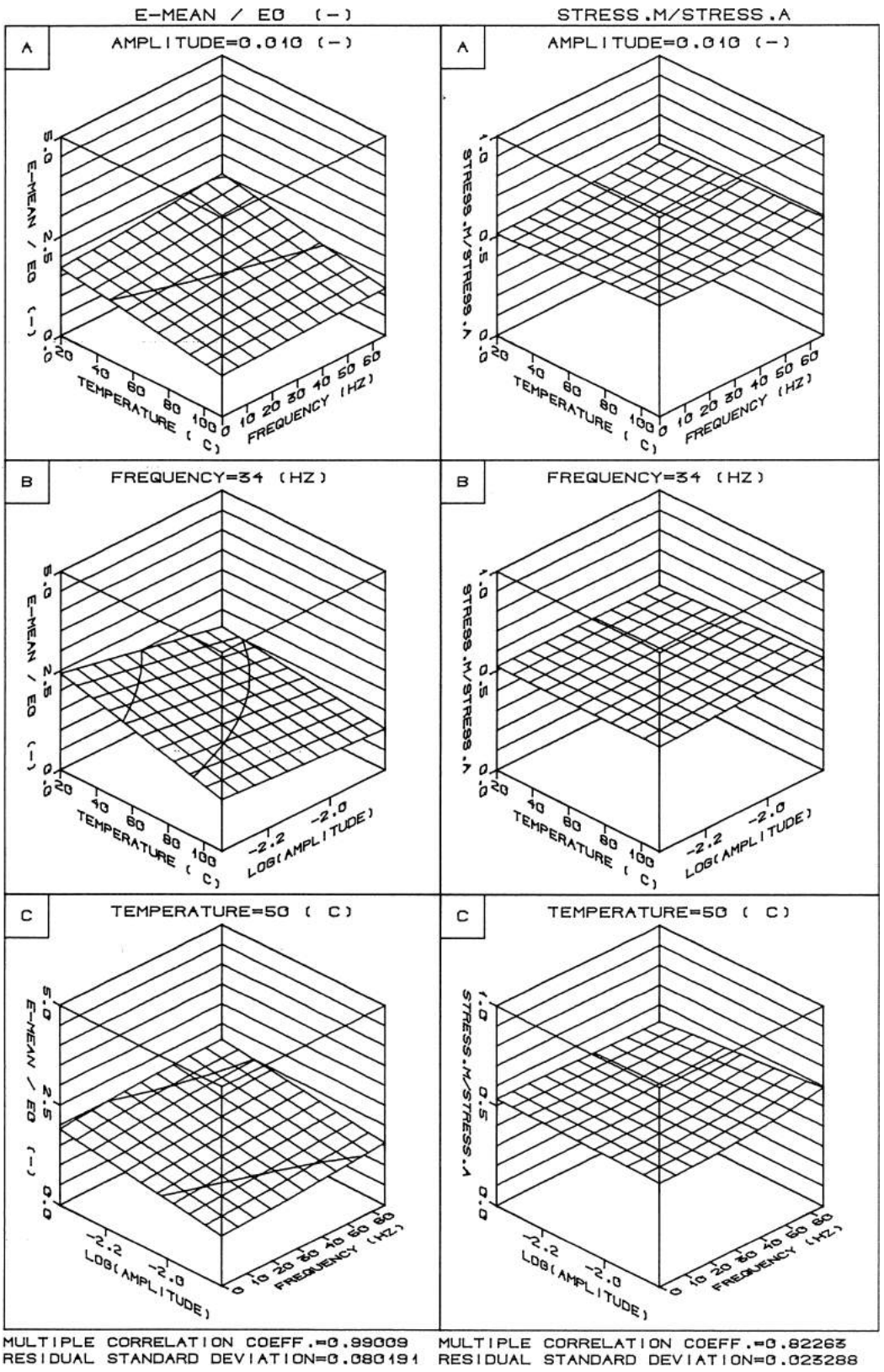

Figure 6.10 *(b) Material 2, orientation 22, 24 test values, 12 degrees of freedom.*

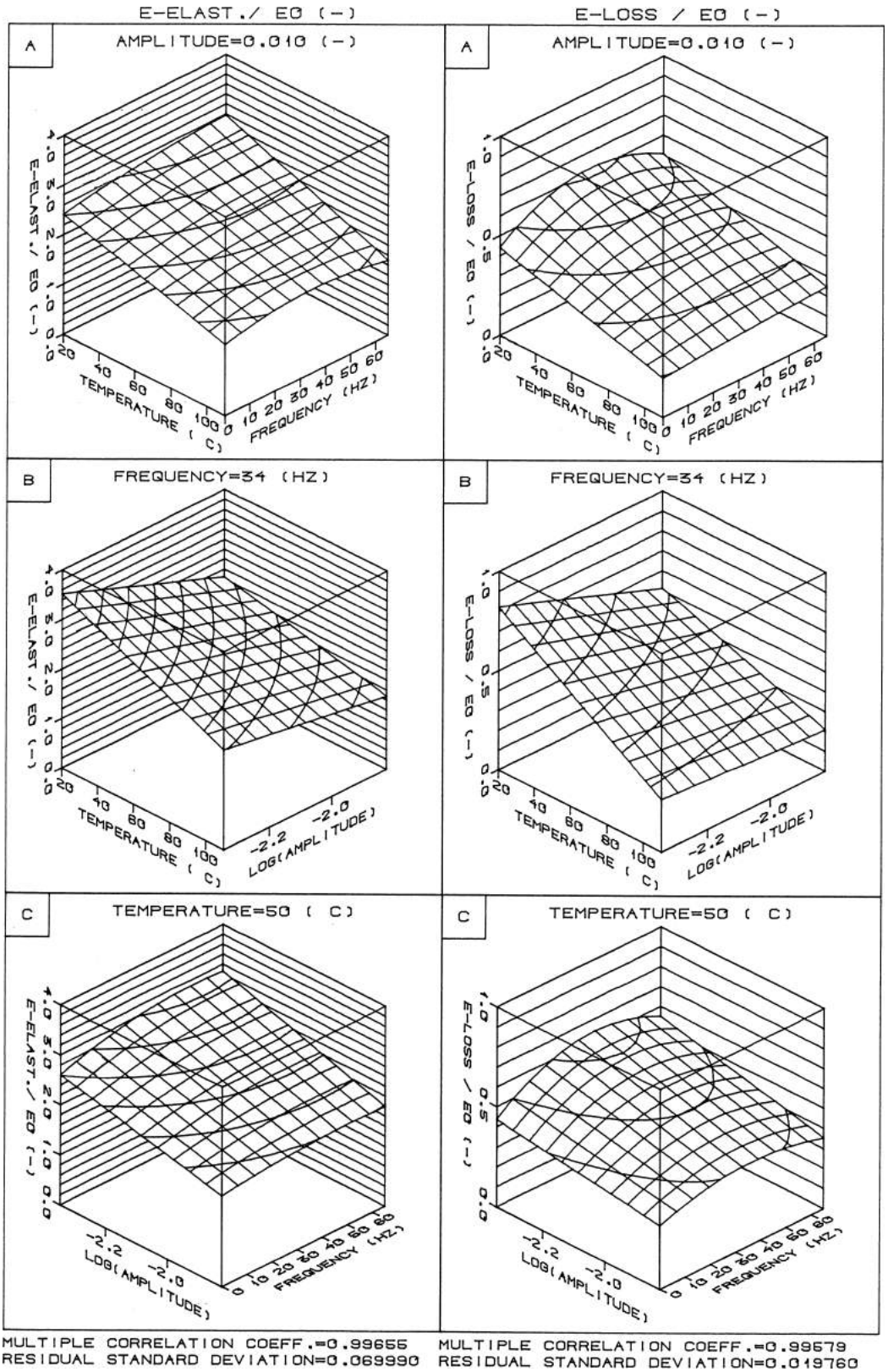

Figure 6.11 *(a) Material 2, orientation 33, 24 test values, 12 degrees of freedom.*

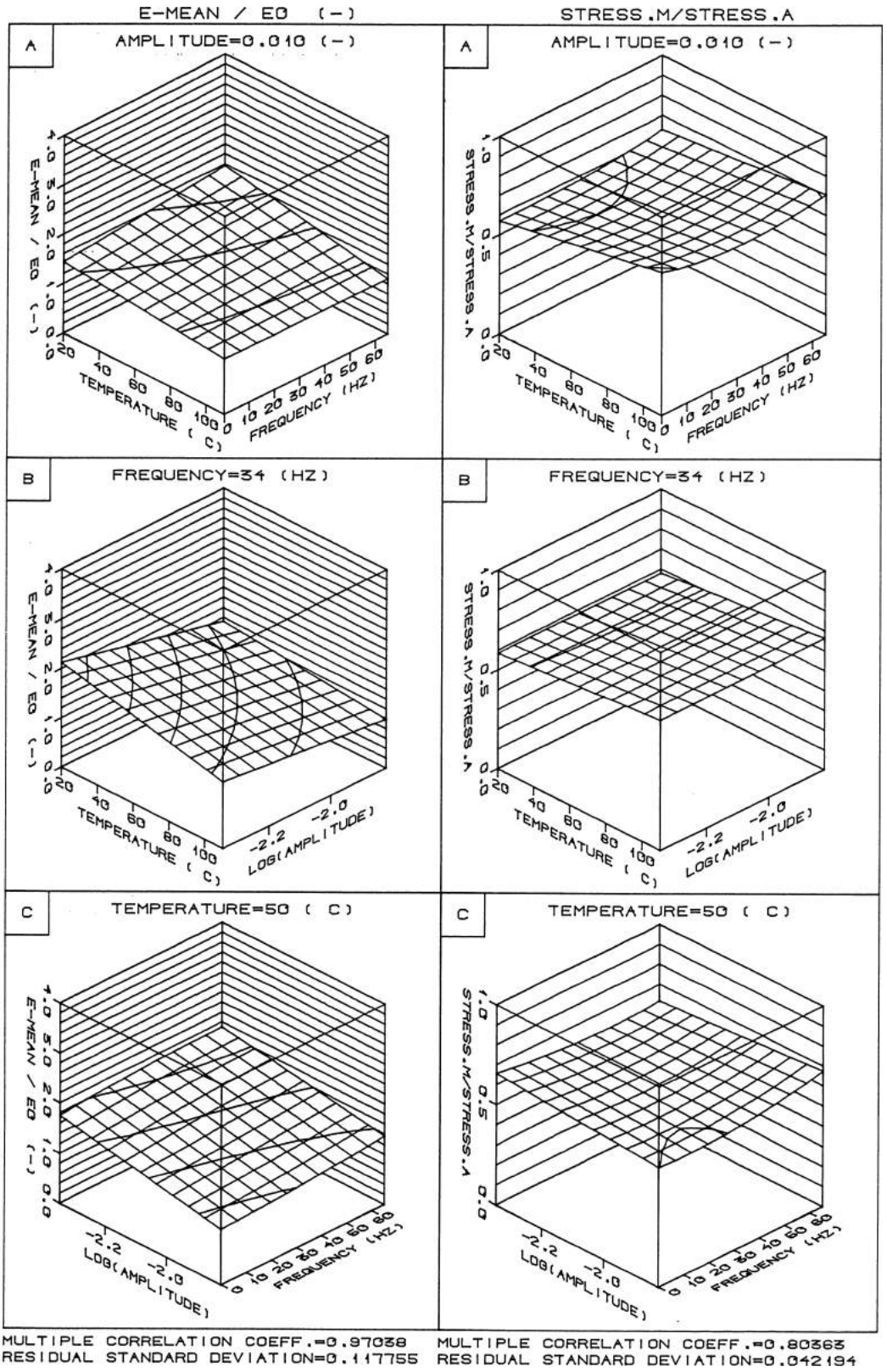

Figure 6.12 *(b) Material 2, orientation 33, 24 test values, 12 degrees of freedom.*

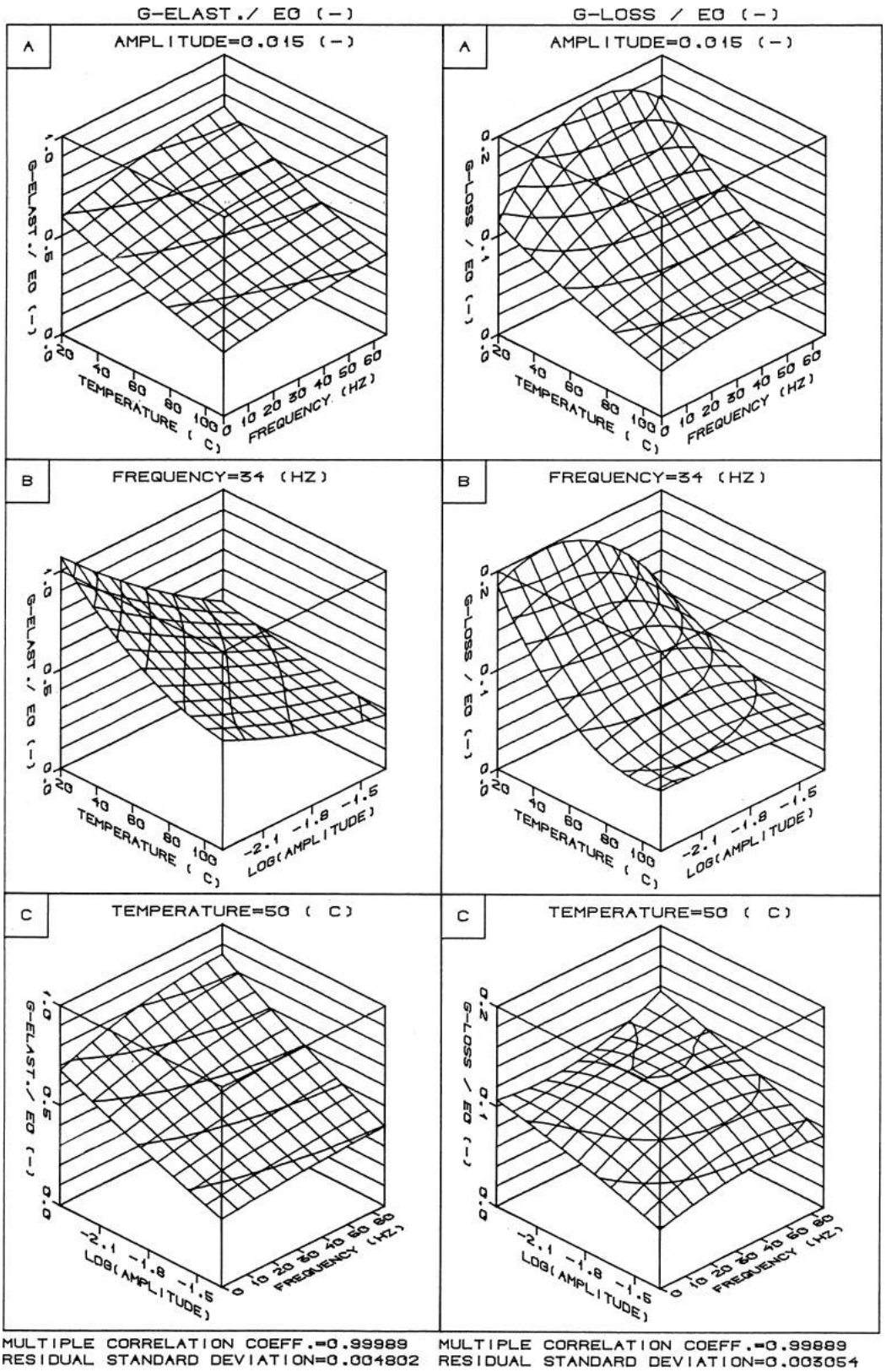

Figure 6.13 *(a) Material 2, orientation 13, 42 test values, 18 degrees of freedom.*

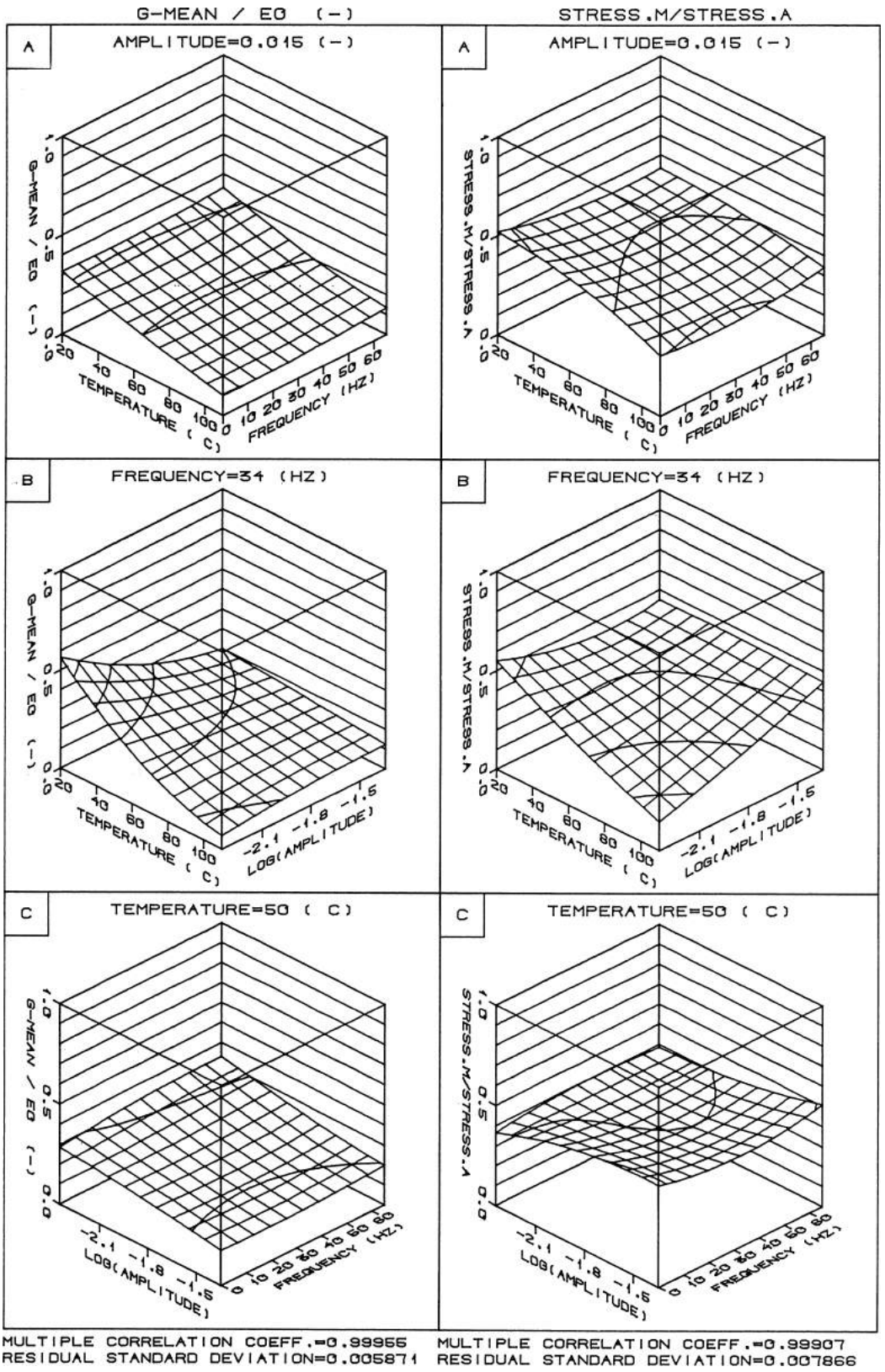

Figure 6.14 *(b) Material 2, orientation 13, 42 test values, 18 degrees of freedom.*

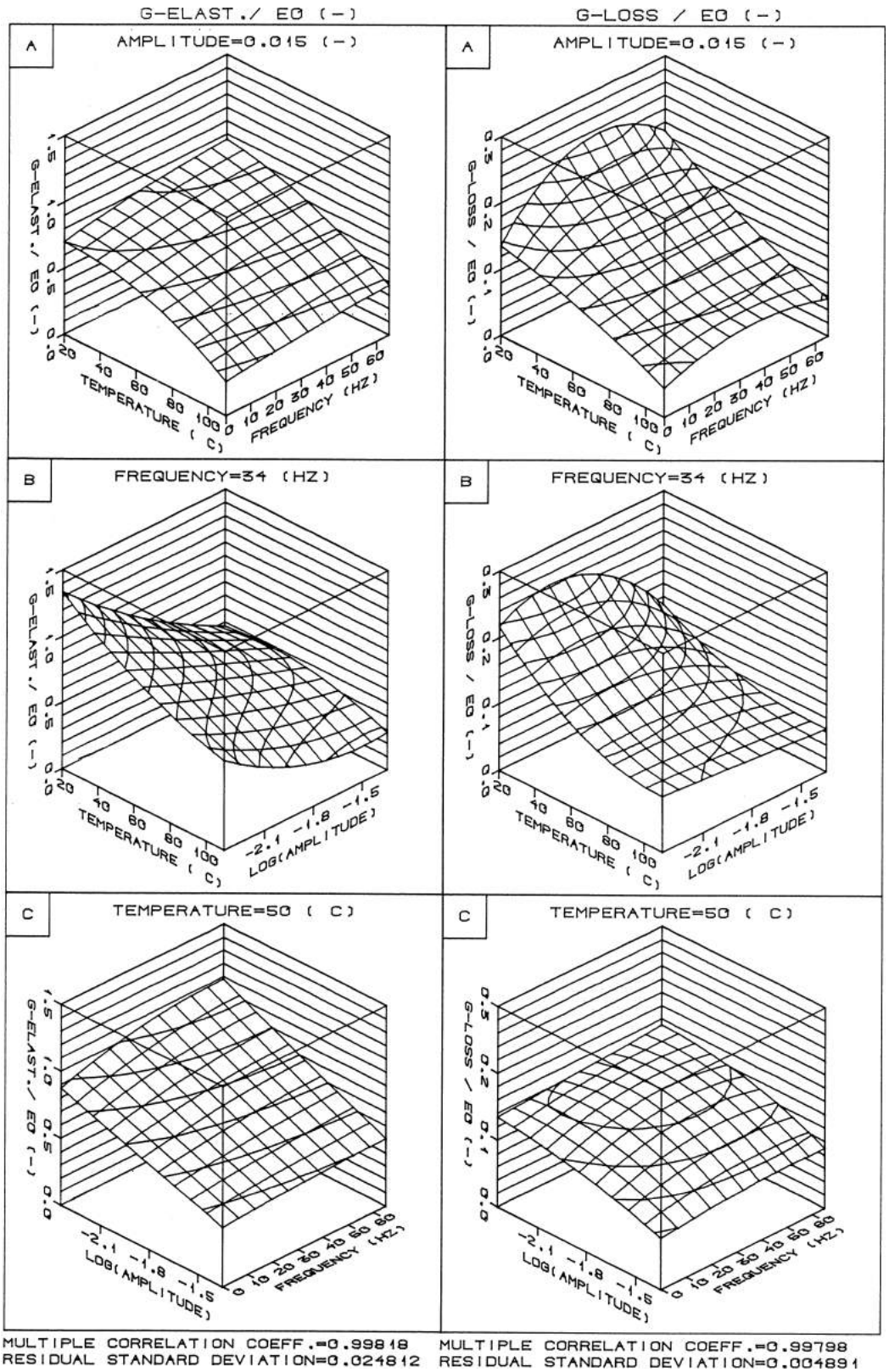

Figure 6.15 *(a) Material 2, orientation 23, 42 test values, 18 degrees of freedom.*

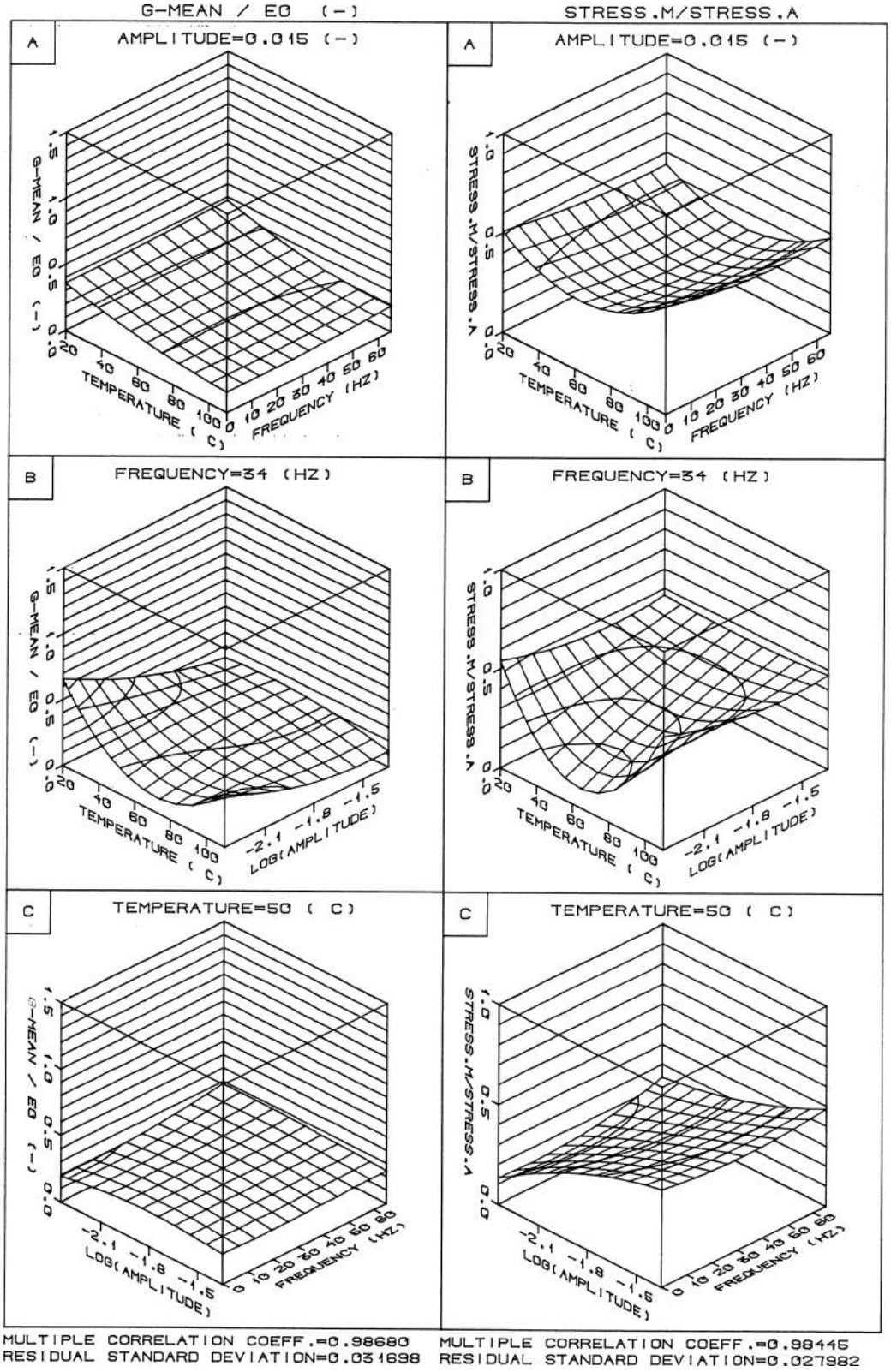

Figure 6.16 *(b) Material 2, orientation 23, 42 test values, 18 degrees of freedom.*

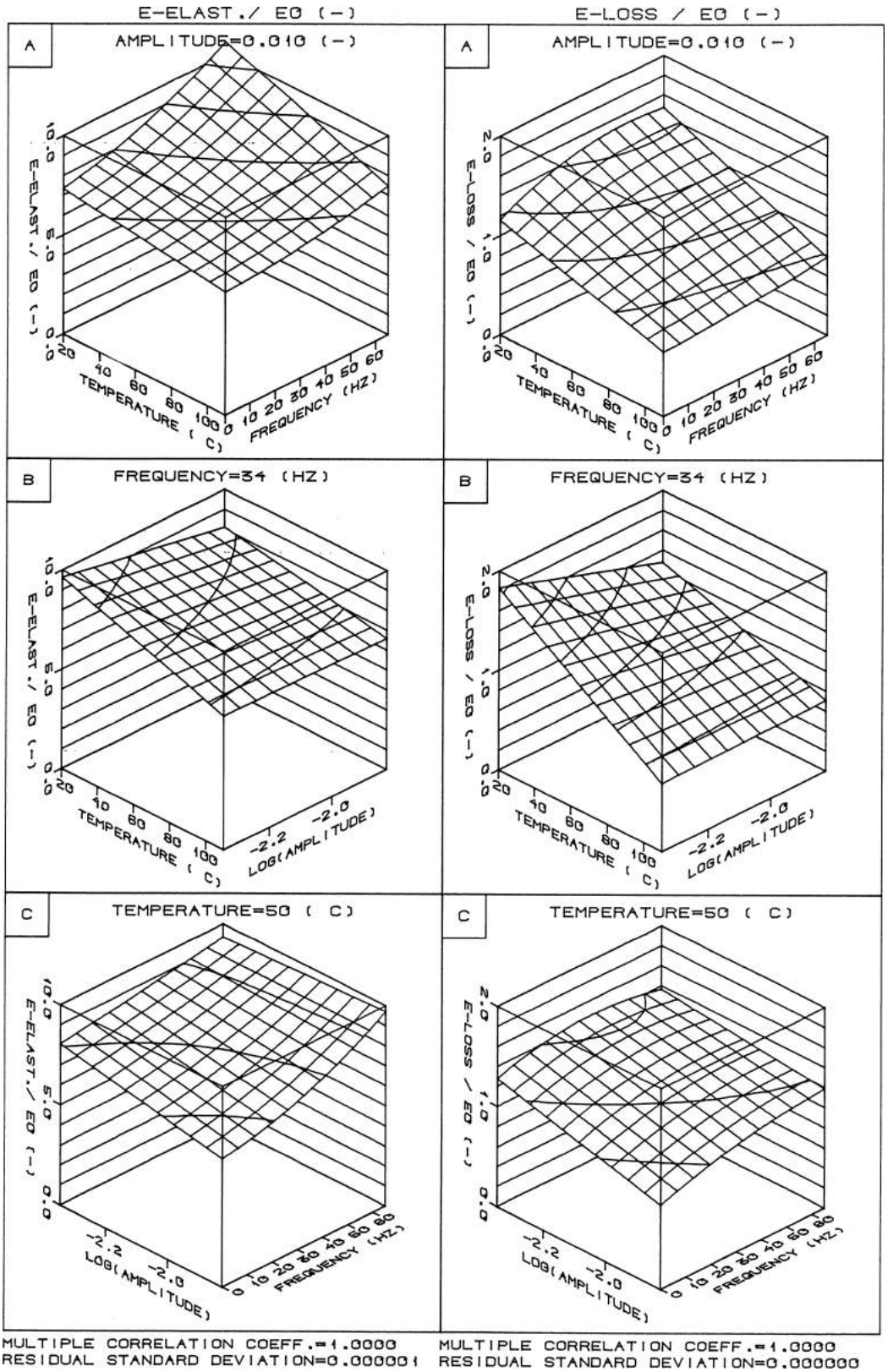

Figure 6.17 *(a) Material 3, orientation 11, 12 test values, 0 degrees of freedom.*

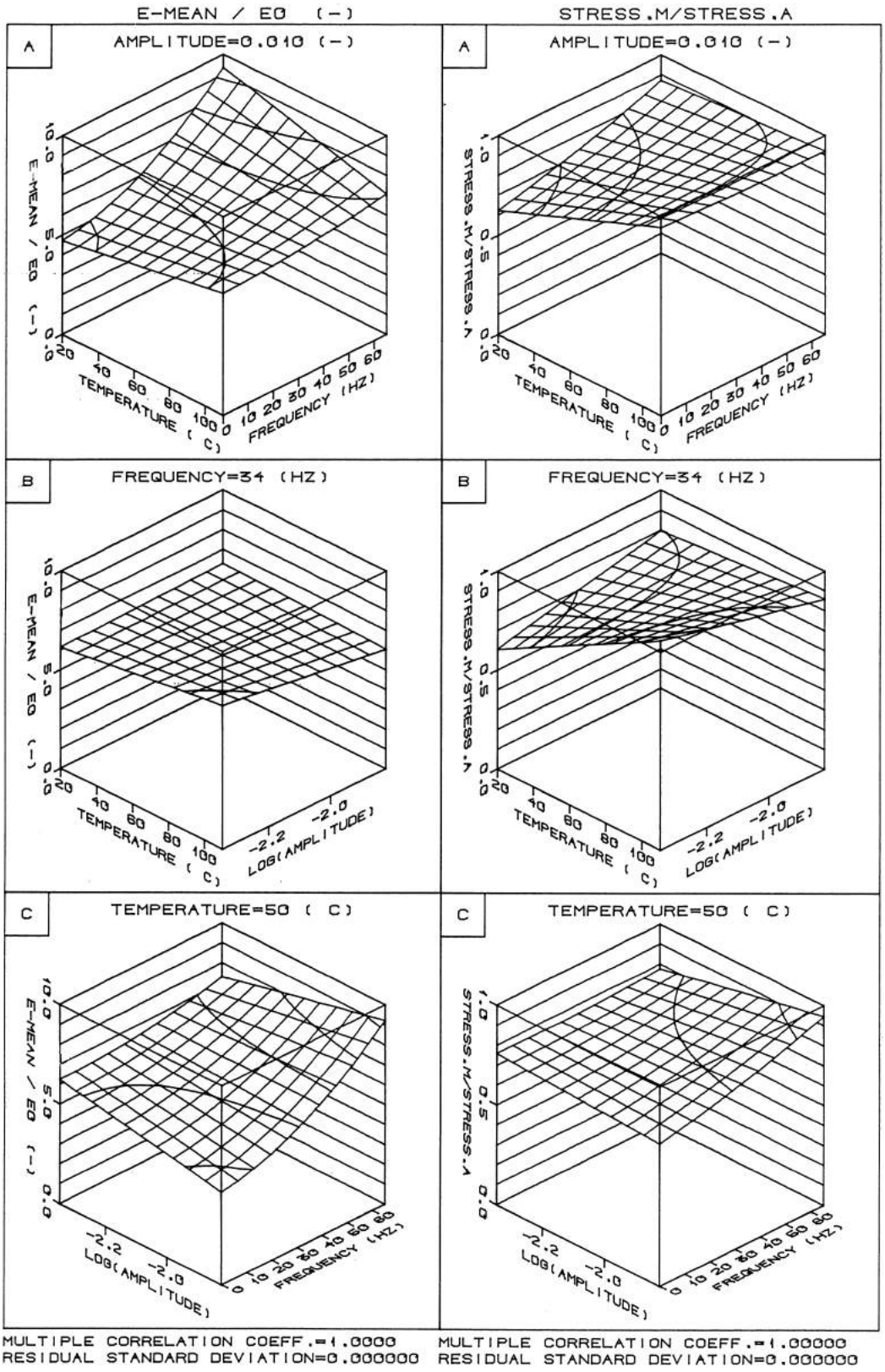

Figure 6.18 *(b) Material 3, orientation 11, 12 test values, 0 degrees of freedom.*

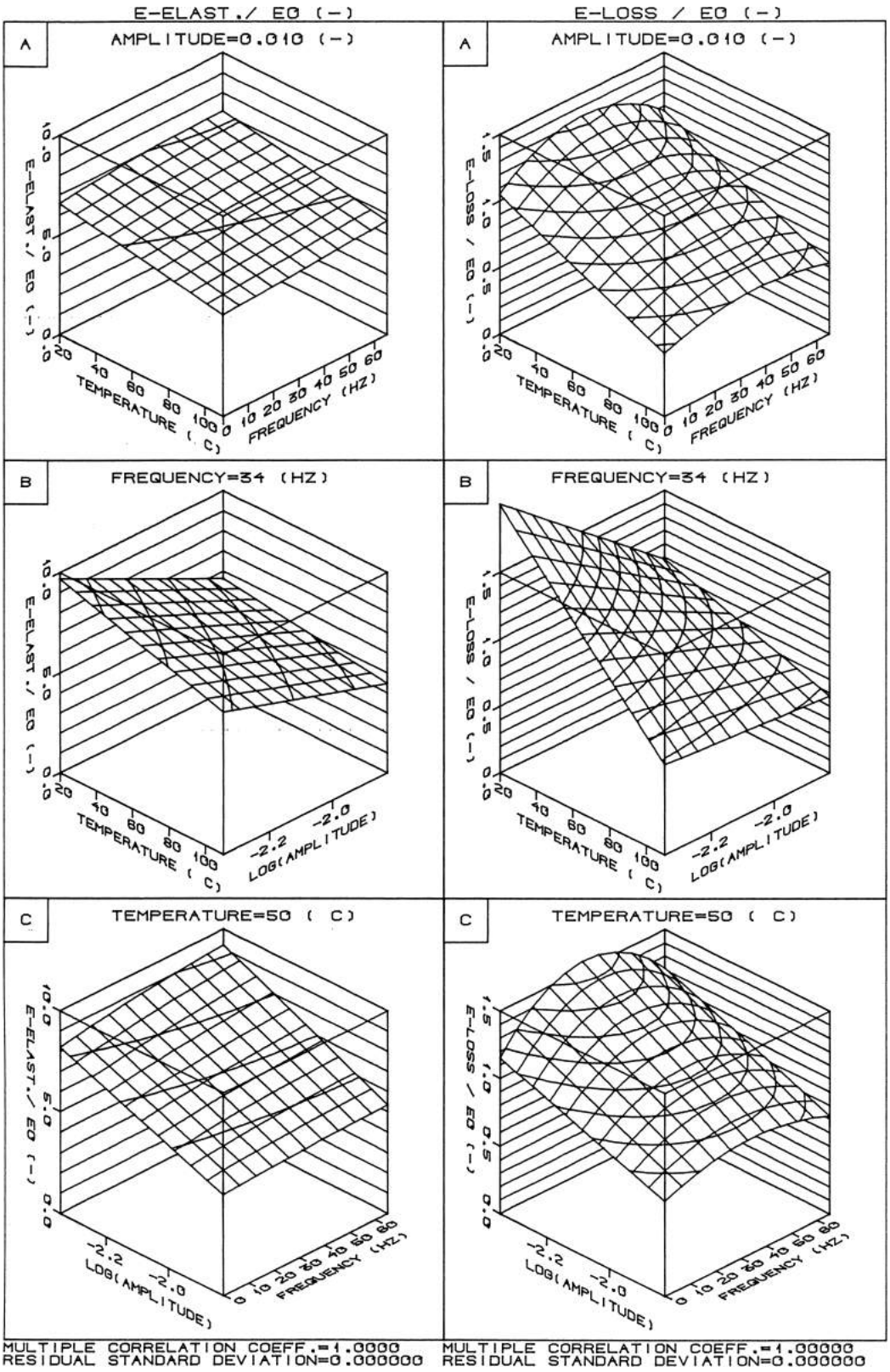

Figure 6.19 *(a) Material 3, orientation 33, 12 test values, 0 degrees of freedom.*

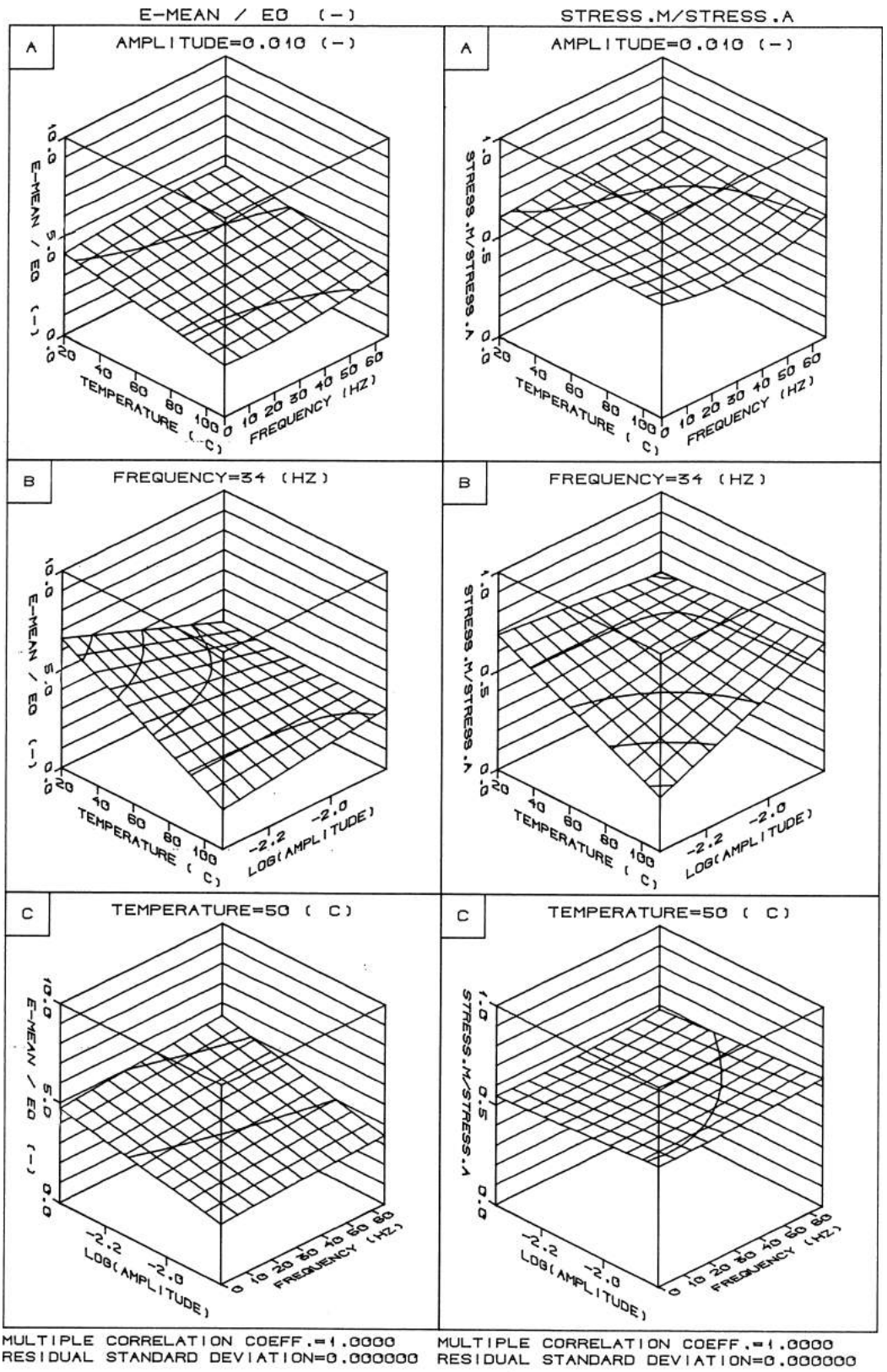

Figure 6.20 *(b) Material 3, orientation 33, 12 test values, 0 degrees of freedom.*

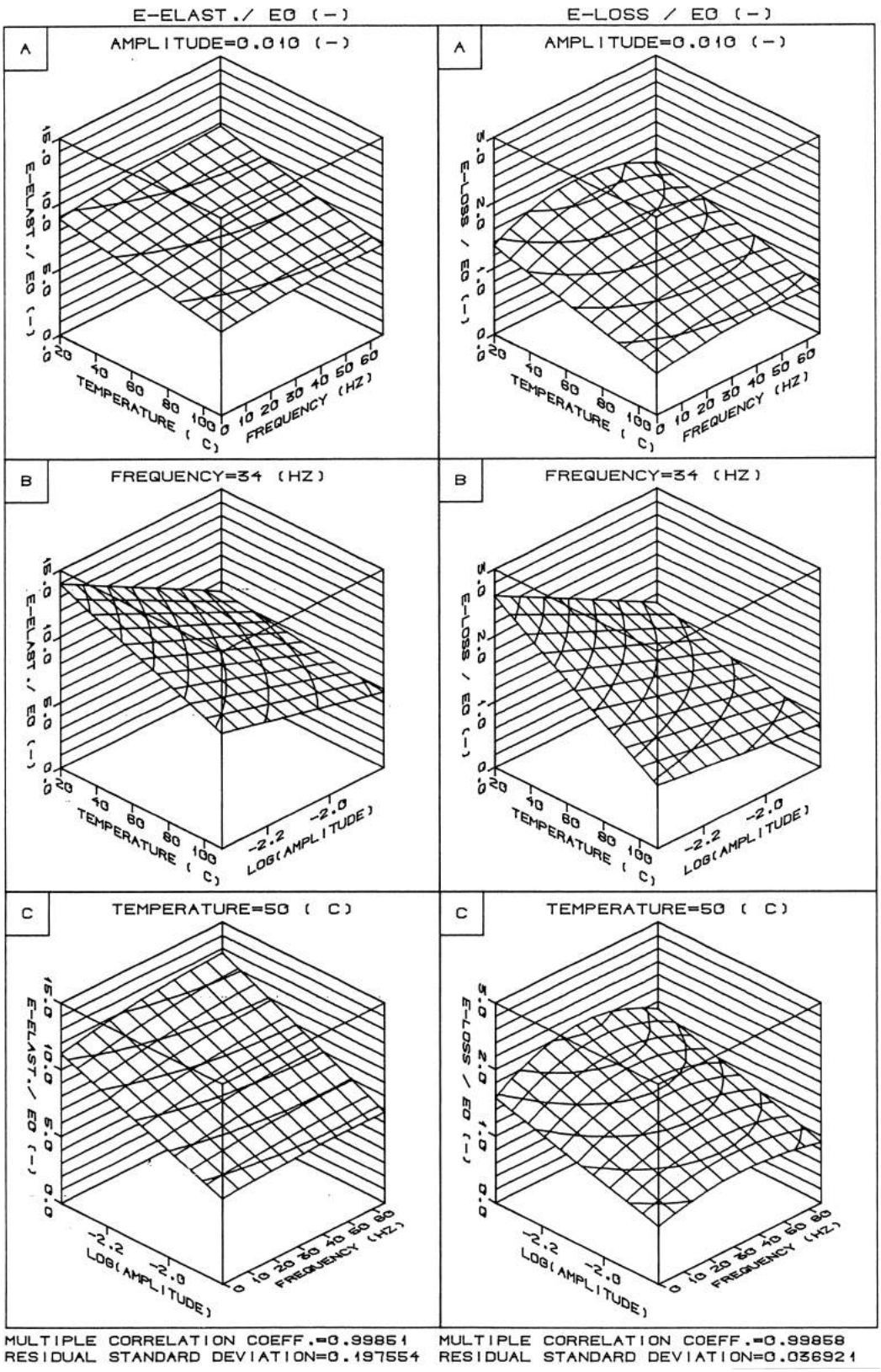

Figure 6.21 *(a) Material 3, orientation 3232, 24 test values, 12 degrees of freedom.*

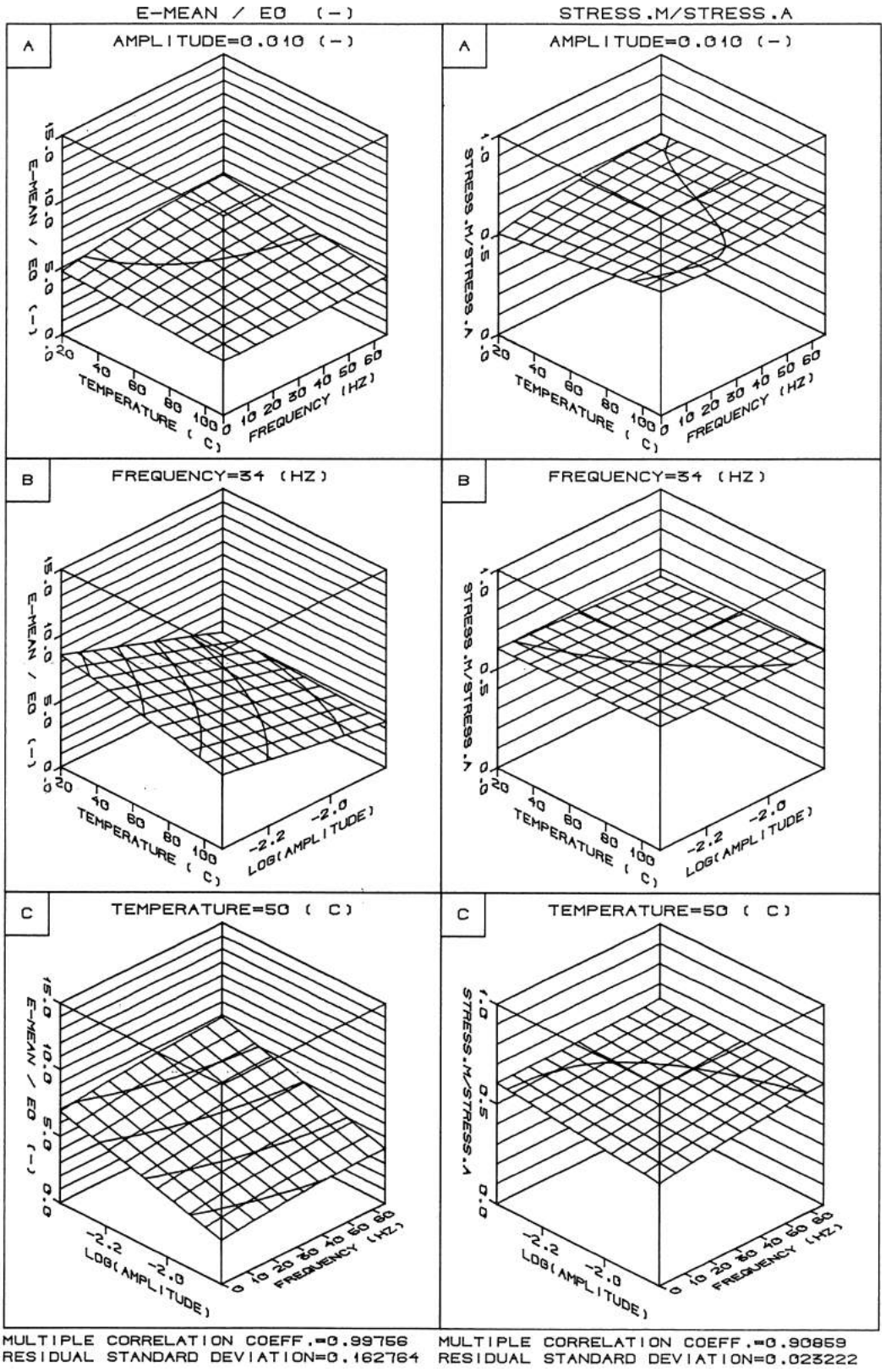

Figure 6.22 *(b) Material 3, orientation 3232, 24 test values, 12 degrees of freedom.*

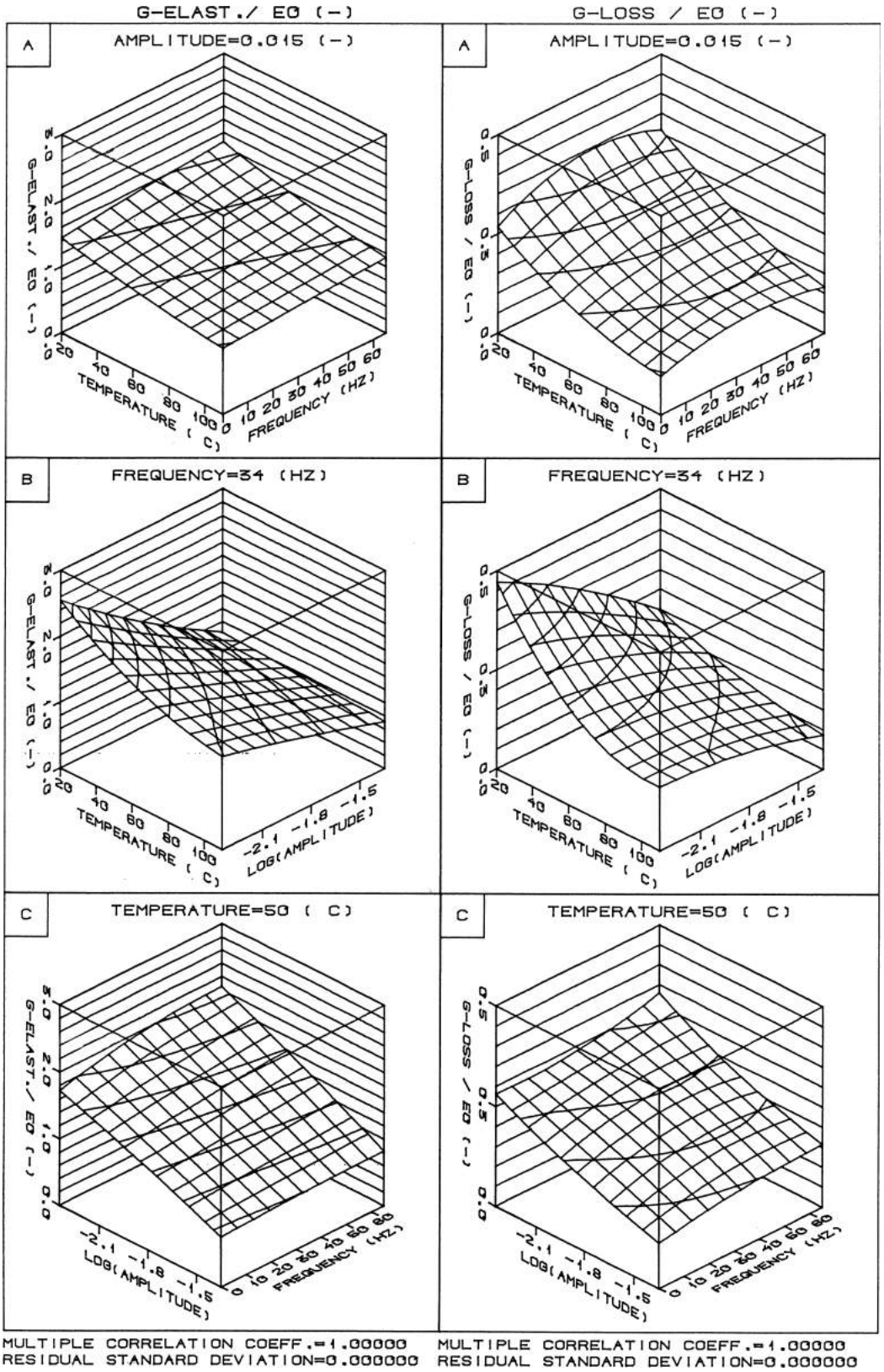

Figure 6.23 *(a) Material 3, orientation 13, 24 test values, 0 degrees of freedom.*

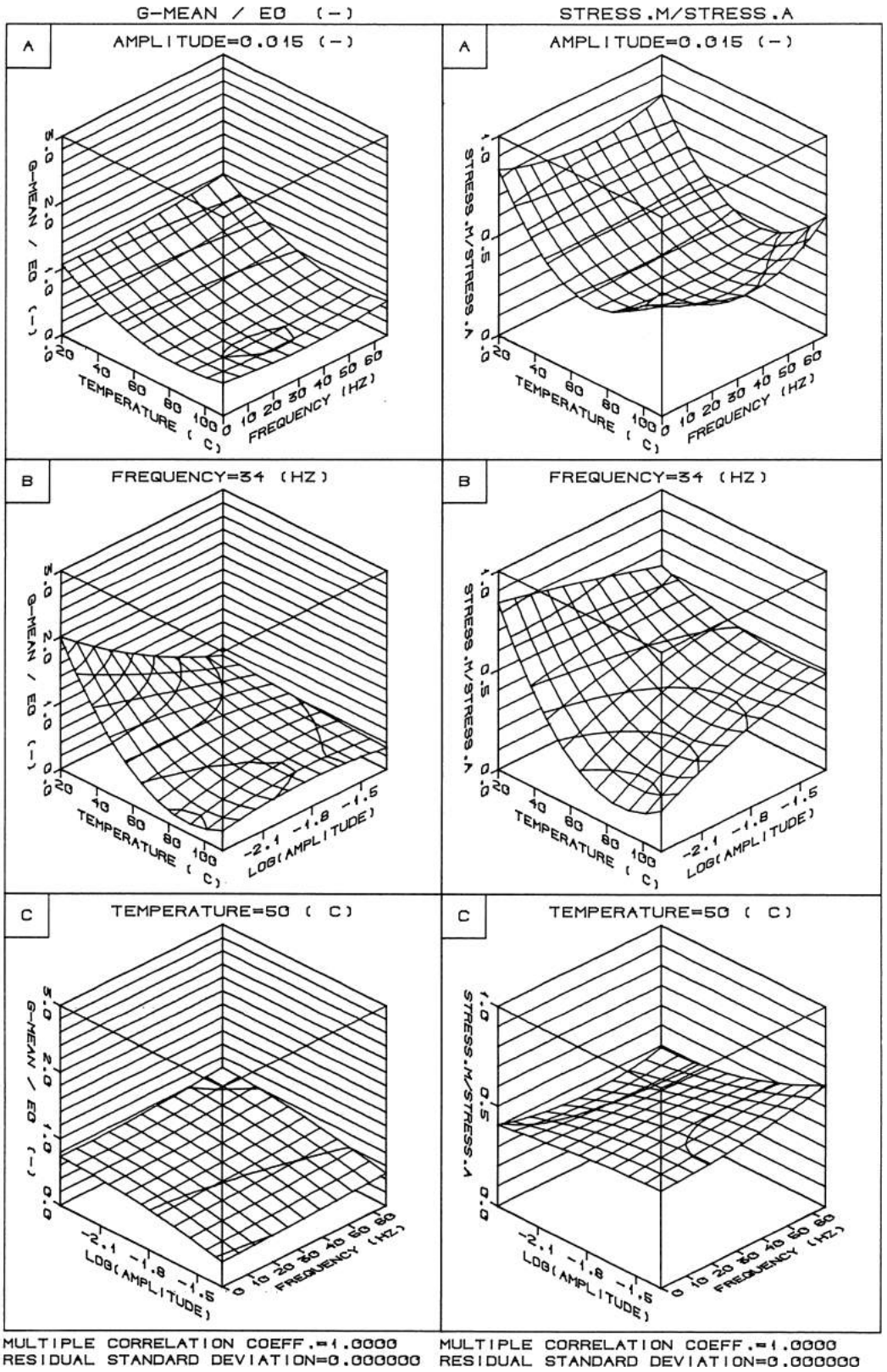

Figure 6.24 *(b) Material 3, orientation 13, 24 test values, 0 degrees of freedom.*

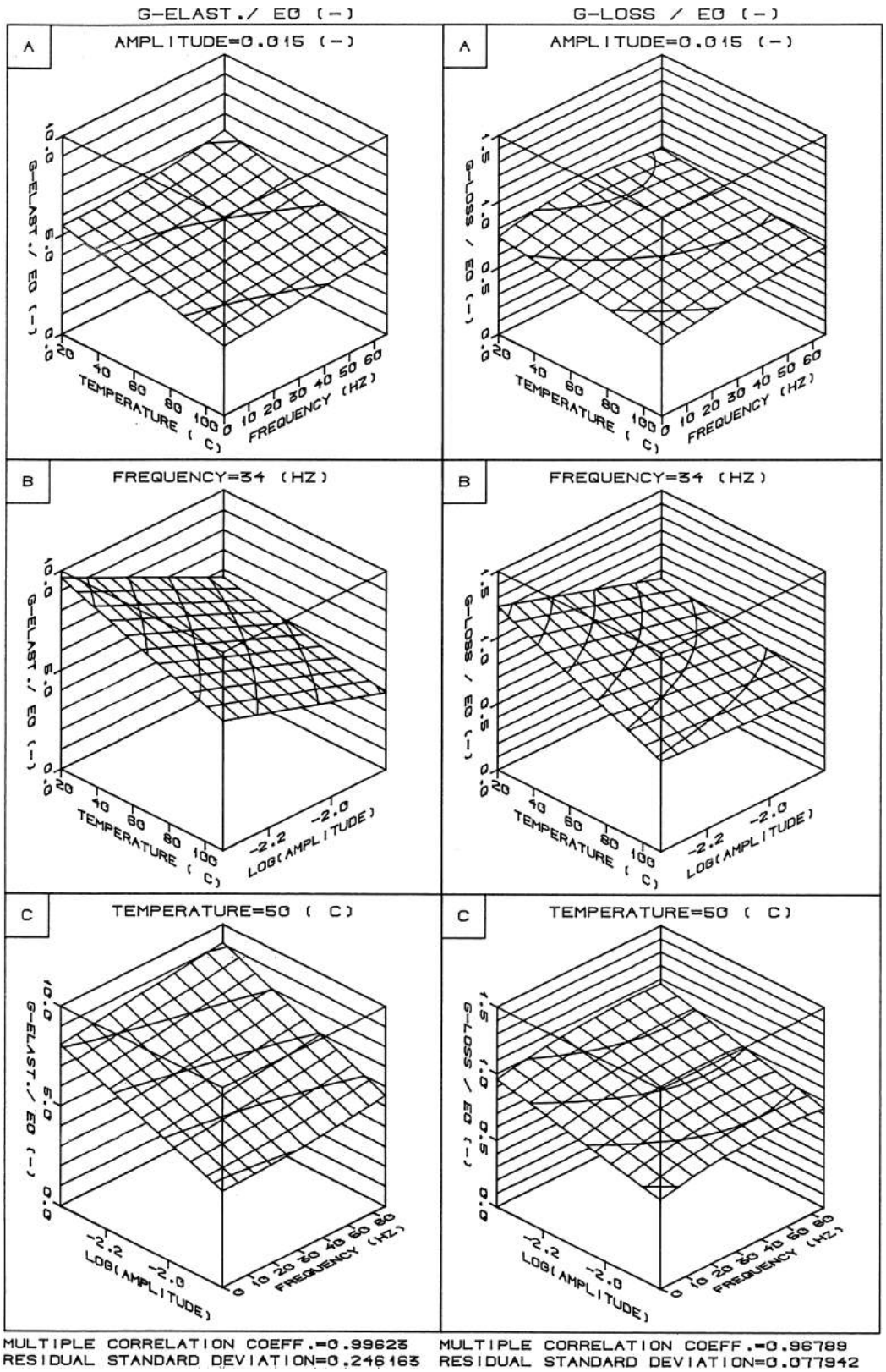

Figure 6.25 *(a) Material 3, orientation 23, 17 test values, 5 degrees of freedom.*

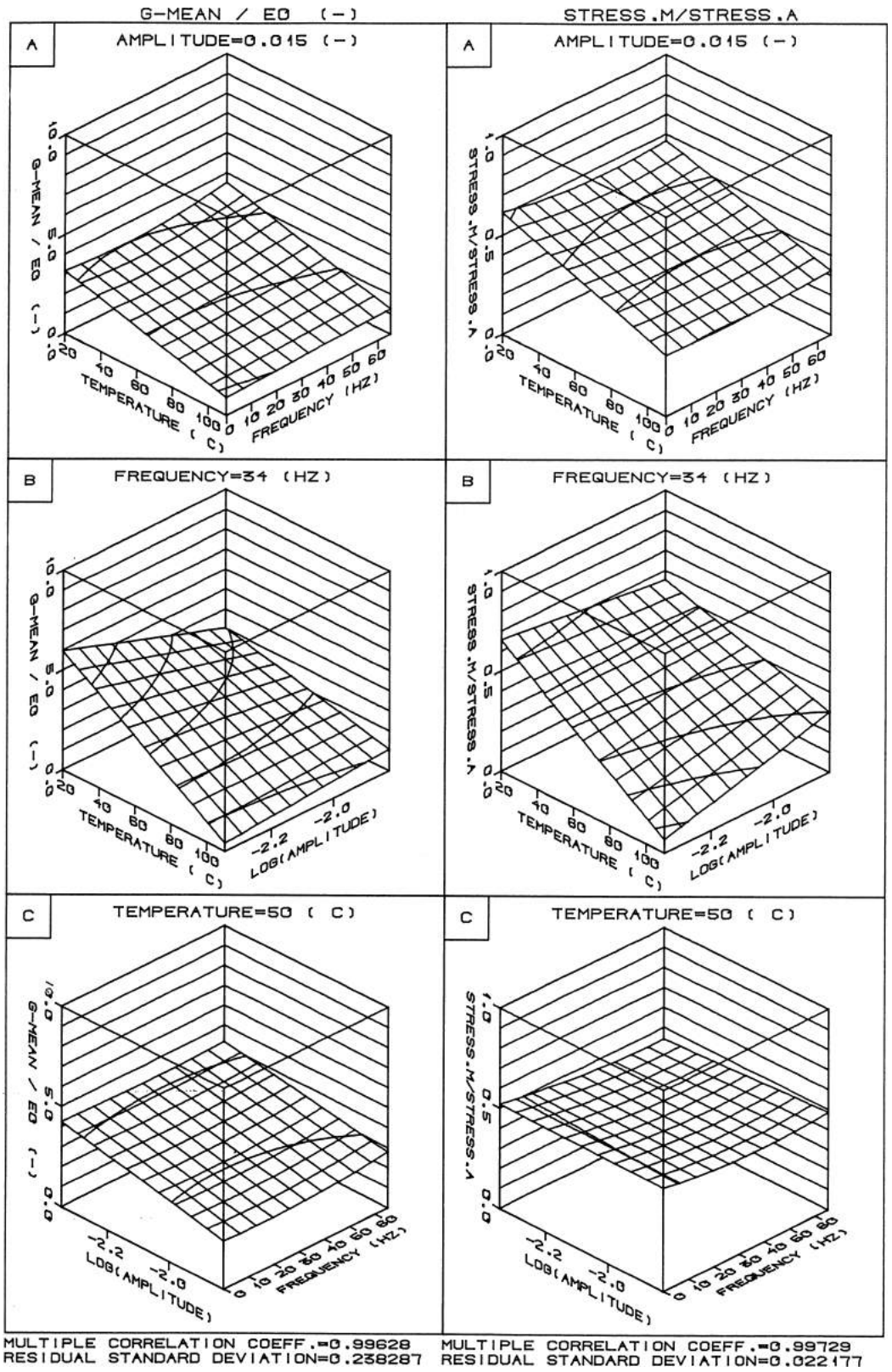

Figure 6.26 *(b) Material 3, orientation 23, 17 test values, 5 degrees of freedom.*

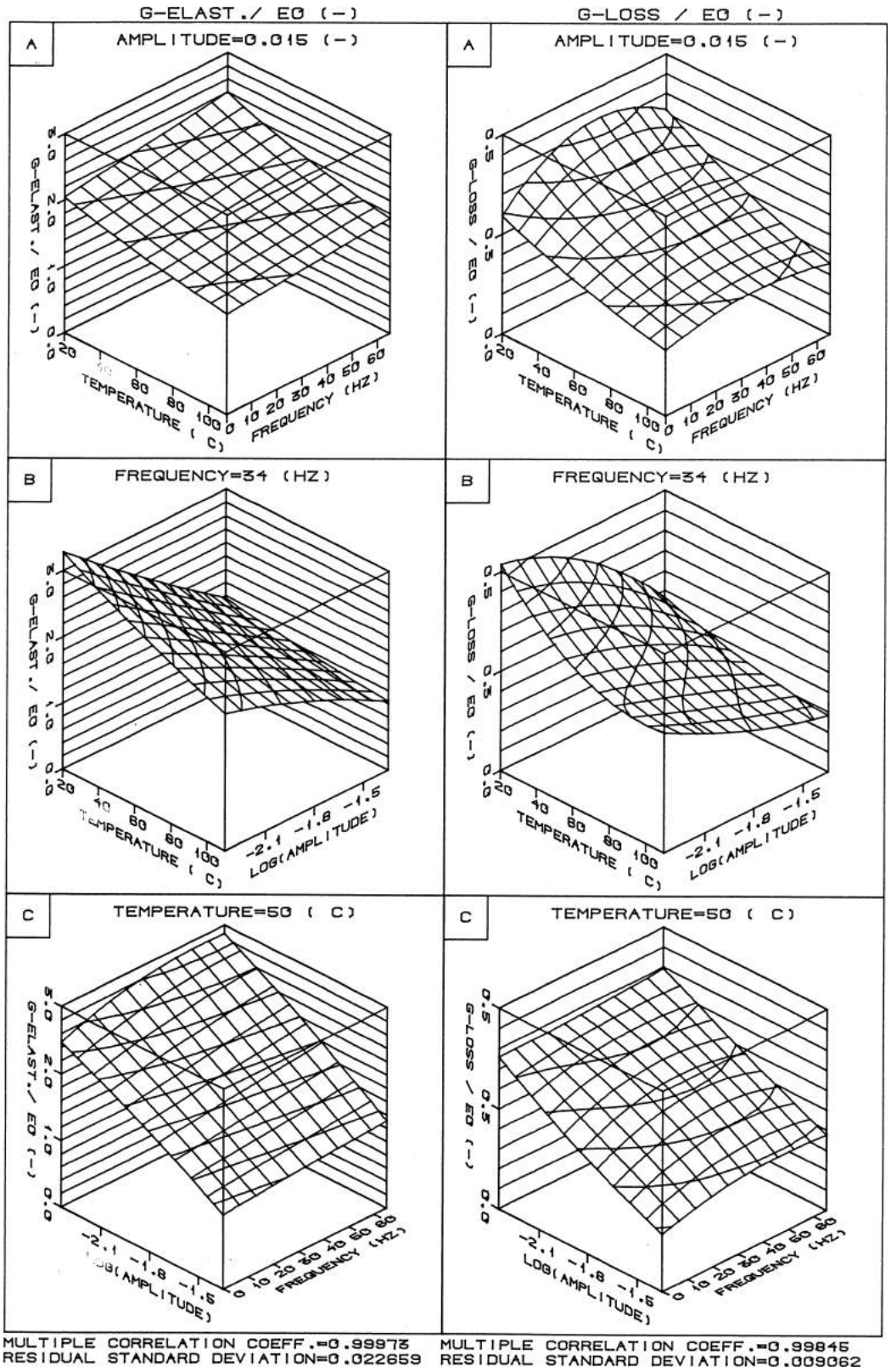

Figure 6.27 *(a) Material 3, orientation 2332, 42 test values, 18 degrees of freedom.*

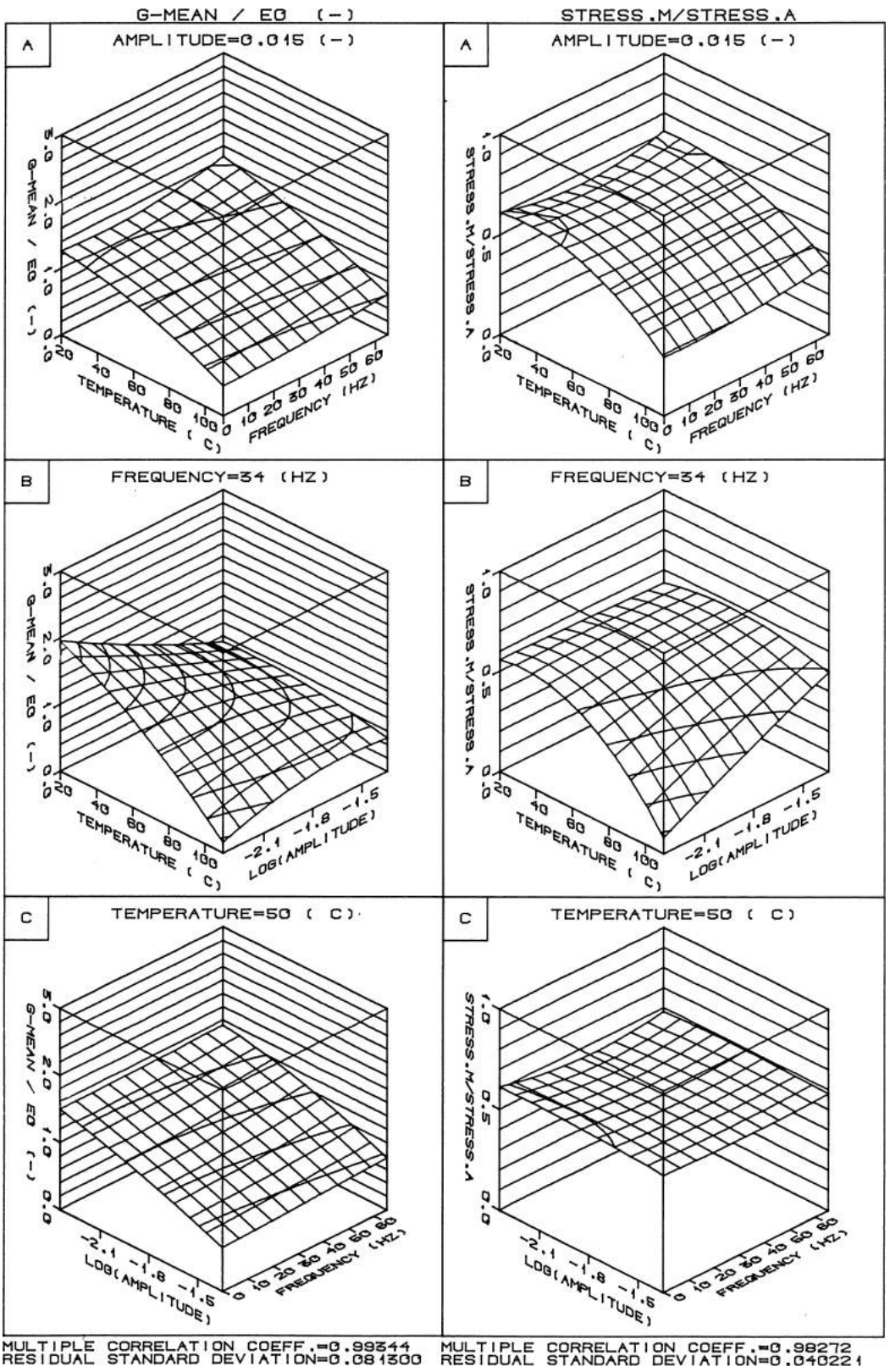

Figure 6.28 *(b) Material 3, orientation 2332, 42 test values, 18 degrees of freedom.*

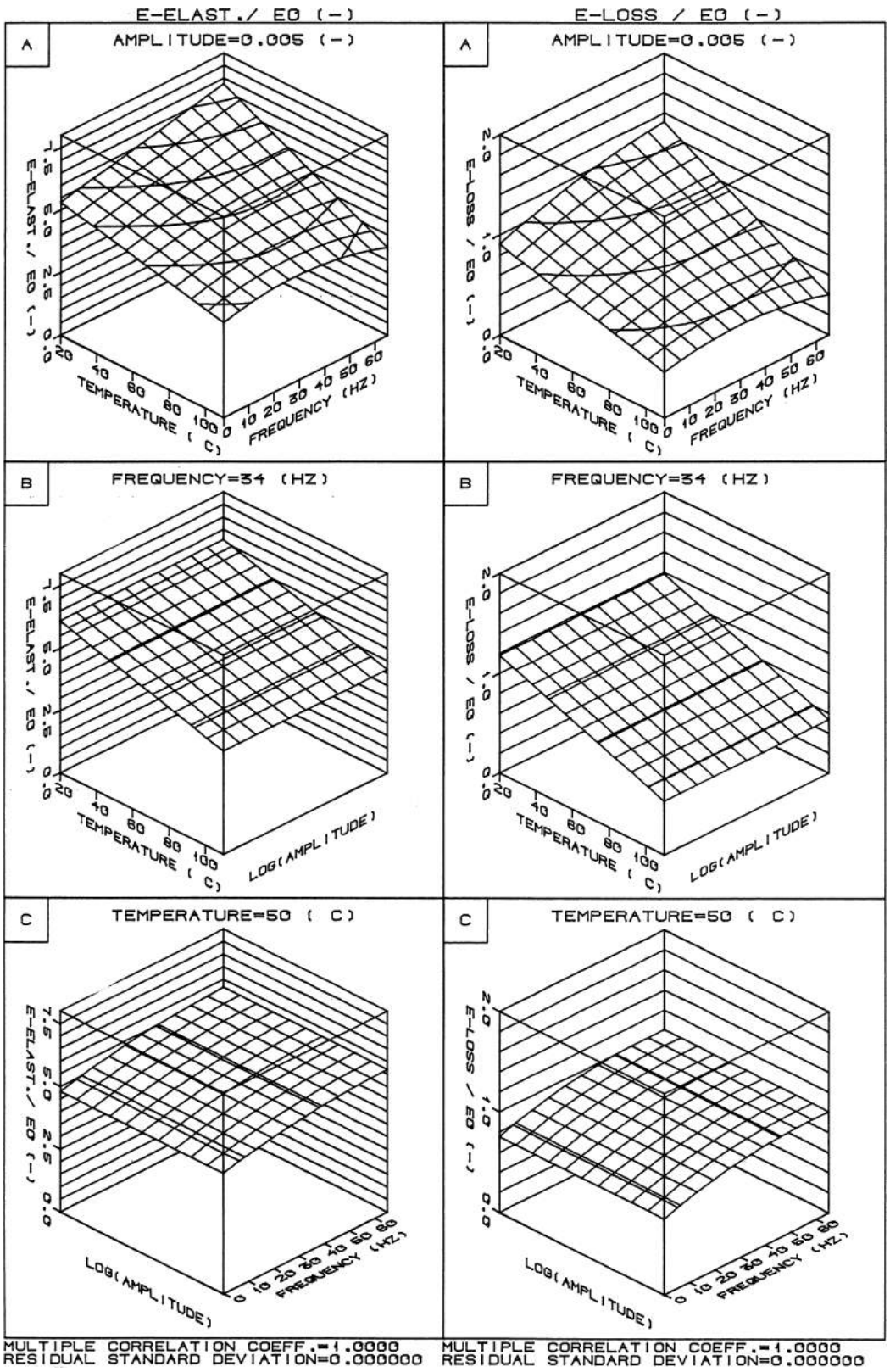

Figure 6.29 *(a) Material 4.2, orientation 33, 6 test values, 0 degrees of freedom.*

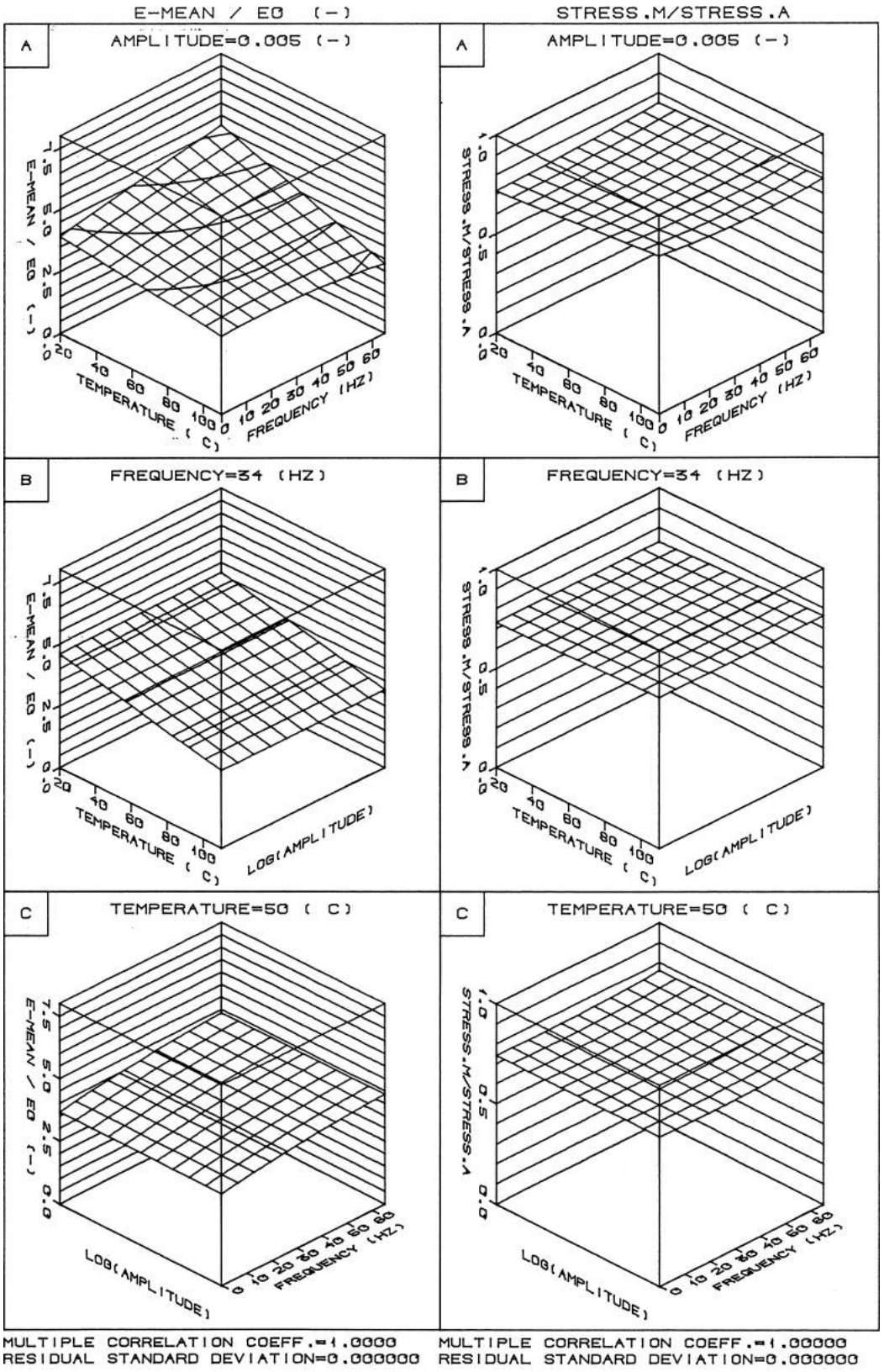

Figure 6.30 *(b) Material 4.2, orientation 33, 6 test values, 0 degrees of freedom.*

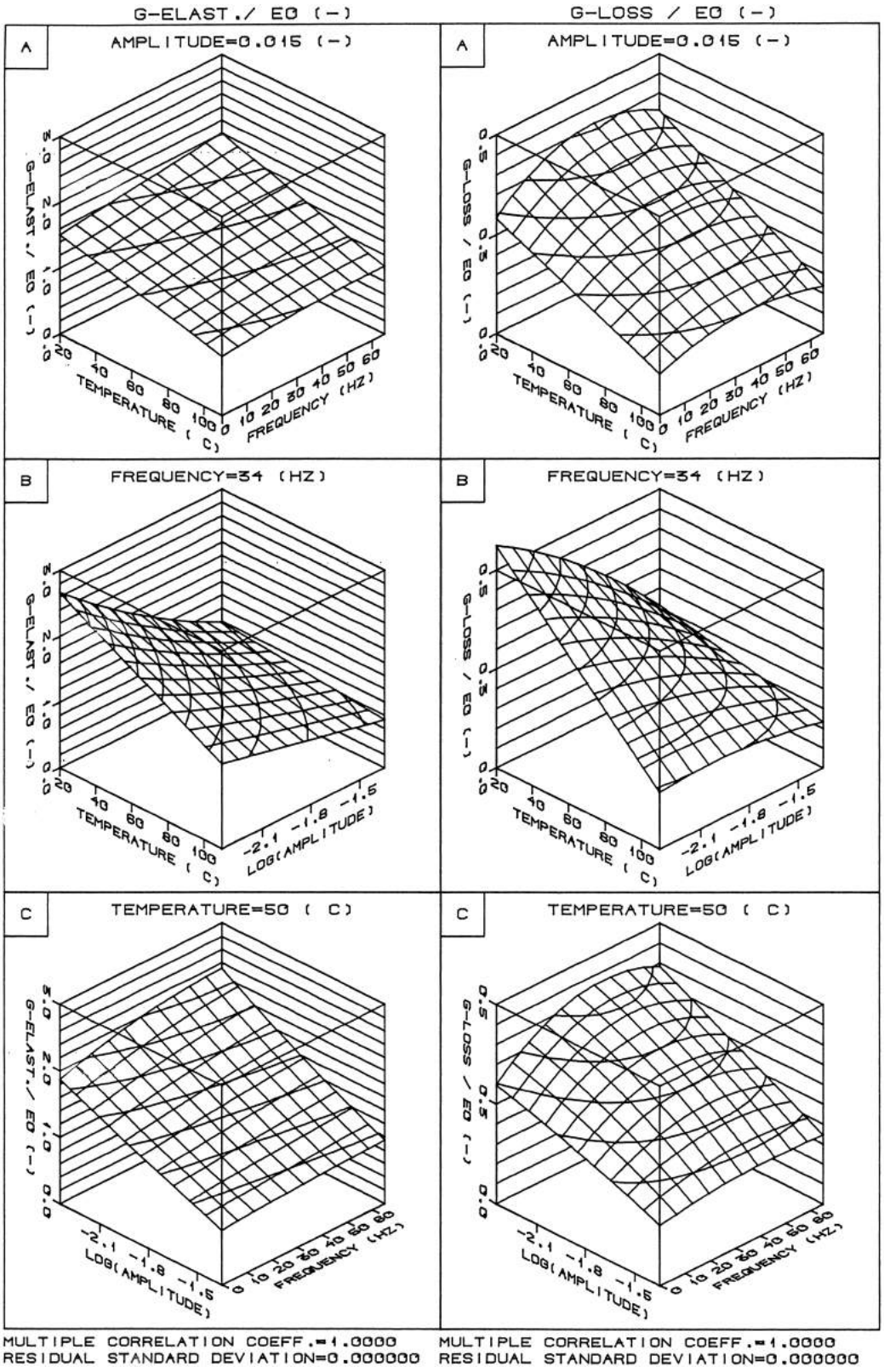

Figure 6.31 *(a) Material 4.2, orientation 32, 18 test values, 0 degrees of freedom.*

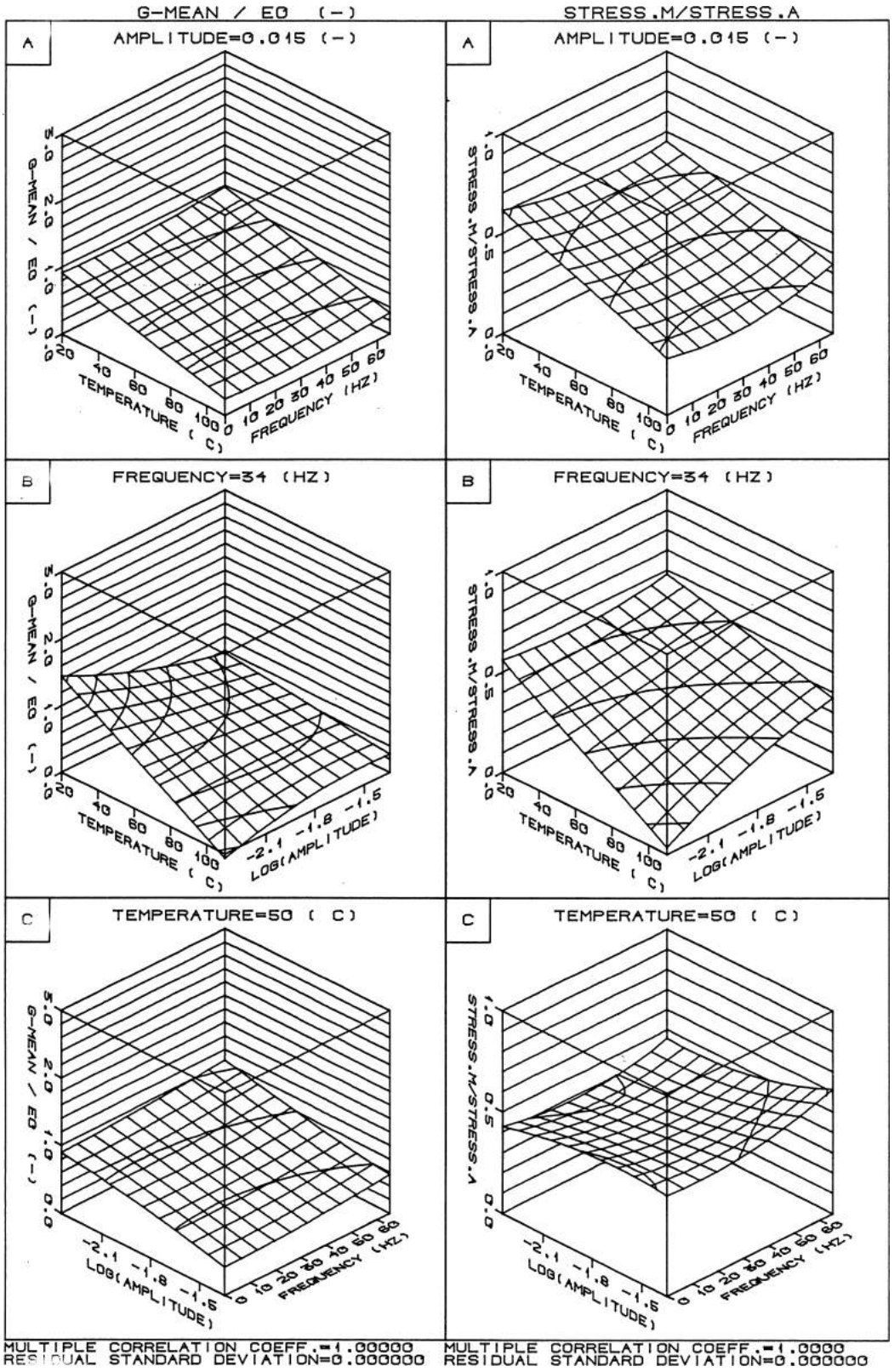

Figure 6.32 *(b) Material 4.2, orientation 32, 18 test values, 0 degrees of freedom.*

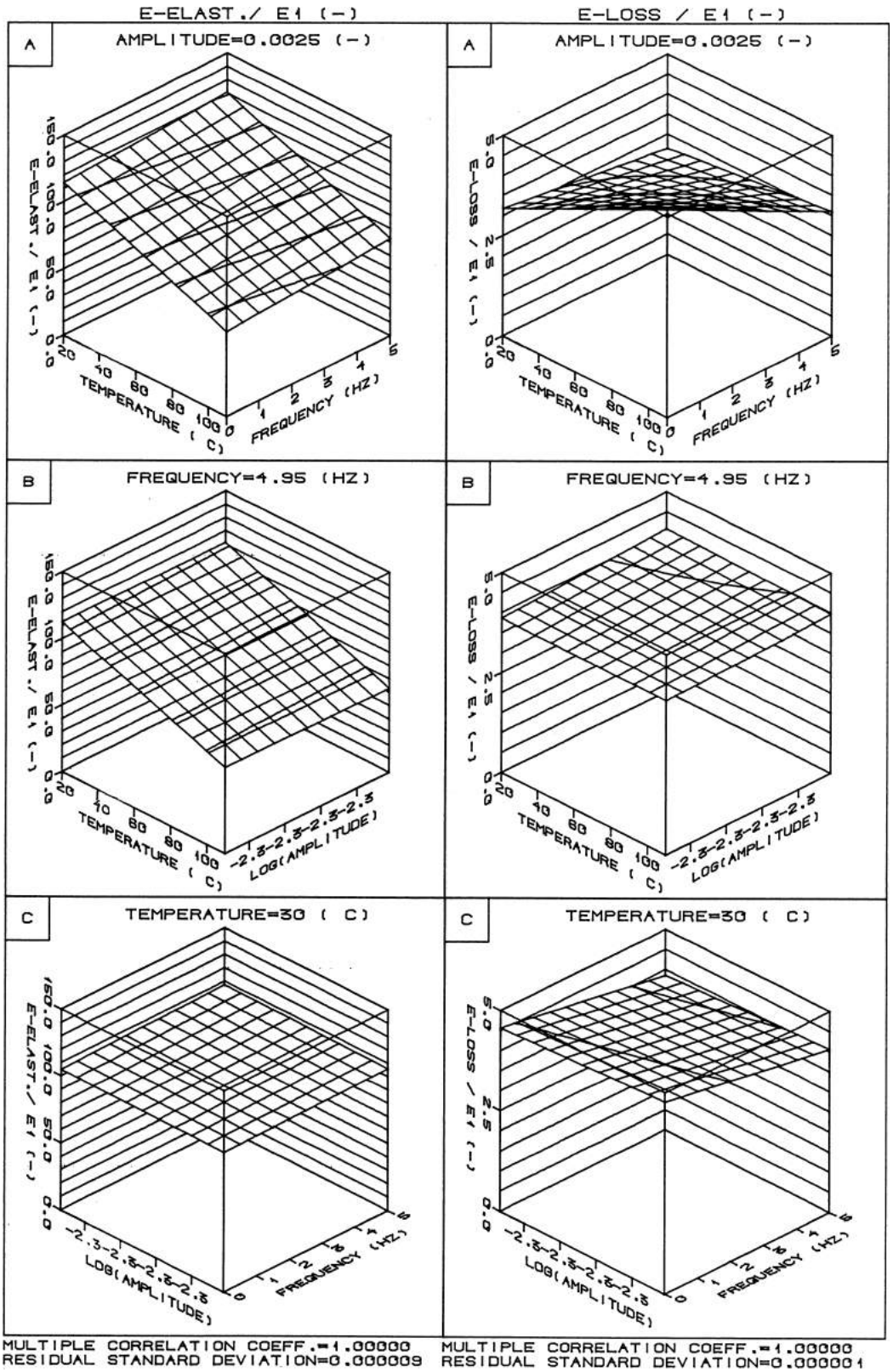

Figure 6.33 *(a) Material 4.2, orientation 22, 6 test values, 0 degrees of freedom.*

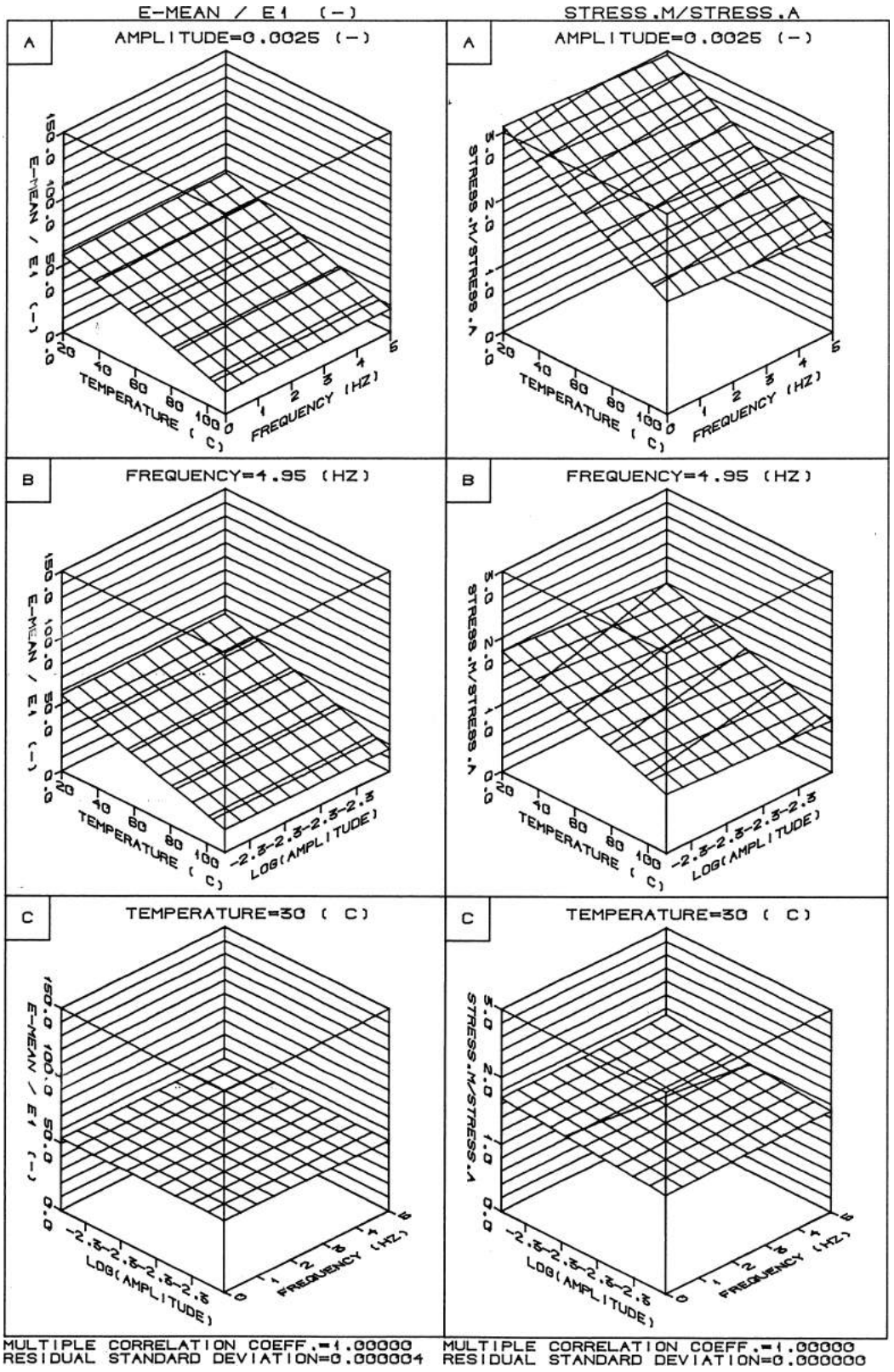

Figure 6.34 *(b) Material 4.2, orientation 22, 6 test values, 0 degrees of freedom.*

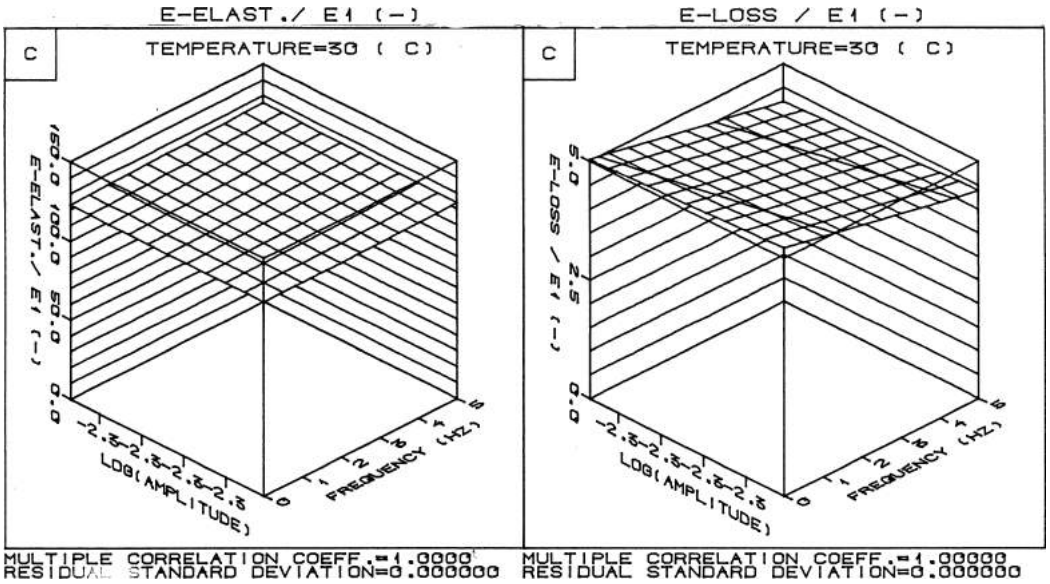

Figure 6.35 *(a) Material 4.1, orientation 22, 3 test values, 0 degrees of freedom.*

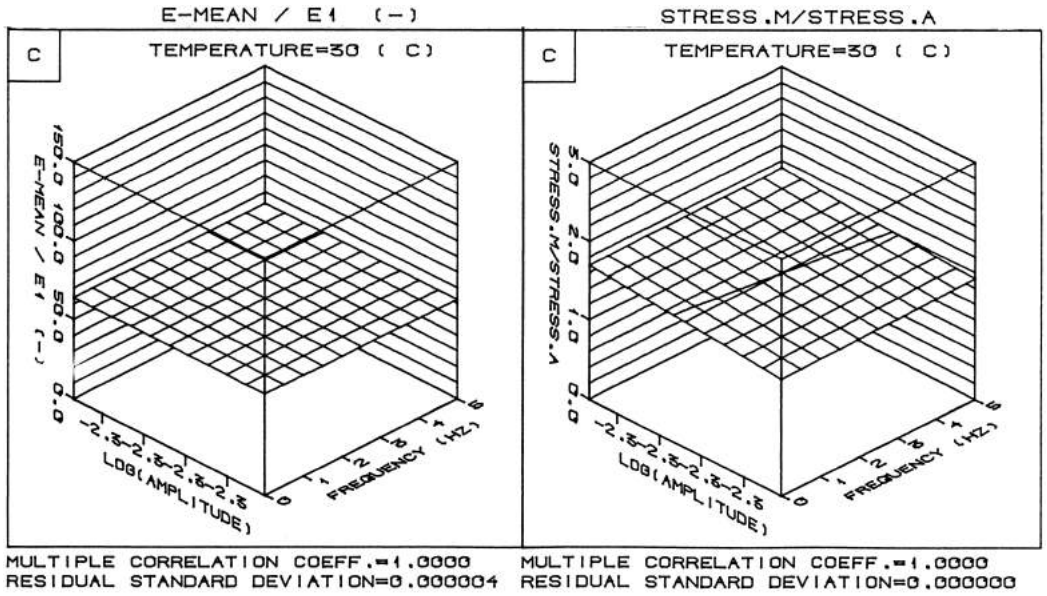

Figure 6.36 *(b) Material 4.1, orientation 22, 3 test values, 0 degrees of freedom.*

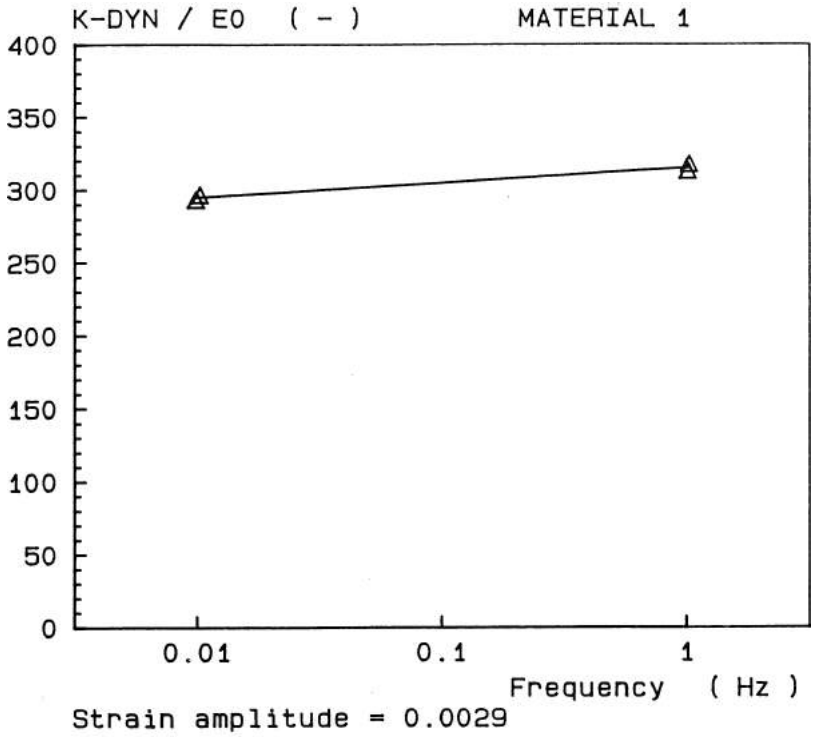

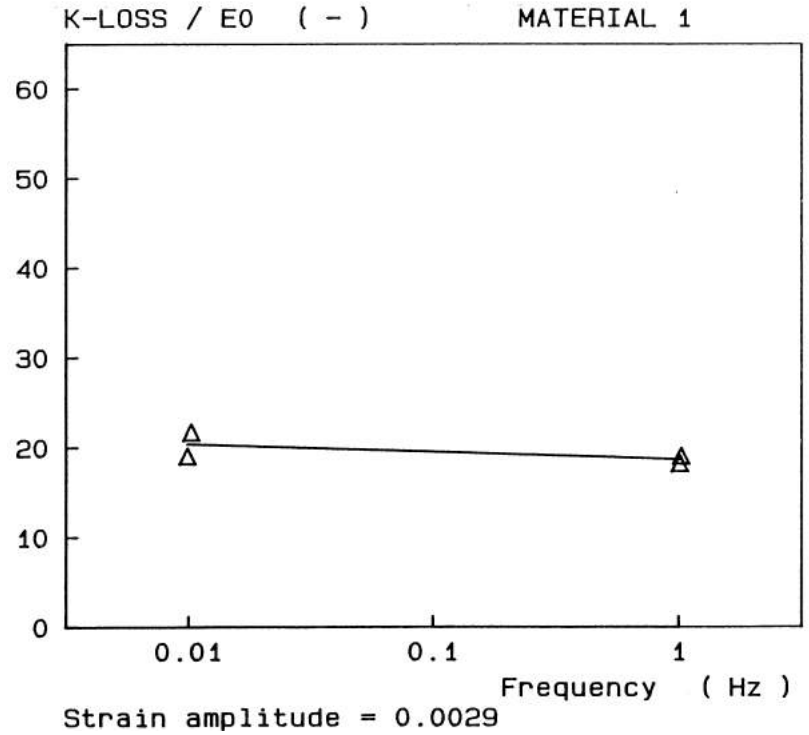

Figure 6.37 *Bulk moduli, material 1.*

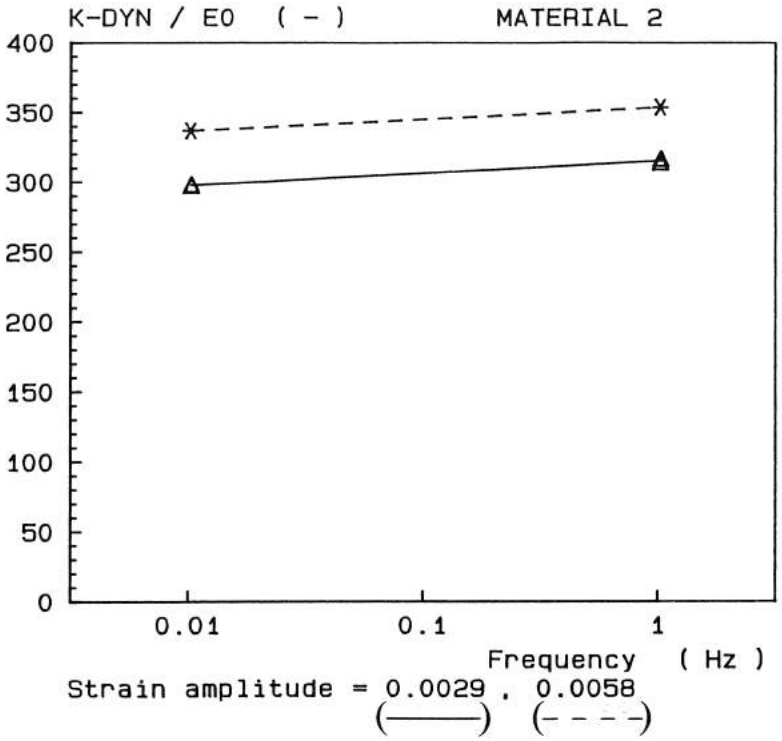

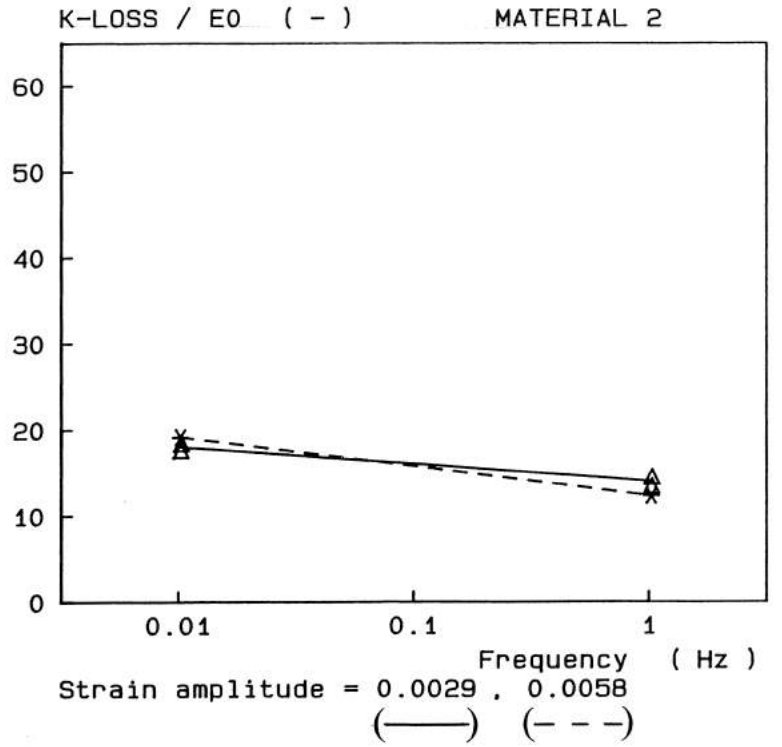

Figure 6.38 *Bulk moduli, material 2.*

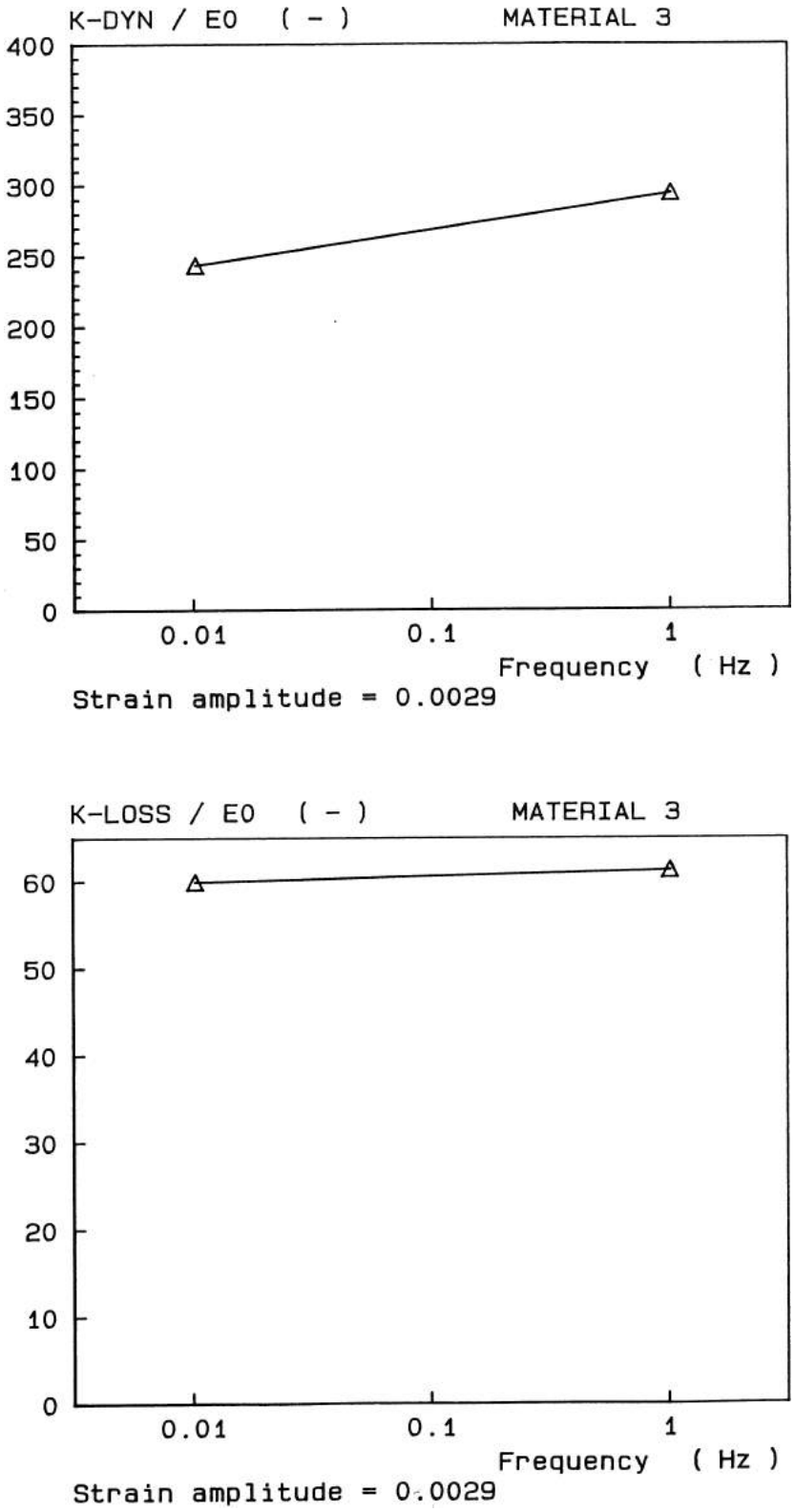

Figure 6.39 *Bulk moduli, material 3.*

6.6 Ageing

For material 1 a whole set of tests were performed 6 months later on test material that had been stored at room temperature. The only change which could be detected was that the maximum value of the elastic modulus which occurs for low strain and room temperature, was reduced by about 2 - 5 percent. Thus our conclusion is that there were no significant changes for this period and environment.

7
Conclusions

The material characteristics of elastomer composites used in V-belt applications are highly dependent on strain, temperature and, to a lesser extent, frequency. The fiber reinforced materials are anisotropic, with one material direction differing from the others. The label “transversal isotropic” can be used. For one of the materials the reinforced direction is up to 4 times stiffer than the other directions. Using the concept of complex modulus, some aspects of the material properties can be described. We assume that these variables vary only within certain intervals characteristic for V-belt applications.

Strain amplitudes of 0.005 to 0.045 cover the interval in which elastomer composites are sensitive to strain softening or structure breakdown. The reinforced material direction is the most sensitive one. For all the materials and material directions a reduction in elastic modulus of a factor 2 - 3 is found to be normal.

A temperature increase from room temperature to 100 - 120 degrees Celsius causes the same reduction as for the variation in strain amplitude above.

The frequency of the sinusoidal deformation is the least important parameter. An increase of 10 - 20 percent of the elastic modulus over a frequency interval of 3 - 60 Hz is normal. The loss modulus is slightly more dependent on frequency.

The bulk modulus is about three orders of magnitude greater than the shear modulus. This means that in many designs these materials may be regarded as incompressible.

The results for the cord were deviant. In this case, the temperature was found to be the only important parameter, especially for the loss modulus. The changes are small compared with changes in the rubber materials mentioned above.

Our conclusion is that in any material description made for elastomers composites for this application, several variables should be studied. The order of importance among these should be anisotropy, strain effects, temperature effects and at finally frequency effects.

For polyester cord the temperature is the most important variable.

8
Acknowledgements

Many thanks to the personnel at Dayco Technical Center, who made this study possible. Special thanks to Mr and Mrs Clyde O. Johnson who made my stay in Springfield most enjoyable.

Bibliography

[1] Dayco Corporation., Springfield Technical Center, Springfield, MO, USA, 1988.

[2] C.J. Derham. In: *Rubb. Chem. Tech.* 50 (1977), p. 397.

[3] C.J. Derham. "Paper F". In: *NRPRA 3rd Rubb. in Eng.ng. Conf.* 1973.

[4] F.R. Eirich (Editor). *Science and technology of rubber*. New York: Academic press, 1978.

[5] P.K. Freakley and A.R. Payne. *Theory and practice of engineering with rubber*. Ripple Road, Barking, Essex, England: Applied Science Publishers Ltd, 1978.

[6] P. Fritzson. *MULREG - A Statistic, Database and Graphic program system. User reference manual*. 1st ed. Idatron HB. Linköping, Sweden, 1984.

[7] G. Gerbert. *Heat in V-belt drives*. Department of Mechanical Engineering, Lund Technical University, Lund, Sweden: Division of Machine Elements, 1981.

[8] J.A.C. Harwood, L. Mullins, and A.R. Payne. In: *Journal of Applied Polymers Science* 9 (1965), pp. 3011–3021.

[9] G.D. Hubbard. *Rubber properties for stress-strain analyses*. Symposium on analysis and design of rubber parts. Columbus, Ohio: Battelle Columbus Laboratories, 1984.

[10] *Instruction manual for 1320 series dynamic test systems*. Instron Corp. Canton, Massachusetts.

[11] K.N. Morman. *Rubber viscoelasticity - a review of current understanding*. Dearborn, Michigan, USA: Ford Motor Company, June 1984.

[12] L. Mullins. "Mechanical behaviour of polymers - accomplishments and problems". In: *Elastomers: Criteria for engineering design*. Ed. by C. Hepburn and R.J.W. Reynolds. Ripple Road, Barking, Essex, England: Applied Science Publishers, 1979. Chap. 1, pp. 1–6.

[13] *Norland 3001 Waveform analysis system - user reference manual*. Norland Corp. Fort Atkinson, WI.

[14] A.R. Payne and A.B. Davey. *Rubber in engineering practice*. London: Applied Science Publishers LTD, 1964.

[15] A.R. Payne and R.E. Whittaker. In: *Rubber Chemistry and Technology* 44 (1971), pp. 340–.

[16] B.E. Read and G.D. Dean. *The determination of dynamic properties of polymers and composites*. New York: John Wiley and Sons, 1978.

[17] G.H. Staab and T.G. Richard. "An experimental investigation of cog-root strains in V-belts using brifrigent coatings". In: *SESA Journal of the society for experimental stress analysis, Experimental Mechanics* (Dec. 1982).

[18] B. Stenberg. *Gummimaterialets dynamisk-mekaniska egenskaper - Hysteres och Utmattning (The dynamic-mechanical properties of rubber material - Hysteresis and Fatigue*. Report from PGI no. 19. Sundsvall, Sweden: PGI, 1981.

[19] A.G. Thomas and M.M. Hall. *Testing procedure for measurement of dynamic properties of vulcanized rubber*. Shrewsbury, England: Rubber in engineering design group, RAPRA, 1973.

[20] M. Zachrisen. *Surrender - A subroutine package for rendering bivariate surfaces*. Runit. Trondheim, Norway, 1979.

Part VI

Change of V-belt geometry in a running transmission

Report VI

Change of V-belt geometry in a running transmission

Dag Fritzson

Report No. 1988-05-24
Division of Machine Elements
Department of Mechanical Engineering
Chalmers University of Technology
Göteborg, S-412 96 Sweden

Abstract

The interaction between belt and pulley in a V-belt drive has been investigated. Parameters studied were running time, surface roughness and pressure angle of the pulley. The results show that the belt geometry conforms to the pulley geometry in short time compared to a normal belt service life.

Contents

1
Introduction

This paper is part of a study intended to contribute to our understanding of V-belt transmissions, especially stresses or strains in the belt during a load cycle. In order to do this, it is necessary to know the pressure distribution and friction forces against the sides of the V-belt. There can never be a perfect fit between a pulley and a new belt, because there are different pressure angles etc. In this report we have experimentally studied the changes in the geometry of running V-belts for different pressure angles of the pulleys.

2

A V-belt transmission

2.1 Material properties

A typical contemporary V-belt consists of several layers of different elastomer composites. In the longitudinal direction there are cords which carry the forces between the pulleys. A typical elastomer composite for V-belt applications consists of an elastomer, carbon black and several additives. It is also reinforced with fibers in one direction. This gives the material anisotropic characteristics. Elastomers exhibit viscoelastic properties under stress. Typically, a hysteresis loop is obtained during cyclic deformation. The total effects of the additives, in particular of carbon black, increase the hysteresis. V-belts are normally designed cog shaped, as shown in Figure 2.1. This is done in order to decrease energy losses from deformation. The resulting decrease in temperature affects fatigue life positively.

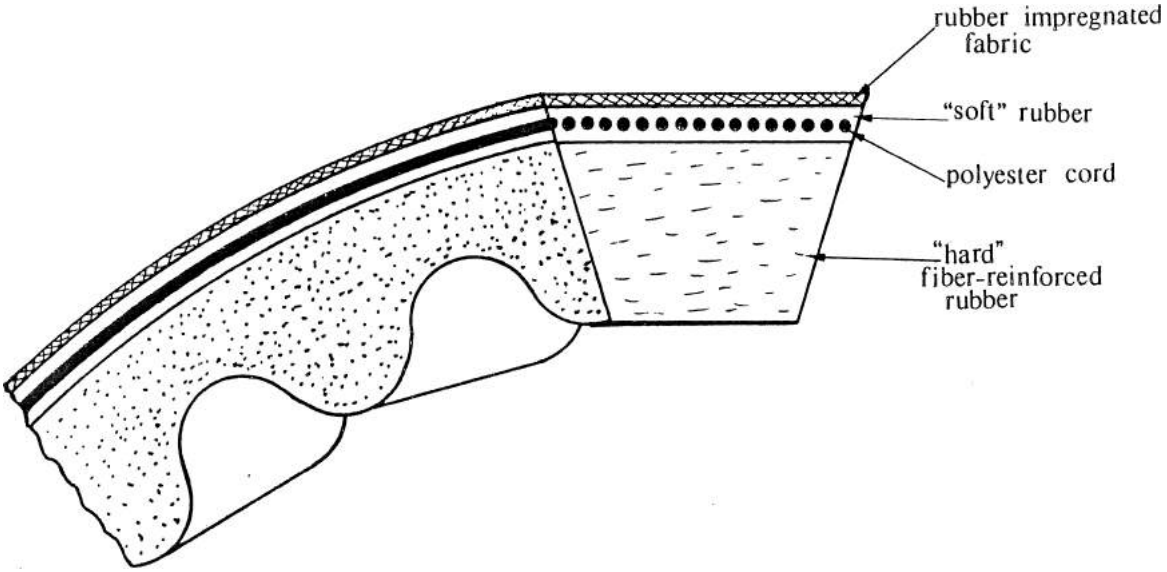

Figure 2.1 *A common V-belt design.*

2.2 Power transmission

The mechanics of a V-belt transmission have previously been investigated in detail [1]. The theory explains the interaction between the belt and pulley. The hard fiber-reinforced rubber of the pressure zone carries all contact forces and transmits friction forces to the cord. To be able to calculate the distribution of pressure against the sides of a belt, the geometry of both the belt and the pulley must be known.

3
Test equipment

3.1 Test rig

A test rig has been designed which makes it possible to run tests on four different V-belts simultaneously [2]. See Figures 3.1 - 3.3).

This is a dead weight test rig. No power is transmitted except to make up for losses. This method is adequate here since this is not so severe a load case as in a real power transmission. Whatever changes in geometry that develop, it is reasonable to assume that they would develop quicker in a real case.

Also, the slip and maximum load are smaller for a given dead weight, than when power is transmitted. Special consideration was taken in designing this test rig to keep

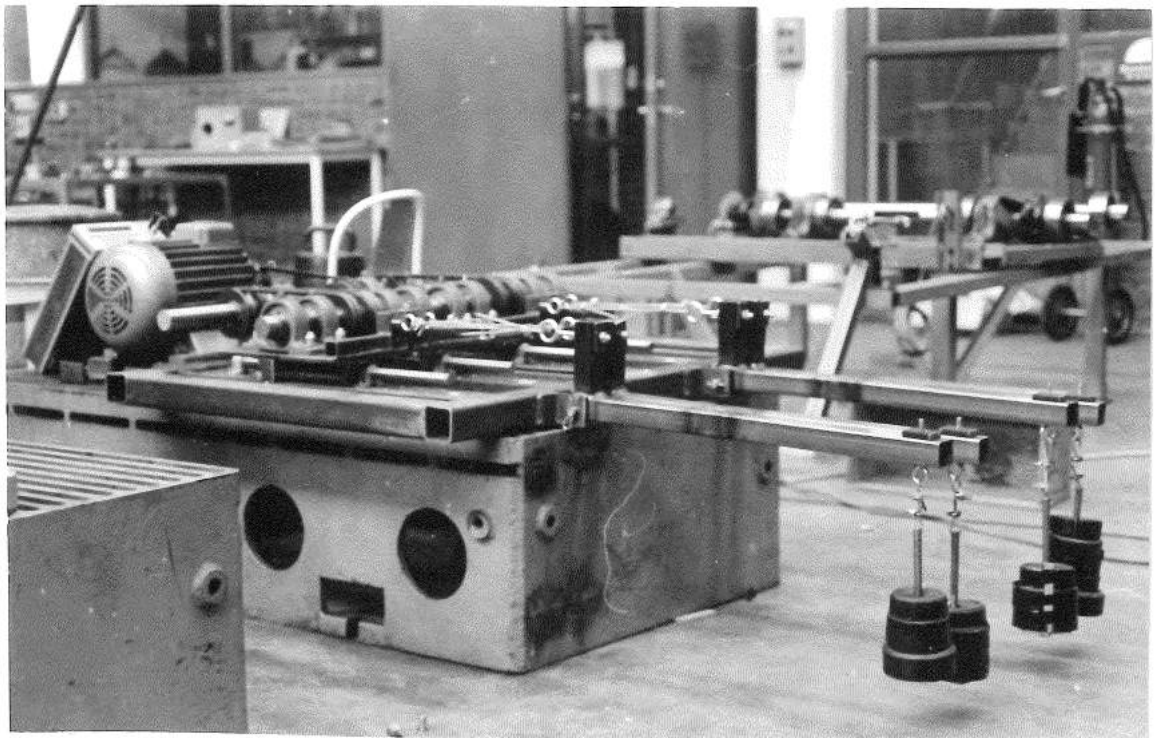

Figure 3.1 *Test rig*

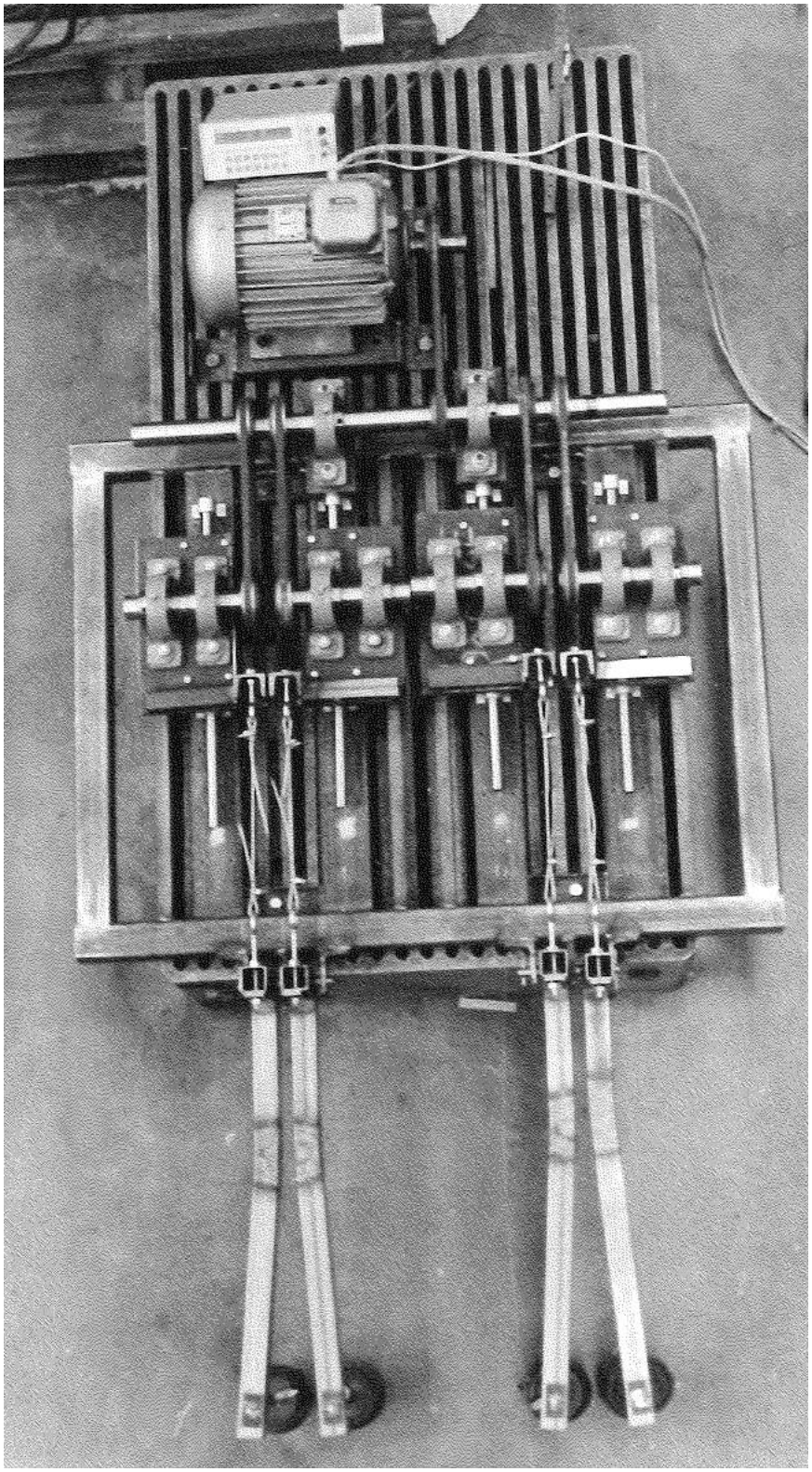

Figure 3.2 *Test rig, Top view*

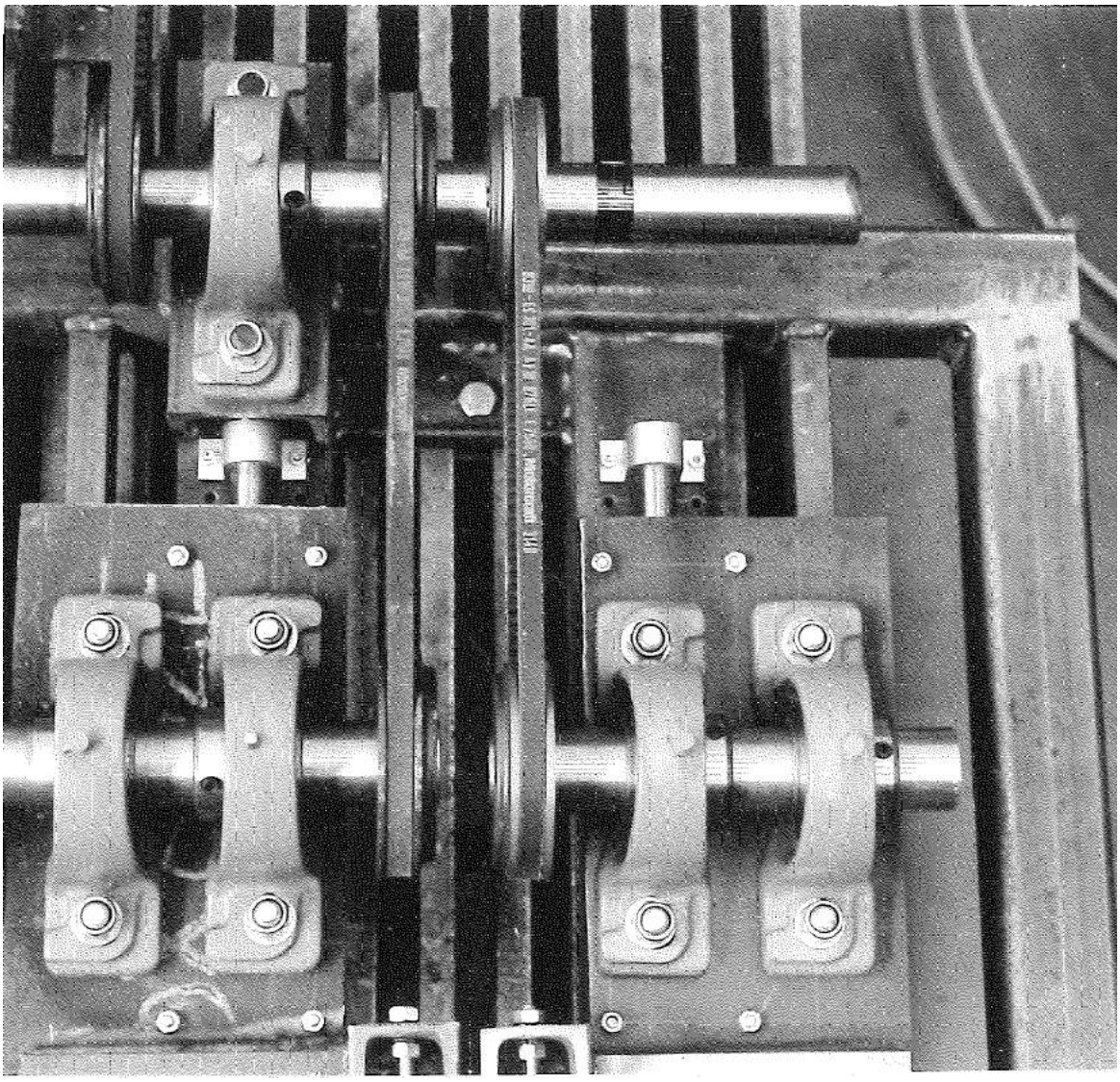

Figure 3.3 *A section of the drive from the test rig.*

the shafts parallel for all interesting load cases, and to be able to mount/dismount a belt in just a few seconds. The latter is important as geometric changes have to be measured in a special test machine and not at the test rig. The two pulleys of each of the four drives can easily be exchanged for new ones, in order to obtain a different pressure angle or diameter.

3.2 Belt and pulley measurement methods

In order to be able to study changes in V-belt geometry as a function of time the method used must have the following properties:

1. The belt should not be damaged in any way.

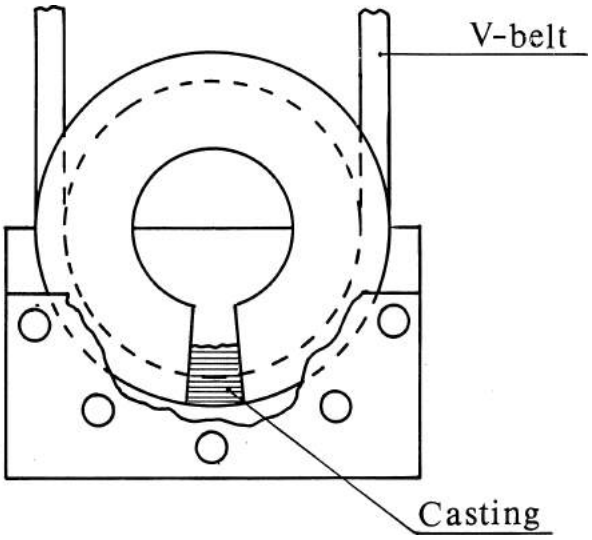

Figure 3.4 *Equipment for recording belt shape by casting plastic resin around the belt.*

2. Geometric changes should be measured while the belt has the same curvature radius as when it is running.

3. The method has to be accurate enough to detect changes in the order of 0.01 mm.

4. Measurements should be made at the same position in the belt each time.

Two methods for measuring the shape of the belt have been developed in detail [2]. In the first method the belt was put into a special fixture to the desired radius. Subsequently the shape of the belt was recorded by casting plastic resin over the part studied. A resin called Kulzer Technovit 3040 was used. It worked quite well without excessive heat or damage to the belt. The plastic sample was then ground flat on a surface orthogonal to the circumferential direction of the belt. The sample shape was measured using a microscope by digitizing several points along each edge. The angle between the two edges was then calculated from the coordinates obtained.

Our second method is simply direct measurement of the belt using three dial indicators. The belt is placed in a fixture that holds the belt with the desired curvature radius. Successive readings are made from the top of the belt towards the bottom. Using these coordinates, the angle is calculated.

In order to evaluate the two methods, three independent complete measurements were made according to each method at exactly the same spot on the belt. Complete measurement included fastening the belt at the fixture, performing measurement or casting with plastic and finally taking the belt out of the fixture again. The first method included measurement of several coordinates of the plastic sample using a microscope. The surprising result was that the dial indicator method gave much better accuracy than the casting method as shown in Figures 3.8 and 3.9.

The pressure angle was calculated by fitting a first order polynomial to the coordinates using linear regression. Then the angle between the lines was calculated.

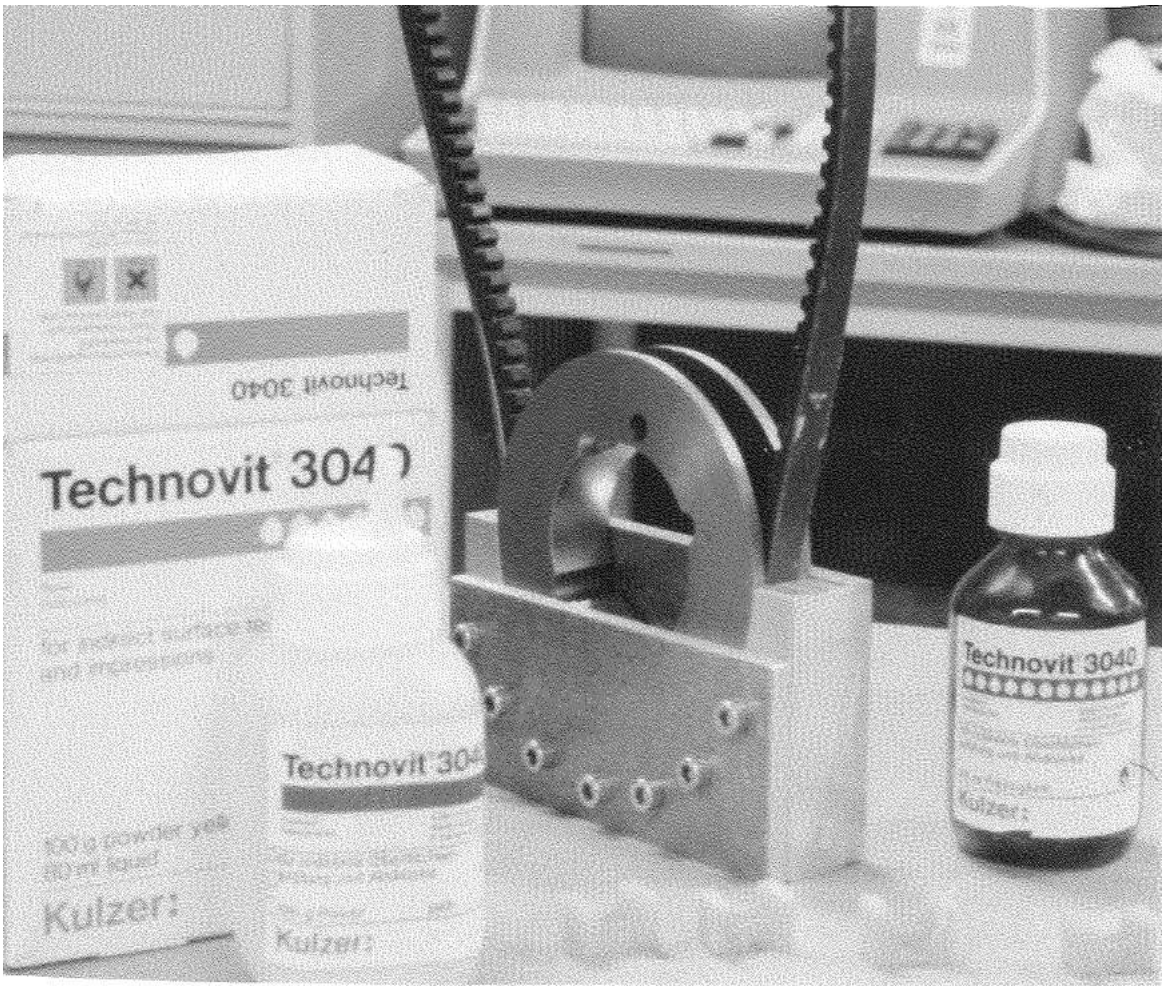

Figure 3.5 *Casting the sample from which the edges are digitized using a microscope.*

This angle calculation was done on the coordinates from both types of measurement methods.

The results that the dial indicator method was better can be explained by the fact that there are fewer steps in the dial indicator method and fewer sources of error. There were some difficulties in defining the edge of the cast, as the plastic filled up all porosity of the belt. This was visible on the plastic sample. In the dial indicator method the rounded tip of the probe had some integrating effects which gave better precision. As shown in Figure 3.8 an error of plus/minus 0.05 to 0.1 degrees can be expected for the dial indicator method. Thus, the dial indicator method was used in all succeeding tests. The pulleys were measured by first casting the shape and then measuring it. In this case the accuracy was better as the pulley has a smooth flat surface, and an error of the same order of magnitude as for the dial indicator method could be expected. In this investigation the aim was to study angular changes from 0.1 to 4 degrees, and so all results are rounded off to one decimal place. As discussed previously the accuracy is of the same order of magnitude as the lower limit. This influences the last digit of all data presented in this report. The reader must keep this in mind when studying the diagrams and figures.

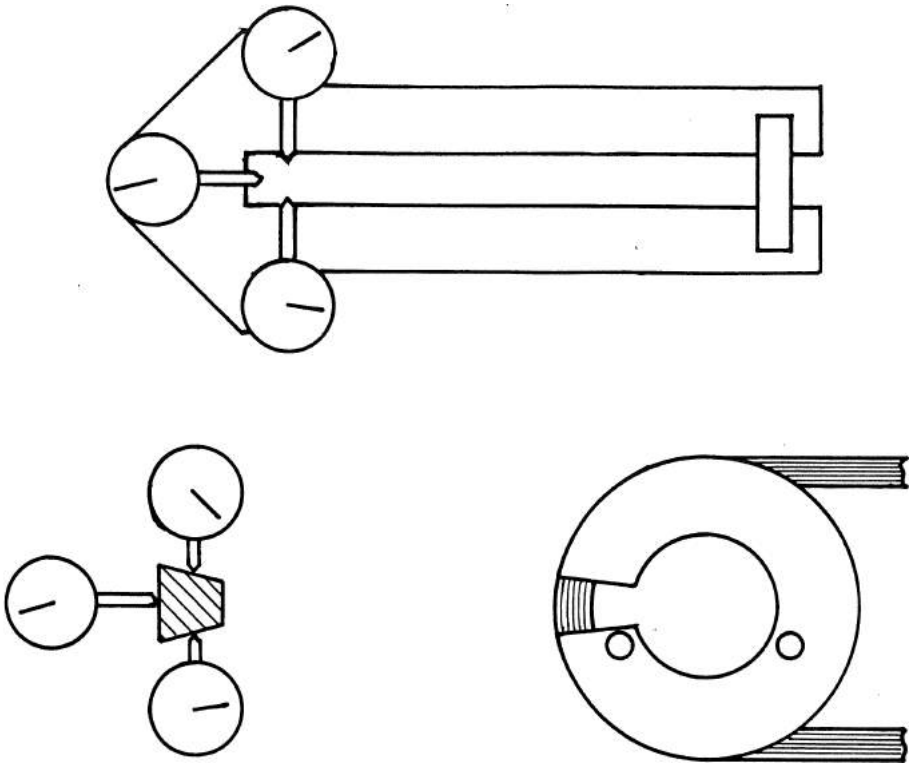

Figure 3.6 *The belt fixture for direct measurement of the shape of the belt.*

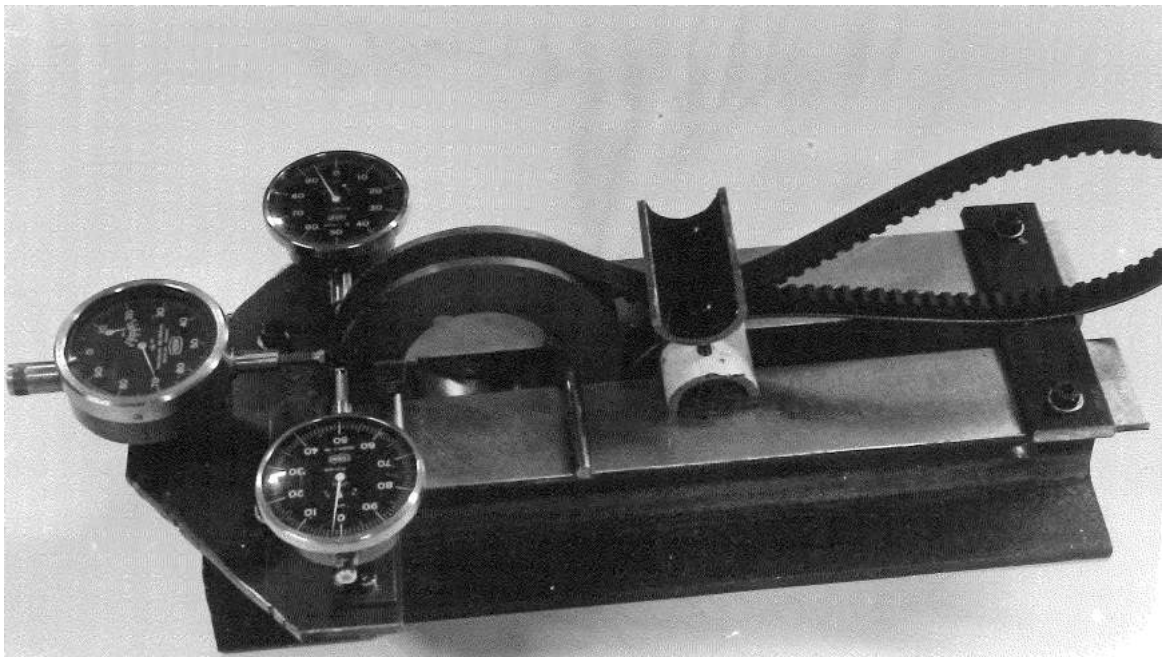

Figure 3.7 *Measuring a belt using three dial indicators.*

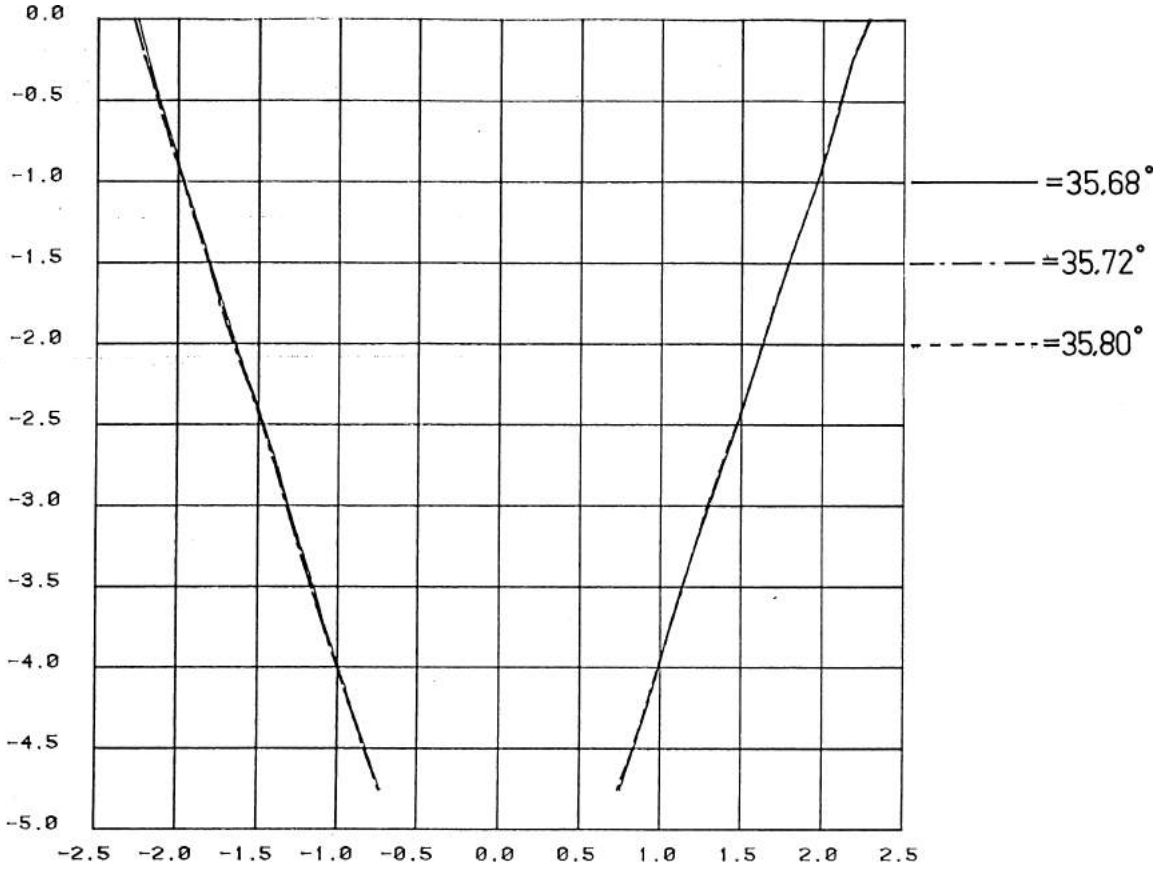

Figure 3.8 *Three independent measurements of a belt with the dial indicator method. The diagram is shortened 5.9 mm in the X-direction.*

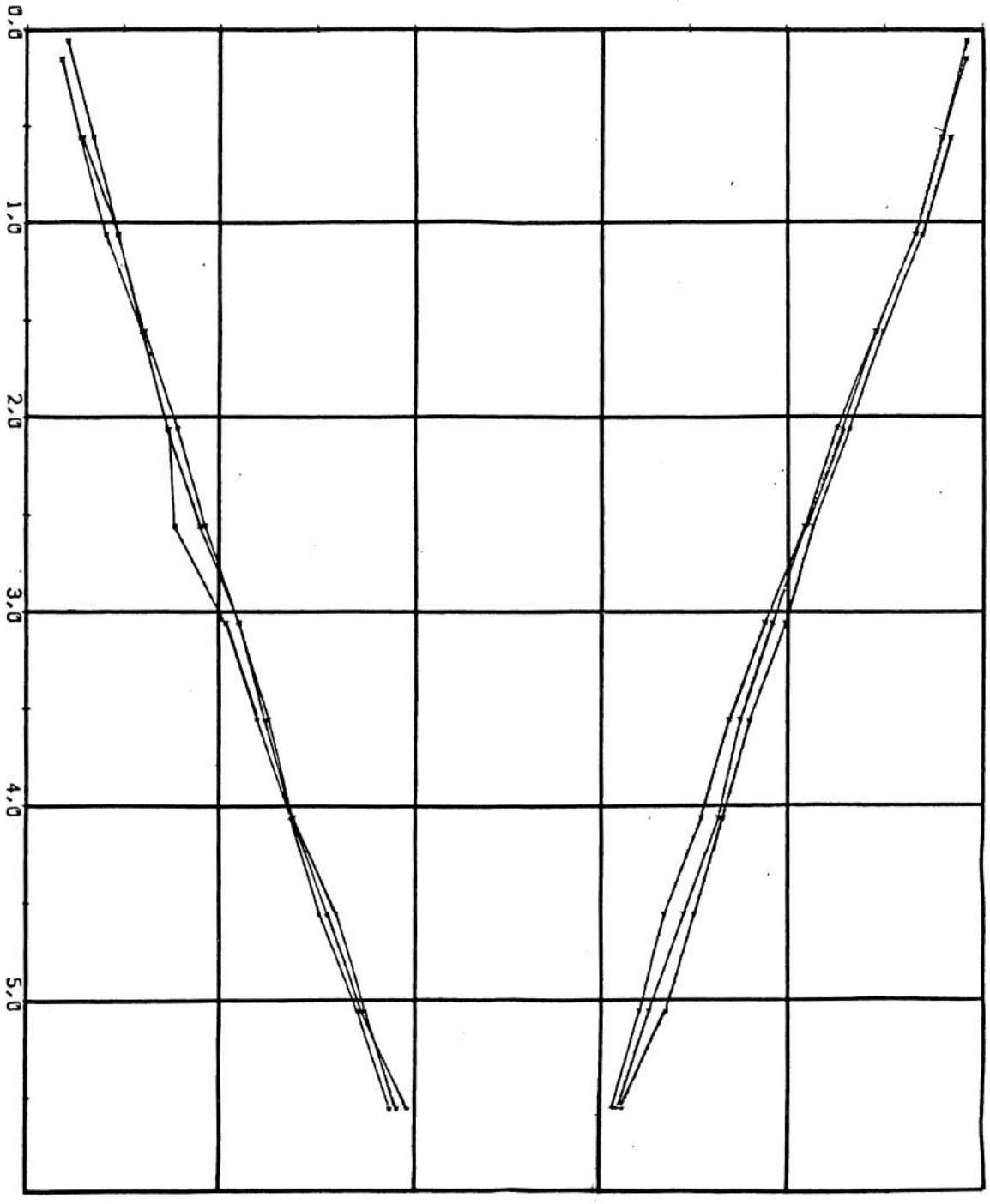

Figure 3.9 *Three independent measurements of a belt using the casting method. The diagram is shortened 5.9 mm in the X-direction.*

4
Experiments

4.1 Test cases studied

Our goal was to study the three different combinations of belt and pulley geometry as illustrated in Figure 4.1. In addition to geometry, the effect of surface roughness was studied in one additional test case.

The first case (A) is when the belt has a smaller initial pressure angle than the pulley.

The second case (B) is when the belt has a greater initial pressure angle than the angle of the pulley.

In the third case (C) the pressure angle of the pulley was set so the difference in pressure angle between the belt and pulley would be as small as possible, considering the fact that there are variations in the pressure angle between different belts or positions on the belt.

The fourth case (D) is nearly the same as case (B) with regard to pressure angles, except that the surface roughness is smaller than in the previous cases. In this case the surface roughness of the pulleys is about R_a 1 μm in the radial direction compared to about R_a 4 μm in the other cases.

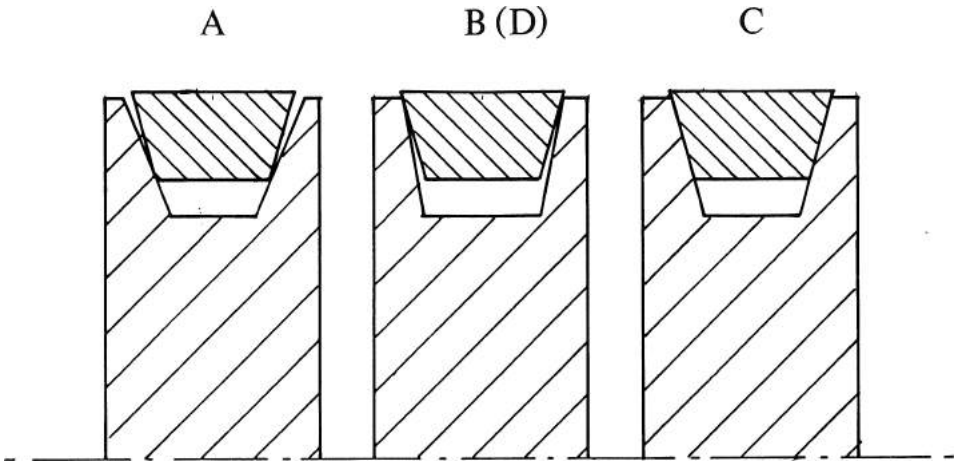

Figure 4.1 *The geometry of belt and pulley in the three test cases.*

The V-belts used were Roulunds 83HF-6C301-AA AV10876LE E7560 (Motorkraft 3140) and the nominal diameter of the pulleys was 0.1 m. The rotation speed was 2980 rpm and the dead weight load 350 N for all tests. Some calculations were done with manual design methods for this drive configuration at normal power transmission and fatigue life. From those calculations the total load of 350 N was classified as a relatively weak load case. All tests were done at normal indoor temperature, about 20 degrees Celsius.

4.2 Test procedure

The tests were performed in the following way. First the belt was marked at a certain position and measured using the dial indicator method previously described. Then the belts were mounted on the test rig, force was applied and the motor was started. At fixed intervals the rig was stopped, and the belts dismounted and measured at the marked positions. The temperature of the belts was also measured. This procedure was repeated throughout the test period.

The data obtained was entered into a computer data file. The pressure angle for each test case was calculated by first fitting a first order polynomial to the coordinates using linear regression, and then calculating the angle between the curves. The shape was also plotted in a diagram, as shown in Figure 4.2.

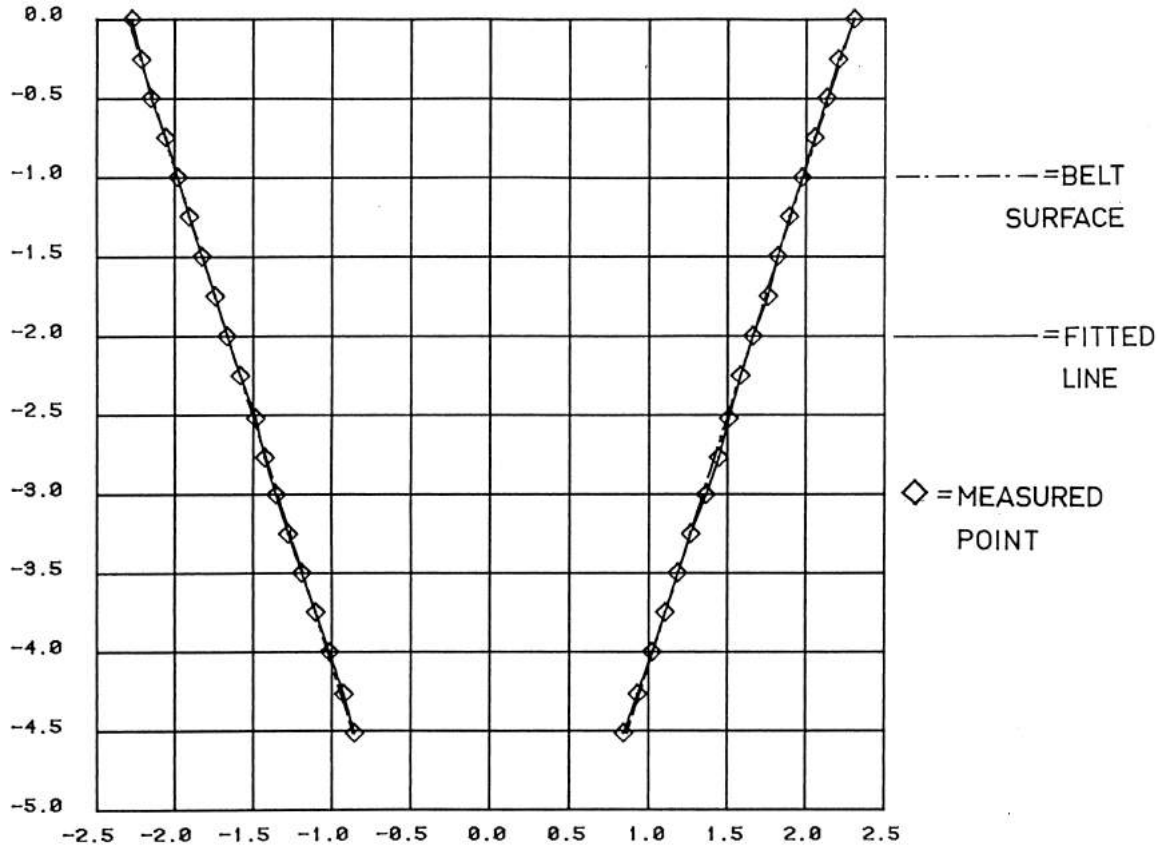

Figure 4.2 *A measurement of a belt shape and a fitted first order polynomial. The figure shows the actual shape but is shortened by 5.9 mm in the horizontal direction.*

4.3 Test series one

In this test series cases A,B,C and D were run. The readings were done after 0, 52 and 70 hours. The results are presented in the Figures 4.3 - 4.7, where only the fitted straight lines are shown. The figures are shortened by 5.9 mm in the horizontal direction. All dimensions are in mm.

From Figure 4.7 it can be seen that after 70 hours there are no differences in angle between the belt and pulley for cases A, B and C. In case D, which is the one with smoother surface, more time has to elapse before the difference becomes negligible. In Figures 4.3 to 4.6, not only can the change in angle be detected, but the whole belt becomes narrower. The temperature of the belts was about 45 degrees Celsius during the tests. Some of the heat may have come from the bearing units through the shaft and pulley. The temperature of the bearings was about 55 degrees Celsius.

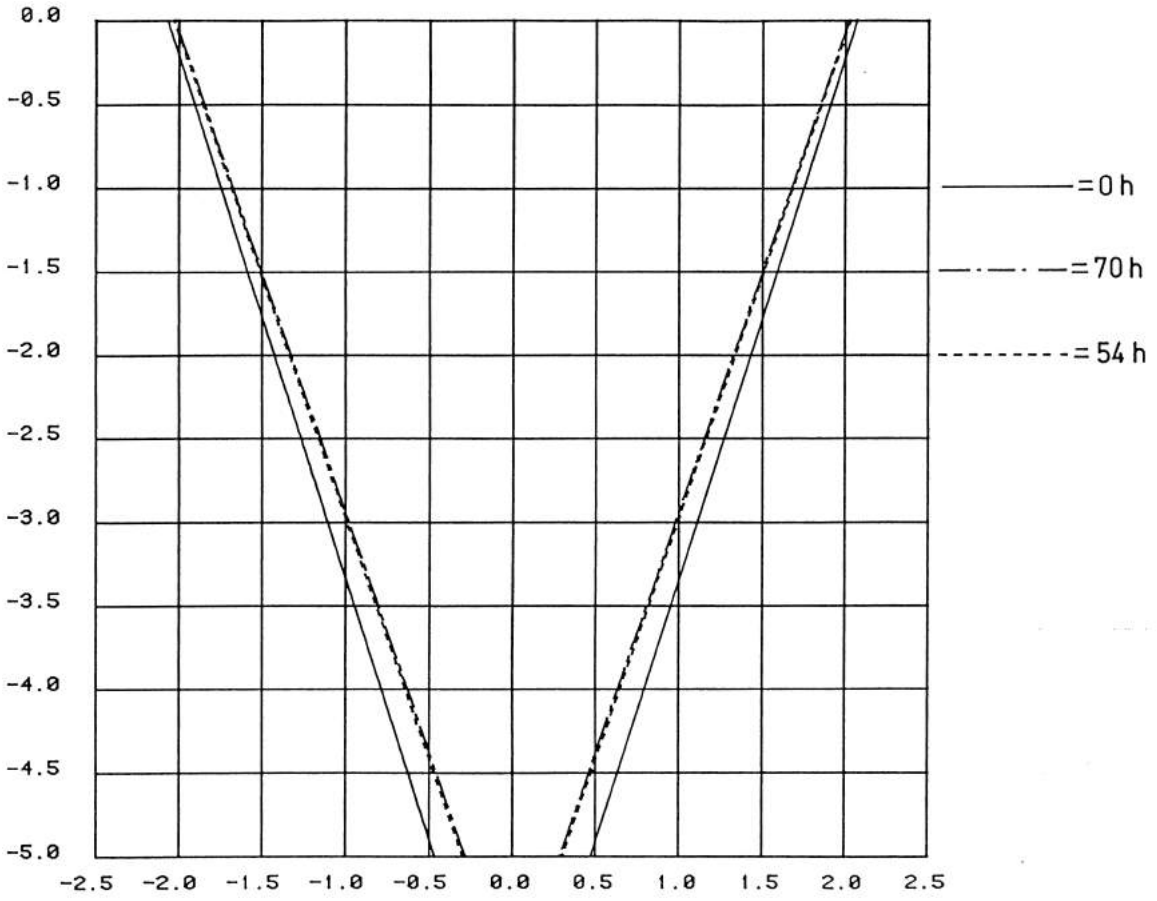

Figure 4.3 *Test series 1 and case A. Pulley angle 38.5 degrees, belt angle initially smaller.*

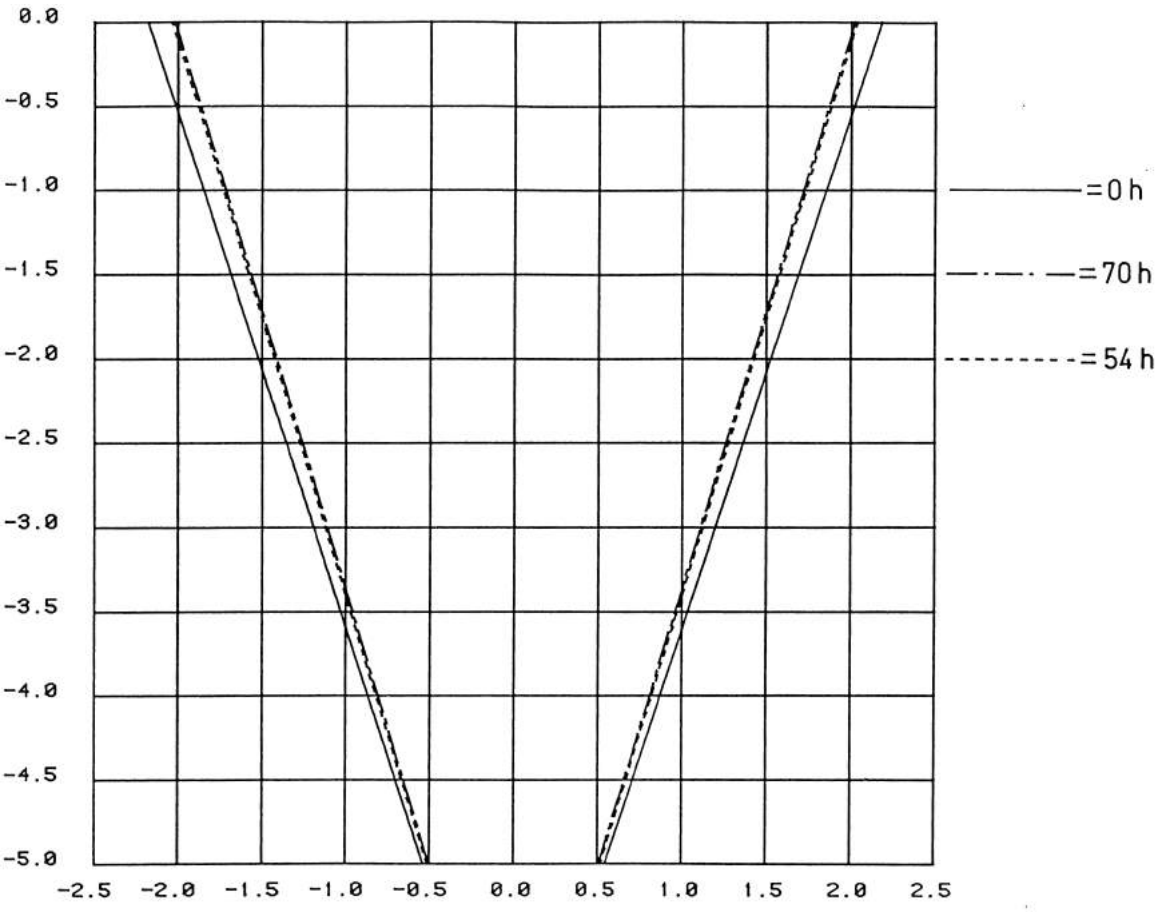

Figure 4.4 *Test series 1 and case B. Pulley angle 33.8 degrees, belt angle initially larger.*

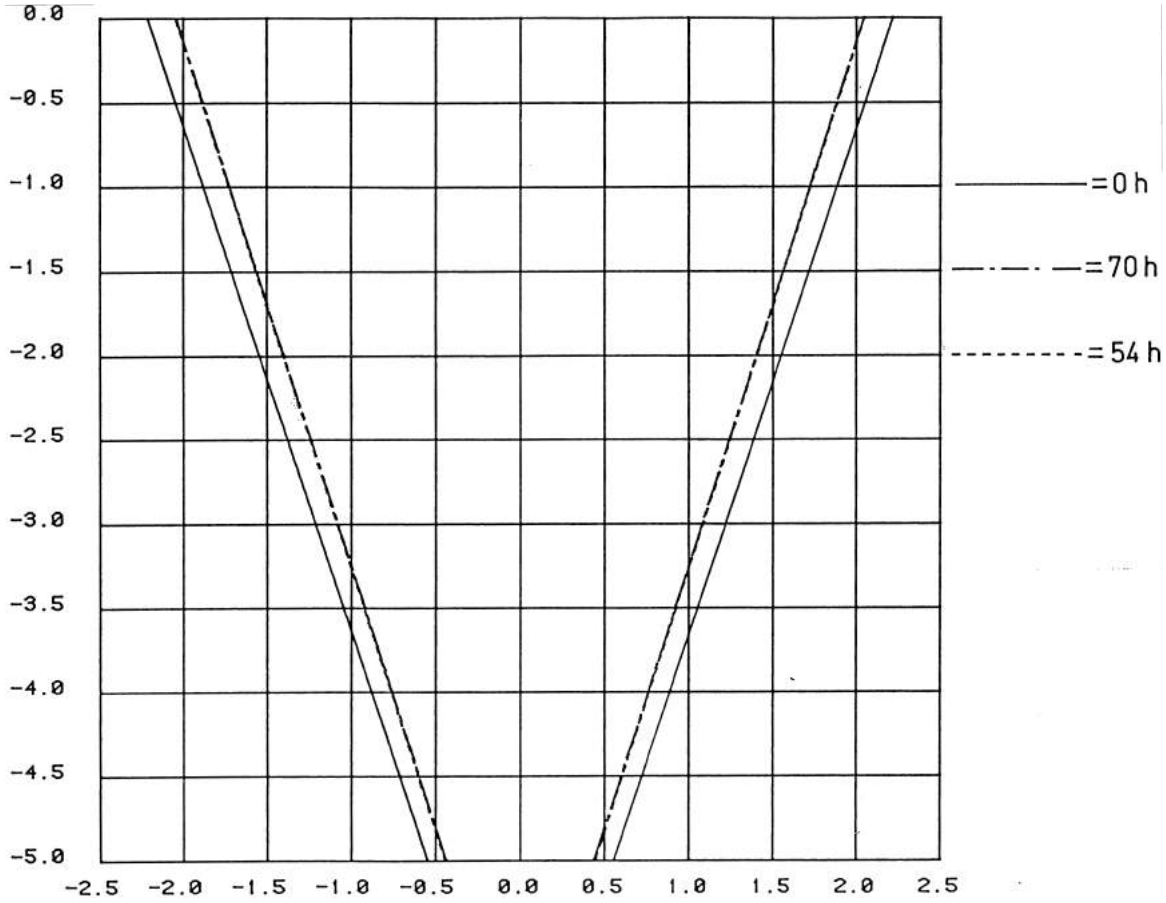

Figure 4.5 *Test series 1 and case C. Pulley angle 35.5 degrees and belt angle initially nearly the same as or slightly greater than pulley angle.*

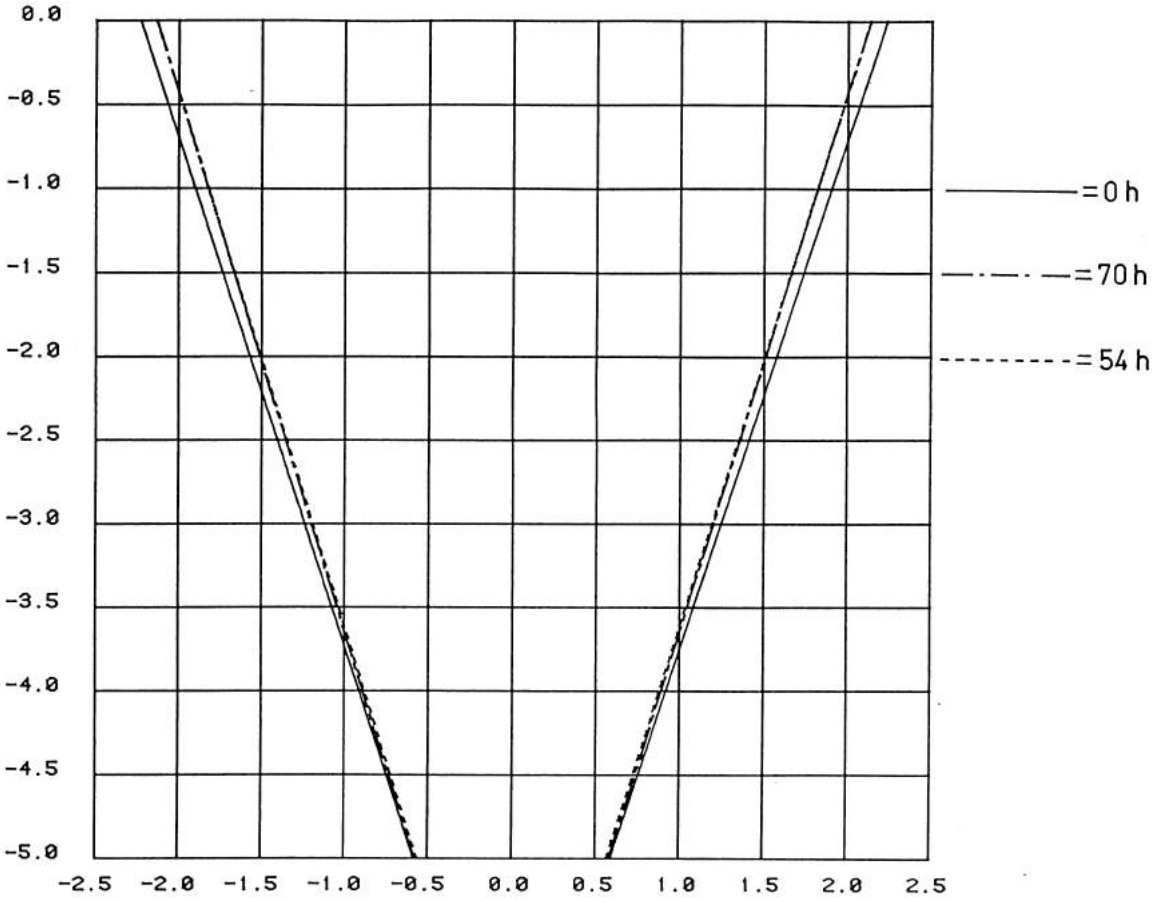

Figure 4.6 *Test series 1 and case D. Pulley angle 33.6 degrees, belt angle initially larger. The surface of the pulley is smoother than in the other cases.*

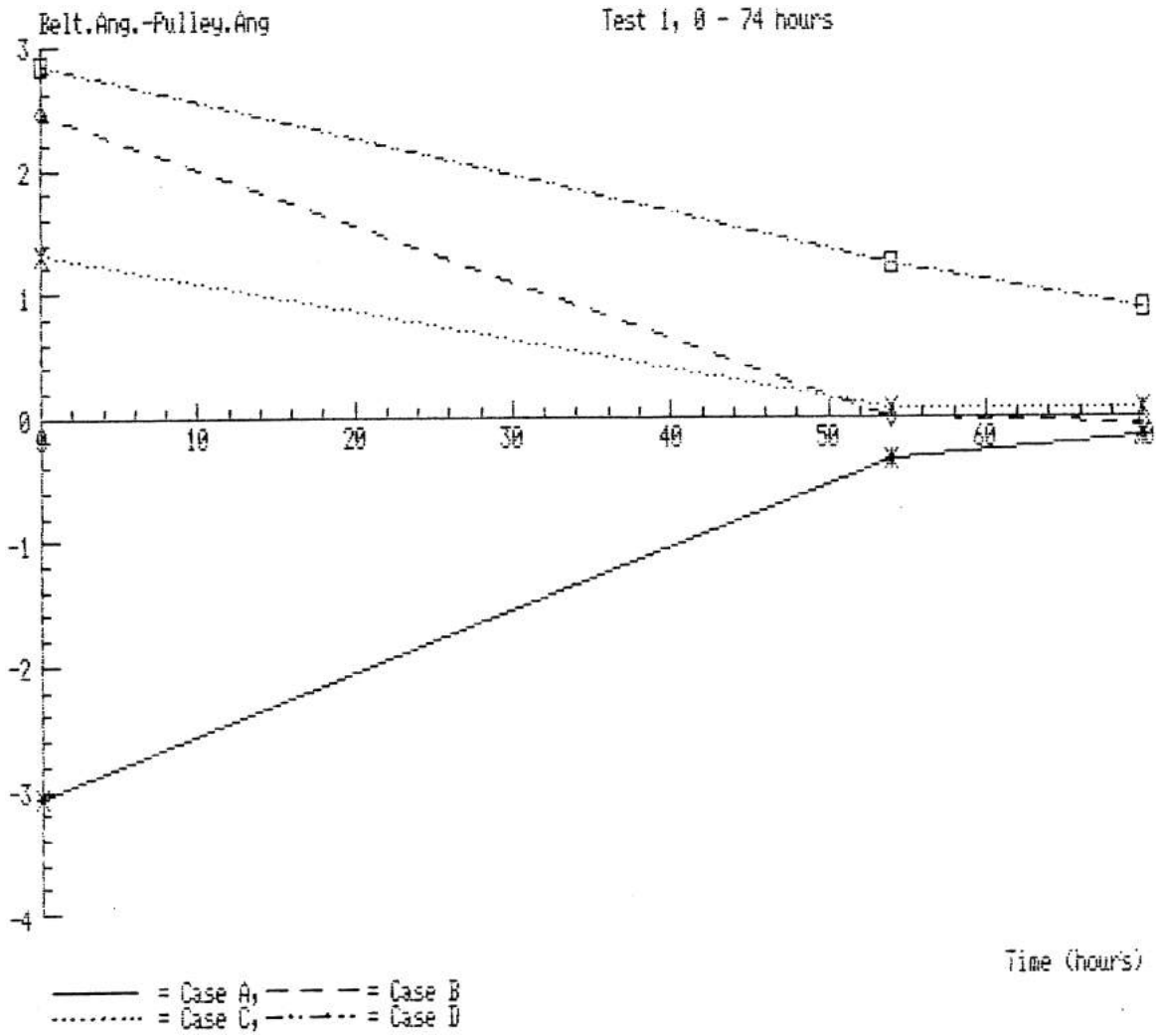

Figure 4.7 *The difference between the belt angle and pulley angle as a function of time is shown for all four test cases of test series 1.*

4.4 Test series two

From test series one it could be seen that most changes took place before the measurements were made. Therefore a second test series with shorter time intervals was performed. In this test series cases A,B and D were run. Readings were taken a 0, 1, 5.25, 10.25 and 15 hours. The results are presented as fitted straight lines in the Figures 4.8 - 4.11.

From Figure 4.11 it can be seen that the angle change rate is greatest during the first hour. Figures 4.8 to 4.10 show that most of the changes in shape and angle occur during the first hour. Later it is primarily the angle that changes and not the width of the belt. The belt temperature did not exceed 45 degrees Celsius during the test series. Some of the heat may have come from the bearing units through the shaft and pulley. The temperature of the bearing units was about 55 degrees Celsius.

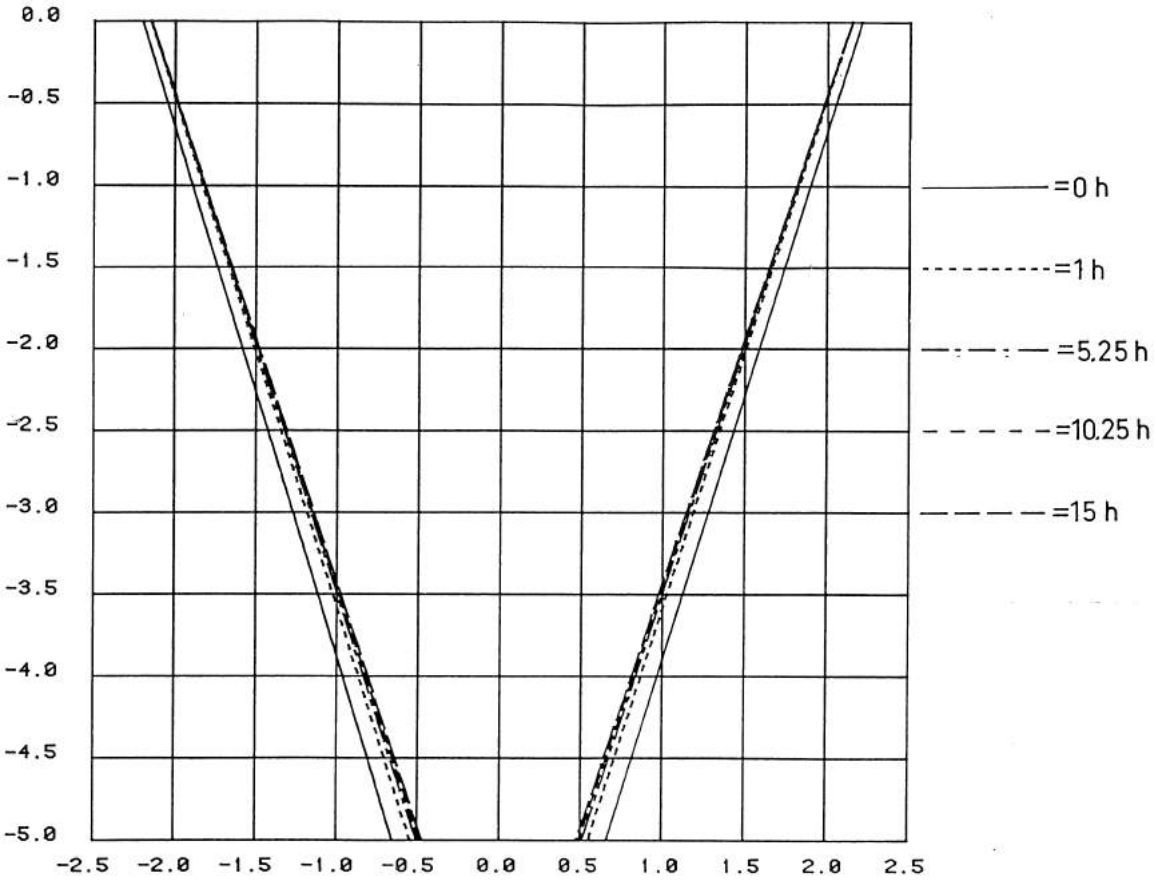

Figure 4.8 *Test series 2 and case A. Pulley angle 38.5 degrees, belt angle initially smaller.*

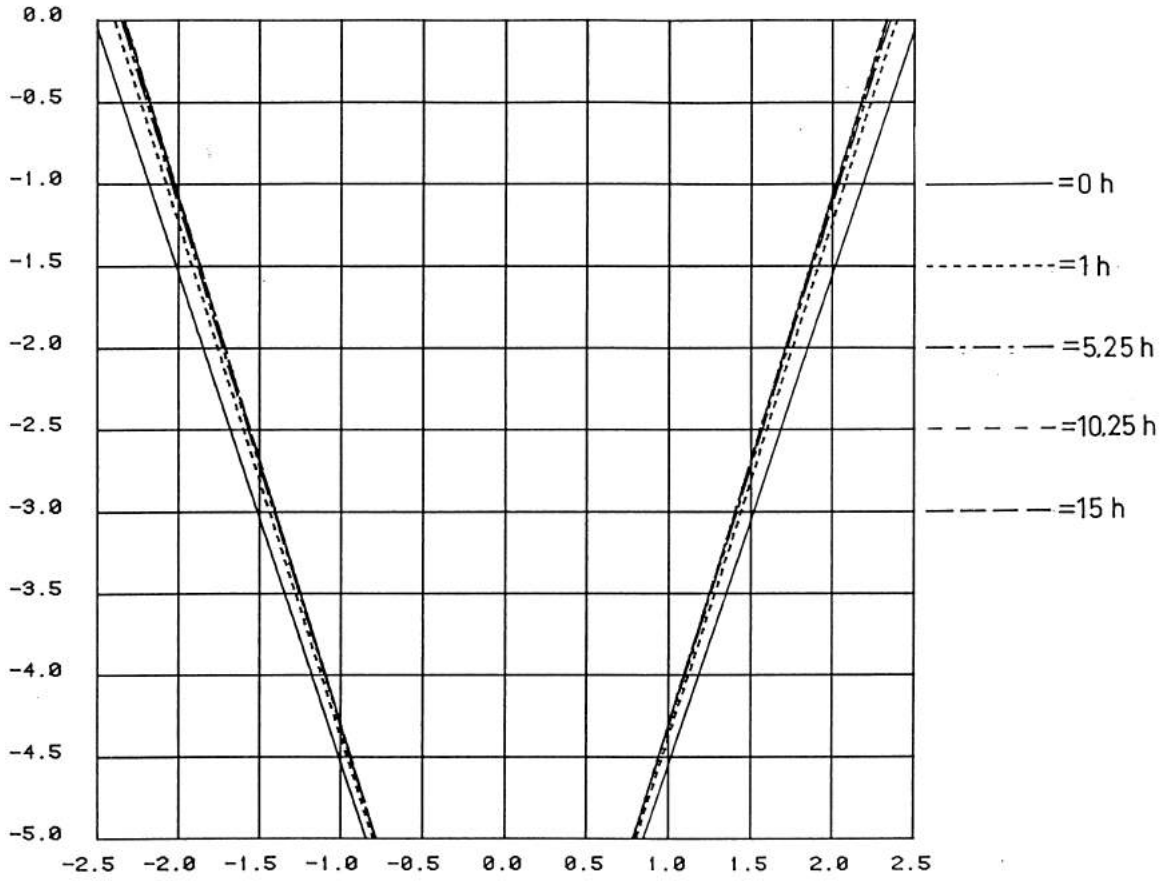

Figure 4.9 *Test series 2 and case B. Pulley angle 33.8 degrees, belt angle initially larger.*

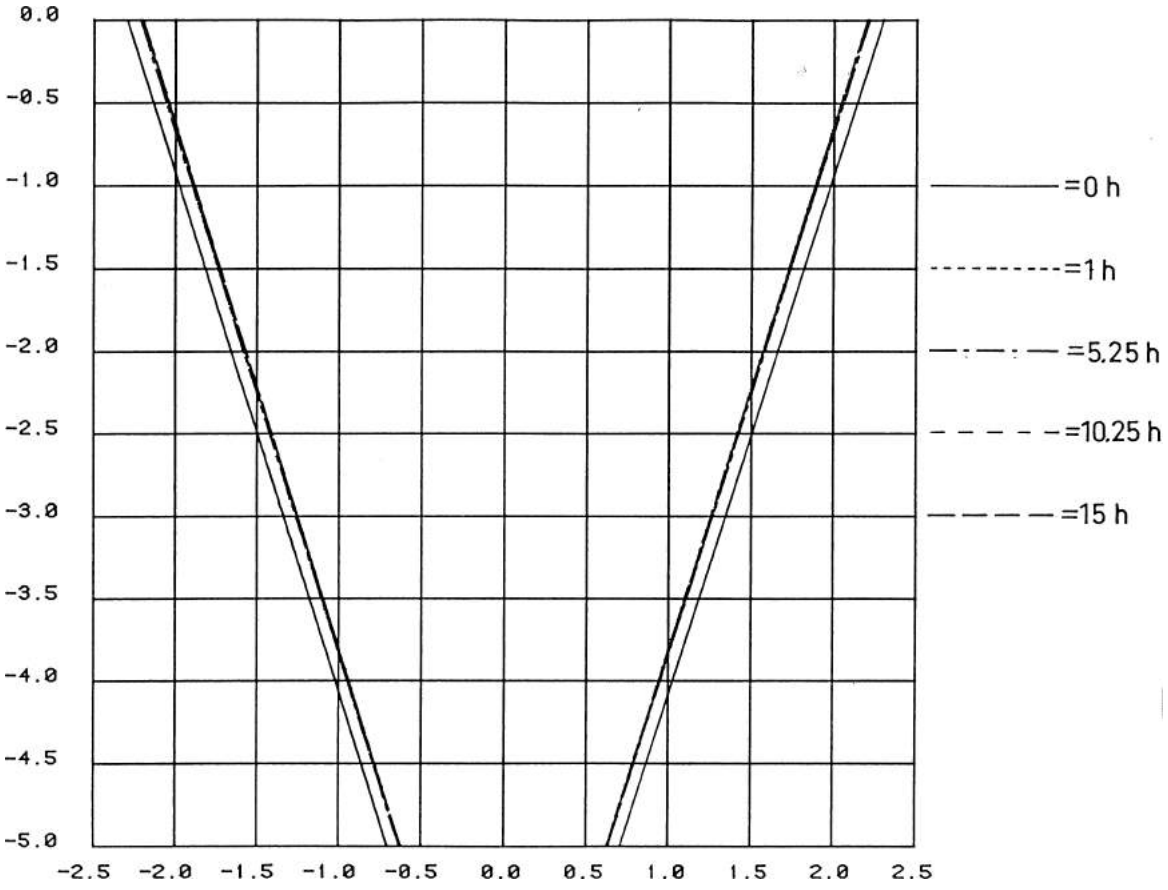

Figure 4.10 *Test series 2 and case D. Pulley angle 33.6 degrees, belt angle initially larger. The surface of the pulley is smoother than in the other cases.*

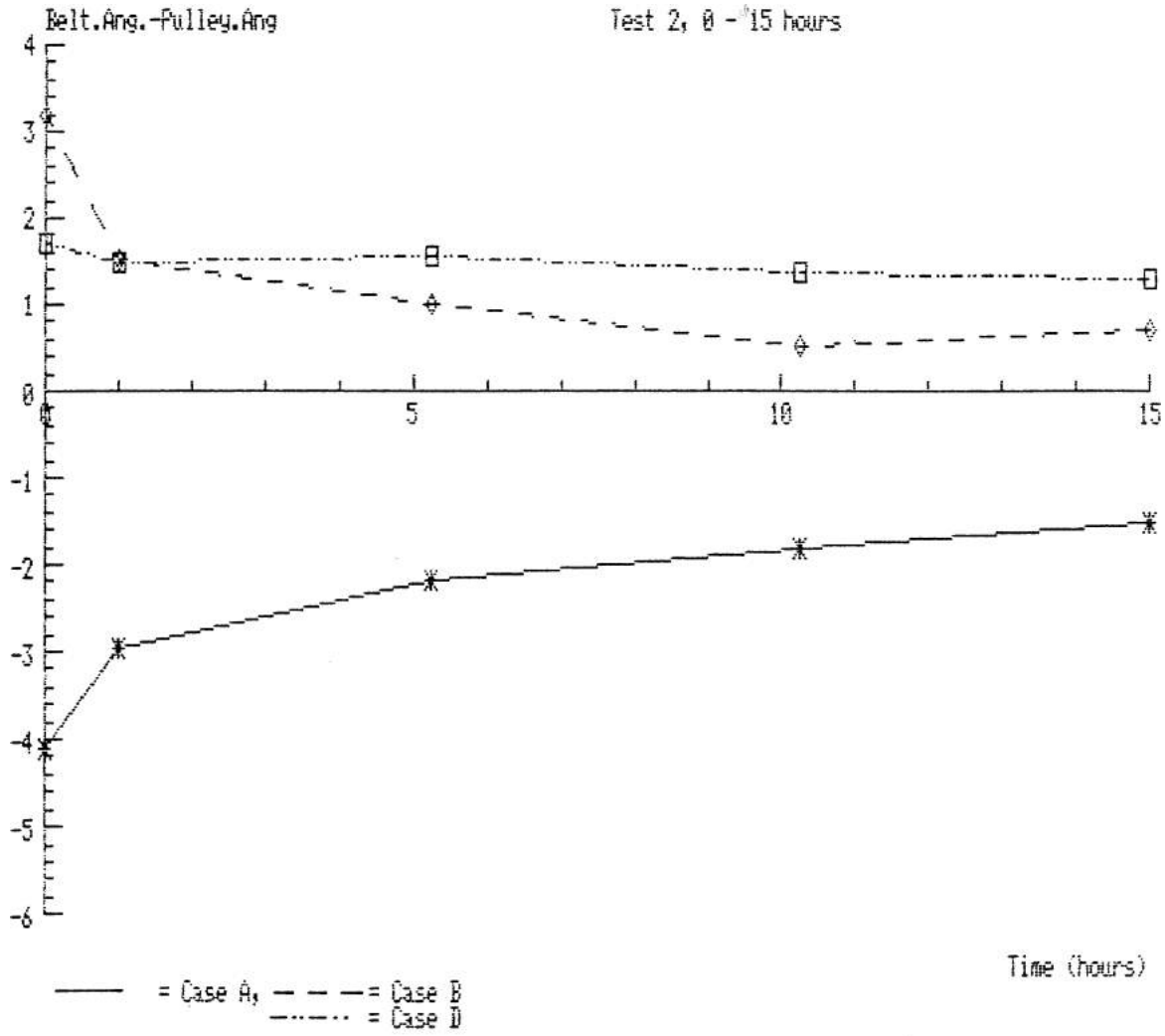

Figure 4.11 *The difference between belt angle and pulley angle is shown as a function of time for all three test cases of test series 2.*

5
Results and discussion

This investigation shows that belt geometry quickly conforms to pulley geometry. The time for this process is very short compared to a normal belt service life. The greatest changes both in width and pressure angle occur during the first hour of running time. This is also true for pressure angle deviations of plus minus 3 to 4 degrees and light load. In accordance with this result, it becomes possible to assume that the belt fits the pulley almost perfectly when calculating the pressure distribution. If the rate of the process is proportional to pressure, a logical assumption is constant pressure over the belt height.

What mechanisms cause this behavior? The presence of dust from the rubber, and the fact that surface roughness has some influence, are proof that abrasive wear is one of the mechanisms. V-belts are made of rubber composites subject to viscoelastic behavior. Therefore it may be suspected that some of the permanent changes are caused by viscoelastic creep. The question of the most important mechanism has not been investigated in this report. One way to distinguish them might be to run tests at different temperatures. Viscoelastic behavior for this kind of rubber is usually highly temperature dependent. Neither has the case of different pulley diameters in the drive been studied. It seems reasonable that the belt adapts most to the pulley where the pressure and slip are most severe.

Bibliography

[1] G. Gerbert. *Force and slip behaviour in V-belt drives*. Acta Polytechnica Scandinavica, Mech. Eng. Series No. 67. The Finnish Academy of Technical Sciences, Helsinki, Finland, 1972.

[2] C. Walther et al. *Bestämning av kilremmars dimensionsförändringar under drift. (Determination of change in V-belts shape during running conditions)*. Project of third year of MSc. studies. Göteborg, Sweden: Chalmers University of Technology, 1984.